

Synthesis and Structural Evaluation of Neutral Acyclic Receptors for Recognition of Ionic Analytes in Solid- and Solution-State

A Dissertation

*Submitted in partial fulfillment for the degree of
Doctor of Philosophy*



Ashesh Das

(Roll No. 166122101)

Thesis Supervisor: Prof. Gopal Das

**Department of Chemistry
Indian Institute of Technology Guwahati
Assam -781039, India**

Synthesis and Structural Evaluation of Neutral Acyclic Receptors for Recognition of Ionic Analytes in Solid- and Solution-State

A Dissertation

*Submitted in partial fulfillment for the degree of
Doctor of Philosophy*



Ashesh Das

(Roll No. 166122101)

Thesis Supervisor: Prof. Gopal Das

**Department of Chemistry
Indian Institute of Technology Guwahati
Assam-781039, India**

DEDICATED TO MY

FAMILY & FRIENDS



INDIAN INSTITUTE OF TECHNOLOGY GUWAHATI

Department of Chemistry

STATEMENT

I do hereby declare that the matter embodied in this thesis is the result of investigations carried out by me in the Department of Chemistry, Indian Institute of Technology Guwahati, Assam – 781039, India, under the supervision of Dr. Gopal Das, Professor, Department of Chemistry, Indian Institute of Technology Guwahati, Assam – 781039, India. In keeping with the general practice of reporting scientific observations, due acknowledgements have been made wherever this work is based on the findings of other investigators.

Date: January 2022

(Aresh Das)

Place: IIT Guwahati



INDIAN INSTITUTE OF TECHNOLOGY GUWAHATI

Department of Chemistry

CERTIFICATE

This is to certify that **Mr. Aresh Das** (Roll No. 166122101) has been working under my supervision since December, 2016 as a regular registered Ph. D. student. His thesis entitled **“Synthesis and Structural Evaluation of Neutral Acyclic Receptors for Recognition of Ionic Analytes in Solid- and Solution-State”** is an authentic record of the results obtained from the research work carried out under my supervision in the Department of Chemistry, Indian Institute of Technology Guwahati, Assam - 781039, India. I am forwarding his thesis to submit for the award of degree of Doctor of Philosophy, from this institute. I hereby certify that he has fulfilled all the requirements, according to the rules of this institute regarding the investigations embodied in his thesis and this work has not been submitted elsewhere for a degree.

Dr. Gopal Das

(Thesis Supervisor)

Professor, Department of Chemistry

IIT Guwahati, Assam - 781039, India

Acknowledgement

This opportunity to extend my gratitude should commence with my parents, whose love and inspiration has always been strength for me. Their eternal blessing and constant support has guided me this far and positively, this will take me far forward in future to achieve the success they dreamt of. I would also like to recognize my elder brother (dada) Abhisek Das, who has been a source of encouragement and inspiration throughout my life.

I wish to express my sincere gratitude towards my PhD supervisor Prof. Gopal Das, whose wide experience and personal guidance have given me freedom to think, plan and execute my ideas to develop the quality of work throughout the processes and especially for his unique style of leading the group that are reflected in happy faces of the group members. I would also like to be grateful to my doctoral committee members, Prof. Sandip Paul, Dr. Lal Mohan Kundu and Dr. Shyam P. Biswas for their advice and suggestions. I would also like to thank ex-Head Prof. T. Punniyamurthy, present-Head Prof. G. Das, scientific officer Dr. Babulal Das and other staff members of the Department of Chemistry, IIT Guwahati for providing the necessary facilities.

I take this opportunity to thank my wonderful Lab seniors Abhijit da, Barun da, Soham Da, Nilotpal da, Rupinder da, Biswajit da, Arnab da, Santanu da, Senjuti, J. K da as well the amazing Lab mates Biswajit Roy da, Debojit, Megha, Sagnik, Deepa and Debolina for their co-operation in my research work, without which it would not been easy to complete the PhD thesis. I would like to be thankful to Biswajit da (Dr. Biswajit Roy) for his constant and immense help throughout my research career. It was great to work and spend times with these interesting human beings and I will always cherish the memories of their jokes, laughter and humor throughout my life. Most of these people have a positive approach towards life and I wish them success in every aspects of their life.

Some friends without whom the list would be incomplete are, my college friend Ranajit, Purusottam, Milan, Chirantan, my childhood friends Bibek, Pradip, Nilanjan, and my school mates Indrani, Manirul, Sourav and Sayan, my research batch mates Satyajit, Gobinda, Basab, Avijit, Tanumoy, Mihir, and Nasim whose friendship had enriched my life and we often spend some good time whenever together. Still many names are missing whose contribution and help is worth mentioning.

asesh

The contents of this report entitled “**Synthesis and Structural Evaluation of Neutral Acyclic Receptors for Recognition of Ionic Analytes in Solid and Solution State**” have been divided into six chapters based on the results of experimental work performed during the research period.

Chapter 1: Introduction

This chapter comprises a brief introduction on ‘supramolecular chemistry’ concerning the recognition of ionic analytes within the preorganized cavity or self-association of artificial receptors molecule. As the anion coordination field continues to develop rapidly in the recent past, selective and specific detection of anion has appeared to be a promising and dynamic area of supramolecular chemistry due to their diverse roles in biology, medicine, catalysis, and the environment. As anions have a variety of shapes and sizes such as spherical, planar, tetrahedral, octahedral, etc. compared to only spherical metal ions, it has been always challenging and fascinating to understand these non-covalent interactions to get basic concepts about the field. Moreover, for proper as well as successful interactions, binding sites in a host molecule must have appropriate size or geometry and distinct functionalities to bind or accept the guest one induced *via* various non-covalent interactions leads to a supramolecular guest-host complex. Numerous acyclic hosts, basically simple mono podal or dipodal receptors have been planned and synthesized for anionic guests over the last two decades with multiple hydrogen-bonding interactions. Consequently, we stress the area of recent developments of rigid isomeric dipodal receptor systems basically for encapsulation or entrapment of anion/hydrated anions or anionic associations, besides few simple isomeric tripodal anion-receptor systems also in solid and solution state. Important theoretical research developed by Hay *et al* which revealed that the position of electron-withdrawing substituents on the terminal aryl moiety have significant consequences on the stability of anion complexes. Even the simplest urea and thiourea receptors derived from various synthesized single or diamine units having multi-armed H-bonding functionality did not have any promising structural identification in anion-coordination chemistry from the last decades may be ascribed to their highly electron-rich moieties and no electron-withdrawing terminal units.

A plentiful of small ions and molecules play pivotal roles in human life. They also exist in organisms and the environment. As a result, the detection of these targets is highly important. While cation such as Al^{3+} shows activities in many biological processes, such as the central nervous system of humans, and induces Alzheimer’s disease and Parkinson’s disease. Meanwhile, the widespread use of Al^{3+} in medicines (antacids), bleached flour, the paper

industry, food additives, aluminum-based pharmaceuticals, storage/ ionic form Al^{3+} cooking utensils makes it vulnerable to be exposed to the environment in its trivalent form, which often causes drinking water contamination. Whereas being an essential element in the human body, Zn^{2+} is involved in cellular metabolism, gene transcription, regulation of metalloenzymes, neurotransmission, and apoptosis. Despite its several crucial roles in many Zn^{2+} containing enzymes and DNA-binding proteins, imbalance of Zn^{2+} in the body may cause several neurological diseases. On the other hand, copper, an essential trace element of the human body and being present in the active sites of several enzymes, plays many indispensable roles to sustain important physiological processes.

Anions also have a significant role to play in various biochemical courses. For instance, pyrophosphate is a biologically essential target because it is the product of ATP hydrolysis inside a cell. Fluoride ions are biologically important as it protects teeth and is used in the treatment of osteoporosis. Anions too are known to have a hazardous nature. Exposure to the same fluoride ion causes fluorosis. Nowadays, anthropogenic activities such as heavy use of fossil fuels and industrial agriculture are known to cause the release of a high level of carbon dioxide (CO_2) into the atmosphere. So, eventually, the efficient entrapment and activation of CO_2 as bicarbonate anion, using neutral synthetic receptors, has an impactful demand in the fixation of the environmental CO_2 . On the other hand, tetrahedral sulphate (SO_4^{2-}) anions have adverse effects on the nuclear waste recovery process, while eutrophication, etc., is responsible for the accumulation of tetrahedral phosphate anions in aquatic habitats. HSO_4^- also are known to affect human health by causing breathing difficulties, burning pain in the mouth, chest pain, burning of the esophagus, diarrhea, etc. HSO_3^- is a well-known reducing agent, and under an acidic environment, releases SO_2 , which is one of the important air pollutants, predominant in the air, generating from extensive combustion of fossil fuels. However, HSO_3^- is a toxic substance with detrimental (including allergic) effects such as asthma, gastrointestinal diseases, skin allergies, DNA cleavage, and chronic bronchitis. All these discussions about the importance of ionic targets regarding their hazards and biological roles emphasize the need for the detection of these species. Since these species are potential in their action in minute scale or concentration; the detecting tools must be very sensitive either. Optical probes that selectively recognize these ionic species are known as selective probes. These probes can be classified into two categories, namely chemosensors and chemodosimeters. In a chemosensor, the concurrent recognition event is supported by the presence of fluorophore/chromophore as interaction with the guest analyte changes the electron distribution of the chemosensor. The response of which is perceived through

differential colorimetric and fluorescence signals. Whereas, chemodosimeter is that the receptor of the former is replaced by a reaction site of the latter. The reaction site undergoes a chemical reaction with the analyte. Apart from the external factors like temperature, media, etc. the selectivity of a dosimeter count on factors such as reactivity of the analyte and the specificity of the reaction.

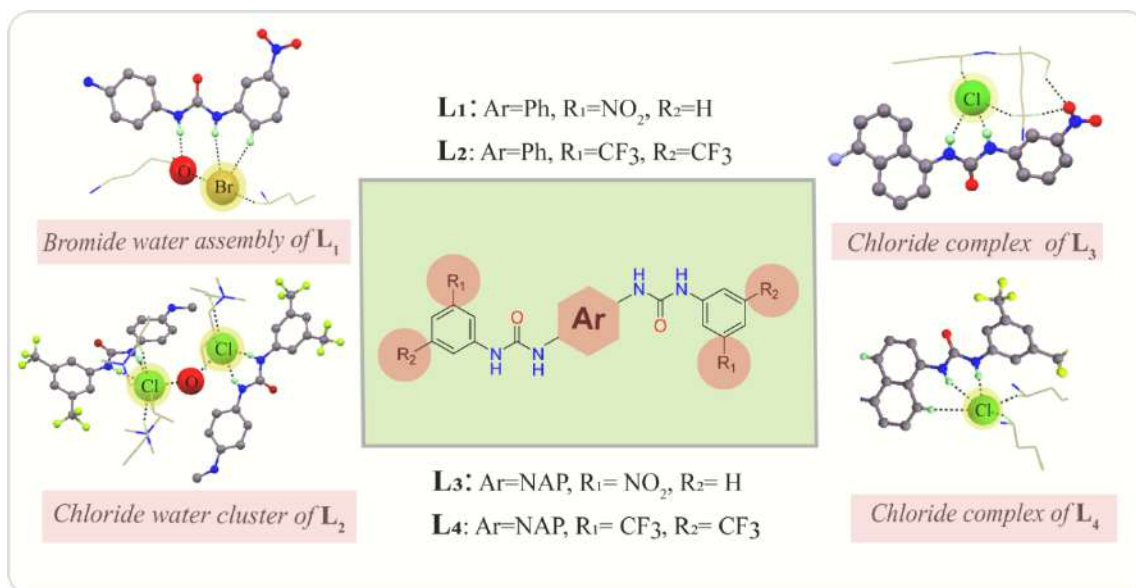
Chapter 2: Experimental methods and characterization

In this chapter, a detailed comprehensive report of the various reagents used in the synthesis of the receptors, their synthetic pathways, crystallization details, binding study, and specifications of analytical instruments employed in the characterization of receptors and their complexes.

Chapter 3: Design and Synthesis of Neutral Acyclic Receptors: A Case Study to Verify the Effect of Substitution on Halide/Hydrated Halide Binding (*CrystEngComm*, 2020, 22, 2197-220)

Four neutral dipodal receptors have been purposefully designed and synthesized by varying the substituents from phenyl to naphthyl moiety to investigate the anion coordinating activities of bis-urea receptors. Crystal structure investigation of the complexes correctly validates the fact that the receptors **L**₁–**L**₄ form halide as well as hydrated halide complexes. Most interestingly in complex **2a**, the phenyl based neutral bis-urea receptor **L**₂ binds with two chloride ions *via* participation of N–H···Cl[−] interaction from the adjacent urea group and aromatic C–H···Cl[−] interaction along with the construction of a halide–water–halide bridged architecture supported by another. Meanwhile, another phenyl-based bis-urea receptor **L**₁ binds to one bromide ion (**1b**) which is coordinated with two water molecules (from the lattice) forming a suitable 2:1 anion–receptor interaction. In all cases, the coordinated –NH protons from adjacent urea moieties play an important role in terms of coordination and are oriented in a trans fashion to the core substituent. The transformation from the phenyl to naphthyl ring shows a clear distinction in halide binding which is very much consistent with the size as well as hydrophobic nature of the substituents. From solid-state structural analysis, it also appears that the receptor lies about an inversion center in the respective complexes. ¹H NMR titration study reveals that efficient binding interaction observed for Chloride than Bromide which may be concluded from the binding constant in solution state which is consistent with their solid-state binding data. The binding interaction with halides reveals that the adjacent urea moieties orient themselves in *anti*-fashion in solid-state. The change in the

electronic nature of the terminal substituents and the core part of the receptors has made the difference in binding both in the solid and solution phase. The results obtained will help us to design new receptors for efficient binding of anions from the solution.

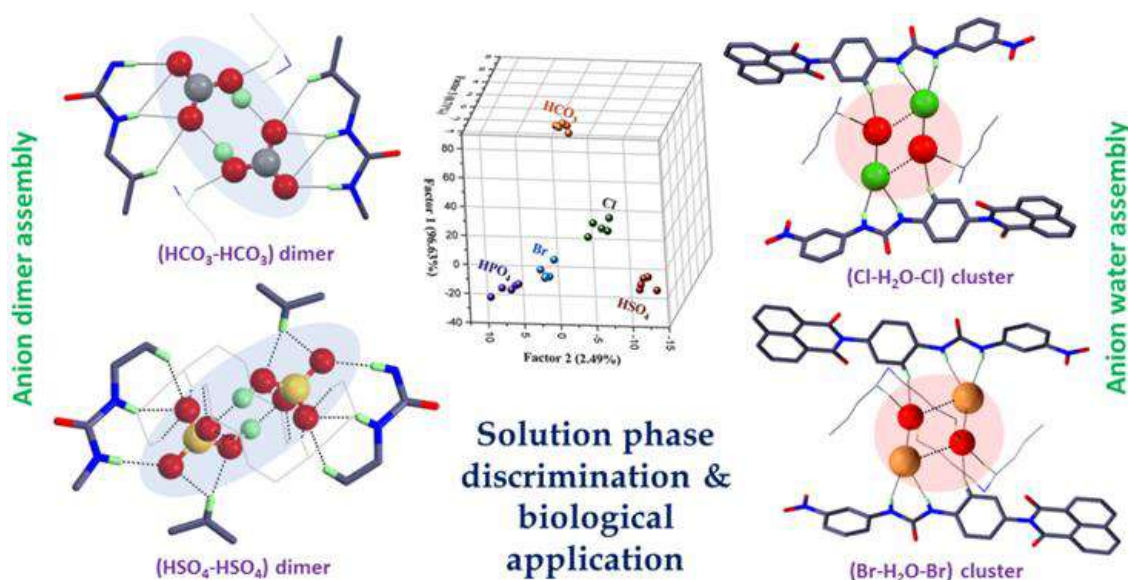


Chapter 4: Centro-Symmetric Dimeric Oxyanion Assembly Supported by Multi-arm Hydrogen Bonds (HBs): A Case Study in Linear Discriminant Analysis and as Antibacterial Agents (Under revision)

In this Chapter, Two naphthalimide based linear monourea receptors (L_5 and L_6) exhibit anion (oxyanions and halides) binding in solid and solution states. Receptor L_5 could render fluoride/hydroxide-induced aerial CO₂ fixation efficiently, leading to the air-stable assembling of di-anions enclosed by *n*-TBA cations *via* short-range hydrogen bonding interactions (HBs) in solid-state. Besides, HBs based cyclic dimeric assembly of bisulphate anion sealed by the linear tetrameric assembly of host molecule was also evidenced from solid-state architecture. Upon addition of an excess amount of chloride and bromide anion, L_5 linearly assembled to capture a cyclic chloride-water and bromide-water tetrameric cluster backed up by various solid-state H-bonding interactions.

The solid-state investigation identified the presence of $R_2^2(8)$ arrangement of centrosymmetric and cylindrical [HCO₃⋯HCO₃]²⁻ dimer (fluoride/hydroxide ion-tempted) and very familiar distorted cylindrical [HSO₄⋯HSO₄]²⁻ assembly involving anions homodimers *via* strong hydrogen bonds (HBs) interactions between the anions (O⋯O distances are 2.681 Å for planar bicarbonate dimer and 2.911 Å for tetrahedral bisulphate dimer) by overcoming the long-range repulsive interactions between the di-ions. Another notable outcome of this report involves the formation of a cyclic halide-water cluster by the linear assembled receptor

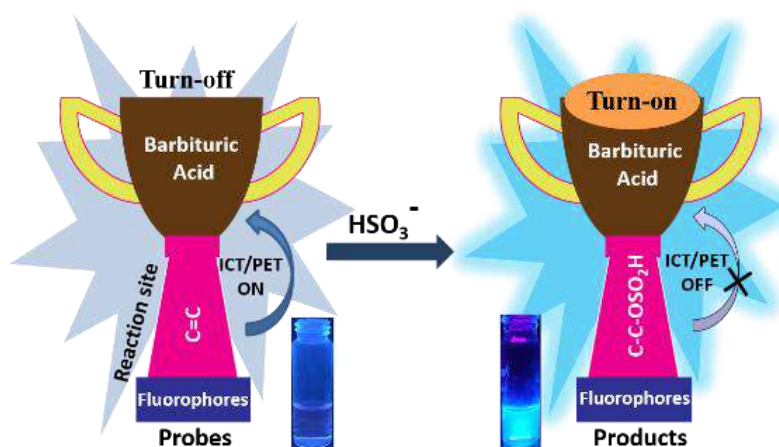
molecule as evidence from both the solid and solution phase. Nonetheless, in a hydrophobic environment, entrapped anion complexes, especially entrapped anion-water adduct complexes, are very important. Nevertheless, such complexes, especially entrapped anions and hydrated anions (halide and oxyanion both) assembly in a hydrophobic milieu, are of enormous attention and would be convenient to form novel types of host-guest assemblies. LDA analysis revealed that both the receptors were able to effectively discern, as evident from the 2D and 3D score plots, a set of five anions comprising of oxyanions and halides with all the aforementioned anions. As a matter of interest, the strong H-bonding interaction between L_5 and HCO_3^- , speculated by the NMR studies, could also be correlated with the LDA results. Interestingly, the ligands displayed antibacterial activity against model bacterial pathogens, rendering notable growth inhibition in the case of *E. coli* MTCC 433, and were non-toxic at their working concentrations. Future studies focussing on the structure-activity relationship and adjuvant activity can expand the therapeutic prospect of the ligand against pathogenic bacteria.



Chapter 5: Fluorescence ‘Switch-On’ Sensors for Selective Detection of HSO_3^- : Verifying the Reactivity of the Exocyclic Vs. Non-Exocyclic C=C Double Bond (Submitted)

The present report deals with specific colorimetric (naked-eye) and fluorometric sensing of HSO_3^- by a pair of chemodosimetric probes, namely L_7 and L_8 . The D- π -A structure-based probes exhibited an outstanding HSO_3^- -dependent response with excellent selectivity and lower detection limit values. These probes displayed colorimetric and fluorometric ‘turn-on’ responses toward HSO_3^- based on Michael-type addition reaction with very high selectivity

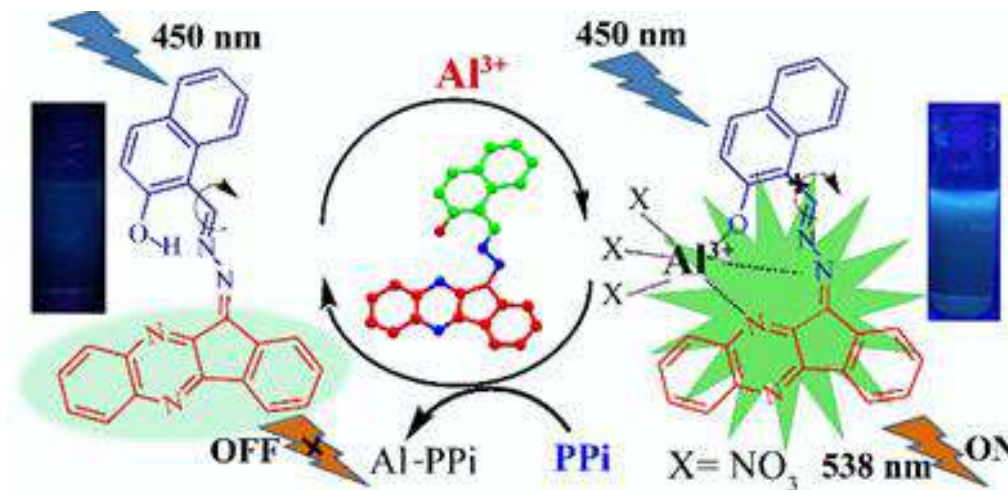
and sensitivity over other anions. Both the probes have a dynamic conjugated system with pyrene/anthracene and barbituric units connected through a C=C bond-forming D- π -A structure. Upon addition of HSO_3^- to each of the probes, the disruption of the active π - π conjugation of the C=C double bond took place, leading to a fluorescence enhancement. It is proven that the extra conjugated non-exocyclic C=C double bond (in probe **L**₈) did not take part in reaction with excesses HSO_3^- . This phenomenon substantiated that only the activated exocyclic C=C double bond was prone to any nucleophilic attack, owing to a more electrophilic nature compare to its non-exocyclic counterpart. Probe **L**₇ was proved to have a quick response time (~3 min) along with working capability in low and high pH as well. We have also performed various environmental application studies on probe **L**₇, such as the detection ability of analytes in paper strips and real water samples.



Chapter 6A: ‘CHEF’-based Sensing of Al(III) and Inorganic Pyrophosphate through OFF-ON-OFF Emission along with “Naked-eye” Detection of Cu(II) (*J. Photochem. Photobiol. A* 2021, **418, 113442)**

This chapter includes naphthyl-functionalized ninhydrin-based multi-analyte probe, **L**₉, which displayed a 'turn-on' emission response towards Al^{3+} via chelation-enhanced fluorescence (CHEF) process in a mixed medium. The probe was proved to be selective and sensitive for Al^{3+} over most of the biologically relevant cations. Upon undergoing chelation with Al^{3+} ions, the PET process gets hindered and improved structural rigidity of the overall system, leading to a remarkable emission response. This selective probe featured the fluorescence sensing of Al^{3+} with ~20 nm red-shift. A limit of detection (LOD) 1.97 μM , considerably lower than the USEPA standard for Al^{3+} in drinking water. The probe was also capable of selectively and colorimetrically detecting Cu^{2+} (LOD 0.34 μM) with a considerable red-shift (~130 nm) in the UV-vis spectra. The *in situ* prepared **L**₉- Al^{3+} complex could selectively sense phosphate ions,

particularly pyrophosphate (PP_i). The suggested detection pathway is the complexation with aluminum, followed by the decomplexation of the ensemble by PP_i anions. Interestingly, the interaction between L_9 - Al^{3+} ensemble and *ct*-DNA elicited a distinctive systematic emission 'turn-off' response from the highly emissive ensemble. The probe also found applications in testing actual aqueous samples



Chapter 6B: Chromone-based Symmetric Dipodal Probe as Multi-analytic Sensor: Prospective Chemosensing Applications under Physiological Conditions

A chromone-based symmetrical dipodal probe L_{10} was planned and synthesized for multi-analyte detection both in an aqueous and organic medium. The probe was decorated with $-\text{NH}$ functionalities to attain fluorescence indications upon binding with basic anion; the detection ability of the probe for fluoride ions in the organic medium was studied using 'turn-off' emission change with the limit of detection as low as 6.8×10^{-8} M as well as a visual change in color from yellow to reddish-pink under UV light. The *in situ* prepared [$\text{L}_{10}\text{-F}$] adducts could potentially sense Zn^{2+} ions with a 'turn-on' response *via* the metal-induced release of the free probe. Interestingly, as a multiple analyte sensor, L_{10} could display an excellent 'turn-on' emission response towards Al^{3+} *via* chelation-enhanced fluorescence (CHEF) process in a fully aqueous medium. This probe included the fluorescence sensing of Al^{3+} with ~ 15 nm red-shift with a limit of detection (LOD) of $6.9 \mu\text{M}$, considerably lower than the USEPA standard for Al^{3+} in drinking water. Moreover, the *in situ* prepared [$\text{L}_{10} - \text{Al}^{3+}$] complex could selectively sense phosphate ions, particularly pyrophosphate (PP_i) anion in the identical experimental conditions. The suggested detection pathway is the complexation with aluminum, followed by the decomplexation of the ensemble by PP_i anions. The

spectroscopic analyses were recorded to support the recognition mechanism of the aforementioned analytes by the reported probe molecule **L**₁₀.



Conclusion and Future scope

In summary, this report provides some significant outcomes in the field of 'supramolecular anion recognition chemistry' where the anions or the hydrated anions or anionic associations are formed by some simple isomeric monopodal or dipodal artificial acyclic receptors (**L**₁-**L**₆) decorated by the positional or electronic effect of terminal aryl substituents or anionic dimension or molecular host architectures in solid-state. Interestingly the dipodal receptors **L**₁-**L**₄ formed various halides/hydrated halide complexes whereas, among simple monopodal receptors **L**₅ and **L**₆, only **L**₅ was able to form $[\text{HCO}_3 \cdots \text{HCO}_3]^{2-}$ as well as $[\text{HSO}_4 \cdots \text{HSO}_4]^{2-}$ dimeric assembly which got stabilized by various non-covalent interactions. Although both the receptors **L**₅ and **L**₆ also showed the tendency to form various halides/hydrated halides complex like **L**₁-**L**₄. On the other hand, two simple reaction-based chemodosimeter namely, **L**₇ and **L**₈, were designed to verify the reactivity of C=C double bonds towards sensing of HSO_3^- through colorimetric and fluorimetric response.

Finally, we are interested in detecting the anions through some different techniques. So consequently, **L**₉ was synthesized and the same displayed a selective 'turn-on' emission response towards Al^{3+} via chelation-enhanced fluorescence (CHEF) process with colorimetric detection of Cu^{2+} . The in situ prepared **L**₉- Al^{3+} complex could selectively sense phosphate ions, particularly pyrophosphate (**PP**_i). The suggested detection pathway is the complexation-decomplexation pathway. Another probe **L**₁₀ was found to detect Al^{3+} and F^- followed by subsequent detection of **PP**_i and Zn^{2+} through fluorescence emission response.

Throughout the thesis we have focused on synthesis of simple dipodal or monopodal acyclic receptors to detect various biologically important anions in both solid- and solution-phase. But currently we are putting more efforts on synthesis of multi-arm or cyclic receptors in order to check the response towards various ionic species. So that we can introduce more applications in terms of catalyst, membrane transport etc. which are considered to be the most versatile area in supramolecular chemistry. We believe that designing novel anion receptors and its binding study would contribute to both solid state chemistry and analytical chemistry community for enhancing cognizance and development in the particular field of research.

Chapter 1: Introduction

1.1. Supramolecular Chemistry: A brief overview of Host-guest chemistry	1
1.2. Molecular recognition	2
1.3 Outline of Anion recognition chemistry	2
1.3.1 Logic behind the targeting of anions	3
1.3.2 Anion receptor chemistry: Fundamental concept on anion binding studies	3
1.4 Why rigid aromatic diamine as the core agents?	7
1.5 Advantages of fluorescence-based methods for detection of anionic guest	11
1.6 Receptor design	11
1.7 Probe selectivity: what is chemosensor and chemodosimeter?	11
1.8 Various types of reaction mechanism contribute to sensing	14
1.9 Chemosensor for anionic guest	15
1.10 Chemodosimetric detection of anionic guest	16
1.11 Fluorometric detection of metal ion	17
1.12 Concluding Remarks and objective of the thesis	20
References	22

Chapter 2: Experimental Methods and Characterization

2.1. Materials	25
2.2. General Methods	25
2.3. Synthesis and characterization of the compounds (L ₁ - L ₁₀)	26
2.3.1 Synthesis and characterization of receptors L ₁ - L ₂	26
2.3.2 Synthesis of receptors L ₃ - L ₄	26
2.3.3 Synthesis & characterization of anion bound complexes (L ₁ , L ₂)	27
2.3.4 Synthesis and characterization of anion bound complexes (L ₃ , L ₄)	29
2.3.5 General method for the preparation of receptors L ₅ and L ₆	30
2.3.5.1 Synthesis and characterization of L ₅ and L ₆	30
2.3.5.2 Synthesis & characterization of anion bound complexes 5a-d , 6a-d	31
2.3.6 Synthesis and characterization of probes L ₇ and L ₈	33
2.3.6.1 Synthesis of 5-(pyrene-2-ylmethylene) pyrimidine-2, 4, 6(1H, 3H, 5H)-trione (L ₇)	33
2.3.6.2 Synthesis of (E)-5-(3-(anthracene-9-yl) allylidene) pyrimidine- 2, 4,	33

6(1H, 3H, 5H)-trione (L₈)	
2.3.7. General methods for Synthesis of probe L₉	34
2.3.7.1 Synthesis of Compound A	34
2.3.7.2 Synthesis of Compound B	34
2.3.7.3 Synthesis and characterization of the probe L₉	35
2.3.8 Synthesis and characterization of probe L₁₀	35
2.4. Crystallographic refinement data	36
2.5. UV–Vis and Fluorescence Spectral Studies	37
2.6. Multivariate experimental set-up	37
2.7. Antibacterial Activity of Ligands and Complexes	37
2.8. Cytotoxic Effect of Ligands and Complexes	38
2.9. Evaluation of the Apparent Binding constant	38
2.10. Finding the detection limit	39
2.11. Quantum yield calculation	40
2.12. Time response study and rate constant determination	40
2.13. Details of computational analysis	40
2.14. Interaction and tracking calf thymus DNA (<i>ct</i> -DNA)	40
References	70

Chapter 3: Design and Synthesis of Neutral Acyclic Receptors: A Case Study to Verify the Effect of Substitution on Halide/Hydrated Halide Binding

3.1. Background and Focus of the Chapter	71
3.2. Design principle of the dipodal receptors L₁-L₄ and structural aspect of anion coordination	72
3.2.1. Structural analysis of halide bound complexes of L₁, L₂, L₃, L₄	73
3.2.1.1 Comparative Structural Analysis Chloride complex [(<i>n</i> -TBA) ₂ {(L₁)(Cl) ₂ }] (1a) and [(<i>n</i> -TBA) ₂ {(L₂)(Cl) ₂ (H ₂ O)}] (2a)	73
3.2.1.2 Comparative Structural Analysis Bromide complex [(<i>n</i> -TBA) ₂ {(L₁)(Br) ₂ (H ₂ O) ₂ }] (1b) and [(<i>n</i> -TBA) ₂ {(L₂)(Br) ₂ }] (2b)	75
3.2.1.3 Comparative Structural Analysis Chloride complex [(<i>n</i> -TBA) ₂ {(L₃)(Cl) ₂ }] (3a) and [(<i>n</i> -TBA) ₂ {(L₄)(Cl) ₂ }] (4a)	76
3.2.1.4 Comparative Structural Analysis Bromide complex [(<i>n</i> -TBA) ₂ {(L₃)(Br) ₂ }] (3b) and [(<i>n</i> -TBA) ₂ {(L₄)(Br) ₂ }] (4b)	77

3.3. ¹ H NMR study of dipodal complexes in solution	78
3.4. Conclusion	80
References	81
Annexure 3	83

Chapter 4: Centro-Symmetric Dimeric Oxyanion Assembly Supported by multi-arm Hydrogen Bonds (HBs): A Case Study in Linear Discriminant Analysis and as Antibacterial Agents

4.1 . Background and Focus of the Chapter	95
4.2. Structural aspects of anion binding with L₅-L₆	96
4.2.1 Solid-state evidence of HBs based anion···anion dimer formation	97
4.2.2 Structural analysis of anion bound complexes of receptors L₅ and L₆	99
4.2.2.1 A comparative structural analysis of complexes 5a and 5b	99
4.2.2.2 Structural analysis of cyclic hydrated-chloride complex (5c)	102
4.2.2.3 Cooperative <i>vs.</i> non-cooperative binding in Bromide complexes (5d , 6d)	103
4.2.2.4 Effect of electronic substitution on anion coordination	105
4.2.2.5 Comparative anion interaction studies of the complexes in solution state	105
4.2.2.6 Hirshfeld Surface Analyses	107
4.2.2.7 Discrimination among anions using multivariate analysis	109
4.2.2.8 Antibacterial and Cytotoxic Potential	110
4.3 Conclusion	112
References	113
Annexure 4	115

Chapter 5: Selective Chemodosimetric ‘Turn-On’ fluorescence sensor for HSO₃⁻ : Comparing the reactivity of the exocyclic *vs.* non-exocyclic C=C double bond

5.1. Background and Focus of the Chapter	131
5.2. Results and discussion	132
5.2.1 The rationale behind designing the probes for HSO ₃ ⁻ detection	132
5.2.2 The selective colorimetric response towards HSO ₃ ⁻	133
5.2.3 Selective Fluorescence Response towards HSO ₃ ⁻	135

5.2.4 Interference studies and Effect of pH	138
5.3. A plausible mechanism of bisulphite sensing	139
5.4. DFT studies of probes and their HSO ₃ ⁻ adduct	142
5.5. Application of HSO ₃ ⁻ detection in paper strips, real water sample	143
5.6 Determination of bisulphite in real food sample	145
5.7. Conclusion	145
References	145
Annexure 5	147

Chapter 6A: ‘CHEF’-based Sensing of Al(III) and Inorganic Pyrophosphate through OFF-ON-OFF Emission along with “Naked-eye” Detection of Cu(II)

6A.1. Background and Focus of the Chapter	157
6A.2. Structural aspects of the chemosensor L₉	158
6A.3. Crystal structure of the chemosensor L₉	159
6A.4. Optical studies	159
6A.4.1 Selective colorimetric response towards Cu ²⁺ ion	159
6A.4.2 Selective fluorescence 'turn-on' response towards Al ³⁺ ion	160
6A.5 Plausible binding mechanism	162
6A.6 Plausible sensing mechanism	163
6A.7 Detection of Al ³⁺ in real water samples and paper strips	165
6A.8 Application of the L₉ - Al ³⁺ ensemble on anion and <i>ct</i> -DNA binding studies	167
6A.9 Conclusion	170
References	171
Annexure 6A	172

Chapter 6B: Chromone-based Symmetric Dipodal Probe as Multi-analytic Sensor: Prospective Chemosensing Applications under Physiological Conditions

6B.1. Background and Focus of the Chapter	179
6B.2. Structural aspects of the chemosensor L₁₀	180
6B.3 Optical studies in presence of analytes	180
6B.3.1 Absorption Studies towards F ⁻	180
6B.3.2 Fluorescence “off-on” response for Al ³⁺	182
6B.3.3 Fluorescence “on-off” response for F ⁻	184

6B.4 Plausible binding mechanism of L ₁₀ with Al ³⁺	185
6B.5 Plausible sensing mechanism of L ₁₀ with F ⁻	186
6B.6 Application of the [L ₁₀ - Al ³⁺] Ensemble on Anion Studies	186
6B.7 Application of the [L ₁₀ - F ⁻] Ensemble on Metal Studies	187
6B.8 Conclusion	189
References	190
Annexure 6B	191
Conclusion and Future prospective	197
Curriculum Vitae	199

Chapter 1

Introduction



1.1 Supramolecular Chemistry: A brief overview of Host-guest chemistry

Supramolecular Chemistry is defined by a very popular quote of a pioneer Nobel laureate chemist, Jean-Marie Lehn: “*the chemistry beyond the molecule, having a higher number of ordered complexity originated from the association of two or more chemical subunits connected by various types of intermolecular forces*”. One can also use some other phrases like “the chemistry of the noncovalent bond” and “non-molecular chemistry”. The field of supramolecular chemistry broadly deals with various types of weaker and reversible forces that have an important role to associate various discreet molecular species in host-guest self-assembly such as H-bonding, ion-ion, ion-dipole interactions, π - π interactions, anion- π interactions, Van-der Waals forces, hydrophobic effect, etc.^{1.1-1.3} where the traditional chemistry mainly focuses on the covalent bond and coordination based interactions. So it has been always challenging and fascinating to understand these noncovalent interactions to get basic concepts about the field. Basic concepts which are widely examined in supramolecular chemistry majorly include molecular self-assembly, molecular recognition, host-guest chemistry and dynamic molecular architecture (Fig. 1.1).^{1.4-1.6} Where in the elementary sense, the relatively larger molecule is considered as ‘host’ while the smaller one is its ‘guest’. In another way, a host molecule is believed to have an effective binding unit (e. g. H-bond donors, Lewis base donors such as an enzyme or synthetic cyclic/acyclic compounds etc.) and the guest molecules should have the binding ability in the complex (e.g. H-bond acceptor entities like simple inorganic anion, anion-water cluster or anionic assembly, any mono-atomic cation, or a very sophisticated molecule such as hormone, pheromone).^{1.7} Moreover, for proper as well as successful interactions, binding sites in a host molecule must have appropriate size or geometry and distinct functionalities to bind or accept the guest one induced via various non-covalent interactions leads to a supramolecular guest-host complex. According to another pioneer supramolecular chemist (Nobel laureate) Donald Cram, “A host-guest relationship involves a complementary stereo-electronic arrangement of binding sites in host and guest”. In the view of thermodynamic stability of a supramolecular host-guest complex can be enhanced by the use of a macrocyclic effect or a chelate effect. When cyclic host molecules with related types of binding sites are compared to acyclic hosts molecules, it is clear that the macrocyclic effect makes cyclic hosts such as crown ethers up to 10^4 times more stable than acyclic hosts. As a result, the interactions of guests residing in the pre-organized macrocyclic cage are comparatively straightforward to understand but the case for acyclic receptors remain more elusive. The idea of host preorganization, which is the modification of conformational change in

response to guest binding, has emerged as a central concept that exemplifies a significant increase in the total free energy of guest complexation.

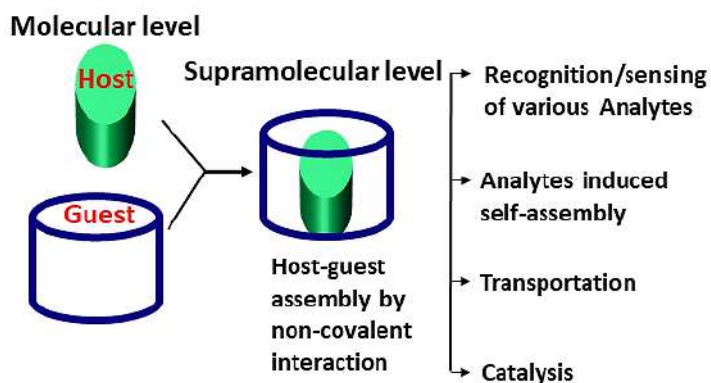


Figure 1.1 Molecules to structured assemblies in Host-guest complex

1.2 Molecular recognition

The fundamental concepts of supramolecular chemistry originated from molecular recognition where molecular receptors efficiently bind a substrate to produce supramolecule upholding the “lock and key” principle. Molecular recognition is facilitated by a variety of molecular interactions, including electrostatic, van der Waals, hydrophobic, and hydrogen bonding interactions. For a proficient recognition, proper designing of the receptor is very important to compliment the substrate to be captured and a balance between the conformation as well as configuration makes the process easy and effortless. Co-operativity of the binding units from the complementary host and guest molecules, preorganization of the host molecule, supportive assistances from these relationships may also regulate the degree of selectivity and efficacy in the molecular recognition process.^{1.8} Moreover, the extend of complementarity of the host molecule increase the binding energy of the host-guest complex. For a successful complexation, the combined contribution of steric as well as proper electronic charge distribution from guest surface to host cavity encouraged by various non-covalent interactions between two molecules associated in binding, play an important role. In addition, to afford the maximum supramolecular attractive forces, spatial arrangement of the guest and host molecules are very crucial while diminishing the repulsive forces.^{1.9}

1.3 Outline of Anion recognition chemistry

1.3.1 Logic behind the targeting of anions

Anion recognition has become an emerging area in the past year due to its omnipresence throughout the biological system and its essential roles in our bodies along with its ubiquity in the climate. The prime carrier of genetic information (DNA) and the elementary transporter of

energy (chemical) in a living organism adenosine triphosphate, ATP (70% of various enzyme-substrate as well as cofactors) are anionic. Iodide and bicarbonate are involved in hormone biosynthesis in the thyroid gland and pH control, respectively, while cellular chloride concentrations are leading to a variety of diseases, including cystic fibrosis (CF).^{1.10-1.11} Acid rain contains anions such as sulphate and nitrate, and improper use of fertilizers containing phosphates and nitrates can cause eutrophication of lakes and other waterways.^{1.12} Cyanide is considered to be an extremely toxic agent which inhibits the cellular respiratory system through binding with the heme unit of the cytochrome c oxidase enzyme. Arsenate is a naturally occurring polluting agent that can diverse the blood flow circulation through vascular disease.^{1.13} Thus as the negative effect of certain anions cannot be neglected the selective detection of anions has become an essential area in supramolecular chemistry in recent times due to its important contribution in biological, medicinal, catalysis as well as environmental processes. Considering all the adverse and beneficial impacts of anions, it has turned out to be an intense inspiration that has insistently convinced investigation of recognizing and sensing anionic moieties.

1.3.2 Anion receptor chemistry: Fundamental concept on anion binding studies

In contrast to simple transition-metal chemistry, the binding coordination of anionic guest with synthetic host molecules (receptors) is defined as "supramolecular chemistry". The initial development of anion recognition chemistry was quite slow due to relatively larger size, diffuse nature compares to isoelectronic cations, flexible geometries, narrow pH response, the higher degree of hydration energy, large polarisable nature of anion make it less effective for electrostatic interactions.^{1.2-1.3} Despite having these essential problems, anion-receptor chemistry got acceleration by overcoming all the basic difficulties. However, most of the electrostatic interactions are not found to follow a definite direction but it is possible to achieve anion-bound complexes supported by the difference in charge distribution throughout the overall framework without the interference of any electrostatic ionic forces. Thus the major foundation of binding or recognition of the anionic guest utilizing the neutral receptor molecules relies on various electrostatic connections, H-bonding, hydrophobic interactions, metal coordination and their combination.^{1.14} Recent year anion receptor chemistry has become a primary subject in biology where a minimum of 14 mitochondrial transporter system of proteins has been studied till now that can facilitate various biological cell transport through phospholipid bilayers. Out of them, some important systems become responsible for the trafficking of ADP, phosphate, ATP, citrate, glutamate, fumarate, sulphate, oxaloacetate halide anions and maleate. Fig. 1.2 reveals

that X-ray structural analysis has directly supported the understanding and basic concept of enzymatic substrate consisting of anions that are connected via several hydrogen-bonding interactions.

Jean-Marie Lehn first (as early as 1978) suggested the anion recognition chemistry as “anion coordination chemistry” which is being already referred to by many researchers working on that area.^{1,15,1,16} He has established many outcomes between the supramolecular anion chemistry and the simple transitional metals-based coordination chemistry. He has also demonstrated how the systematic examination of proper size, preorganization properties, and charge complementarity, and hydrogen bonding effect has a vital contribution in the anion binding process.

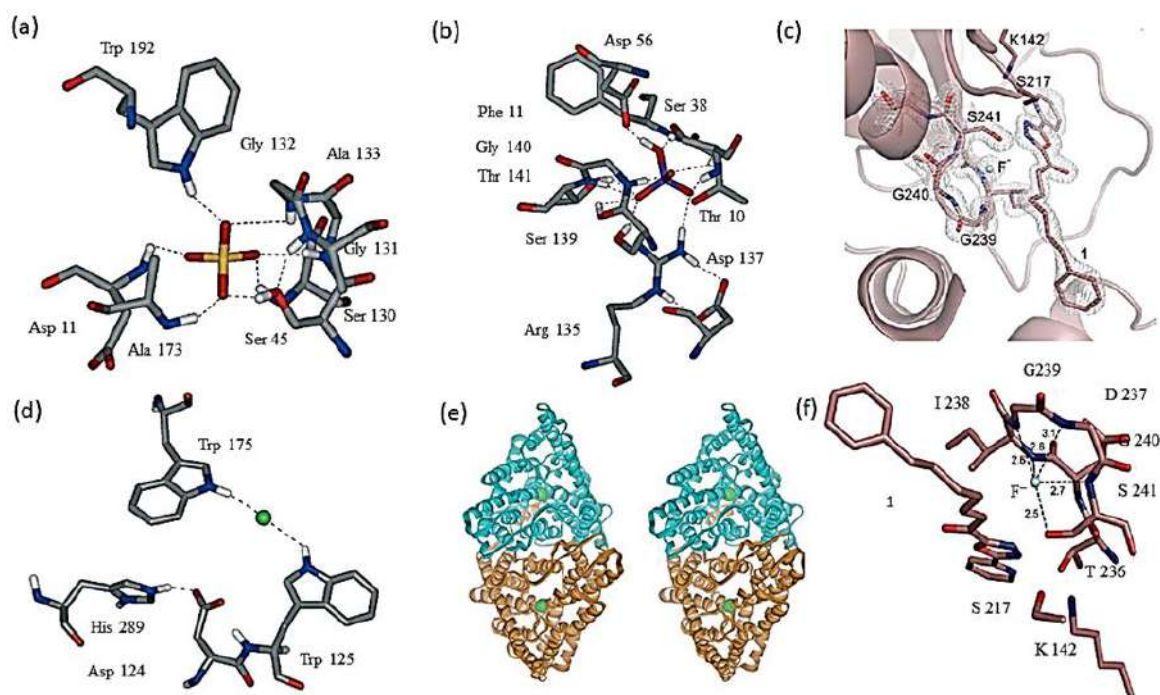


Figure 1.2 Anion binding in biology (a) showing the X-ray crystal structure of the sulphate-bound motif in the sulphate-bonded protein where the anion is stabilized by seven hydrogen bonding interactions via NH or OH proton donor groups; (b) displaying the phosphate-binding architecture in phosphate-binding protein;^{1,17} (c) showing noncovalent interaction with fluoride ion associated with FAAH active site **1** where the $2F_o - F_c$ electron density is recorded at 1.5σ contour are depicted as white meshes;^{1,18} (d) revealing the presence of bound chloride ion within the active site of haloalkane dehalogenase Enzyme; (e) Showing a ribbon representation (stereo-view) of the StCIC dimer and the subunits are coloured as brown and cyan were a chloride anion in the selectivity filter (green sphere);^{1,7} (f) Fluoride bonded noncovalent FAAH-**1** structure reside into the oxyanion hole;^{1,9}

The coordinative interactions between the receptor molecules and the anions are predominantly governed by various hydrogen bonds /or electrostatic connections whereas the previous one has a greater impact on the advancement of selective binding via topological complementarity. Moyers, Bonnesen and co-workers have defined some important features regarding the anion

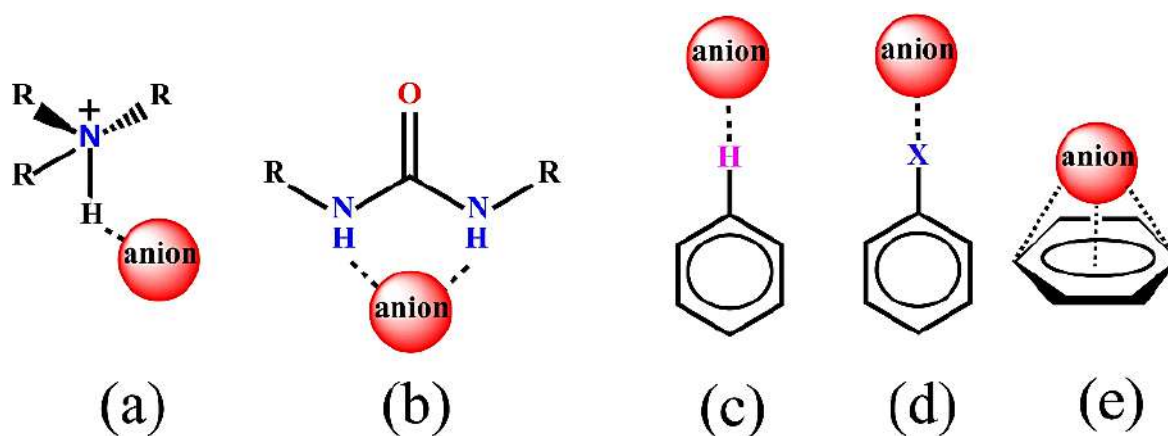
binding study in the view of analytical sense where several influencing properties such as anion size, charge distribution, acidity, hydrophobicity, and basic nature have an impact on the selective anion exchange process.^{1.10} They have also clarified that for a fruitful recognition of anion by selective receptors, it is very crucial to adopt the appropriate orientation of hydrogen bonds associated with the proper designing of the molecular framework. So, the negative charge on the anion for an anionic guest is considered to be primary valence, and the secondary valence is distributed through hydrogen bonds towards the anion of interest.^{1.11} In this context, Bowman-James and co-workers have pointed out that to design the strategies of optimized host-guest complementary structure coordination numbers have an important cofactor.^{1.12} The most effective way to catch the anions is to use their negative charge, therefore ammonium or quaternary ammonium attached frameworks have been considered as a fundamental receptor of choice because they can deliver a sufficient electrostatic attraction that is enhanced by hydrogen bond interactions with the coordinated anions. The performance of urea or thiourea, pyrrole, amide, and indole-based receptors in the construction of neutral anion-receptors complexes *via* favourable hydrogen bonding interactions has been the topic of intense research.^{1.13, 1.14} When an electron-withdrawing substituent is inserted into the host receptor molecule, the -NH protons become highly acidic in nature and another hand strongly basic anion is present, such as fluoride, hydroxide, or acetate even can deprotonate in some cases.^{1.15, 1.16} Several structural modifications have been utilized on the hydrogen bonding support to enhance the acidity of the -NH protons upon introducing potential electron-withdrawing groups (like -NO₂ and -CF₃) whereas, the π -systems are also negotiated followed by the formation of a necessary void or cavity with a rigid (like calixarene or polynorbornene) or flexible structural framework that creates an environment for binding with appropriate given anion. Previously, Custelcean *et al.* have examined the basic contribution of anions in crystal engineering due to their diverse impact on the formation of good crystals.^{1.17} Moreover, besides the hydrogen bonding interaction, some other interactions are responsible for anion coordination present in the crystal structure Scheme 1.1.

(a) *Metal coordination bonds* ($M^+ - A^-$): This type of Lewis acid-base interaction is relatively proficient and selective, with a high-level directional character in some cases. As a result, anion-metal amalgamation is frequently discovered to have a significant impact on crystal formations. Their properties range from entirely electrostatic to heavily covalent.

(b) *Coulombic and van der Waals forces*: These kinds of electrostatic interactions are present in all crystals and operate in the background. However, because they are non-directional, they are challenging to use for structural control.

(c) *Halogen bonds* ($D-X\cdots A^-$): The halogen bond donor and acceptor, respectively, are an electrophilic halogen ($X = \text{Br}, \text{I}$) and a high electron-rich centre (in this case the anion). Halogen bonds are substantially directional ($\angle D-X-A$ close to linear), and behave similarly to hydrogen bonds in many cases.^{1,18}

(d) *Anion- π interactions*: This is electrostatic but it is very scantily reported in the literature due to the competition with $C-H\cdots A^-$ hydrogen bonds which looks more successful than the previous one.^{1,19} Another weak competitor is σ interaction caused by a small amount of charge transfer from anions to host molecule.



Scheme 1.1 Different types noncovalent anion binding interactions; (a) Ammonium cation involved in $N-H\cdots A^-$ interaction; (b) self-complementary $N-H\cdots A^-$ connection involving a urea unit; (c) $C-H\cdots A^-$ contact by an aryl function; (d) $C-X\cdots A^-$ halogen bonding by a halocarbon ($X = F^-, Cl^-, Br^-, \text{ and } I^-$); and (e) Anion- π communication.

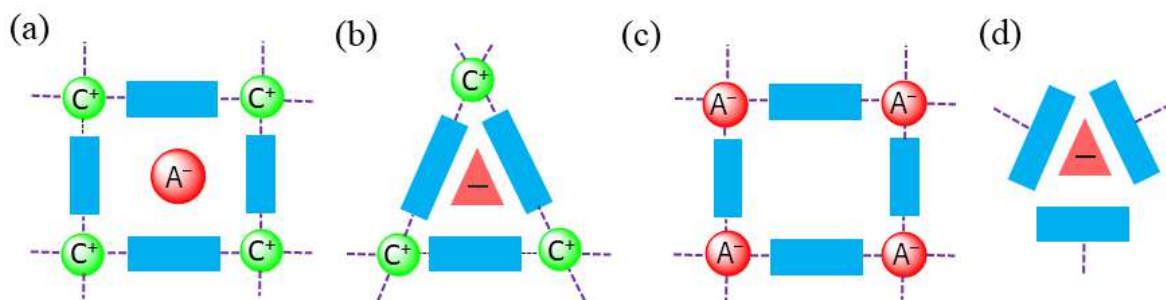
Additionally, types of anions play an important role in crystal formation (Scheme 1.2) Custelcean *et al.* have summarized four types of features that are playing a crucial role in crystal formation.

(a) *Spectator*: for this type of situation, the anion remains silent towards any structural role in the crystal but is present just to balance charge distribution; The type of situation belongs to the cationic frameworks based crystals (coordination polymeric network or MOFs) having large pores or networks engaged by with hardly interacting, messy counter ions and solvent molecules.

(b) *Structure-directing*: the anion has an important contribution in crystal structure formation, but it has no role in making a molecular assembly except behaving as a templating agent for a particular motif.

(c) *Building unit*: the anion directly contributes as a building block unit for a framework to be assembled via the construction of precise and directional connections.

(d) *Secondary building unit (SBU)*: the anion act as a primary species which supports forming of a molecular assembly in the aggregated state.



Scheme 1.2 Structural motif of anions in crystals as; (a) spectator; (b) structure-directing (templating); (c) building unit; and (d) SBU component.

1.4 Why rigid aromatic diamine is favoured as a core for the receptors?

Simple aromatic diamine based neutral receptors for anions encapsulation are scantily reported in the literature to compare to tri or multi-podal receptors because of having a lesser number of

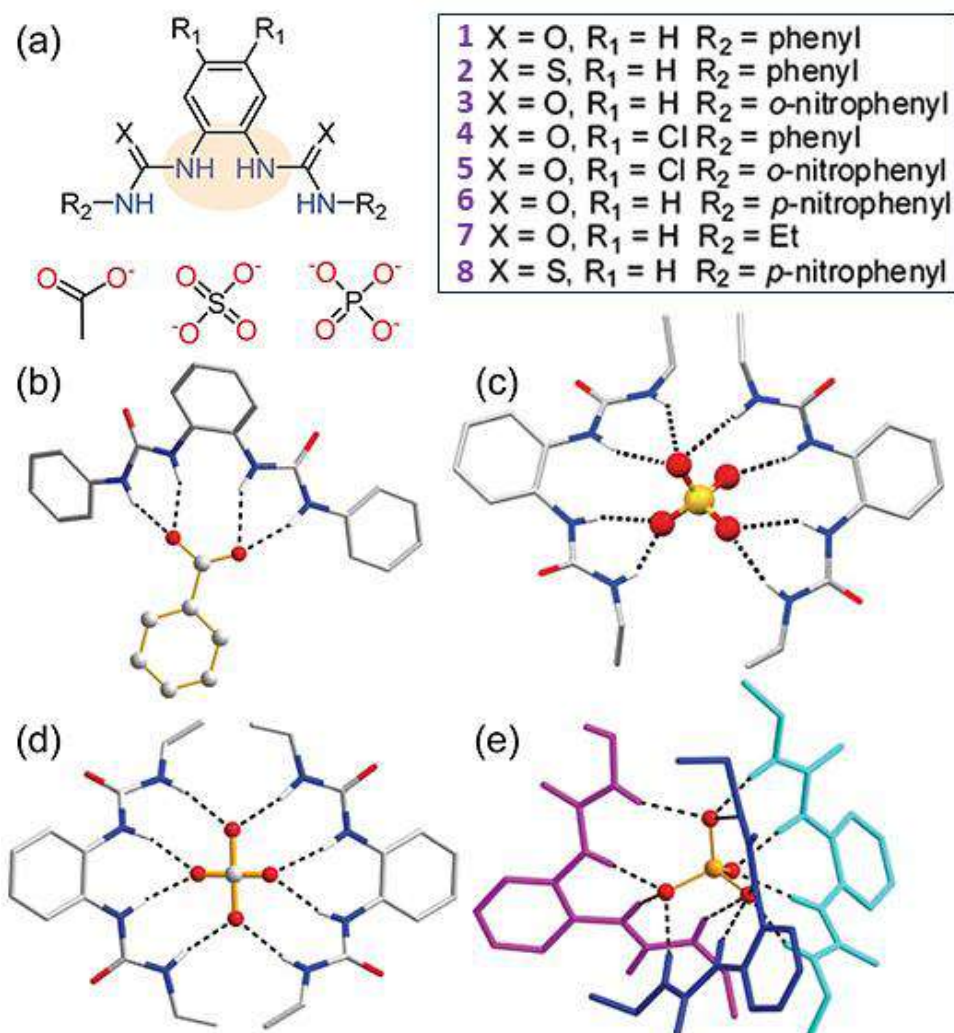


Figure 1.3 (a) Illustrative assemblies of receptors **1-8** binding with monovalent AcO^- , tetrahedral divalent SO_4^{2-} and trivalent PO_4^{3-} anion; (b) Fragment Crystal structure of **1**. Benzoate molecule. Crystal structures of (c) $(\mathbf{7})_2 \cdot \text{SO}_4^{2-}$, (d) $(\mathbf{7})_2 \cdot \text{CO}_3^{2-}$, and (e) $(\mathbf{7})_3 \cdot \text{PO}_4^{3-}$ anion.

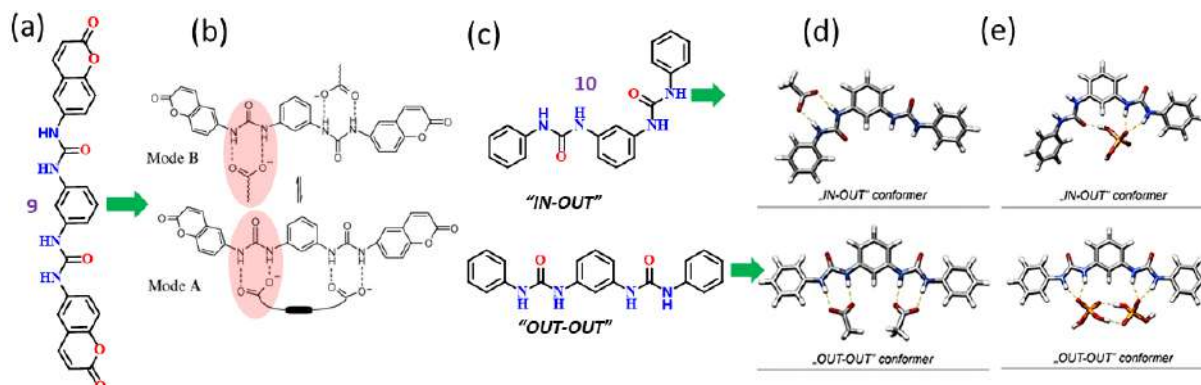


Figure 1.4 Showing (a) molecular structure of coumarin linked ditopic receptor **9**; (b) Possible binding modes of di-carboxylates with **9**; (c) probable conformers for compounds **10**, which has been considered throughout the whole calculations; (d) the most favorable conformers of both monoanionic and dianionic acetate complexes of **10**; and (e) the most stable and preferable conformers of 1:1 and 1:2 $\text{H}_2\text{PO}_4^{2-}$ (DHP) complexes of **10**.

NH groups, low pre-organized void, and a smaller chance of forming cooperative anion bound complexes in solid-state. Very recently, planning and designing of rigid *ortho*-/*meta*-/*para*-phenylenediamine derived neutral bis-urea receptors for fruitful recognition of biologically active anions, especially various-shaped oxyanions, has always been an emerging topic in the area of supramolecular chemistry due to its excellent capability of forming different arrays of hydrogen bonds with the oxo-anionic species. Gale and coworkers have elaborated the anion binding natures of **1-8** (Fig. 1.3a), which shown excellent selectivity towards Y-shaped carboxylate anions compared to other anions considered (HSO_4^- , H_2PO_4^- , Cl^- , Br^-).^{1,20, 1.21} By simply varying the functionalities (receptors **1-8**) the binding nature has been changed both in solid and solution state. Whereas, Wu and coworkers demonstrated that receptors **6-8** were also able to bind with tetrahedral SO_4^{2-} , planar CO_3^{2-} anions as well as trivalent PO_4^{3-} anion. Bowman-James and his groups described the binding of the receptor **7** with divalent sulfate ion with the formation of the 2:1 host-guest complex.^{1,22} Also, receptor **7** forms guest-host complexes with various oxyanions as evidenced from crystal structures of $(\mathbf{7})_2 \cdot \text{SO}_4^{2-}$, $(\mathbf{7})_2 \cdot \text{CO}_3^{2-}$, and $(\mathbf{7})_3 \cdot \text{PO}_4^{3-}$ (Fig. 1.3c-e). On the other hand, *meta* phenylenediamine-based urea receptors have been core-focused for environmentally as well as biologically active anion binding purposes. But very few are reported so far compare to its *ortho* isomer due to the high preorganization energy and the highly cooperative nature of hydrogen bonding sites. K. Ghosh and coworkers have reported 1, 3 diamines based coumarin attached dipodal bis-urea receptor **9** (Fig. 1.4a), which could successfully distinguish isomeric aromatic dicarboxylate anions

through fluorometric detection in DMSO polar solvent. The complexation between the ditopic coumarin receptor has also been confirmed by ^1H NMR, UV-vis as well as fluorescence studies. All these analytical tools assure that both the forms **A** and **B** (Fig. 1.4b) show a perfect equilibrium in solution.^{1,23}

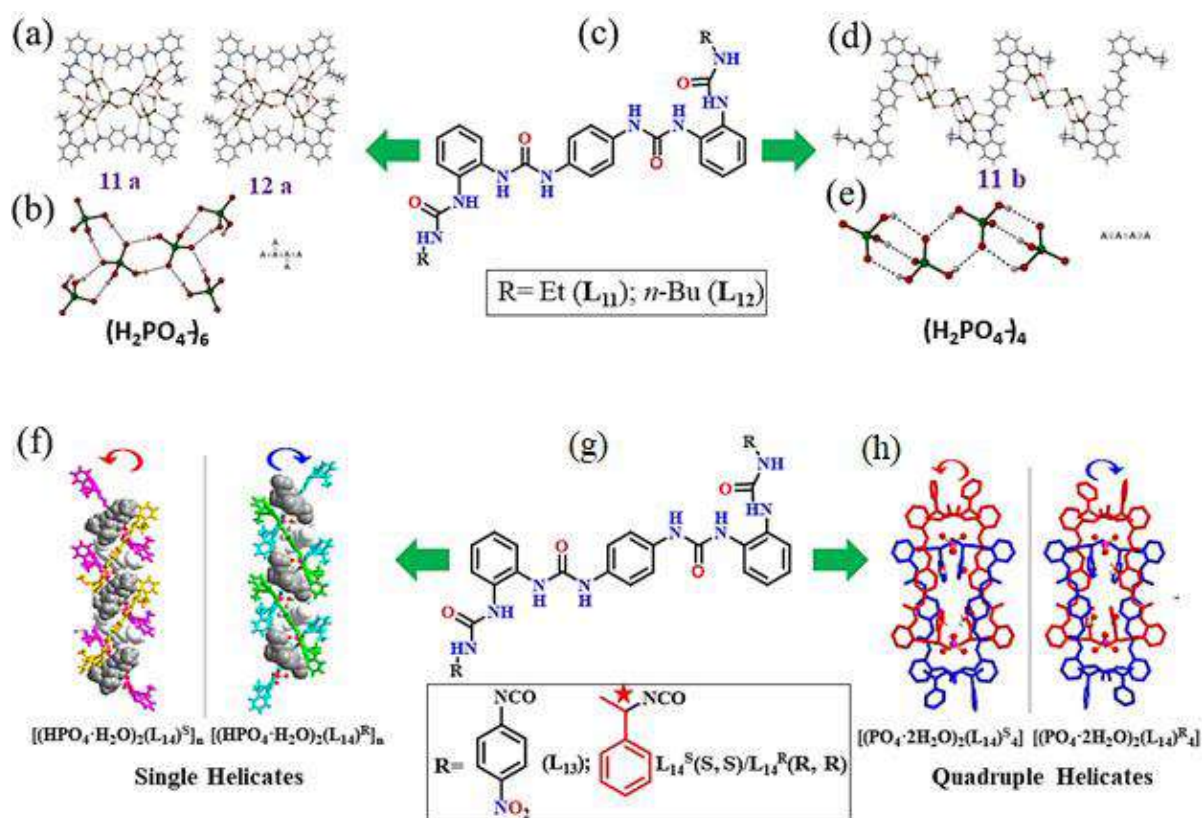


Figure 1.5 Crystal structures of **11a** and **12a** showing (TBA cations and acetone solvent are omitted for clarity). (a) $(\text{H}_2\text{PO}_4^-)_6$ hexameric association inserted between two receptor molecules and secured by sixteen H-bonds from eight urea groups; (b) Expanded view of the $(\text{H}_2\text{PO}_4^-)_6$ assembly (**11a**, **12a**) represented by hydrogen-bonding interactions; (c) molecular geometry of receptor **L₁₁** and **L₁₂**; (d) $(\text{H}_2\text{PO}_4^-)_4$ tetramers (**11b**) of **L₁₁** connected through various hydrogen-bonded interactions; (e) Expanded view of the $(\text{H}_2\text{PO}_4^-)_4$ assembly of **11b** represented by hydrogen-bonding interactions; Infinite extension of the single helical structure of (f) the P isomer (complex **L₁₄^S**) and M isomer (complex **L₁₄^R**) with the inserted TBA^+ cations (the front TBA^+ ions are shown as grey colour, while the back ones in are light grey); (g) the molecular structure of receptor **L₁₃** and **L₁₄**; and crystal structures of the quadruple helicates $(\text{TMA})_6[(\text{PO}_4 \cdot 2\text{H}_2\text{O})_2\text{L}^{\text{S/R}}_{14}]_4$ (h) chiral view of the **A₂L₁₄** as quadruple helicate architectures.

V. Tomišić and groups have prepared *meta*-phenylenediamine-based aromatic bis- urea receptor **10** and investigated their anion binding nature in DMSO solvent.^{1,24} It was observed that *meta*-derivatives showed almost equal contribution between the “out-out” and “in-out” conformers (Fig. 1.4c) to assist favorable deprotonation in presence of various anionic groups where its para isomers found to be in “out-out” conformers exclusively. Computational analysis of $10\text{H}_2\text{AcO}^-$ complex proposed that acetate ion binds with only one urea arm (monoanionic

complex within narrow energy region of $4.0 \text{ kcal/mol}^{-1}$) in case of “in-out” conformer but for the “out-out” conformer dianionic acetate complex was formed predominantly (Fig. 1.4d). On the other hand, *meta*-derivatives showed more efficacy (with almost 10 times greater stability constants) towards dihydrogen phosphate anion (DHP) compare to acetate, But the complex $10\text{H}_2\cdot\text{DHP}$ showed an array of interactions that is sterically favorable and energetically stable for its “in-out” conformer among all examined conformers. Whereas, di-anionic $10\text{H}_2\cdot(\text{H}_2\text{PO}_4^-)_2$ complex preferred the “out-out” conformation to afford intermolecular hydrogen bond pronouncedly (Fig. 1.4e).

Para-phenylenediamine-based urea/thiourea receptors for anion recognition of biologically active anions are very rare in literature due to high preorganization energy as well as large pod distance that makes it difficult to chelate smaller anionic species. Still, some research groups have already taken the risk and planned to design the anion receptors by utilizing 1, 4 diamines as a core unit. Out of them, A. Rajbanshi and co-workers have synthesized and reported two urea-functionalized receptors (**L**₁₁ and **L**₁₂) (Fig. 1.5c) and isolated a single crystal of [**L**₁₁(H₂PO₄)₃] (TBA)₃(H₂O)₂(acetone)_n (**11a**) [**L**₁₂(H₂PO₄)₃] (TBA)₃(H₂O)₂(acetone)_n (**12a**) (Fig. 1.5a, b).^{1,25} Close inspection of the single-crystal study revealed that **11a** and **12a** are isostructural and comprise of centrosymmetric (H₂PO₄⁻)₆ hexameric assembly enclosed between two symmetry- identical receptor molecules (Fig. 1.5b). On the other hand, single crystals of [**L**₁₁(H₂PO₄)₄] (TBA)₄ (**11b**) were obtained by crystallizing TBA dihydrogen phosphate with **L**₁₁ from acetone/diethyl ether/trimethylamine solvent (Fig. 1.5d). Crystal structure analysis disclosed that receptor **L**₁₁ linked the (H₂PO₄⁻)₄ tetrameric assembly into extended chains through hydrogen bonding interactions coming from urea groups of the receptor (Fig. 1.5e). Single-crystal structural investigation verified the formation of (H₂PO₄⁻)_n aggregates which was also surveyed by CSD analysis, established that these clusters display unique topologies and hydrogen-bonding connectivity.

Biao Wu and groups have synthesized a pair of bis-urea receptor molecules **L**₁₃ and **L**₁₄, linking a para-phenylene unit with a chiral carbon (α -methyl benzyl group PhC*H(CH₃) –) to recognize the phosphate ion through the formation of homochiral triple helicates and/ or tetrahedral cascades (Fig. 1.5g).^{1,26} But interestingly, two new anion-receptor-based supramolecular structures **L**₁₄^S and **L**₁₄^R were achieved as quadruple helicates extending as single standard helices infinitely depending on the presence of counter-cations which played a crucial role in defining the consequence of the ACDA (anion coordination-driven assembly) shown in Fig. 1.5f. The smaller cation TMA⁺ induced the formation of homochiral quadruple helicates (TMA)₆[(PO₄·2H₂O)₂**L**₁₄^{S/R}] (Fig. 1.5h) whereas, relatively larger TBA⁺ cation resulted in an

infinite single helix structure $(TBA)_{2n}[(HPO_4 \cdot H_2O) L_{14}^{S/R}]_n$ with these chiral receptors in presence of dihydrogen phosphate molecule.

1.5 Advantages of fluorescence-based methods for detection of anionic guest

Another way of detecting various analytes via distinct molecular receptors depends on the fact that the recognition of anion may produce some valuable responses, which can be optical (change of color or fluorescence) sol-gel transition, or an electrochemical, that can confirm the presence as well as in some cases the concentration of a guest anion.^{1.27} However, out of these various types of sensing techniques, optical sensors based recognition of anion are widely favoured for their simplicity, ease to handle, inexpensive, rapid response time, and consistent signal understanding capacity,^{1.28, 1.29} where either molecular interactions or a reaction-based chemical process changes the optical outputs. Predominantly we may have categorized optical sensors into two parts (1) colorimetric or absorbance-based sensors (2) luminescent or fluorescence-based sensors. The receptor or host molecule (the recognition site) is linked with a chromophore and/or fluorophore named as a signalling unit, which could respond to the recognition process through noticeable as well as detectable colorimetric and/or fluorometric indication.^{1.30} As a result, out of various detection tools of an analyte, fluorescence-based detection of an analyte having a suitable signal to noise ratio, fast response, flexible nature, extensive stability, low-cost, stress-free sample preparation, relatively simple handling, and trouble-free investigation from both visual and instrumental methods^{1.31}

1.6 Receptor design

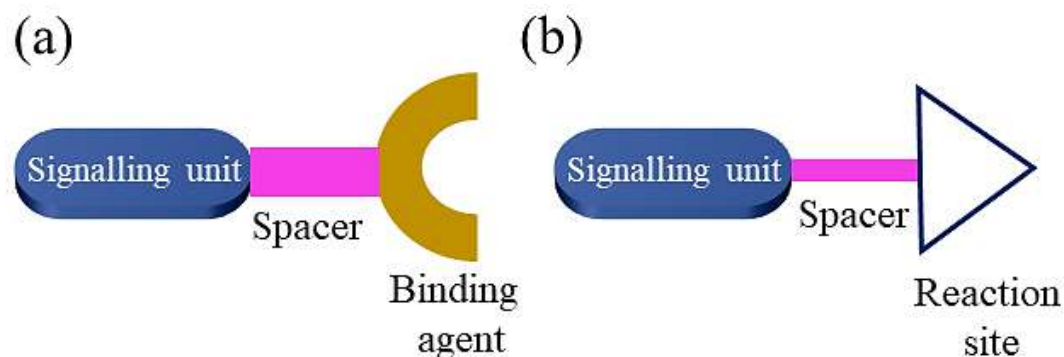
To design an appropriate fluorescent chemosensor for both metal and anion, two parts are essential, (1) a chelating or coordinating unit and (2) a signaling unit. The receptor must possess a binding unit decorated by electronegative atoms like N, O, and S, which generally come from NH/OH/CH/SH fragments from various moieties used to bind the guest anion. The signaling agent may be directly linked with a binding group through conjugation or it can be separated by a proper spacer group.^{1.32, 1.33}

1.7 Probe selectivity: what is chemosensor and chemodosimeter?

Optical probes that diagnose the analytes with considerable selectivity are identified as selective probes. These selective probes can be categorized into two parts – (1) chemosensors and (2) chemodosimeters. Based on binding with anion these probes can be classified into various types depending on output responses, such as (a) ‘Turn Off’ sensors (fluorescence quenching); (b) ‘Turn On’ sensors (fluorescence enhancement); (c) ‘Ratiometric’ sensors (with red or blue shift

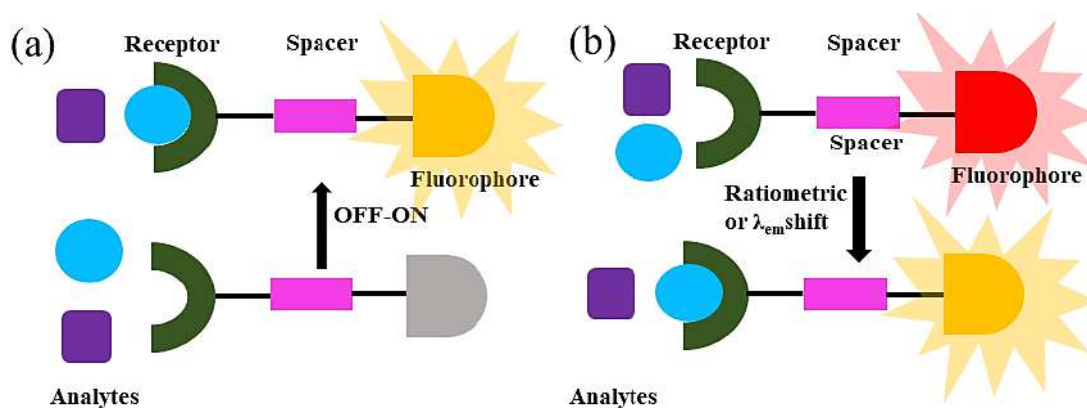
emission maximum). But “turn on” based sensing phenomena are striking most to the researcher for their high-class positive responses as compared to the “Turn Off” sensing.

A chemosensor can generate an output signal in fluorescence spectra upon interaction with a specific analyte (target substance). Typically, a chemosensor consists of three essential parts:



Scheme 1.3 The general constructions of (a) a chemosensor and (b) a chemodosimeter

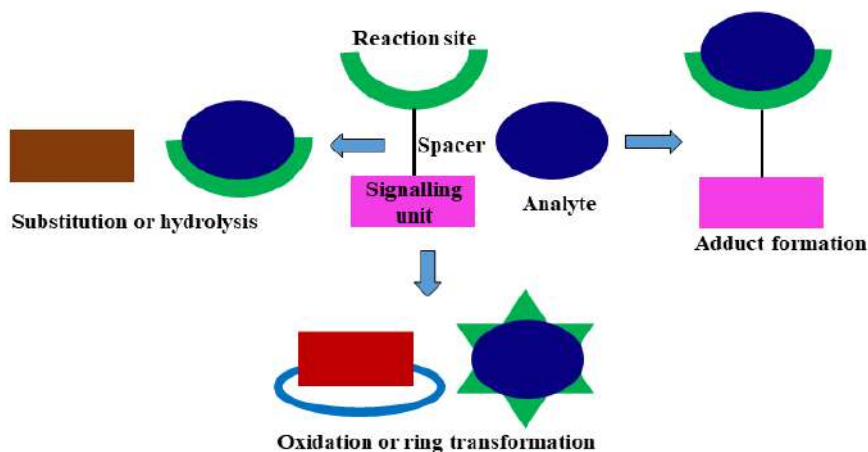
(a) A receptor or binding moiety, (b) A suitable spacer, and (c) signalling transducer or generator unit (Scheme 1.3a). Whereas, the signalling unit is a fluorophore group which produce fluorescence output. The recognition of the analyte is confirmed through interaction between the receptor (sensor) and the analyte molecule that results in a change on a noticeable signal. The proper size, shape, and requisite energy of the analyte and the corresponding receptor mainly contribute to the stabilization of the receptor-guest complex. The efficacy of a sensor molecule predominantly depends on selectivity, sensitivity, binding potential, and effectiveness of signal transduction. But the spacer is a chemical linker that carryout several mechanistic information and its length is responsible for various emission properties. Like the chemosensors, chemodosimeters also consist of three compartments: (a) a suitable reaction site, (b) a proper chemical spacer, and (c) signalling unit (Scheme 1.3b). From the structural point of view, the major modification of a chemosensor and a chemodosimeter is based on the fact that the receptor or the binding unit of the earlier is exchanged by a reaction site of the latter. It is done due to make a successful interaction between the analyte and the receptor.



Scheme 1.4 Schematic representation of (a) chemosensor based on fluorescence emission intensity and (b) chemosensor based on the emission wavelength.

Besides this, some other external factors such as temperature, media, etc. may also interfere in the reactivity of the subjected analyte and the selectivity of the reaction. Various non-covalent interactions between the analyte (cations, anions, and molecules) and chemosensor produce an output signal within a few seconds, following the ‘lock and key’ rule (Scheme 1.4). Here, the analyte, upon binding with the receptor, is only involved in sharing the structural complementarity within the molecular cavity (the ball in contrast with the rectangle). These types of interactions usually maintain a reversibility nature.^{1,34} In this case; the concentration of analyte and the free, as well as the bound sensor, are mutually inclusive. These classes of probes have become an emerging area for their reusability nature.

But for a chemodosimeter type sensing, they go through a reaction with the subjected analyte leading to a chemical transformation which usually involves the breaking as well as the making of the covalent bonds (Scheme 1.5). As a result, a specific daughter product is being formed which does not show similarities with the free probes in terms of both structural aspects and optical properties. In most cases the process is irreversible, so rarely recovered for reuse, unlike chemosensors. These kinds of reaction transformations are very precise as well as highly insensitive to the environment, and beneficial in terms of high selectivity.



Scheme 1.5 Schematic representation of various kinds of mechanistic pathways involved in chemodosimetric recognition for analyte.

1.8 Various types of reaction mechanisms contribute to sensing

To behave like a fluorescence sensor, the emission properties (e.g. enhancement or quenching of fluorescence intensity) associated with the detection of various analytes must undergo noticeable change via certain mechanistic pathways. The emission characteristics, in fact, are influenced by various fluorescence toning mechanisms involved in the detection and measurement of the chemical species that are being subjected. Thus, the parent molecule and the newly formed products exhibit different electronic charge distributions in their different energy states. The respective changes in electronic charge distribution of the probe upon binding with guest analytes can be investigated by some mechanisms. Out of them, intramolecular charge transfer (ICT), photoinduced electron transfer (PET), chelation induced enhanced fluorescence (CHEF), twisted intramolecular charge transfer (TICT), fluorescence resonance energy transfer (FRET), C=N isomerization, electronic energy transfer (EET), excimer/exciple formation and aggregation-induced emission (AIE) are the most important process involved.^{1.35, 1.36} Where ICT, ESIPT, and FRET mechanisms majorly shift the position of the wavelength in emission spectra (ratiometric phenomena).

The host molecule responds towards anionic guest via the following four chemical mechanisms-(1) protonation-deprotonation techniques, (2) complexation (involve direct and displacement), (3) breaking and making of covalent bonds and redox reactions.^{1.37} However, from the thesis point of view, we have only discussed only complexation-based chemosensors. Various non-covalent interactions play a crucial role in planning proper complexation-based sensors. Mainly two types of sensors are important here:1) direct complexation and 2) competitive displacement complexation based sensors.

1.9 Chemosensor for anionic guest

It has always been challenging to design a good sensor for an anion due to the high hydration effect of anion in an aqueous medium. Out of all the reported approaches for anion recognition, chemosensing is believed to be the most efficient technique due to its advantages such as high sensitivity and excellent applicability with rapid and high-throughput recognition. Over the past several decades, a substantial number of chemosensors have been developed for anion detection *via* various capturing mechanisms using host-guest interactions or chemical reactions.

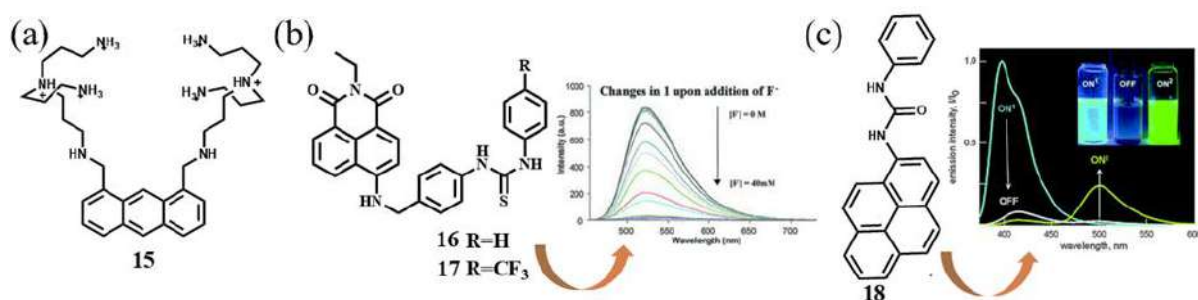


Figure 1.6 (a) and (b) structural representation of some recently developed chemosensors (**15-17**); (c) receptor **18** displaying exciting “on1–off–on2” fluorescence emission response towards F^- .

In 1994, Czarnik and co-workers developed an anthracene-based fluorescent chemosensor **15** for detection of phosphate family (mainly PPI) containing polyazaalkane groups.^{1,38} **15** displays efficient selectivity towards PPI among others including phosphate (Pi), in spite of having a similar structure to that of PPI. (Fig. 1.6a) The high selectivity of **15** towards PPI originates from the two poly-ammonium arms that are geometrically organized to hold the six external oxygen atoms of the PPI. The invention of fluorescent PET anion sensors that work on the basis of charge neutral receptors did not take place until the turn of the millennium; this was accomplished concurrently by several of the writers of this article.

The receptors **16** and **17** attached with naphthalimide unit that act as ICT bearing chromophore, show emission at 525 nm in DMSO upon excitation at 444 nm.^{1,39} Upon addition of F^- , AcO^- and $H_2PO_4^-$ to the probe solution resulted in a quenching of the emission intensity, whereas Cl^- and Br^- had no impact. This quenching is attributed to a PET process that originates from the highly charged receptor-bound anion complex to the photo-excited fluorophore unit. (Fig. 1.6b) The quenching effect is particularly strong for F^- , and it was accompanied by the appearance of a new band centered at 536 nm leading to a distinct colour shift from light yellow to deep purple, which was attributed to deprotonation of the 4-amino moiety (enhancement of the ICT chromophore's push-pull character). Moreover, other anions (AcO^- and $H_2PO_4^-$) produced 1:1 complexes (anion: receptor), whereas F^- produced 2:1 complexes majorly.

Fabbrizzi and Amendola group has developed an excellent pyrene-based fluorescent sensor **18**, which consists of a urea unit as a binding group. Sensor **18** shows an exciting “on¹–off–on²” fluorescence emission response towards F^- (Fig. 1.6c).^{1,40} Initially, **18** displays distinctive pyrene emission at 394 nm (on¹) in acetonitrile. However, after the addition of F^- , the intensity decreases (off) which can be attributed to an electron transfer phenomenon initiating from the locally excited complex and involving the transformation of the locally excited complex to less emissive tautomer. Interestingly, a yellow fluorescence appears with the further addition of F^- leading to a new emission band at 500 nm (on²), which can be attributed to a charge-transfer

process originated by the deprotonated receptor; the F^- deprotonation phenomena is very commonly used by many researchers in analogous systems. The authors revealed these optical characteristics can be perceived in other neutral receptors having N–H fragments, which may provide new approaches to develop fluorescent sensors for anions.

1.10 Chemodosimetric detection of anionic guest

Chemodosimeter delivers recognition of analyte *via* irreversible transduction and are comparatively less affected by the condition of the surroundings and offer distinct benefit in terms of high selectivity as discussed earlier. The phenomena involve the reaction between the target analyte such as cation, anion, or neutral molecule and the probe molecule (called as chemodosimeter) and are related with substantial chemical conversion including both breakings as well as forming of the covalent bonds. The products formed in this method are different from the starting chemodosimeter associated with different optical properties. However, few

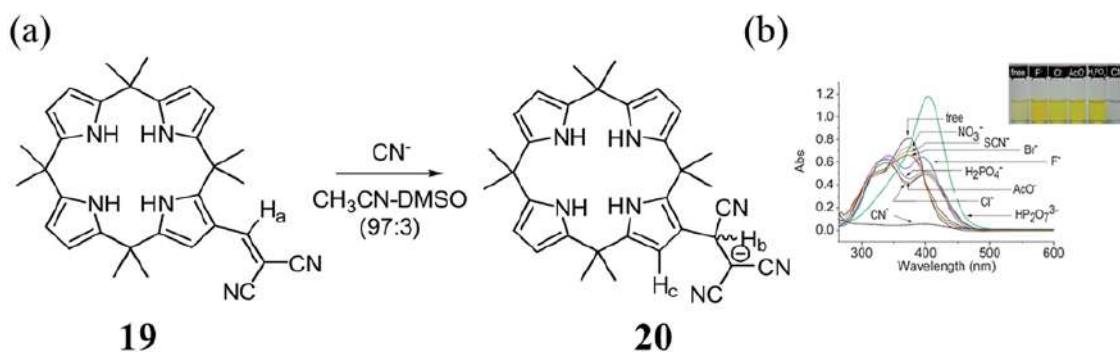


Figure 1.7 (a) The plausible pathway of the nucleophilic addition of CN^- to **19**. (b) Change of the UV-Vis spectra free receptor **19** (41.2 μ M) after the addition of 20 Equiv. of several anions in CH_3CN -DMSO (3%). Inset: Color changes associated with **19** (1.03 mM) seen upon addition of 20 equiv of F^- , AcO^- , Cl^- , $H_2PO_4^-$ and CN^- in CH_3CN -DMSO (3%).

reports have been discussed here very briefly with different chemodosimeters towards anions. First Michael addition based cyanide detection by calix[4]pyrrole derived chemodosimeter **19** turned yellow to colourless upon addition of CN^- ions and exhibited bathochromic shift from 374 nm to 403 nm upon addition of other anions viz. F^- , Cl^- , Br^- , NO_3^- , CN^- , SCN^- , $HP_2O_7^{3-}$, $H_2PO_4^-$ and AcO^- .^{1,41} The nucleophilic addition of CN^- to the C=C double bonds of **19** leads to the formation of adduct **20**, whereas “normal” N–H-anion H-bonding interactions play a vital role for the rest of the anions which are bound to the calix[4]pyrrole cavity. (Fig. 1.7)

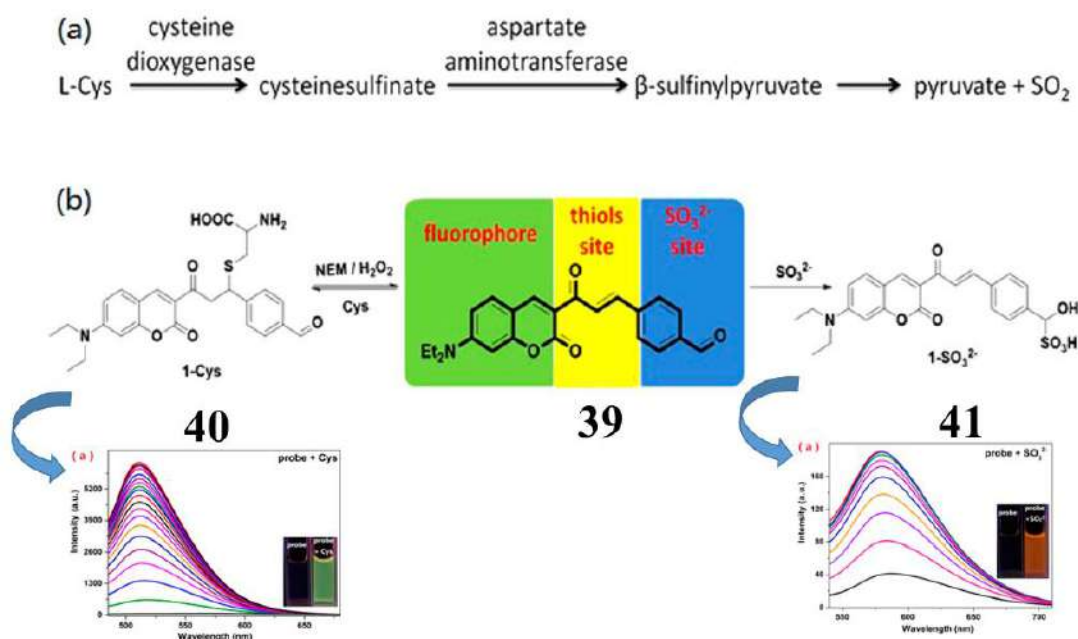


Figure 1.8 Showing (a) aerobic metabolism of Cys in Mammalian Cells and (b) design of the Dual-Site Fluorescent Probe for Cys Metabolism Visualization.

Y. Yue and coworkers have rationally developed a coumarin derivative-based probe **21** for the simultaneous recognition of Cys and its metabolite molecule, SO_2 . The probe exhibited two different fluorescents “turn-on” responses toward Cys and SO_2 (Fig. 1.8). ^1H NMR titration and HR-MS data demonstrated that $-\text{SH}$ -induced fluorescence enhancement was originated from the nucleophilic attack of sulfhydryl toward the α , β -unsaturated ketone in **21**. These results verified the ability of the probe to detect thiols and SO_3^{2-} through two reaction sites which may be successfully employed for imaging both A549 cells and zebrafish. Additionally, the probe could also image the enzymatic conversion of Cys to SO_2 in living A549 cells reversibly. The present report demonstrates the ability of the probe to image the endogenous produced SO_2 without cultivation of the SO_2 donors.^{1,42}

1.11 Fluorometric detection of metal ion

For a successful and selective metal binding, one of the following criteria is mandatory: 1) for a particular ion, proper fitting inside the sensor induced ring or cavity, like crown ethers, have various ring sizes for alkali or alkali earth metal ion.; 2) It is very important to have an effective number of donor atoms associated with the chemosensor for the successful formation of five – and six-membered ring, like EDTA unit for Ca^{2+} ; 3) hard-soft acid-base rules, such as the nitrogen or oxygen-containing receptors have a high tendency for hard metal ions (Al^{3+} , Cr^{3+} , Fe^{3+}). Here some examples of chemosensors with their high affinity of metal ions are studied with their associated binding mechanism.

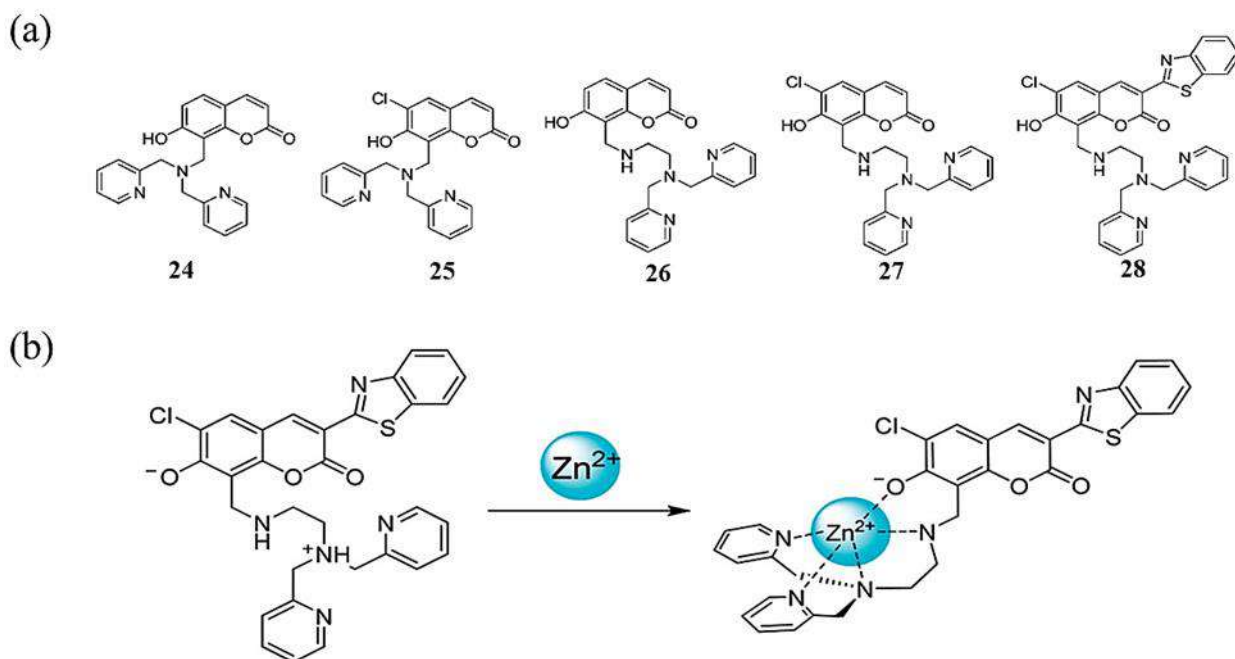


Figure 1.9 Depicting (a) molecular structures of the synthesized probes (**24-28**) (b) plausible detection mechanism of **28** towards Zn^{2+} .

Kikuchi *et. al.*^{1.43} examined the connection between the electron-rich unit of the 7-hydroxy group and the excitation as well as emission responses of several molecules, thus finding the ratiometric probes **24-27** (Fig 1.9) comprising a dipicolylamine (DPA) moiety at 8-position. Out of all the developed fluorophores, **25-27** showed ratiometric fluorescent nature while only **27**, can be employed as a probe for Zn(II) in living cells when excited at visible light. In these probes, the direction of excitation and emission wavelength depends on the 7-hydroxy group whether it is protonated or deprotonated. As the electron-donating aptitude is expected to increase in the order of $-\text{OH} < -\text{OM} < -\text{O}^-$, complexation with Zn(II) results in a redshift on both absorption and emission bands in predominant phenol form, but displays blue-shifts if phenolate form is major.

S. Kim and co-workers described a simple salicylimine-based sensor **29** to quantify the presence of Al^{3+} via a “turn-on” fluorescence response. Upon addition of Al^{3+} , the fluorescence emission intensity of the sensor was enhanced at 510 nm leading to a 1:1 complex between the **29** and the Al^{3+} at room temperature.^{1.44} With the increasing concentration of Al^{3+} , the emission gradually increased up to 27 Equiv. where the other metal ions, such as Na^+ , Ag^+ , K^+ , Ca^{2+} , Mg^{2+} , Hg^{2+} , Mn^{2+} , Co^{2+} , Ni^{2+} , Cu^{2+} , Zn^{2+} , Cd^{2+} , Pb^{2+} , Cr^{3+} , Fe^{3+} , and In^{3+} remained silent on the fluorescence (Fig 1.10). Here, the authors examined the metal-binding nature of the π -conjugated receptor **29** and revealed the tridentate ligand as a chemosensor, which displays fluorescence enhancement upon selective binding to Al^{3+} .

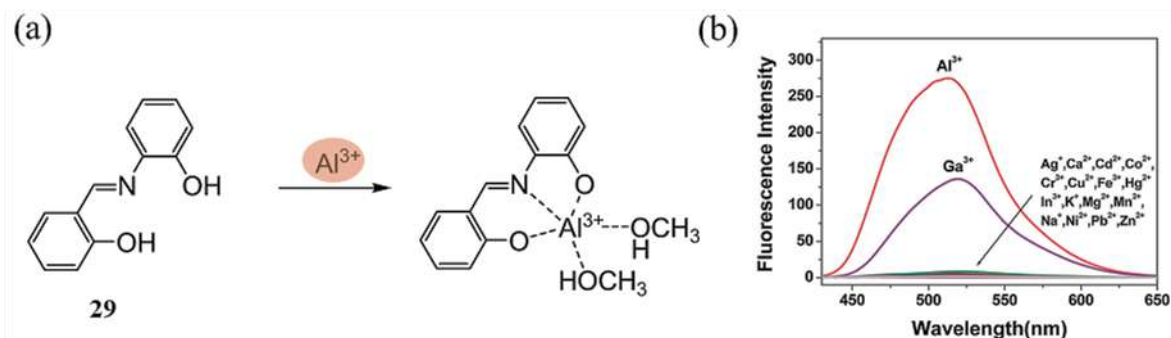


Figure 1.10 (a) Chemical structures of the receptor **29** and a 1:1 complex of **29** and Al^{3+} in $\text{CH}_3\text{OH}:\text{H}_2\text{O}$; (b) Fluorescence spectra of **29** ($1\ \mu\text{M}$) before and after addition of metal salts ($12\ \mu\text{M}$) of Ag^+ , Ca^{2+} , Cd^{2+} , Co^{2+} , Cr^{3+} , Cu^{2+} , Fe^{3+} , Hg^{2+} , In^{3+} , K^+ , Mg^{2+} , Mn^{2+} , Na^+ , Ni^{2+} , Pb^{2+} , and Zn^{2+} in $\text{CH}_3\text{OH}:\text{H}_2\text{O}$ (1:1).

H. S. Jung and *et.al.* developed a new coumarin-based fluorogenic probe (**30**), bearing 2-picolyl unit, for selective detection of Cu^{2+} ion in aqueous medium at pH range 4-10, (Fig. 1.11a, b) and the “turn-off” mechanism was verified by femtosecond time-resolved fluorescence spectroscopy (TRF) and quantum calculations.^{1,45} Further to realize the importance of 2-picolyl unit attached with the probe, which additionally offers extra binding site towards Cu^{2+} ion with support of the coumarin amide group, the group have designed **31** and **32** having 3-picolyl and 4-picolyl units linked with coumarin amide, respectively (Fig. 1.11c). But interestingly, unlike **30**, neither of them exhibits any discrete behaviour on the absorption or fluorescence spectra after the addition of Cu^{2+} ion.

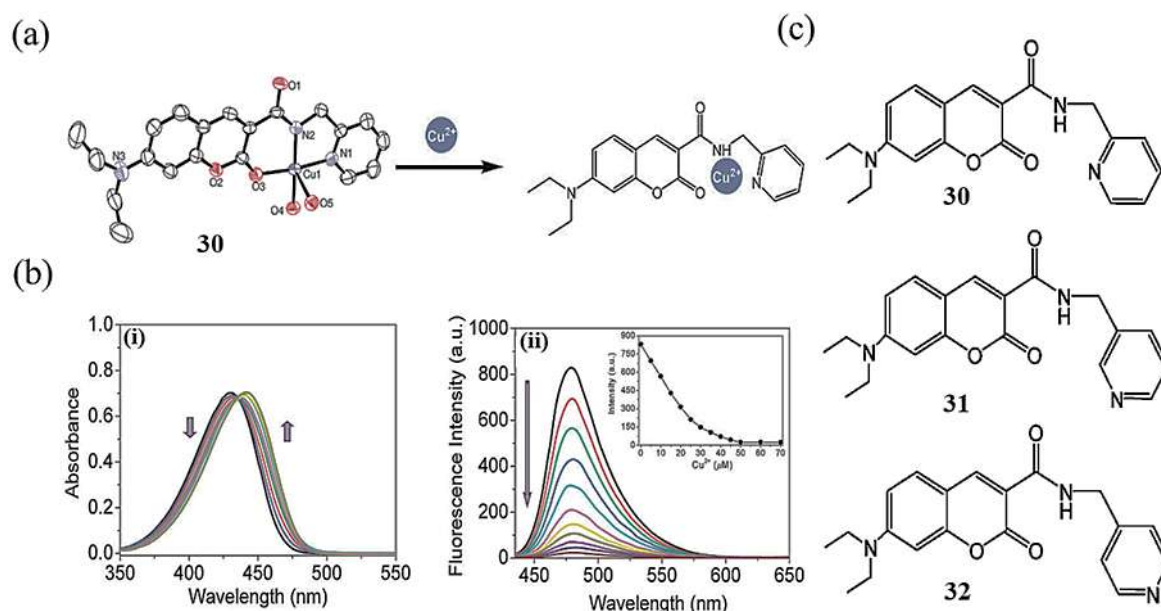


Figure 1.11 Showing (a) probable sensing mechanism of **30** in the presence of Cu^{2+} ; (b) (i) absorption spectra and (ii) fluorescence spectra of **30** (20 and $5\ \mu\text{M}$, respectively) after addition of different concentrations of Cu^{2+} ions in aqueous solution (HEPES: DMSO = 9:1, v/v) (0.01 M) upon excitation at 430 nm; (c) the molecular structure of the probes **30–32**.

Quinoxaline-based derivatives as chemosensors for metal ions in solution are well reported promissory fields in the last decades. In 2004^{1,46}, Wang et al. reported two quinoxaline/pyrrol/imine-based macrocycles (**33a** and **33b**) for selective sensing of Hg^{2+} in aqueous medium *via* formation of 1:1 metal-chemosensor complexes, which generate fluorescence quenching for the emission band with its maximum at 358 nm (Fig. 1.12). Chemosensors **33a** and **33b** showed remarkable selectivity for Hg^{2+} , even in the competitive medium.

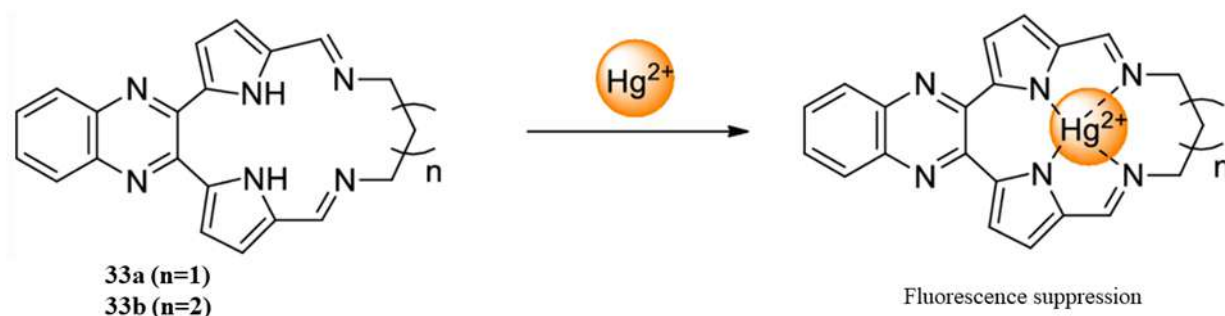


Figure 1.12 Hg^{2+} sensing by chemosensors **33a** and **33b** in aqueous medium.

1.12 Concluding Remarks and objective of the thesis

In summary, this thesis offers some of the fundamental and substantial concepts of supramolecular anion recognition chemistry where the anions/hydrated-anions or anionic association/dianionic assembly are captured by some series of simple isomeric monopodal or dipodal artificial acyclic receptors modulated by positional or electronic effect of core or terminal aryl substituents or dimension of anion or molecular host buildings supported by various non-covalent interactions in solid-state, which are also corroborated by various solution-state anion binding experiments along with UV-Vis spectroscopy, Hirshfeld surface analysis, FT-IR analyses, Multi-variant analysis of host-guest complexes. It may develop significantly and bring enormous improvements in specific applications like drug transmembrane anion transport, delivery, extraction, salt solubilisation, catalysis. In general, various types of the experimental studies reveal the anionic guest induced capsular, open book' like a polymeric extension, cylindrical assembly, 'Human-kidney'-like encapsulation or polymeric extended association are generated *via* neutral host-guest assembly in most of the cases. Some interesting feature/s in presence of a specific anion/hydrated anions or anionic associations have revealed by some specific receptor or group of isomeric receptor in solid-state. Although the findings presented in this thesis are tremendously useful from a fundamental standpoint, additional challenging areas of supramolecular chemistry must be explored,

primarily from an application point of view. From the detailed survey of the literatures, it can be determined that the acyclic receptors containing urea/thio-urea moiety within rigid/flexible frameworks linked with properly positioned binding sites can identify anionic species either in solid- or in the solution-state. Anionic species are ubiquitous in nature with various chemical and physiological effects on the environment, medicine, biology. For simultaneous anion recognizing, aiming to design simple ninhydrin/naphthyl/coumarin derivative based chemosensors or pyrene/anthracene linked chemodosimeters for detection of biologically important analytes, is also a goal of this thesis. However, the consistency on selectivity is always in questioned whenever anions with similar chemical nature are also present, like the case of fluoride and acetate or bisulphite and silphite. The probes are in variance with each other in many aspects; one can find them in the following chapters. Some probes were designed to interact with specific analytes whereas some are non-specific and separate a set of analytes through pattern-based recognition. **Chapter 1** provides general overviews about the thesis. **Chapter 3** includes four neutral dipodal receptors have been purposefully designed and synthesized by varying the substituents from phenyl to naphthyl moiety to investigate the anion coordinating activities of bis-urea receptors. Crystal structure investigation of the complexes correctly validates the fact that the receptors **L**₁–**L**₄ form halide as well as hydrated halide complexes. Most interestingly in complex **2a**, the phenyl based neutral bis-urea receptor **L**₂ binds with two chloride ions *via* participation of N–H···Cl[–] interaction from the adjacent urea group and aromatic C–H···Cl[–] interaction along with the construction of a halide–water–halide bridged architecture supported by another. Meanwhile, another phenyl-based bis-urea receptor **L**₁ binds to one bromide ion (**1b**) which is coordinated with two water molecules (from the lattice) forming a suitable 2:1 anion–receptor interaction. In **chapter 4**, two naphthalimide based linear monourea receptors (**L**₅ and **L**₆) exhibit anion (oxyanions and halides) binding in solid and solution states. Receptor **L**₅ could render fluoride/hydroxide-induced aerial CO₂ fixation efficiently, leading to the air-stable assembling of di-anions enclosed by *n*-TBA cations *via* short-range hydrogen bonding interactions (HBs) in solid-state. Besides, HBs based cyclic dimeric assembly of bisulphate anion sealed by the linear tetrameric assembly of host molecule was also evidenced from solid-state architecture. Upon addition of an excess amount of chloride and bromide anion, **L**₅ linearly assembled to capture a cyclic chloride-water and bromide-water tetrameric cluster backed up by various solid-state H-bonding interactions. **Chapter 5** includes specific colorimetric (naked-eye) and fluorometric sensing of HSO₃[–] by a pair of chemodosimetric probes, namely **L**₇ and **L**₈. The D-π-A structure-based probes exhibited an outstanding HSO₃[–]-dependent response with excellent selectivity and lower detection limit

values. These probes displayed colorimetric and fluorometric 'turn-on' responses toward HSO_3^- based on Michael-type addition reaction with very high selectivity and sensitivity over other anions. It is proven that the extra conjugated non-exocyclic C=C double bond (in probe **L**₈) did not take part in reaction with excesses HSO_3^- . This phenomenon substantiated that only the activated exocyclic C=C double bond was prone to any nucleophilic attack, owing to a more electrophilic nature compare to its non-exocyclic counterpart.

Whereas naphthyl-functionalized ninhydrin-based multi-analyte probe, **L**₉ displayed a 'turn-on' emission response towards Al^{3+} *via* chelation-enhanced fluorescence (CHEF) process in a mixed medium. The probe was proved to be selective and sensitive for Al^{3+} over most of the biologically relevant cations. Upon undergoing chelation with Al^{3+} ions, the PET process gets hindered and improved structural rigidity of the overall system, leading to a remarkable emission response. This selective probe featured the fluorescence sensing of Al^{3+} with ~20 nm red-shift. The probe was also capable of selectively and colorimetrically detecting Cu^{2+} with a considerable red-shift (~130 nm) in the UV-vis spectra. The *in situ* prepared [**L**₉- Al^{3+}] complex could selectively sense phosphate ions, particularly pyrophosphate (PPi) (**Chapter 6A**). **Chapter 6B** describes coumarin-based symmetrical dipodal probe **L**₁₀ was planned and synthesized for multi-analyte detection both in an aqueous and organic medium. The probe was decorated with -NH functionalities to attain fluorescence indications upon binding with basic anion; the detection ability of the probe for fluoride ions in the organic medium was studied using 'turn-off' emission change. The *in situ* prepared [**L**₁₀-F⁻] adducts could potentially sense Zn^{2+} ions with a 'turn-on' response *via* the metal-induced release of the free probe. Interestingly, as a multiple analyte sensor, **L**₁₀ could display an excellent 'turn-on' emission response towards Al^{3+} *via* chelation-enhanced fluorescence (CHEF) process in a fully aqueous medium. Moreover, the *in situ* prepared [**L**₁₀- Al^{3+}] complex could selectively sense phosphate ions, particularly pyrophosphate (PP_i) anion in the identical experimental condition. The suggested detection pathway is the complexation with aluminum, followed by the decomplexation of the ensemble by PP_i anions.

References

- 1.1 K. T. Holman, J. L. Atwood, and J. W. Steed, *Advances in Supramolecular Chemistry*, vol. 4, ed. G. W. Gokel, JAI Press, London, 1997, 287–331.
- 1.2 J. W. Steed and J. L. Atwood, *Supramolecular Chemistry*, John Wiley and Sons Ltd., Chichester, 2nd ed, 2009, **731**, 2-3, 225-226.
- 1.3 J. W. Steed, D. R. Turner, K. Wallace, *Core concepts in supramolecular chemistry and nanochemistry*, John Wiley & Sons, Chichester, 2007, **731**, 1-4, 52-53.
- 1.4 G. V. Oshovsky, D. N. Reinhoudt and W. Verboom, *Angew. Chem. Int. Ed. Engl.*, 2007, **46**, 2366.
- 1.5 X-N. Xu, L. Wang, G-T. Wang, J-B. Lin, G-Y. Li, X-K. Jiang and Z-T. Li, *Chem. Eur. J.*, 2009, **15**, 5763.

- 1.6 Y. Liu, X. Liu and R. Warmuth, *Chem. Eur. J.*, 2007, **13**, 8953.
- 1.7 D. J. Cram, *Angew. Chem., Int. Ed. Engl.*, 1986, **25**, 1039-1057.
- 1.8 J. M. Lehn, *Angew. Chem., Int. Ed. Engl.*, 2015, **54**, 3276-3289.
- 1.9 C. A. Schalley, John Wiley & Sons, Chichester, 2012, 5-6.
- 1.10 F. Delange, *Thyroid*, 1994, **4**, 107-128.
- 1.11 S. M. Rowe, S. Miller and E. J. Sorscher, *N. Engl. J. Med.*, 2005, **352**, 1992-2001.
- 1.12 B. Moss, *Chem. Ind.* 1996, **11**, 407-411.
- 1.13 S. L. Winski, D. E. Carter, *J. Toxicol. Environ. Health A*, 1998, **53**, 345-55.
- 1.14 P. D. Beer and P. A. Gale, *Angew. Chem., Int. Ed. Engl.*, 2001, **40**, 486-516.
- 1.15 J. M. Lehn, Cryptates: The chemistry of macropolycyclic inclusion complexes. *Acc. Chem. Res.* 1978, **11**, 49-57.
- 1.16 J. M. Lehn, Cryptates: Inclusion complexes of macropolycyclic receptor molecules. *Pure Appl. Chem.* 1978, **50**, 871-892.
- 1.17 J. L. Sessler, P. A. Gale and W. S. Cho, *Anion Receptor Chemistry*, The Royal Society of Chemistry, Cambridge, UK, 2006.
- 1.18 M. Mileni, J. Garfinkle, C. Ezzili, B. F. Cravatt, R. C. Stevens, and D. L. Boger, *J. Am. Chem. Soc.* 2011, **133**, 11, 4092-4100.
- 1.19 M. Mileni, J. Garfinkle, C. Ezzili, B. F. Cravatt, R. C. Stevens, and D. L. Boger, *J. Am. Chem. Soc.* 2011, **133**, 11, 4092-4100.
- 1.10 B. A. Moyer and P. V. Bonnesen, Physical factors in anion separations, *Supramolecular Chemistry of Anions*; Wiley-VCH: New York, 1997; chapter 1.
- 1.11 D. J. Mercer and S. J. Loeb, *Chem. Soc. Rev.*, 2010, **39**, 3612-3620.
- 1.12 K. B. James, *Acc. Chem. Res.*, 2005, **38**, 671-678.
- 1.13 P. A. Gale, *Chem. Commun.*, 2008, 4525.
- 1.14 C. Caltagirone and P. A. Gale, *Chem. Soc. Rev.*, 2009, **38**, 520-563.
- 1.15 P. A. Gale, *Acc. Chem. Res.*, 2006, **39**, 46.
- 1.16 A-F. Li, J-H. Wang, F. Wang and Y-B. Jiang, *Chem. Soc. Rev.*, 2010, **39**, 3729-3745.
- 1.17 R. Custelcean, *Chem. Soc. Rev.*, 2010, **39**, 3675-3685.
- 1.18 P. Metrangolo, T. Pilati, G. Terrane, S. Biella and G. Resnati, *CrystEngComm*, 2009, **11**, 1187.
- 1.19 B. P. Hay and V. S. Bryantsev, *Chem. Commun.*, 2008, 2417.
- 1.20 S. J. Brooks, P. A. Gale and M. E. Light, *Chem. Commun.*, 2005, 4696-4698
- 1.21 S. J. Brooks, P. R. Edwards, P. A. Gale and M. E. Light, *New J. Chem.*, 2006, **30**, 65-70.
- 1.22 C. Jia, Q.-Q. Wang, R. A. Begum, V. W. Day and K. Bowman-James, *Org. Biomol. Chem.*, 2015, **13**, 6953-6957
- 1.23 K. Ghosh, S. Adhikari, R. Fröhlich, I. D. Petsalakis and G. Theodorakopoulos, *J. Mol. Struct.*, 2011, **1004**, 193-206.
- 1.24 D. Barišić, N. Cindro, M. J. Kulcsár, M. Tireli, K. Užarević, N. Bregović and V. Tomišić, *Chem. Eur. J.*, 2019, **25**, 4695-4706.
- 1.25 A. Rajbanshi, S. Wan, and R. Custelcean, *Cryst. Growth Des.*, 2013, **13**, 2233-2237.
- 1.26 B. Li, B. Zheng, W. Zhang, D. Zhang, X.-J. Yang, and B. Wu, *Cryst. Growth Des.*, 2019, **19**, 6527-6533.
- 1.27 P. A. Gale and C. Caltagirone, *Chem. Soc. Rev.*, 2015, **44**, 4212-422.
- 1.28 A. T. Wright and E. V. Anslyn, *Chem. Soc. Rev.*, 2006, **35**, 14-28.
- 1.29 N. Busschaert, C. Caltagirone, W. V. Rossom, and P. A. Gale, *Chem. Rev.* 2015, **115**, 15, 8038-8155.
- 1.30 C. Suksai, and T. Tuntulani, Chromogenic anion sensors, *Chem. Soc. Rev.*, 2003, **32**, 192-202.
- 1.31 T. Gunnlaugsson, M. Glynn, G. M. Tocci, P. E. Kruger and F. M. Pfeffer, *Coord. Chem. Rev.*, 2006, **250**, 3094-3117.
- 1.32 A. W. Czarnik, American Chemical Society: Washington, DC, 1993, **538**.
- 1.33 X. Q. Chen, M. Sun and H. M. Ma, *Curr. Org. Chem.*, 2006, **10**, 477-489.
- 1.34 V. Dujols, F. Ford and A. W. Czarnik, *J. Am. Chem. Soc.*, 1997, **119**, 7386-7387.
- 1.35 D. Wu, A. C. Sedgwick, T. Gunnlaugsson, E. U. Akkaya, J. Yoon and T. D. James, Fluorescent chemosensors: the past, present, and future, *Chem. Soc. Rev.*, 2017, **46**, 7105-7123.
- 1.36 A. Gupta and N. Kumar, *RSC Adv.*, 2016, **6**, 106413-106434.
- 1.37 X. Li, X. Gao, W. Shi, and H. Ma, *Chem. Rev.* 2014, **114**, 590-659.
- 1.38 D. H. Vance and A. W. Czarnik, *J. Am. Chem. Soc.*, 1994, **116**, 9397-9398.

Chapter 1

- 1.39 T. Gunnlaugsson, P. E. Kruger, T. C. Lee, R. Parkesh, F. M. Pfeffer, and G. M. Hussey, *Tetrahedron Lett.*, 2003, **44**, 6575–6578.
- 1.40 V. Amendola, G. Bergamaschi, M. Boiocchi, L. Fabbrizzi and L. Mosca, *J. Am. Chem. Soc.*, 2013, **135**, 6345–6355.
- 1.41 S. J. Hong, J. Yoo, S. H. Kim, J. S. Kim, J. Yoon and C. H. Lee, *Chem. Commun.*, 2009, **189**.
- 1.42 Y. Yue, F. Huo, P. Ning, Y. Zhang, J. Chao, X. Meng, and C. Yin, *J. Am. Chem. Soc.*, 2017, **139**, 3181–3185.
- 1.43 S. Mizukami, S. Okada, S. Kimura and K. Kikuchi, *Inorg. Chem.*, 2009, **48**, 7630.
- 1.44 S. Kim, J. Y. Noh, K. Y. Kim, J. H. Kim, H. K. Kang, S. W. Nam, S. H. Kim, S. Park, C. Kim, and J. Kim, *Inorg. Chem.* 2012, **51**, 6, 3597–3602.
- 1.45 H. S. Jung, P. S. Kwon, J. W. Lee, J. H. Kim, C. S. Hong, J. W. Kim, S. Yan, J. Y. Lee, J. H. Lee, T. Joo, and J. S. Kim, *J. Am. Chem. Soc.* 2009, **131**, 2008–2012.
- 1.46 L. Wang, W. K. Wong, L. Wu and Z.Y. Li, *J Am Chem Soc.*, 2004, **34**, 934–935.

Chapter 2

Experimental Methods & Characterization



This chapter combines comprehensive information about the various materials and methodology followed to synthesize and characterize the acyclic receptors/probes (**L1- L10**). It also includes specifics of general equipment, binding studies, minutes of crystallization along with the different types of experimental setups and important calculations used to study the interaction with different analytes.

2.1 Materials

All of the reagents and solvents were available from commercial suppliers and used hereafter without further purification. *Ortho*-Phenylenediamine, 1,5-Diaminonaphthalene, 3-nitrophenylisocyanate, 3, 5-bis (trifluoromethyl) phenyl-isothiocyanate, ninhydrin, 2-hydroxy-1-naphthaldehyde, Hydrazine, 1, 8-Naphthalimide, *Para*-Phenylenediamine, 1-naphthyl isocyanate, Pyrene-2-carbaldehyde, 3-(anthracene-9-yl) acrylaldehyde, Barbituric acid, Diethylenetriamine, 3-Formyl-6-methylchromone were purchased from Sigma-Aldrich (U.S.A). All the quaternary ammonium salts were also purchased from Sigma-Aldrich (U.S.A) whereas, organic and inorganic acids such as CH₃COOH, CF₃COOH, HF, H₂SO₄, HCl, HBr, HI, HNO₃ were obtained either from Merck or LOBA chemicals (India). All sodium, potassium salts, and deuterated solvents such as DMSO-d₆, CDCl₃ for NMR studies were acquired from Merck chemicals (India) and used as received. Solvents used in the synthesis and crystallization experiments were obtained either from Merck, India, and dried using standard techniques, wherever mentioned in the synthetic procedures.

2.2 General Methods

Bruker-D8 Venture X-ray diffractometer with Cu-K α radiation at $\lambda = 0.15418$ nm was used to record the powder X-ray diffraction patterns of dried crystalline powder of the crystal complexes. During absorption studies, Perkin-Elmer Lambda-25 UV–Vis spectrophotometer was used to achieve the absorption spectra where a quartz cuvette with path length 10 mm in the wavelength range of 250–750 nm was used. Horiba Fluoromax-4 spectrofluorometer was used to obtain the fluorescence spectra with quartz cuvettes of 10 mm path length at 298 K in the emission spectroscopy studies. The mass spectra were obtained using an Agilent Technologies 6520 Accurate mass spectrometer. The infrared spectra were recorded on a Perkin-Elmer Spectrum One FT-IR spectrometer with KBr pellets in the range 4000–400 cm⁻¹. NMR spectra were recorded and documented on Varian FT-400 MHz and Bruker 600 MHz instruments. Parts per million (ppm) were used to represent the value of the chemical shift on the delta scale. All

the abbreviated vocabularies were used to describe spin multiplicities in ^1H NMR spectra *viz.* ‘s’ for singlet; ‘d’ for doublet; ‘t’ for triplet; ‘m’ for multiplet.

2.3 Synthesis and characterization of the compounds (L₁-L₁₀)

2.3.1 Synthesis and characterization of receptors L₁- L₂

The neutral receptors are synthesized by reacting to para-phenylenediamine (0.324 g, 3.0 mmol) with 2.0 Equiv. of the 3-nitrophenylisocyanate (0.985 g, 6.0 mmol) and 3,5-Bis(trifluoromethyl) phenyl isothiocyanate (960 μL , 7.0 mmol) respectively in a 20 ml dry acetonitrile to make a homogeneous solution. Each reaction mixture was stirred at room temperature in a separate 250 mL round-bottomed flask and kept overnight. For the first case (L₁) the excess volume of acetonitrile was reduced in a vacuum, and we get a faint yellow solid product that was filtered off and washed with dry acetonitrile to get rid of the unseating reagents (yield = 82%). And for the next case after vigorous stirring for 24 h, the white precipitate was filtered off and washed several times with acetonitrile, THF, and then dried in a vacuum to yield (L₂)^{2.1} with an overall yield of 70% (Scheme 2.1). After purification of all the ligands and crystallization of all the complexes, they are characterized by using proton NMR, MS, and FT-IR analyses.

L₁: The characterization of receptor has been performed in a similar way that was done previously from our lab.^{2.2}

L₂: Values recorded from ^1H NMR (400 MHz, DMSO- d_6) δ (ppm): 7.417 (s, 4H, Aromatic-H), 7.627 (s, 4H, Aromatic-H), 8.134 (s, 4H, Aromatic-H), 8.892 (s, 2H, Urea-NH_a), 9.337 (s, 2H, Urea-NH_b). The values came from IR spectra revealed the following (using KBr pellet): 3370 $\text{cm}^{-1}\mu\text{s}$ (N-H), 3318 $\text{cm}^{-1}\mu\text{s}$ (C-H), 1660 $\text{cm}^{-1}\mu\text{s}$ (C=O), 1550 $\text{cm}^{-1}\mu\text{s}$ (C=C), 1000-1400 $\text{cm}^{-1}\mu\text{s}$ (C-F) 1219 $\text{cm}^{-1}\mu\text{s}$ (C-N). ESI-MS, $[\text{M}+1]^+$ (m/z) Calculated for C₂₄H₁₄N₄F₁₂O₂: 618.374, Found: 619.1027.

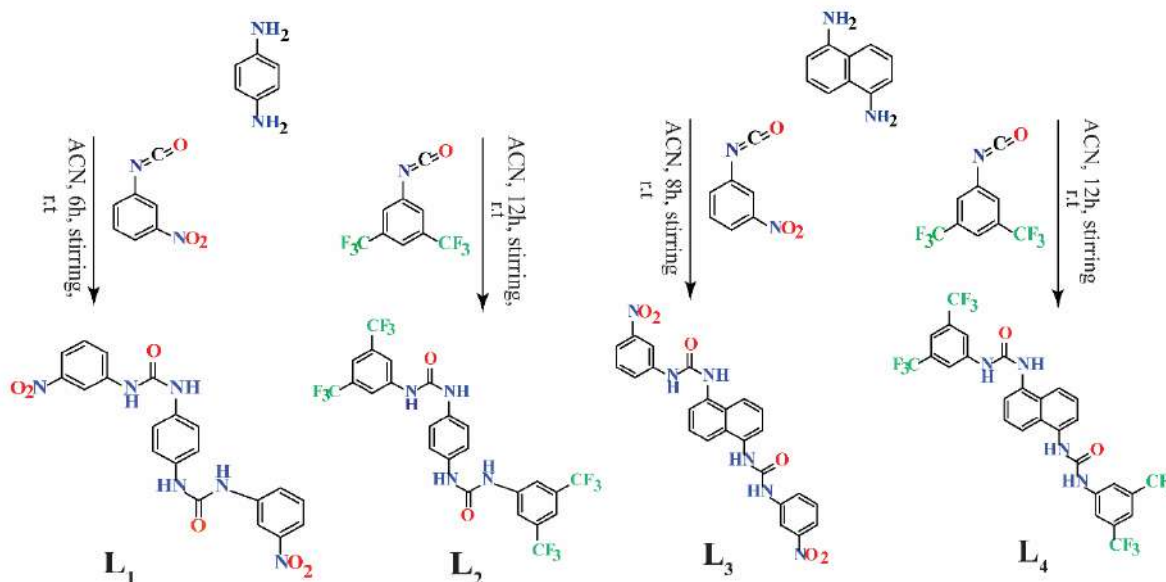
2.3.2 Synthesis of receptors L₃-L₄

Each neutral receptor has been synthesized by the reaction of 1, 5-Diaminonaphthalene (0.5 g, 1.0 mmol) with 2.0 Equiv. of the 3-nitrophenylisocyanate (1.037 g, 2.0 mmol) and 3,5-bis(trifluoromethyl)phenyl isothiocyanate (1094 μL , 7.0 mmol) respectively in a 20 ml dry acetonitrile solution to make it a uniform phase. Each of the mixtures was stirred at room temperature in a separate 250 mL round-bottomed flask and kept overnight for complete reaction. For the first case (L₃), the obtained greenish-yellow solid products were filtered off and washed with dry acetonitrile to eliminate the unreacted species which results to give a yield of 70%. And for the next case (L₄)^{2.3} after vigorous stirring for 24 h, a pale white precipitate

was filtered off and washed with dry acetonitrile to remove the unreacted reagents (yield = 75%) (Scheme 2.1). After purification of all the ligands and crystallization of all the complexes, they are characterized by using proton NMR, MS, and FT-IR analyses.

L3: Values recorded from ^1H NMR (400 MHz, DMSO- d_6) δ (ppm): 7.596-7.623 (t, 2H, \sim 5.2 Hz Aromatic-H), 8.016-8.029 (d, 2H, \sim 5.2 Hz, Aromatic-H), 7.898-7.912 (d, 2H, \sim 5.6 Hz, Aromatic-H), 7.745-7.758 (d, 2H, \sim 5.2 Hz, Aromatic-H), 7.596-7.623 (t, 2H, 10.8Hz, Aromatic-H), 8.629 (s, 2H, Aromatic-H), 8.932 (s, 2H, Urea-NH_a), 8.932 (s, 2H, Urea-NH_b). The values came from IR spectra revealed the following (using KBr pellet): 3356 cm^{-1} μs (N-H), 3218 cm^{-1} μs (C-H), 1666 cm^{-1} μs (C=O), 1500 cm^{-1} μs (C=C), 1000-1124 cm^{-1} μs . ESI-MS, $[\text{M}+1]^+$ (m/z) Calculated for $\text{C}_{24}\text{H}_{18}\text{N}_6\text{O}_6$: 486.129 Found: 487.1478.

L4: Values recorded from ^1H NMR (400 MHz, DMSO- d_6) δ (ppm): 8.171 (s, 2H, Aromatic-H), 7.950-7.930 (d, 2H, \sim 8 Hz, Aromatic-H), 7.932-7.901 (d, 2H, \sim 12.4 Hz, Aromatic-H), 7.669 (s, 4H, Aromatic-H), 7.616 - 7.576 (t, 2H \sim 12.4 Hz, Aromatic-H) 9.039 (s, 2H, Urea-NH_a), 9.705 (s, 2H, Urea-NH_b). The values came from IR spectra revealed the following (using KBr pellet): 3340 cm^{-1} μs (N-H), 3211 cm^{-1} μs (C-H), 1666 cm^{-1} μs (C=O), 1560 cm^{-1} μs (C=C), 1000-1123 cm^{-1} μs (C-F) 1134 cm^{-1} μs (C-N). ESI-MS, $[\text{M}+1]^+$ (m/z) Calculated for $\text{C}_{28}\text{H}_{16}\text{N}_4\text{F}_{12}\text{O}_2$: 668.108, Found: 669.1563.



Scheme 2.1 Synthesis of the receptors **L1-L4**

2.3.3 Synthesis and characterization of anion bound complexes (**L1**, **L2**)

The Chloride/Bromide complexes of either **L1** or **L2** receptors were obtained successfully by adding up an excess of tetrabutylammonium Chloride/bromide salts (10 Eqv.) respectively, into a 10 ml DMF/DMSO solution of either **L1** (0.240 mmol) or **L2** (0.190

mmol) in separate small glass tubes. The resulting solutions were stirred for about 2 hr (for Chloride) and 60 minutes (for Bromide) kept the reaction mixture open without any disturbance to vaporize slowly at room temperature. Plate-like yellowish crystals of Chloride as well as Bromide complexes **1a**, **2a** and **1b**, **2b** were obtained after ~20-30 days. All of those crystals are fitted satisfactorily for single-crystals X-ray analysis. Yield: 70% of **1a** from **L1** and 85% of **2a** from **L2** and 80% of **1b** from **L1** and 75% of **2b** from **L2**.

[(n-TBA)₂{(L₁)(Cl)₂}] (1a): Values recorded from ¹H NMR (400 MHz, DMSO-d₆) δ (ppm): 0.913–0.949 (t, 12H, ~14.4 Hz, TBA-CH₃), 1.261–1.352 (m, 8H, TBA-CH₂), 1.524– 1.603 (m, 8H, TBA-CH₂), 3.138–3.183 (t, 8H, ~18 Hz, N⁺TBA-CH₂), 7.408 (s, 4H, Aromatic-H), 7.541-7.581 (t, 2H, ~16Hz, Aromatic-H), 7.706–7.724 (d, 2H, ~7.2 Hz, Aromatic-H), 7.799-7.820 (d, 2H, ~8.4Hz, Aromatic-H), 8.569 (s, 2H, Aromatic-H), 9.051 (s, 2H, Urea-NH_a), 9.578 (s, 2H, Urea-NH_b). IR (using KBr pellet): 3240 cm⁻¹ μs (N-H), 3051 cm⁻¹ μs (C-H), 1693 cm⁻¹ μs (C=O), 657 cm⁻¹ μs (C-Cl), to 1660 cm⁻¹ μs (C-N).

[(n-TBA)₂{(L₂)(Cl)₂(H₂O)}] (2a): Values recorded from ¹H NMR (400 MHz, DMSO-d₆) δ (ppm): 0.917–0.953 (t, 12H, ~14.4 Hz, TBA-CH₃), 1.264–1.355 (m, 8H, TBA-CH₂), 1.528– 1.605 (m, 8H, TBA-CH₂), 3.142–3.183 (t, 8H, ~16.4 Hz, N⁺TBA-CH₂), 7.416 (s, 4H, Aromatic-H), 7.621(s, 4H, Aromatic-H), 8.131 (s, 2H, Aromatic-H), 9.150 (s, 2H, Urea-NH_a), 9.778 (s, 2H, Urea-NH_b). IR (using KBr pellet): 3340 cm⁻¹ μs (N-H), 3020 cm⁻¹ μs (C-H), 1660 cm⁻¹ μs (C=O), 603 cm⁻¹ μs (C-Cl), 1200cm⁻¹ μs (C-N).

[(n-TBA)₂{(L₁)(Br)₂(H₂O)₂}] (1b): Values recorded from ¹H NMR (400 MHz, DMSO-d₆) δ (ppm): 1.264–1.300 (t, 12H, ~14.4 Hz, TBA-CH₃), 1.318-1.567 (m, 8H, TBA-CH₂), 1.575– 2.545 (m, 8H, TBA-CH₂), 3.142–3.183 (t, 8H, ~16.4 Hz, N⁺TBA-CH₂), 8.565 (s, 2H, Aromatic-H), 7.546-7.587 (d, 2H, ~16.4Hz, Aromatic-H), 7.707-7.724 (d, 2H, ~6.8 Hz, Aromatic-H), 7.803-7.829(d,2H, ~10.4Hz, Aromatic-H), 8.569 (s, 2H, Aromatic-H), 8.786 (s, 2H, Urea-NH_a), 9.226 (s, 2H, Urea-NH_b). The values came from IR spectra revealed that (using KBr pellet): 3282 cm⁻¹ μs (N-H), 3000 cm⁻¹ μs (C-H), 1651 cm⁻¹ μs (C=O), 750-500 cm⁻¹μs (C-Br), C-N to 1660 cm⁻¹.

[(n-TBA)₂{(L₂)(Br)₂}] (2b): Values recorded from ¹H NMR (400 MHz, DMSO-d₆) δ (ppm): 0.911-0.948 (t, 12H, ~14.8 Hz, TBA-CH₃), 1.258-1.350 (m, 8H, TBA-CH₂), 1.525– 1.602 (m, 8H, TBA-CH₂), 3.141–3.183 (t, 8H, ~16.8 Hz, N⁺TBA-CH₂), 7.418(s, 2H, Aromatic-H), 7.622 (s, 4H, Aromatic-H), 8.134 (s, 2H, Aromatic-H), 8.993 (s, 2H,

Urea-NH_a), 9.514 (s, 2H, Urea-NH_b). IR (using KBr pellet): 3270 cm⁻¹ μs (N-H), 3084 cm⁻¹ μs (C-H), 1650 cm⁻¹ μs (C=O), 1000-1400 cm⁻¹ μs (C-F), 750-500 cm⁻¹ μs (C-Br).

2.3.4 Synthesis and characterization of anion bound complexes (L₃, L₄)

The Chloride/Bromide complexes of either L₃ or L₄ receptors were achieved by adding up an excess of tetrabutylammonium Chloride/Bromide salts (10Equivv.), respectively, into a 5 mL DMF/DMSO solution of either L₃ (0.242 mmol) or L₄ (0.198 mmol) separately. All the solutions were kept in an open atmosphere to make it sufficient concentrate. Crystals of Chloride as well as Bromide complexes **3a**, **4a** and **3b**, **4b** were obtained after ~10-30 days are appropriate for single-crystal X-ray analysis, Yield: 74% of **3a** from L₃ and 85% of **4a** from L₄ and 80% of **3b** from L₃ and 75% of **4b** from L₄.

Chloride complex [(n-TBA)₂{(L₃)(Cl)₂}] (3a**):** Values recorded from ¹H NMR (600 MHz, DMSO-d₆) δ (ppm): 0.928–0.952 (t, 12H, ~14.4 Hz, TBA-CH₃), 1.283–1.344 (m, 8H, TBA-CH₂), 1.544–1.596 (m, 8H, TBA-CH₂), 3.150–3.177 (t, 8H, ~16.2 Hz, N⁺TBA-CH₂), 7.587–7.622 (m, 4H, Aromatic-H), 7.752–7.765 (d, 2H, ~7.8 Hz, Aromatic-H), 7.850–7.863 (d, 2H, ~7.8 Hz, Aromatic-H), 7.926–7.940 (d, 2H, ~8.4 Hz, Aromatic-H), 8.022–8.034 (d, 2H, ~7.2 Hz, Aromatic-H), 8.637 (s, 2H, Aromatic-H) 8.992 (s, 2H, Urea-NH_a), 9.692 (s, 2H, Urea-NH_b). IR (using KBr pellet): 3280 cm⁻¹ μs (N-H), 3055 cm⁻¹ μs (C-H), 1693 cm⁻¹ μs (C=O), 654 cm⁻¹ μs (C-Cl).

[(n-TBA)₂{(L₄) (Cl)₂}] (4a**):** Values recorded from ¹H NMR (400 MHz, DMSO-d₆) δ (ppm): 0.920-0.957 (t, 12H, ~14.8 Hz, TBA-CH₃), 1.267-1.359 (m, 8H, TBA-CH₂), 1.532– 1.610 (m, 8H, TBA-CH₂), 3.146-3.188 (t, 8H, ~16.8 Hz, N⁺TBA-CH₂), 7.539-7.571 (t, 2H, ~ 12.8 Hz, Aromatic-H), 8.010-8.029 (d, 2H, 7.6 Hz, Aromatic-H), 8.087-8.109 (d, 2H, ~8.8 Hz, Aromatic-H), 8.189 (s, 2H, Aromatic-H), 9.406 (s, 2H, Urea-NH_a), 10.656 (s, 2H, Urea-NH_b). IR (using KBr pellet): 3280 cm⁻¹ μs (N-H), 3081 cm⁻¹ μs (C-H), 1661 cm⁻¹ μs (C=O), 657 cm⁻¹ μs (C-Cl), 1000-1400 cm⁻¹ μs (C-F).

[(n-TBA)₂{(L₃) (Br)₂}] (3b**):** Values recorded from ¹H NMR (400 MHz, DMSO-d₆) δ (ppm): 0.922–0.959 (t, 12H, ~14.8 Hz, TBA-CH₃), 1.269–1.361 (m, 8H, TBA-CH₂), 1.534–1.612 (m, 8H, TBA-CH₂), 3.148–3.190 (t, 8H, ~16.8 Hz, N⁺TBA-CH₂), 7.574–7.629 (m, 4H, Aromatic-H), 7.753–7.774 (d, 2H, ~8.4 Hz, Aromatic-H), 7.846–7.866 (d, 2H, ~8 Hz, Aromatic-H), 7.930–7.952 (d, 2H, ~8.8 Hz, Aromatic-H), 8.019–8.038 (d, 2H, ~7.6 Hz, Aromatic-H), 8.642 (s, 2H, Aromatic-H) 8.985 (s, 2H, Urea-NH_a), 9.694 (s, 2H, Urea-NH_b). IR (using KBr pellet): 3280 cm⁻¹ μs (N-H), 3081 cm⁻¹ μs (C-H), 1686 cm⁻¹ μs (C=O), 700-550 cm⁻¹ μs (C-Br). 1600 cm⁻¹ μs (C-N).

[(n-TBA)₂{(L₄) (Br)₂}] (**4b**): Values recorded from ¹H NMR (400 MHz, DMSO-d₆) δ (ppm): 1.850-1.887 (t, 12H, ~14.8 Hz, TBA-CH₃), 2.197-2.288 (m, 8H, TBA-CH₂), 2.461-2.539 (m, 8H, TBA-CH₂), 4.075-4.117 (t, 8H, ~16.8 Hz, N+TBA-CH₂), 8.504-8.545 (t, 2H, ~ 16.4 Hz, Aromatic-H), 8.870-8.892 (m, 4H, Aromatic-H), 9.111 (s, 2H, Ar-H) 8.603 (s, 2H, Aromatic-H), 10.016 (s, 2H, NH_a), 10.774 (s, 2H, NH_b). IR (using KBr pellet): 3285 cm⁻¹ μs (N-H), 3077 cm⁻¹ μs (C-H), 1709 cm⁻¹ μs (C=O), 600-800 cm⁻¹ μs (C-Br), 1000-1400 cm⁻¹ μs (C-F).

2.3.5 General method for the preparation of receptors L₅ and L₆

The molecule **P** was synthesized based on the reported literature.^{2,4} To a stirred solution of **P** (0.324 g, 1.2 mmol) in 10 ml acetonitrile, aromatic isocyanate (1.0 mmol) was added in 10 ml of acetonitrile at room temperature. After refluxing for 24 h, the white precipitate was filtered and washed several times with acetonitrile and hexane for eliminating the unreacted starting materials. The white precipitate was collected and characterized.

2.3.5.1 Synthesis and characterization of L₅ and L₆

1,8-Naphthalimide-based synthetic nitrophenyl (**L₅**) and naphthyl (**L₆**) receptor, was synthesized in high yield using the general procedure (Scheme 2.2). The compound thus obtained was characterized using different spectroscopic tools and the desired compound was recrystallized from either DMF or DMSO solution within 10 days for single-crystal analyses (**L₅**). Yield = 90% based on **P**. But after several attempts, we could not develop any single crystal of **L₆**. Yield = 85% based on **P**.

1-(4-(1,3-dioxo-1H-benzo[de]isoquinolin-2(3H)-yl) phenyl)-3-(3-nitrophenyl) urea (**L₅**).

¹H NMR (600 MHz, DMSO-*d*₆) δ 9.33 (s, 1H), 9.05 (s, 1H), 8.60 (s, 1H), 8.55 – 8.46 (m, 3H), 8.00 – 7.89 (m, 3H), 7.85 (d, *J* = 8.2 Hz, 1H), 7.75 (d, *J* = 8.2 Hz, 1H), 7.69 – 7.51 (m, 3H), 7.31 (d, *J* = 8.7 Hz, 2H). δ (ppm): ¹³C NMR (150 MHz, DMSO-*d*₆): δ=164.2, 152.9, 148.7, 141.5, 139.5, 134.8, 131.9, 131.2, 130.5, 129.9, 127.7, 124.8, 123.1, 119.3, 116.8, 112.7. FT-IR spectra (KBr pellet used): 3280-3300 cm⁻¹ μs (urea N-H), 3250-3260 cm⁻¹ μs (aromatic C-H), 2850-2860 cm⁻¹ μs (aromatic C-H), 1625-1650 cm⁻¹ μs (urea C=O), 1538 cm⁻¹ μs (NO₂-asymmetric), 1361 cm⁻¹ μs (NO₂-symmetric). ESI-MS: *m/z* 453.1299 [M+1]⁺ (*m/z*).

1-(4-(1,3-dioxo-1H-benzo[de]isoquinolin-2(3H)-yl) phenyl)-3-(naphthalen-1-yl) urea (**L₆**)

¹H NMR (400 MHz, DMSO-*d*₆) δ 9.25 (s, 1H), 8.87 (s, 1H), 8.53 (d, *J* = 7.8 Hz, 4H), 8.17 (d, *J* = 8.3 Hz, 1H), 8.05 (d, *J* = 7.3 Hz, 1H), 7.98 – 7.88 (m, 3H), 7.69 – 7.46 (m, 6H), 7.31 (d, *J* = 8.7 Hz, 2H). ¹³C NMR (100 MHz, DMSO-*d*₆): δ=164.3, 153.4, 140.0, 134.8, 134.2, 131.9,

131.2, 130.1, 129.9, 128.9, 128.3, 127.7, 126.4, 123.5, 121.8, 118.9 ppm. FT-IR spectra (KBr pellet used): 3493-3500 cm^{-1} μs (Urea N-H), 3370-3400 cm^{-1} μs (aromatic C-H), 2870-2890 cm^{-1} μs (aromatic C-H), 1680 cm^{-1} μs (urea C=O), ESI-MS: m/z 458.1637 $[\text{M}+1]^+$ (m/z).

2.3.5.2 Synthesis and characterization of anion bound complexes **5a-d**, **6a-d**

Complexes **5a-d** and **6a-d** were attained by introducing an excess amount of various *n*-tetrabutylammonium salts (fluoride/hydroxide for complex **5a**) (10 Equiv.) into the 10 mL DMSO solution of **L5/L6** (200 mg, 0.161 mmol) in a small test tube. After the addition of the above salts, the resulting solutions were further stirred for about 10-15 min and left exposed to the air for spontaneous slow evaporation at room temperature. Various types of single crystals were obtained within 10–30 days suitable for SC-XRD analysis. Further, all of them were isolated and dried before characterization by NMR and FT-IR analyses. **5a**: Isolated yield: 75–80%, **5b**: 85%, **5c**: 70-75%, **5d**: 80–85% based on **L5**. And Yield: **6a**: 50–55%, **6b**: 50–55%, **6c**: 60-65%, **6d**: 85% based on **L6**.

Bicarbonate complex of **L5** (**5a**)

^1H NMR (500 MHz, DMSO- d_6) δ 12.48 (s, 1H), 12.07 (s, 1H), 8.71 (s, 1H), 8.52 (d, $J = 6.9$ Hz, 5H), 7.91 (t, $J = 7.4$ Hz, 4H), 7.74 (d, $J = 17.7$ Hz, 4H), 7.52 (t, $J = 8.2$ Hz, 2H), 7.23 (d, $J = 8.4$ Hz, 2H). FT-IR spectra (KBr pellet): 3480 cm^{-1} μs (O-H), 3356 cm^{-1} μs (Urea N-H), 3320 cm^{-1} μs (aromatic C-H), 3200 cm^{-1} μs (aromatic C-H), 1620-1655 cm^{-1} μs (urea C=O), 1530 cm^{-1} μs (NO_2 -*asym*), 1360 cm^{-1} μs (NO_2 -*sym*), 1219 cm^{-1} μs (C-N).

Bisulphate complex of **L5** (**5b**)

^1H NMR (400 MHz, DMSO- d_6) δ 9.68 (s, 1H), 9.39 (s, 1H), 8.64 (s, 1H), 8.52 (t, $J = 8.2$ Hz, 4H), 7.94 – 7.88 (m, 2H), 7.82 (t, $J = 9.0$ Hz, 2H), 7.65 (d, $J = 7.5$ Hz, 2H), 7.58 (d, $J = 8.2$ Hz, 1H), 7.29 (d, $J = 7.4$ Hz, 2H). FT-IR spectra (KBr pellet): broadband at 3420 cm^{-1} μs (O-H), 3256 cm^{-1} μs (Urea N-H), 3220 cm^{-1} μs (aromatic C-H), 3100 cm^{-1} μs (aromatic C-H), 1625-1650 cm^{-1} μs (urea C=O), 1410 cm^{-1} μs (S=O), 1525 cm^{-1} μs (NO_2 -*asym*), 1364 cm^{-1} μs (NO_2 -*sym*), 1219 cm^{-1} μs (C-N).

Hydrated-chloride complex of **L5** (**5c**)

^1H NMR (600 MHz, DMSO- d_6) δ 9.70 (s, 1H), 9.37 (s, 1H), 8.61 (s, 1H), 8.55 – 8.50 (m, 4H), 7.92 (t, $J = 7.7$ Hz, 2H), 7.84 (d, $J = 7.9$ Hz, 1H), 7.76 (d, $J = 8.1$ Hz, 1H), 7.60 (dd, $J = 19.2, 8.4$ Hz, 3H), 7.31 (d, $J = 8.7$ Hz, 2H). FT-IR spectra (KBr pellet): 3400 cm^{-1} μs (Urea N-H), 3250 cm^{-1} μs (aromatic C-H), 2955 cm^{-1} μs (aromatic C-H), 1725 cm^{-1} μs (urea C=O), 1525 cm^{-1} μs (NO_2 -*asym*), 1368 cm^{-1} μs (NO_2 -*sym*), 1219 cm^{-1} μs (C-N), 680 cm^{-1} μs (C-Cl).

Hydrated-bromide complex of L₅ (5d)

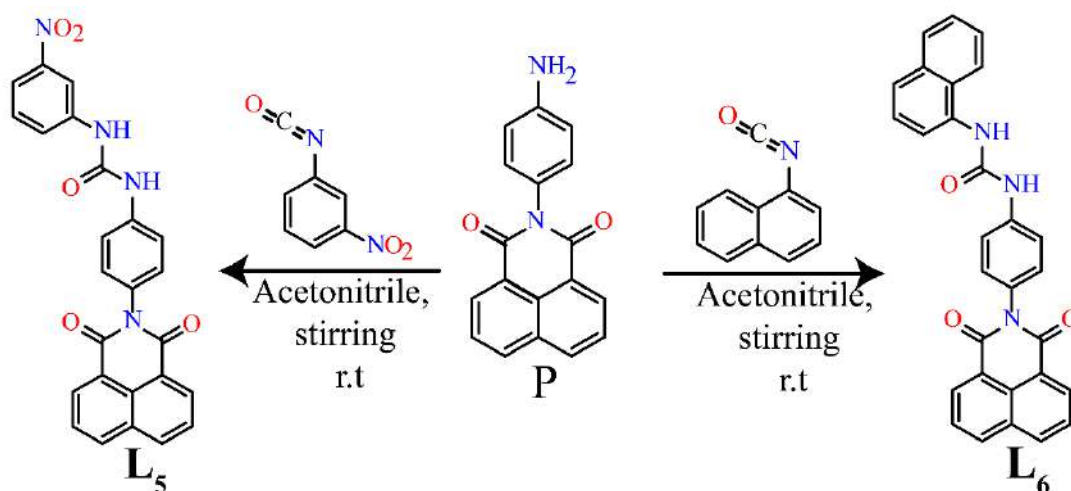
¹H NMR (600 MHz, DMSO-*d*₆) δ 9.40 (s, 1H), 9.12 (s, 1H), 8.61 (s, 1H), 8.56 – 8.49 (m, 4H), 7.92 (t, *J* = 7.7 Hz, 2H), 7.85 (d, *J* = 8.2 Hz, 1H), 7.76 (d, *J* = 8.0 Hz, 1H), 7.65 – 7.56 (m, 3H), 7.32 (d, *J* = 8.6 Hz, 2H). FT-IR spectra (KBr pellet used): 3410 cm⁻¹ μs (Urea N–H), 3100 cm⁻¹ μs (aromatic C–H), 2945 cm⁻¹ μs (aromatic C–H), 1715 cm⁻¹ μs (urea C=O), 1510 cm⁻¹ μs (NO₂-*asym*), 1290 cm⁻¹ μs (NO₂-*sym*), 1220 cm⁻¹ μs (C–N).

Bicarbonate complex of L₆ (6a)

¹H NMR (400 MHz, DMSO-*d*₆) δ 9.34 (s, 1H), 8.94 (s, 1H), 8.52 (d, *J* = 7.7 Hz, 4H), 8.20 (d, *J* = 8.3 Hz, 1H), 8.04 (d, *J* = 7.5 Hz, 1H), 7.93 (q, *J* = 8.4, 7.7 Hz, 4H), 7.69 – 7.64 (m, 4H), 7.62 – 7.55 (m, 2H), 7.50 (t, *J* = 7.9 Hz, 1H), 7.33 – 7.29 (m, 2H). FT-IR spectra (KBr pellet used): broad band at 3313 cm⁻¹ μs (O–H) 3012 cm⁻¹ μs (N–H), 2580 cm⁻¹ μs (C–H), 1650–1655 cm⁻¹ μs (C=O).

Bisulphate complex of L₆ (6b)

¹H NMR (600 MHz, DMSO-*d*₆) δ 9.36 (s, 1H), 8.96 (s, 1H), 8.55 – 8.50 (m, 4H), 8.20 (d, *J* = 8.4 Hz, 1H), 8.04 (d, *J* = 7.5 Hz, 1H), 7.93 (dt, *J* = 15.5, 7.9 Hz, 3H), 7.67 (d, *J* = 8.6 Hz, 3H), 7.61 (t, *J* = 7.6 Hz, 1H), 7.56 (t, *J* = 7.4 Hz, 1H), 7.50 (t, *J* = 7.9 Hz, 1H), 7.31 (d, *J* = 8.6 Hz, 2H). FT-IR spectra (KBr pellet used): broad band at 3020 cm⁻¹ μs (O–H) 3010 cm⁻¹ μs (N–H), 2580 cm⁻¹ μs (C–H), 1670–1675 cm⁻¹ μs (C=O).



Scheme 2.2 Synthesis of the receptors L₅ and L₆

Chloride complex of L₆ (6c)

¹H NMR (600 MHz, DMSO-*d*₆) δ 10.66 (s, 1H), 9.66 (s, 1H), 8.57 (d, *J* = 5.5 Hz, 1H), 8.52 (t, *J* = 8.4 Hz, 3H), 8.12 (d, *J* = 7.6 Hz, 1H), 7.91 (t, *J* = 7.6 Hz, 3H), 7.68 (d, *J* = 8.6 Hz, 2H), 7.61 (d, *J* = 8.1 Hz, 1H), 7.53 (d, *J* = 4.5 Hz, 2H), 7.47 (t, *J* = 7.9 Hz, 1H), 7.27 (d, *J* = 8.6 Hz, 2H).

FT-IR spectra (KBr pellet used): sharp band at 3392 cm^{-1} μs (N-H), 3050 cm^{-1} μs (C-H), 2870 cm^{-1} μs (C-H), $1725\text{-}1730\text{ cm}^{-1}$ μs (C=O), 660 cm^{-1} μs (C-Cl).

Bromide complex of **L₆** (**6d**)

^1H NMR (400 MHz, DMSO- d_6) δ 9.34 (s, 1H), 8.94 (s, 1H), 8.52 (d, $J = 7.7$ Hz, 4H), 8.20 (d, $J = 8.3$ Hz, 1H), 8.04 (d, $J = 7.5$ Hz, 1H), 7.93 (q, $J = 8.4, 7.7$ Hz, 4H), 7.69 – 7.64 (m, 4H), 7.62 – 7.55 (m, 2H), 7.50 (t, $J = 7.9$ Hz, 1H), 7.33 – 7.29 (m, 2H). FT-IR spectra (KBr pellet): sharp band at 3400 cm^{-1} μs (N-H), 3050 cm^{-1} μs (C-H), 2872 cm^{-1} μs (C-H), $1715\text{-}1720\text{ cm}^{-1}$ μs (C=O), 580 cm^{-1} μs (C-Br).

2.3.6 Synthesis and characterization of probes **L₇** and **L₈**

2.3.6.1 Synthesis of 5-(pyrene-2-ylmethylene) pyrimidine-2, 4, 6(**1H**, **3H**, **5H**)-trione (**L₇**)

Pyrene-2-carbaldehyde (76 mg, 1 mmol) and Barbituric acid (BA) (46 mg, 1 mmol) along with 2 ml glacial acetic acid were dissolved in ethanol (15 mL). The resulting mixture was refluxed for ~6 h resulting in a deep red color solid product which was further filtered off and washed several times with ethanol followed by water to afford Probe **L₇**.

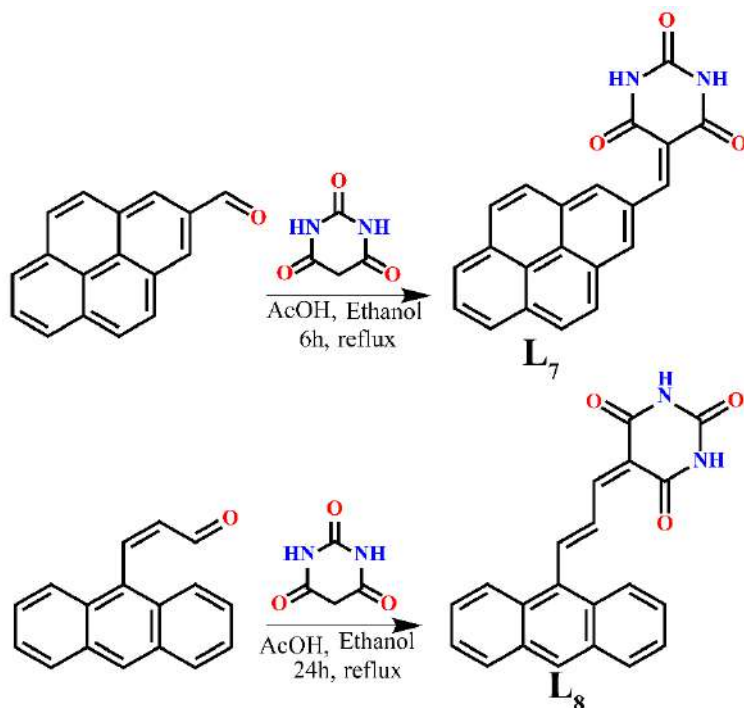
L₇: ^1H NMR (500 MHz, DMSO- d_6 , TMS, δ ppm): 11.190 (s, 1H), 11.483 (s, 1H), 9.118 (s, 1H), 8.404-8.361 (m, 3H, ArH), 8.320-8.281 (m, 3H, ArH), 8.245-8.192 (m, 2H, ArH), 8.136 (t, 1H, $J=7.5$ Hz, ArH); ^{13}C NMR (126 MHz, DMSO- d_6 , TMS, δ ppm): 206.91, 163.59, 161.60, 152.96, 150.89, 133.04, 131.11, 130.66, 129.80, 129.40, 129.20, 128.90, 128.77, 127.77, 127.09, 126.90, 126.77, 124.31, 124.05, 123.83, 121.77; FT-IR: KBr ($\mu\text{s cm}^{-1}$): 3194, 3045, 2850, 1739, 1655, 1548, 1532, 1443, 1417, 1387, 1233, 1185, 843, 970, 517; ESI-MS (positive mode, m/z): Mass spectrum of probe **L₇**, calculated for $\text{C}_{21}\text{H}_{12}\text{N}_2\text{O}_3$ [**M**] = 340.0848, found [**M**+1] $^+$ (m/z) = 341.0956.

2.3.6.2 Synthesis of (E)-5-(3-(anthracene-9-yl) allylidene) pyrimidine-2, 4, 6(**1H**, **3H**, **5H**)-trione (**L₈**)

3-(anthracene-9-yl) acrylaldehyde (77 mg, 1 mmol) and Barbituric acid (BA) (42.2 mg, 1 mmol) along with 3 ml glacial acetic acid were dissolved in ethanol (10 mL). The resulting mixture was refluxed for ~10 h resulting in a red color solid precipitate which was further filtered off and washed several times with ethanol followed by water to afford Probe **L₈**.

L₈: ^1H NMR (500 MHz, DMSO- d_6 , TMS, δ ppm): 11.367 (s, 1H), 11.255 (s, 1H), 8.858-8.809 (m, 1H), 8.735 (s, 1H), 8.428-8.401 (m, 3H), 8.182(d, 2H, $J=7$ Hz, ArH), 7.962 (d, 1H, $J=6.5$ Hz, ArH), 7.641-7.576 (m, 3H, ArH), 7.232-7.211(d, 1H, $J=10.5$ Hz); ^{13}C NMR (126 MHz, DMSO- d_6 , TMS, δ ppm): 163.64, 163.47, 163.13, 153.81, 150.83, 149.37, 146.67, 133.39,

131.42, 131.19, 130.35, 129.89, 129.66, 129.53, 129.28, 127.56, 127.20, 126.20, 125.74, 125.45, 116.84; FT-IR: KBr ($\mu\text{s cm}^{-1}$): 3186, 3046, 2843, 1739, 1767, 1566, 1547, 1439, 1387, 1319, 1192, 1175, 1006, 826, 725, 511; Mass spectrum of probe **L**₈, calculated for C₂₁H₁₂N₂O₃ [**M**] = 342.1004, found [M+1]⁺ (m/z) = 343.1077



Scheme 2.3 Synthesis of the receptors **L**₇ and **L**₈

2.3.7 General methods for Synthesis of probe **L**₉

2.3.7.1 Synthesis of Compound **A**

Room temperature stirring of ninhydrin (1.04 mmol) and *o*-phenylene diamine (1.6 mmol) in methanol with a few drops of concentrated H₂SO₄ for 3 hours give a flappy orange-like precipitate. Detail about **A** has been reported from our lab previously.^{2.5}

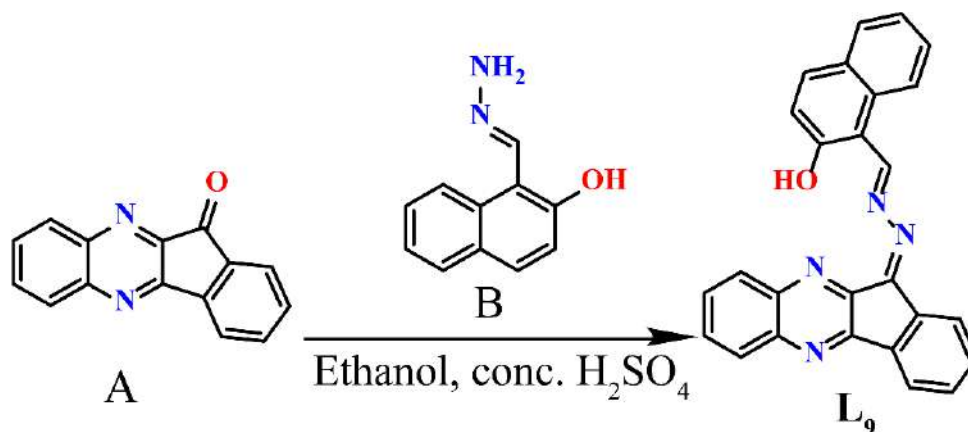
2.3.7.2 Synthesis of Compound **B**

In a 100 ml round-bottomed flask 10 mmol (1.00 g) of 2-hydroxy-1-naphthaldehyde was taken and it was dissolved in 60 mL of methanol by constant stirring. To this solution, excess hydrazine hydrate (5.0 mL, ~100 mmol) was added. The mixture was allowed to stir for 24 h to obtain a pale yellow color solid product, which was filtered and washed thoroughly with methanol. This product constituted the Schiff base having a mono-imine bond and a free amine group of hydrazine. Detail about **B** has been reported from our lab previously^{2.6}

2.3.7.3 Synthesis and characterization of the probe L₉

The synthetic route of L₉ is shown in 1.0 mmol of the compound 1 and 1.0 mmol of product compound 2 was dissolved in ethanol and few drops of sulphuric acid were added and the mixture was stirred for 16 h to obtain a deep red colored solid product L₉ (Scheme 2.4) which was washed several times with methanol and then dried in a desiccator. Later, it was recrystallized from DCM-MEOH (2:1) mixture and left for slow evaporation. Red block type crystal was obtained after 4-5 weeks which were characterized by NMR, FT-IR, ESI-MS, and single-crystal X-ray analysis.

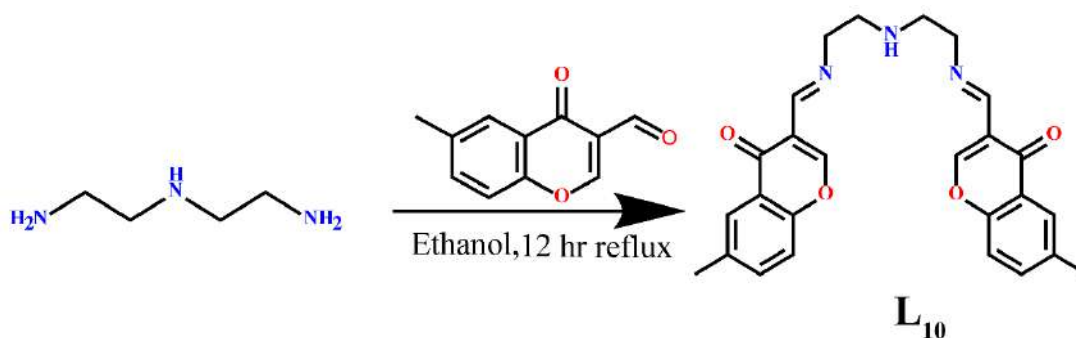
L₉: yield = 75%; ¹H NMR [400 MHz, CDCl₃, TMS, δ (ppm)]: 14.219 (s, 1H), 9.920 (s, 1H), 8.550 (d, 1H), 8.251 (d, 2H), 8.172 (m, 4H), 7.942 (d, 2H), 7.818 (t, 1H), 7.643 (m, 2H), 7.415 (t, 1H), 7.371 (d, 1H). ¹³C [100 MHz, CDCl₃, TMS, δ (ppm)]: 164.980, 164.022, 162.894, 154.791, 154.549, 146.871, 142.114, 141.820, 138.618, 137.529, 135.989, 133.189, 132.382, 131.810, 131.262, 129.519, 129.190, 129.113, 128.059, 127.979, 123.780, 123.001, 122.374, 120.679, 120.250, 108.902. FT-IR: KBr (μs cm⁻¹): 3382, 1623, 1576, 1524, 1450, 1294, 1190, 1120, 1070, 960, 800, 760, 495, ESI-MS (positive mode, m/z): Calculated for C₂₆H₁₆N₄O [M] = 400.1415, found [M+1]⁺ (m/z) = 401.1415.



Scheme 2.4 Synthesis of the receptors L₉

2.3.8 Synthesis and characterization of probe L₁₀

3-Formyl-6-methylchromone (2 mmol) and Diethylenetriamine (1 mmol) were dissolved in EtOH (40 mL). The resulting mixture was refluxed for 12 hr. The solution cooled to room temperature. Evaporation of the brown-coloured solution and work up with CHCl₃/H₂O yields the receptor L₁₀, (Scheme 2.5). The compound was finally dried in a vacuum over silica gel. The product L₁₀ was obtained as a brown coloured solid which was later recrystallized with methanol before proceeding with further experiments.



Scheme 2.5 Synthesis of the receptors **L**₁₀

2.4 Crystallographic refinement data

In each case, from the mother liquor, a crystal of suitable size crystal was selected in silicone oil, and then mounted on the tip of glass fibre and cemented using epoxy resin. The X-ray crystallographic intensity data were collected using Supernova, a single source at the offset, Eos diffractometer using Mo-K α radiation ($\lambda = 0.71073 \text{ \AA}$) equipped with a CCD area detector, and corresponding data refinement and cell reduction were performed by CrysAlisPro.^{2,7} The data integration and reduction were carried out with SAINT and XPREP^{2,8} software, and multi-scan empirical absorption corrections were applied to the data using the program SADABS.^{2,9} All the structures were solved by direct methods using SHELXTL-2014 and 2016 and were refined on F₂ by the full-matrix least-squares technique using the SHELXL-2014 and 2016 program package.^{2,10} Hydrogen atoms were geometrically fixed. Structural illustrations are generated using MERCURY 4.1.3 for Windows.^{2,11} PLATON/SQUEEZE was used to refine the host framework in some host-guest complexes excluding the disordered counter-cation or solvent molecules.^{2,12} All the crystallographic data have been deposited in the CCDC. The CCDC numbers assigned to the complexes $[(n\text{-TBA})_2\{(\text{L}_1)(\text{Cl})_2\}]$ (**1a**) and $[(n\text{-TBA})_2\{(\text{L}_2)(\text{Cl})_2(\text{H}_2\text{O})\}]$ (**2a**), $[(n\text{-TBA})_2\{(\text{L}_1)(\text{Br})_2(\text{H}_2\text{O})_2\}]$ (**1b**) and $[(n\text{-TBA})_2\{(\text{L}_2)(\text{Br})_2\}]$ (**2b**), Chloride complex $[(n\text{-TBA})_2\{(\text{L}_3)(\text{Cl})_2\}]$ (**3a**) and $[(n\text{-TBA})_2\{(\text{L}_4)(\text{Cl})_2\}]$ (**4a**), Bromide complex $[(n\text{-TBA})_2\{(\text{L}_3)(\text{Br})_2\}]$ (**3b**) and $[(n\text{-TBA})_2\{(\text{L}_4)(\text{Br})_2\}]$ (**4b**) are respectively 1937116, 1937114, 1937113, 1937117, 1937120, 1937118, 1937119 and 1937115. For the receptors, **L**₅ and **L**₆, The CCDC numbers assigned to the complexes **5a**, **5b**, **5c**, **5d**, and **6d** are respectively 2075153, 2075154, 2077109, 2075155, 2075156, and 2075157. The R_{int} value exceeds the cut-off limit due to unaccountable disorder (complex **5b**) and a lack of low-temperature instrumentation. Due to the large O–H bonds in water molecules, we were unable to attach a hydrogen atom to a water molecule after many attempts for some anion-bound complexes. The receptor **L**₉ bears CCDC number 2055399. Crystallographic parameters for data collection and crystallographic

refinement details of the receptors and their anion complexes are summarized in the respective chapters.

2.5 UV–Vis and Fluorescence Spectral Studies

Stock solutions of various anions (50×10^{-3} M) were prepared in deionized water. Tetrabutyl/tetraethyl or sodium salts of the corresponding anions were used to make all the stock solutions of the studied anions. In DMSO, stock solutions of **L5** and **L6** (5.0 mM each) were prepared. For UV-vis spectroscopic studies, a 10 μ M solution of each of the ligands was prepared from these stock solutions in a 2 mL quartz cell. The cell was filled with aliquots of the anion solutions (10 eq. w.r.t. the ligand concentration) prepared in Milli-Q water. The stock solutions (5×10^{-3} M) of the probes **L7-L10** were prepared in dry DMSO. For the selectivity study as well as titration experiment in absorption and emission studies, each chemosensor or chemodosimeter solution was further diluted to 1×10^{-3} mol L⁻¹ in the required experimental medium. For the titration experiments in each case, a 1×10^{-3} mol L⁻¹ probe solution was poured in a quartz optical cell of 1 cm optical path length and then titrated with an incremental concentration of concerned anion/cation stock solutions in the experimental medium. For the competitive selectivity studies, emission spectra of the ‘sensor guest’ ensemble are collected in the presence and absence of the competitive ions (10 equivalents).

2.6 Multivariate experimental set-up: The samples were read right away after they were prepared. During the replication of a standard multivariate binding experiment, blank samples (containing only **L1** and **L2** separately) were also replicated (used for normalization of data). The concentrations of the probes were kept constant at 10 μ M. The concentration of tetrabutylammonium anions was 100 μ M. To record the values at saturation points, a 10-to-1 anion-to-probe ratio was chosen. The absorption responses of the probes were measured at various wavelengths, and the results were then used in the LDA study.

2.7 Antibacterial Activity of Ligands and Complexes

The target bacteria used in the study consisted of *Escherichia coli* MTCC 433 and methicillin-resistant *Staphylococcus aureus* MRSA 100. The MRSA strain was kindly provided by Prof. Benu Dhawan, All India Institute of Medical Sciences (AIIMS), New Delhi, and Prof. Kasturi Mukhopadhyay, Jawaharlal Nehru University (JNU), New Delhi. Nutrient broth (NB) was used to propagate *E. coli* MTCC 433 whereas *S. aureus* MRSA 100 was grown in Brain Heart

Infusion (BHI) medium. Stock solutions of the ligands (**L₅** and **L₆**) and their corresponding complexes were prepared in DMSO and before the antibacterial assays, working solutions were freshly reconstituted to achieve the desirable concentrations for the specific experiments. The target bacterial strains were inoculated at 1% level in separate sets in microtiter wells (approximately 5×10^6 CFU/well) having 100 μ L of the specific growth medium and propagated overnight at 37°C and 180 rpm in presence of varying concentrations of the ligands **L₅** and **L₆** and the corresponding complexes (1.0 μ g/mL, 5.0 μ g/mL and 10 μ g/mL each). Following incubation, the growth of treated bacterial cells was recorded by measuring absorbance at 600 nm from replica samples in a microtiter plate reader (Tecan, Austria GmbH). The growth was expressed in percentage compared to the control sample (untreated cells).

2.8 Cytotoxic Effect of Ligands and Complexes

The cytotoxic effect of the ligands **L₅** and **L₆** and the corresponding complexes was evaluated against the human embryonic kidney cell line (HEK 293) by a standard MTT assay as per manufacturer's instructions (Sigma-Aldrich, MO, USA). HEK 293 cells were initially cultured in Dulbecco's Modified Eagle Medium (DMEM) supplemented with 10% fetal bovine serum (FBS) and 1% penicillin-streptomycin antibiotic solution and incubated at 37°C under 5% CO₂. Subsequently, the cells were seeded in separate sets in a 96 well tissue culture plate (10⁴ cells/well) and varying concentrations of **L₅** and **L₆** and the corresponding complexes (1.0 μ g/mL, 5.0 μ g/mL and 10 μ g/mL each) was added separately to the cells. The cells were incubated for a period of 24 h at 37 °C under 5% CO₂. DMSO was used as solvent control in each assay. Following incubation, the growth media was carefully removed and fresh DMEM containing 5% MTT solution was added and the plate was incubated for 4 h at 37°C. Subsequently, the media was gently aspirated and DMSO was added to solubilize formazan. The colorimetric measurement was accomplished at 570 nm with a reference at 655 nm in a multi-plate reader (Tecan, Austria GmbH). MTT assay was performed in six sets for each tested concentration. Data analysis and calculation of standard deviation were performed with Microsoft Excel 2019 (Microsoft Corporation, USA).

2.9 Evaluation of the Apparent Binding constant

For the receptors, **L₉** and **L₁₀**, the apparent binding constant for the formation of the respective complexes was evaluated using the Benesi–Hildebrand (B–H) plot following equation (1).^{2,13-2,14}

$$1/(I - I_0) = 1/\{K(I_{\max} - I_0)[G]\} + 1/(I_{\max} - I_0) \dots\dots\dots (1)$$

I_0 is the fluorescence intensity of the host at emission maximum, I is the observed emission at that particular wavelength in the presence of a certain concentration of the analyte, I_{\max} is the maximum emission value that was obtained during titration with varying analyte concentration, K is the apparent binding constant (M^{-1}) and was determined from the slope of the linear plot.

The binding constant was also calculated from the absorption titration experiment using the Benesi–Hildebrand (B–H) plot following equation (2),

$$1/(A-A_0) = 1/ \{K_a (A_{\max}-A_0) [G]\} + 1/(A_{\max}-A_0) \dots\dots\dots(2)$$

where A_0 and A are the absorbance of the host in the absence and presence of guest ions respectively and A_{\max} is the saturated absorbance of the host in the presence of guest ions and K_a (M^{-1}) is the binding constant and was determined from the slope of the linear plot. For some cases ($L_9/L_{10}-Al^{3+}$), the ensemble-based detection of analyte (M), the association/dissociation constants (K_d) determined from the fluorescence titration experiment using the following equation (3),

$$(F_i-F_{\max}) = \Delta F = [PPi] (F_{\text{sat}} - F_o) / (K_d + [PPi]). \dots\dots\dots(3)$$

F_i is the experimentally determined emission with different. equiv. of M,

F_{\max} is the emission for the ensemble ($L_9/L_{10}-Al^{3+}$), F_{sat} is the saturation value of the emission intensity obtained after the addition of [M]. To obtain $Y = AX + B$, a linear equation, the reciprocal of ΔF versus the reciprocal of the concentration of [M] was plotted and the K_d was calculated from the ratio A/B and the reciprocal of K_d was determined to be the association constant (K_a) in those case.

2.10 Finding the detection limit

The detection limits for the probes (L_{7-10}) with guest ion were calculated on the basis of the fluorescence titration experiments. The fluorescence emission spectrum of the host molecules was measured 10 times, and the standard deviation of blank measurement was also attained from that experiment. To gain the slope, the fluorescence emission intensity plot at a particular wavelength was plotted as a concentration of the analyte. The detection limit was calculated using the following equation

$$\text{Detection limit} = 3\sigma/k \quad (2)$$

Where σ is the standard deviation of blank measurement, and k is the slope achieved from the calibration plot of fluorescence emission.

In the case of ensemble-based detection of an analyte, the LOD was calculated considering σ as the standard deviation of the ensembles ($\mathbf{L}_9/\mathbf{L}_{10}-\text{Al}^{3+}$) and k as the slope between the ratio of emission intensity vs. respective guest molecules.

2.11 Quantum yield calculation

The given formula was used for the determination of quantum yield -

$$\Phi_X = \Phi_R (I_X/I_R) (\eta_X^2 / \eta_R^2) (A_R/A_X) \dots\dots\dots (1)$$

Where the terms Φ , F , A , and η represent the quantum yield, the integrated area covered by the corrected emission spectra, the absorbance intensity at the excitation wavelength, and the refractive index of solvent, respectively ^{2,15}

In addition, R refers to Quinine sulphate (QS) as the standard ($\mathbf{L}_7-\mathbf{L}_8$), and X refers to the target sample. Whereas for \mathbf{L}_9 , Rhodamine 6G dye was comprised as a benchmark with a quantum yield value of 95 % for computing the quantum yield (Φ).

2.12 Time response study and rate constant determination

To do so, the probe \mathbf{L}_7 (50 μM) was exposed towards bisulphite (20, 30, and 40 μM) for 25 min and the emission intensity at 376 nm was recorded. Considering, pseudo-first-order kinetics, the reaction rate constants of \mathbf{L}_7 with bisulphite anion were determined from the time-dependent fluorescence spectra. The rate constants were experimentally evaluated from the following equation: $\ln (F_{\text{max}} - F_t)/F_{\text{max}} = -k't$ where F_t and F_{max} were the corresponding fluorescence intensities at time t and the end of the reactions, respectively, and k' is the rate constant.

2.13 Details of computational analysis

In the case of \mathbf{L}_7 and \mathbf{L}_8 , all the calculations were studied using Gaussian 09 software package.^{2,16} Whereas, "Gauss View" was used for visualization of molecular orbitals. The electronic ground state geometry optimization in the gas phase has been performed using Density Functional Theory (DFT). Becke's three-parameter hybrid exchange functional and Lee-Yang-Parr correlation functional (B3LYP) were utilized in the calculation of Frontier Molecular Orbitals with a 6-31g (d) basis set. An isosurface value of 0.02 has been used for all the compounds to visualize the orbitals involved in HOMO and LUMO.

2.14 Interaction and tracking calf thymus DNA (ct-DNA)

Interaction of DNA with Al^{3+} plays a crucial role as the potential toxicity of aluminium is related to its DNA binding property^{2,17}. For this experiment formation of the $\mathbf{L}_9-\text{Al}^{3+}$ ensemble was initially done by mixing 1.0 equivalent of the ligand with 12 equivalents of Al^{3+} solution.

Subsequently, by varying the concentrations of calf thymus DNA (0 μM -430 μM) which were added in an appropriate amount using a micropipette to the **L9**-Al³⁺ ensemble, the emission spectra were recorded. The emission spectra of the samples were recorded in a scanning mode from 470 nm to 700 nm by fixing the excitation wavelength at 450 nm.

Annexure 2

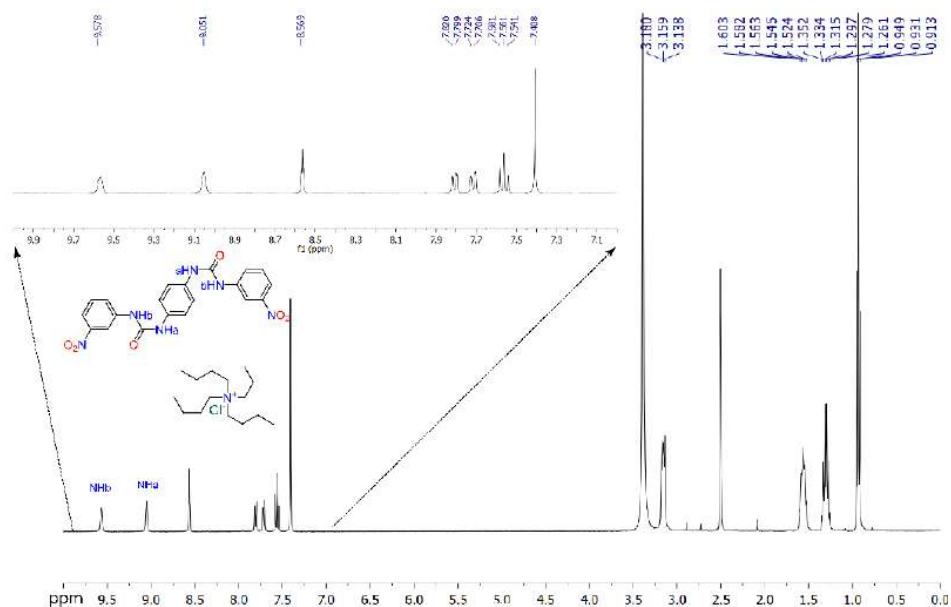


Figure A 2.1 $^1\text{H-NMR}$ spectrum (full as well as expanded) of Chloride complex of L_1 in DMSO-d_6 at 25°C .

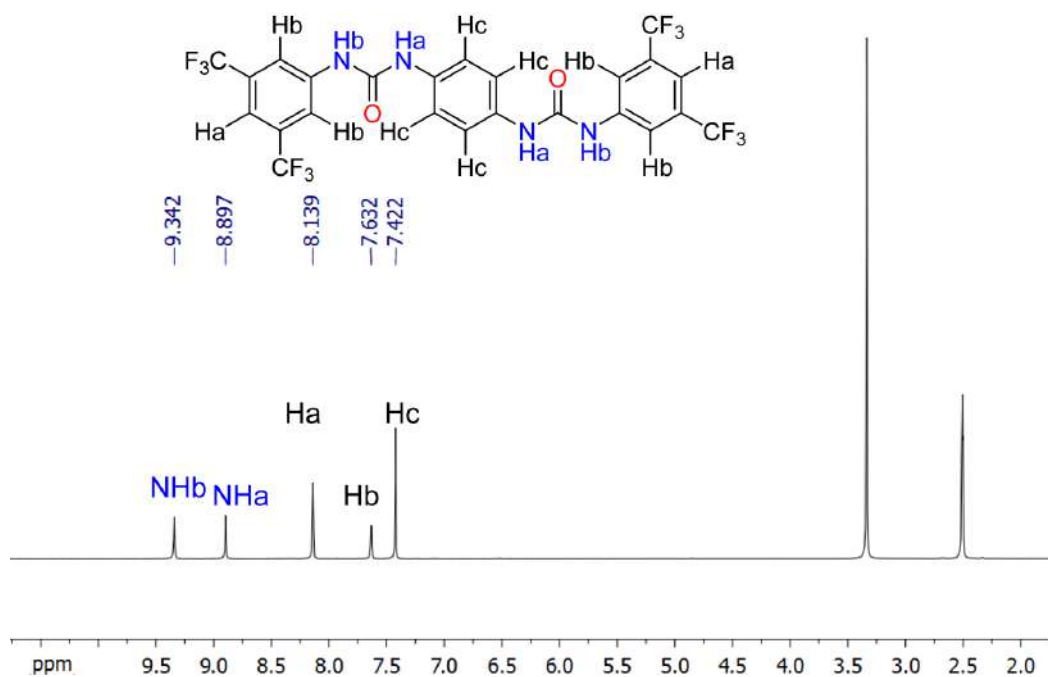


Figure A 2.2 $^1\text{H-NMR}$ spectrum (full as well as expanded) and explanation of all hydrogen atoms of free dipodal receptor L_2 in DMSO-d_6 at 25°C .

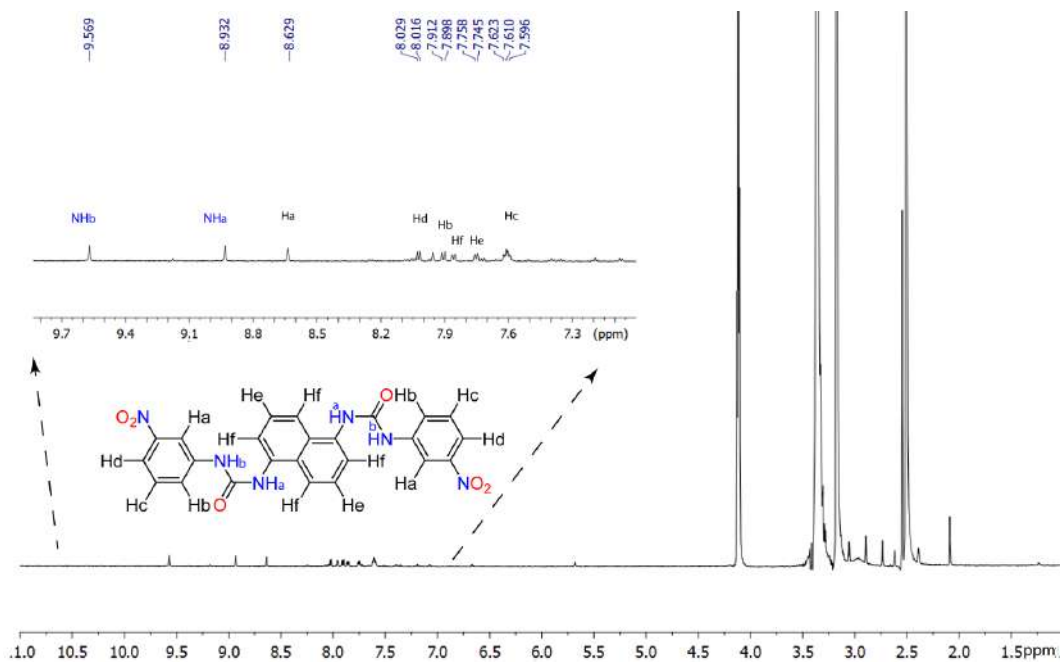


Figure A 2.3 $^1\text{H-NMR}$ spectrum (full as well as expanded) and explanation of all hydrogen atoms of free dipodal bis-urea receptor L_3 in DMSO-d_6 at 25°C .

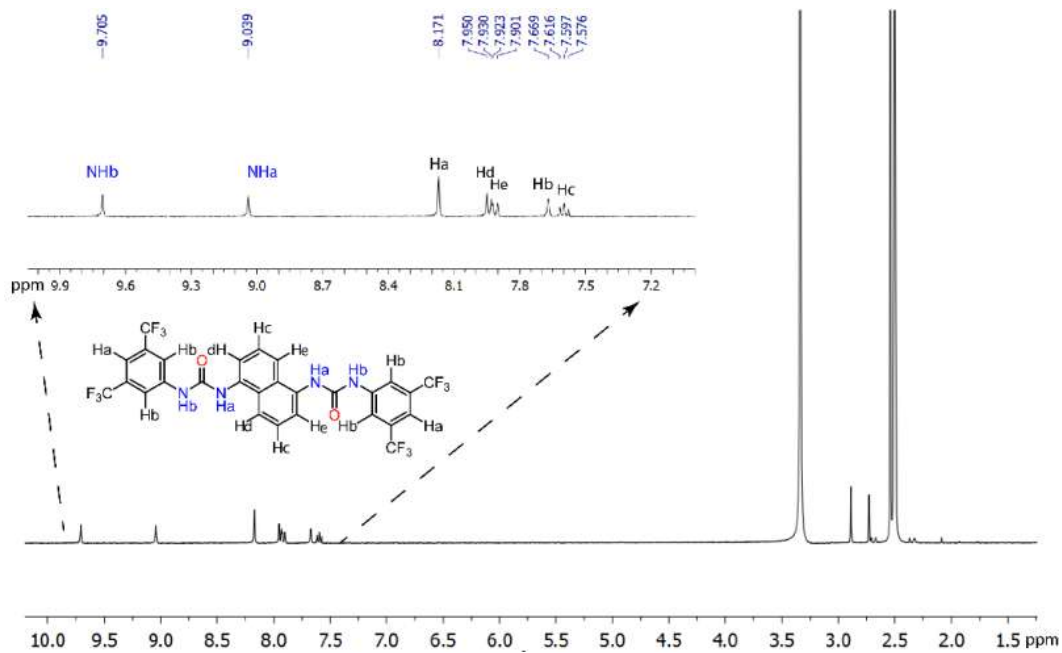


Figure A 2.4 $^1\text{H-NMR}$ spectrum (full as well as expanded) and explanation of all hydrogen atoms of free dipodal bis-urea receptor L_3 in DMSO-d_6 at 25°C .

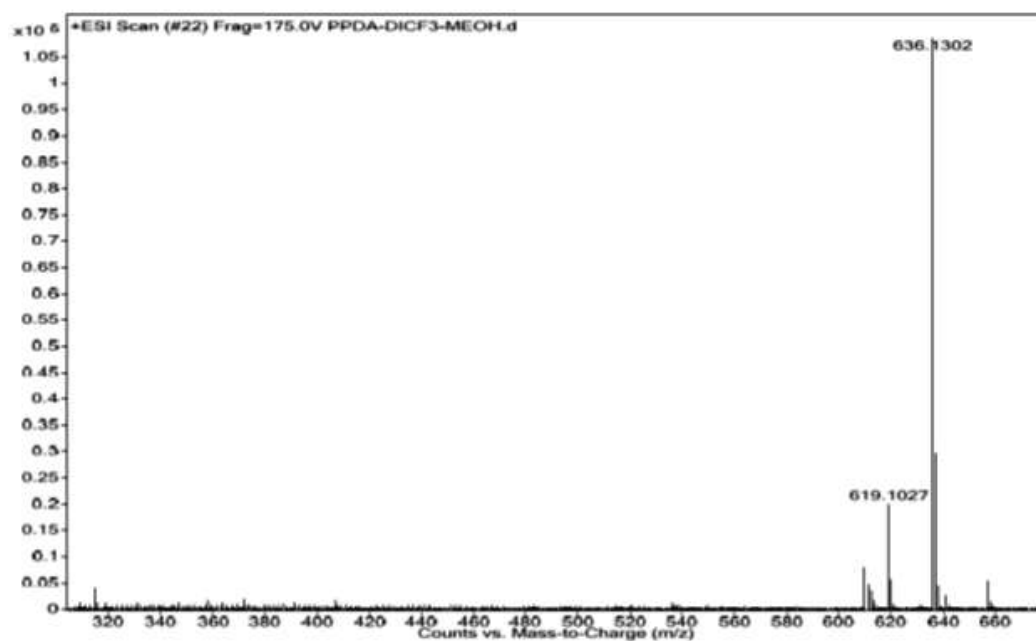


Figure A 2.4 ESI-Mass spectrum of dipodal receptor L_2 in positive mode.

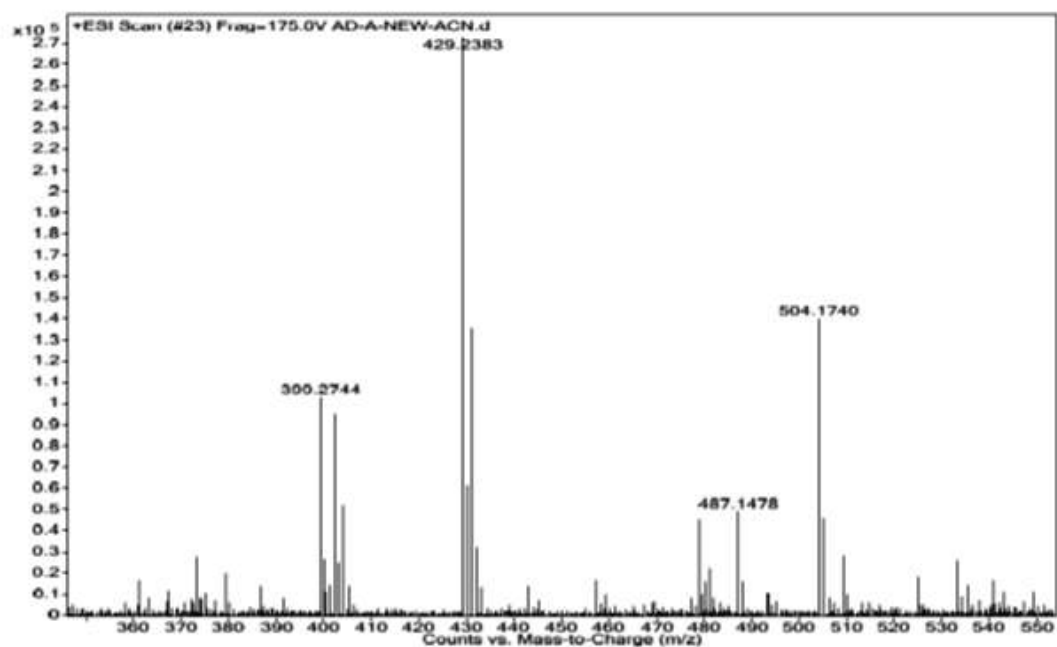


Figure A 2.5 ESI-Mass spectrum of dipodal receptor L_2 in positive mode.

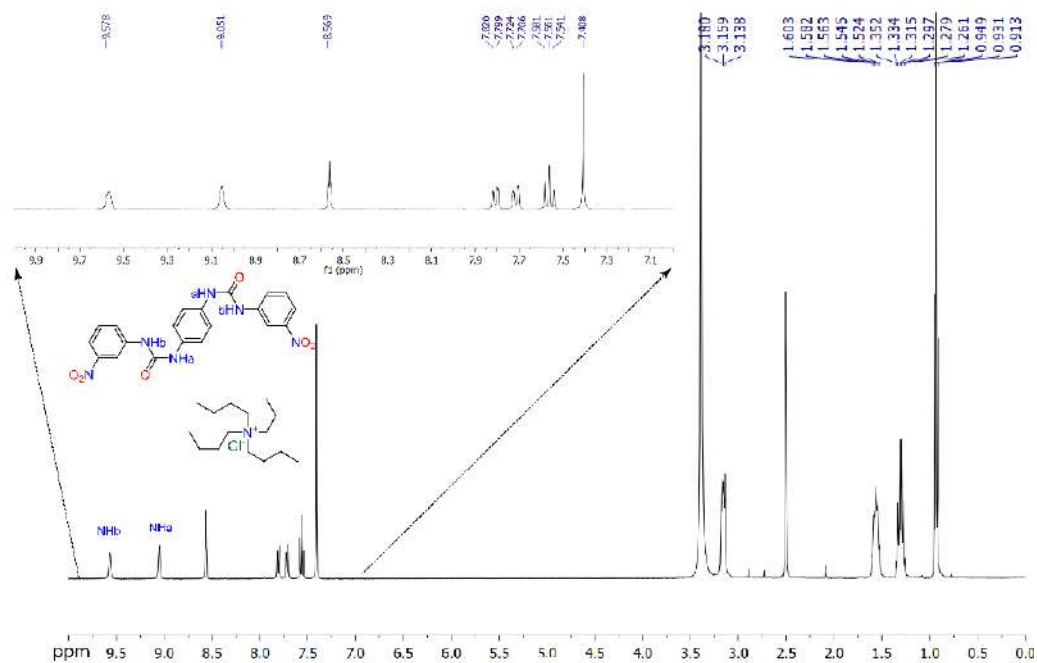


Figure A 2.6 $^1\text{H-NMR}$ spectrum (full as well as expanded) of Chloride complex of **L1** in DMSO-d_6 at 25°C .

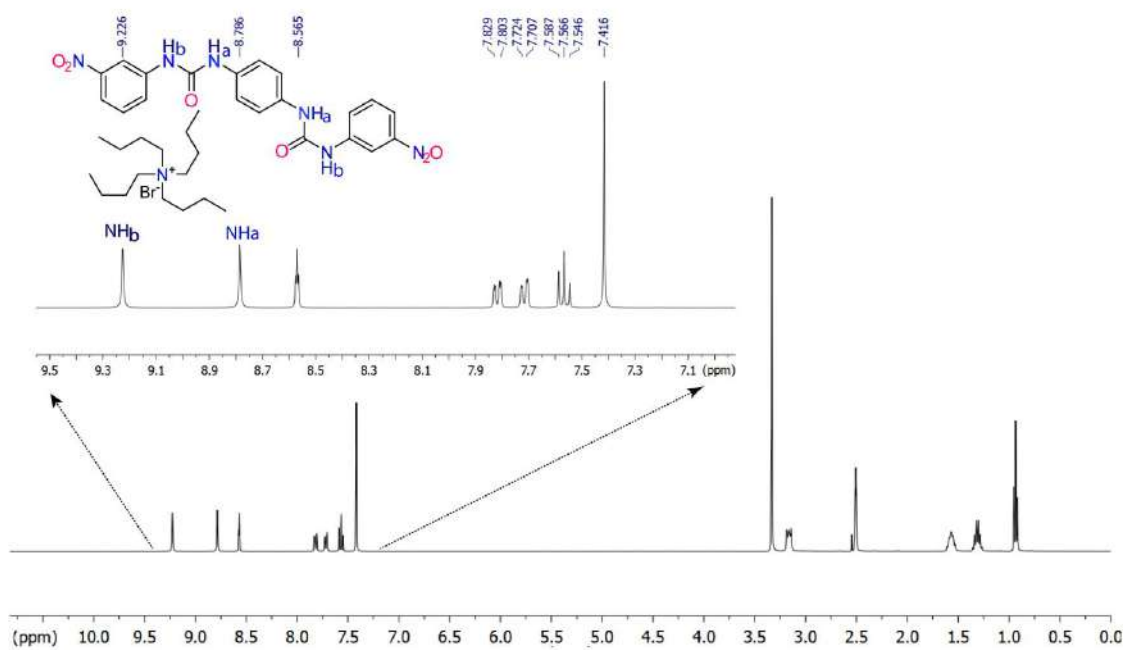


Figure A 2.7 $^1\text{H-NMR}$ spectrum (full as well as expanded) of Bromide complex of **L1** in DMSO-d_6 at 25°C .

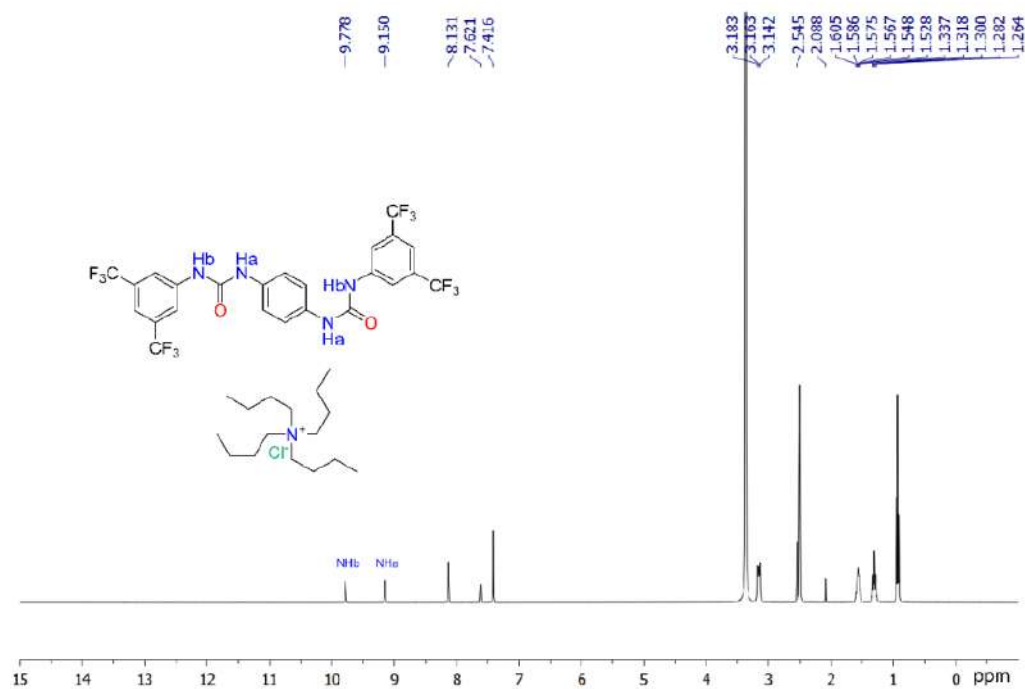


Figure A 2.8 ¹H-NMR spectrum (full as well as expanded) of Chloride complex of **L2** in DMSO-d₆ at 25°C.

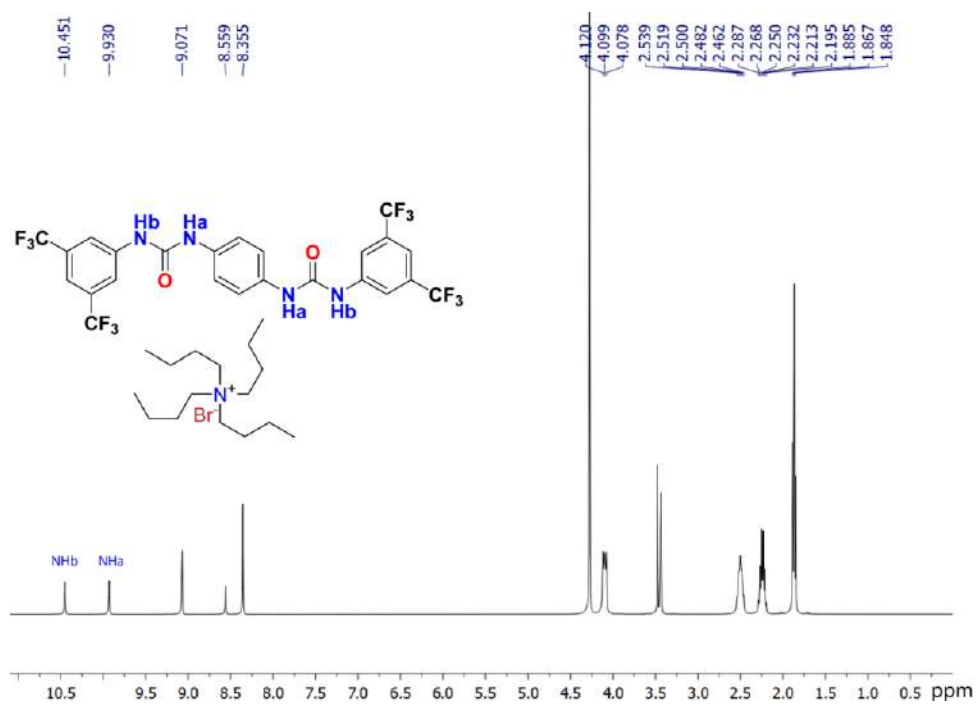


Figure A 2.9 ¹H-NMR spectrum (full as well as expanded) of Bromide complex of **L2** in DMSO-d₆ at 25°C.

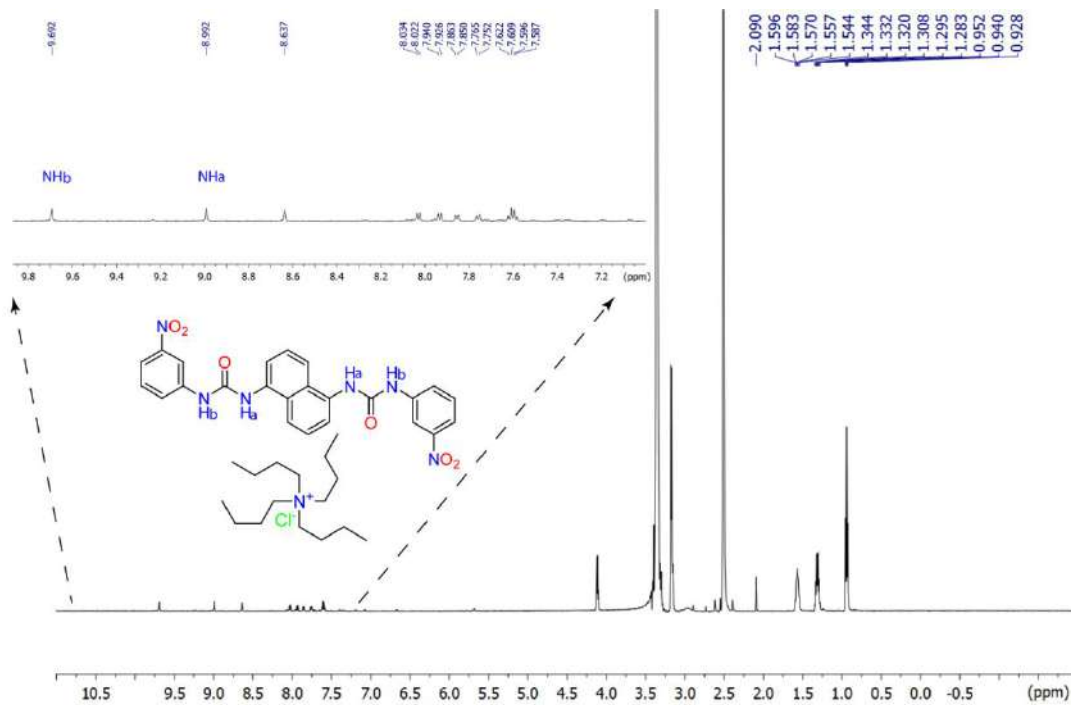


Figure A 2.10 $^1\text{H-NMR}$ spectrum (full as well as expanded) of Chloride complex of L_3 in DMSO-d_6 at 25°C .

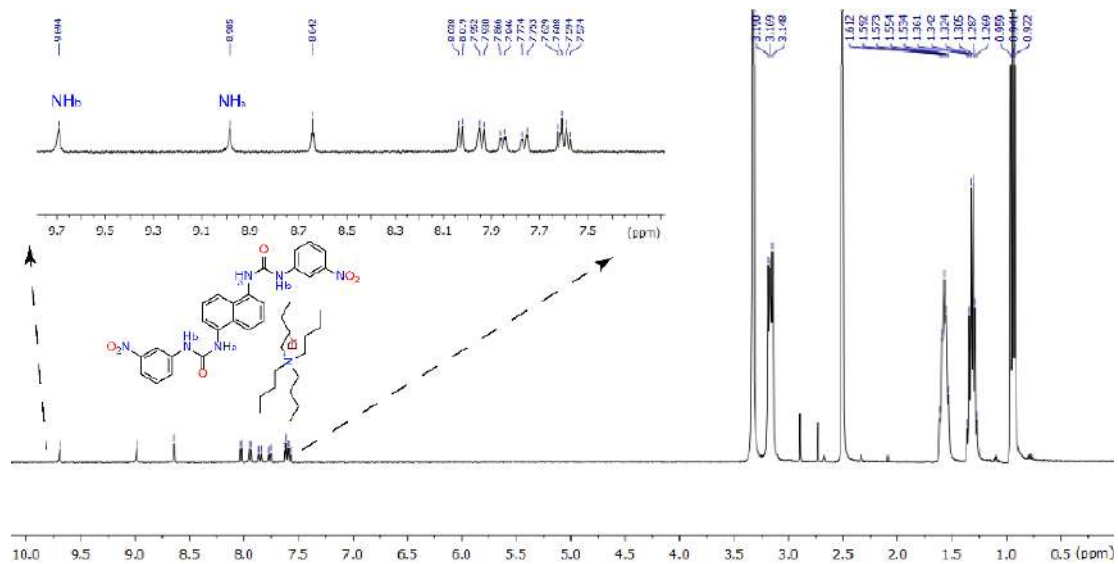


Figure A 2.11 $^1\text{H-NMR}$ spectrum (full as well as expanded) of Bromide complex of L_3 in DMSO-d_6 at 25°C .

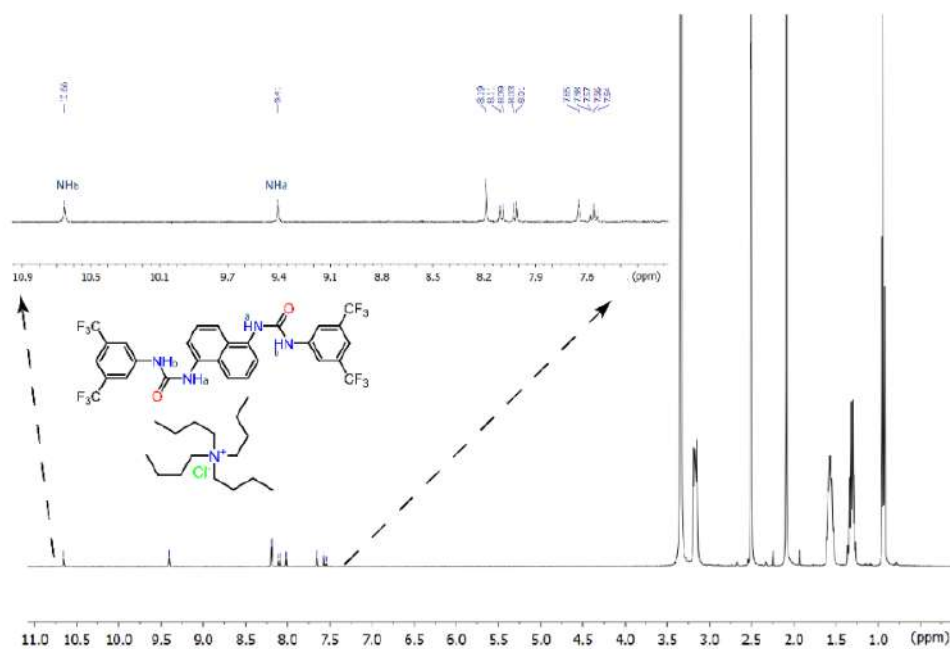


Figure A 2.12 $^1\text{H-NMR}$ spectrum (full as well as expanded) of Chloride complex of L_4 in DMSO-d_6 at 25°C .

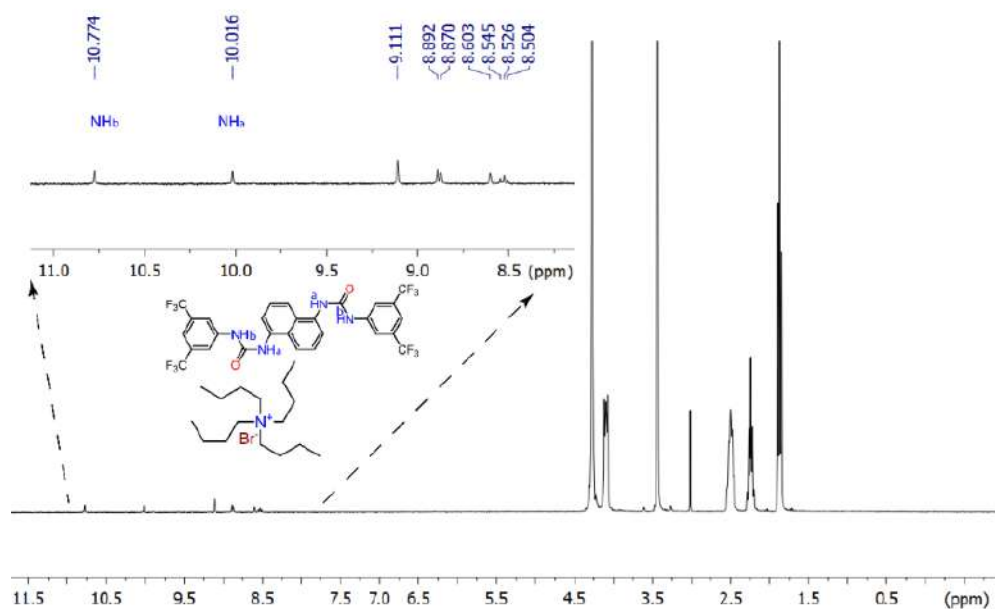


Figure A 2.13 $^1\text{H-NMR}$ spectrum (full as well as expanded) of Bromide complex of L_4 in DMSO-d_6 at 25°C .

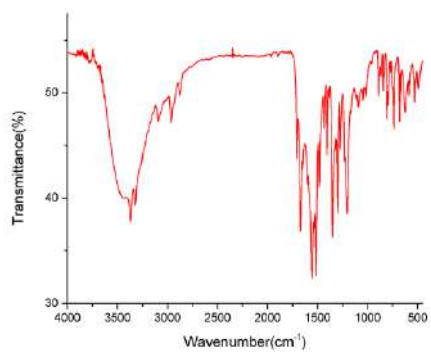


Figure A 2.13 FT-IR spectrum of Chloride complex of receptor **L₁** recorded in KBr pellet.

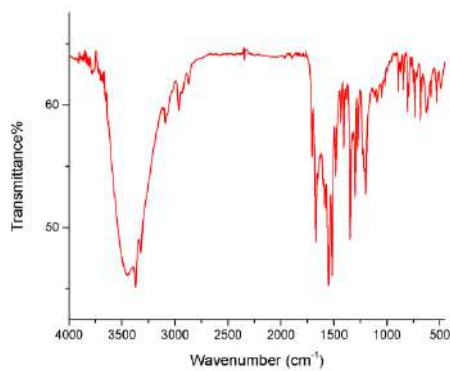


Figure A 2.14 FT-IR spectrum of Bromide complex of receptor **L₁** recorded in KBr pellet.

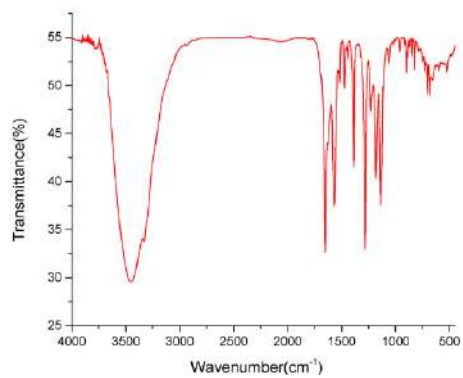


Figure A 2.15 FT-IR spectrum of **L₂** recorded in KBr pellet.

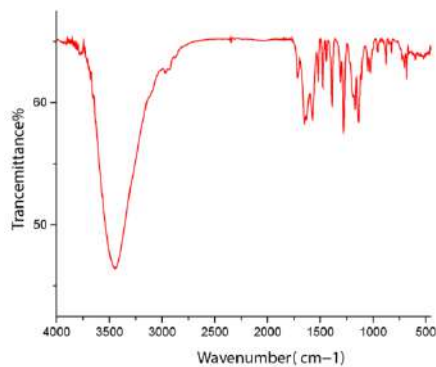


Figure A 2.16 FT-IR spectrum of Chloride complex of receptor **L₂** recorded in KBr pellet.

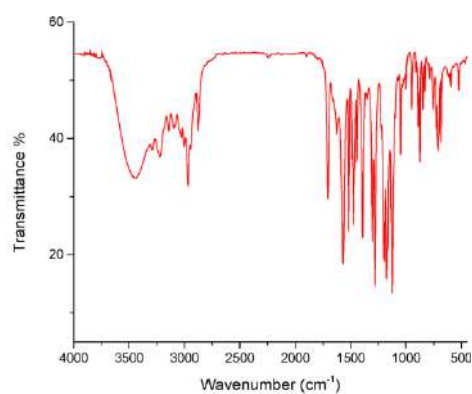


Figure A 2.17 FT-IR spectrum of Bromide complex of receptor **L₂** recorded in KBr pellet.

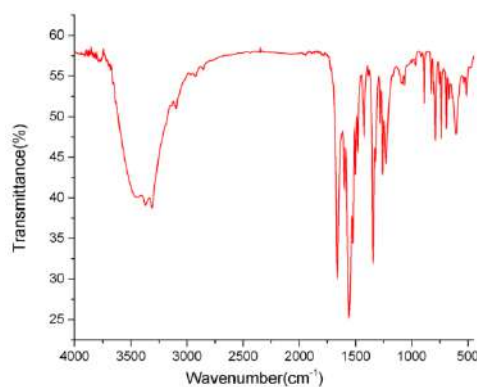


Figure A 2.18 FT-IR spectrum of receptor **L₃** recorded in KBr pellet.

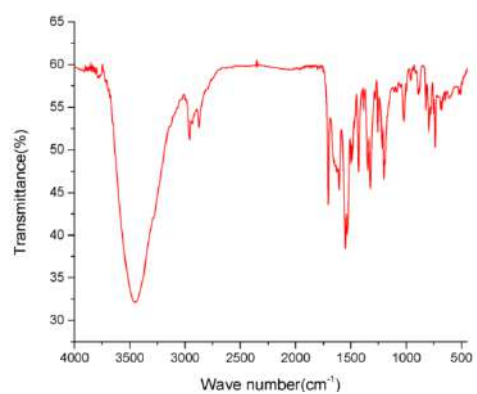


Figure A 2.19 FT-IR spectrum of Chloride complex of receptor **L₃** recorded in KBr pellet.

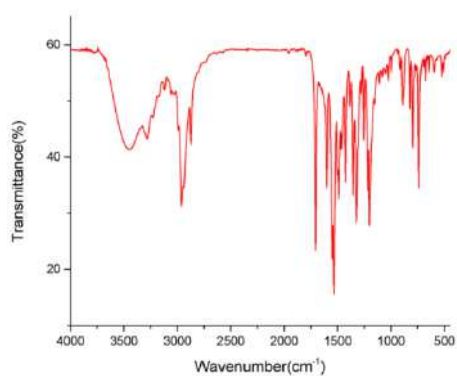


Figure A 2.20 FT-IR spectrum of Bromide complex of receptor **L₃** recorded in KBr pellet.

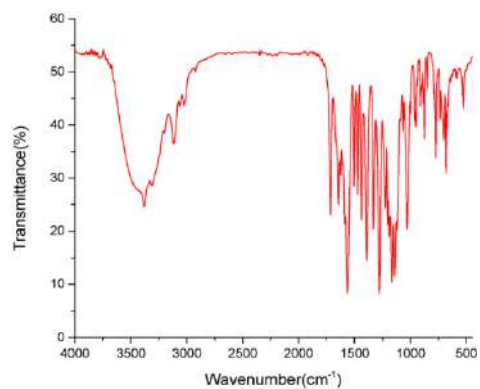


Figure A 2.21 FT-IR spectrum of **L₄** recorded in KBr pellet.

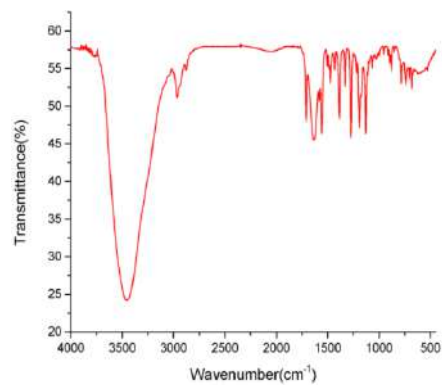


Figure A 2.21 FT-IR spectrum of Chloride complex of receptor **L₄** recorded in KBr pellet.

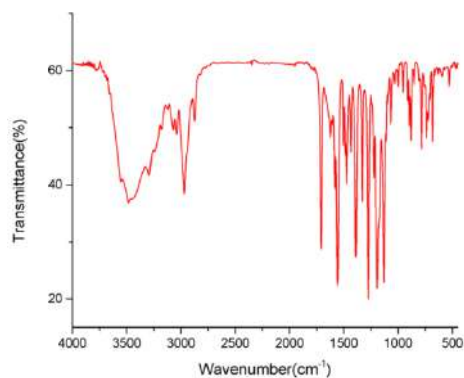


Figure A 2.22 FT-IR spectrum of Bromide complex of receptor **L₄** recorded in KBr pellet.

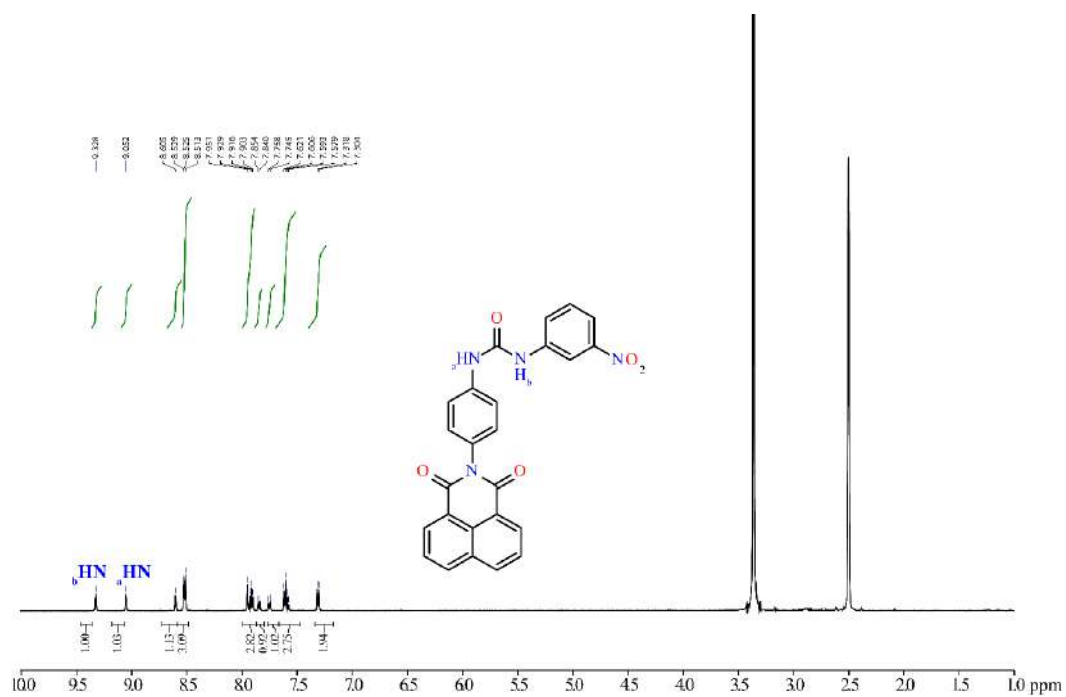


Figure A 2.23 ^1H NMR spectrum of free receptor **L5** in $\text{DMSO-}d_6$ at 25°C .

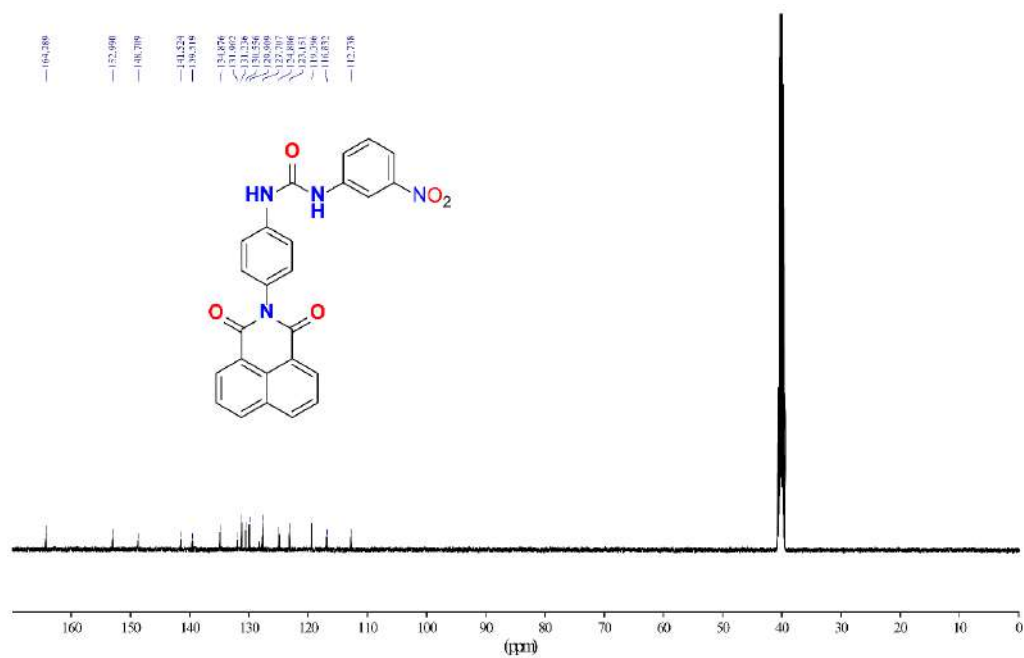


Figure A 2.24 ^{13}C -NMR spectrum of receptor **L5** in $\text{DMSO-}d_6$ at 25°C : (100 MHz, $\text{DMSO-}d_6$).

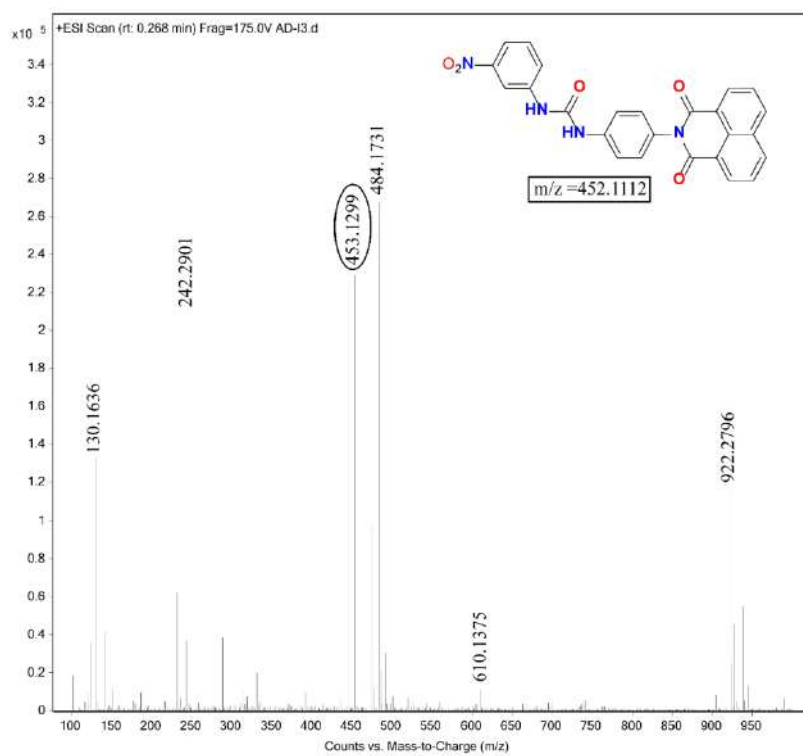


Figure A 2.25 ESI-Mass spectrum of receptor **L**₅ (positive mode).

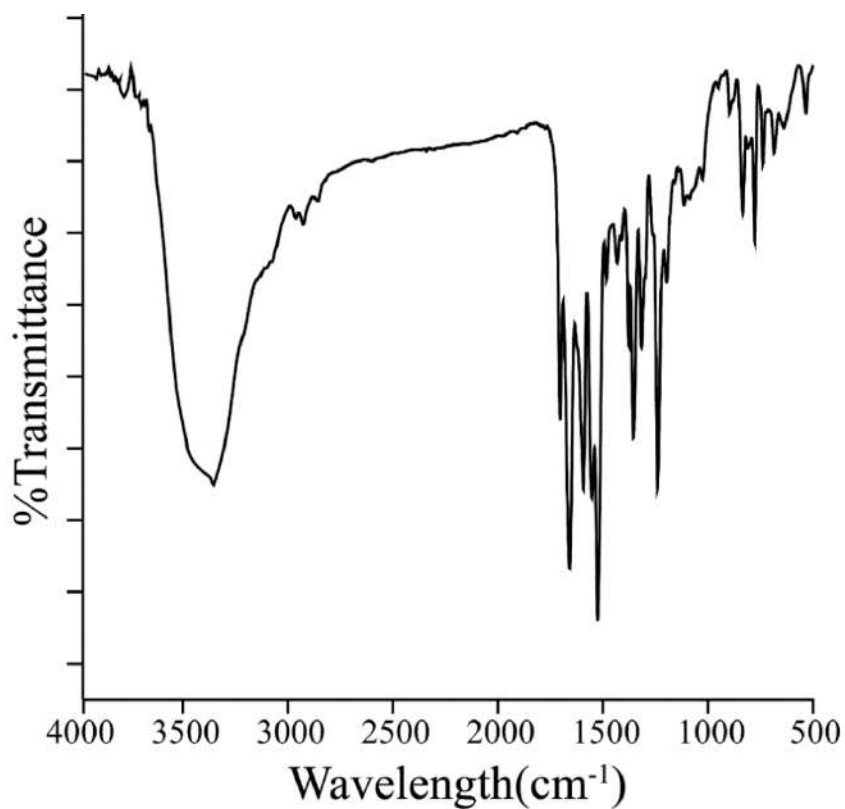


Figure A 2.26 FT-IR spectrum of free receptor **L**₅ recorded in KBr pellet at 25°C.

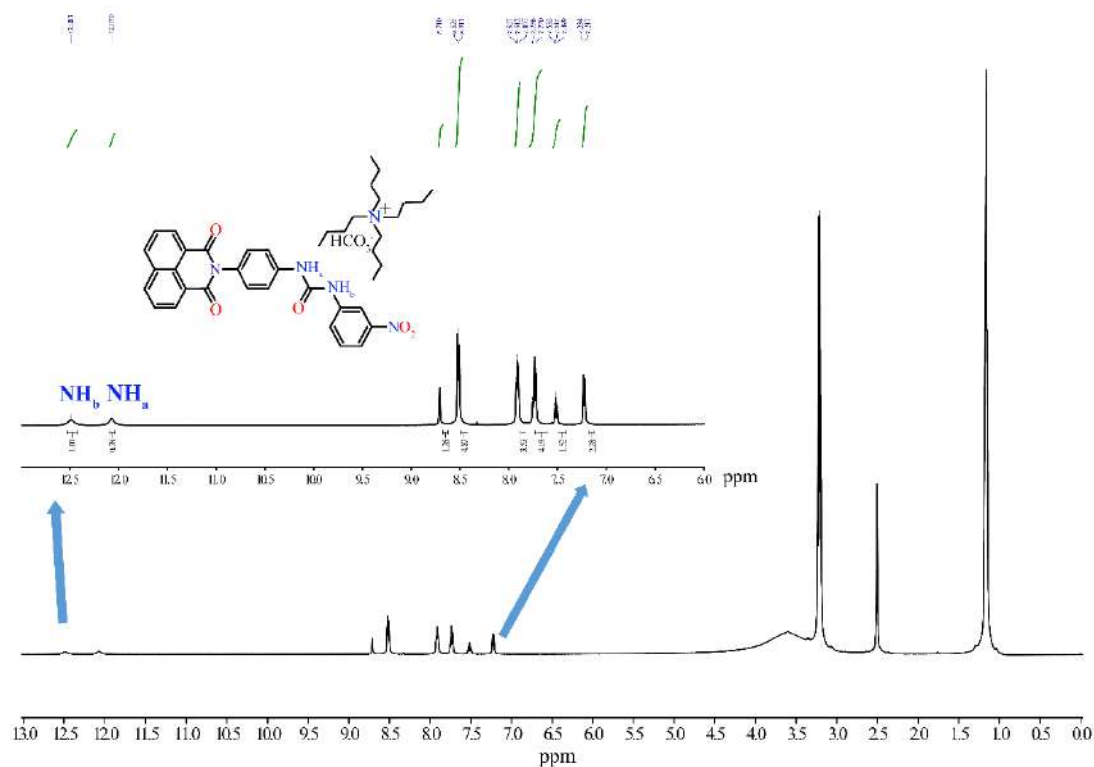


Figure A 2.27 ^1H NMR spectrum of complex **5a** in $\text{DMSO-}d_6$ at 25°C .

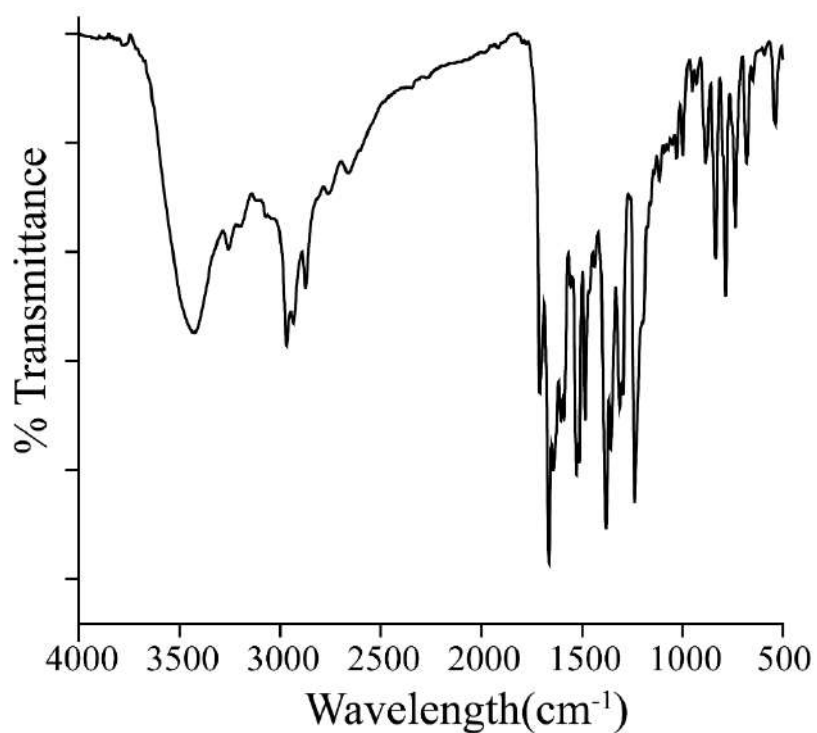


Figure A 2.28 FT-IR spectrum of **5a** recorded in KBr pellet at 25°C .

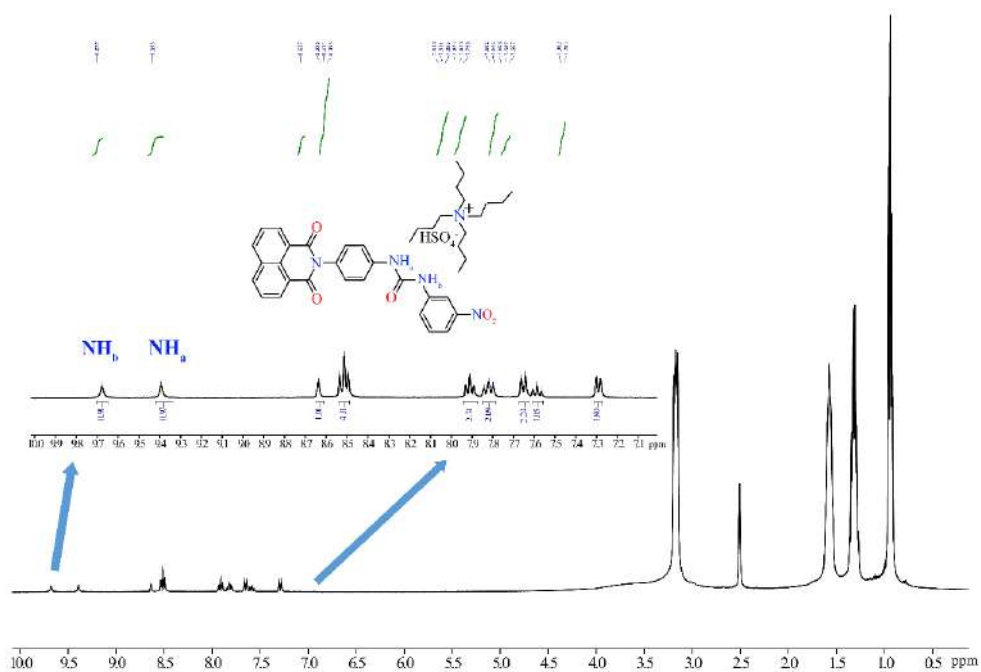


Figure A 2.29 ^1H NMR spectrum of complex **5b** in $\text{DMSO-}d_6$ at 25°C .

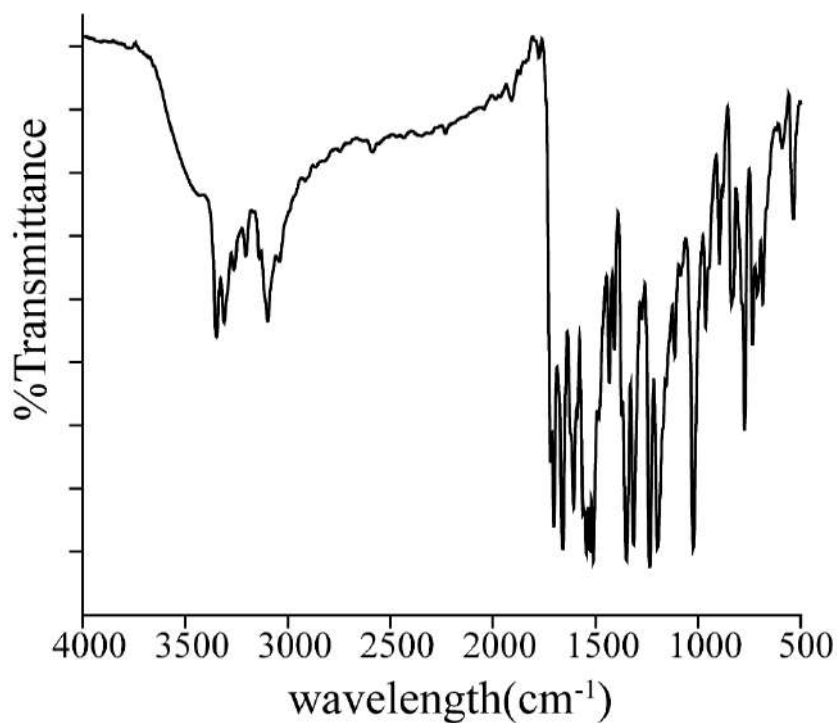


Figure A 2.30 FT-IR spectrum of **1b** recorded in KBr pellet at 25°C .

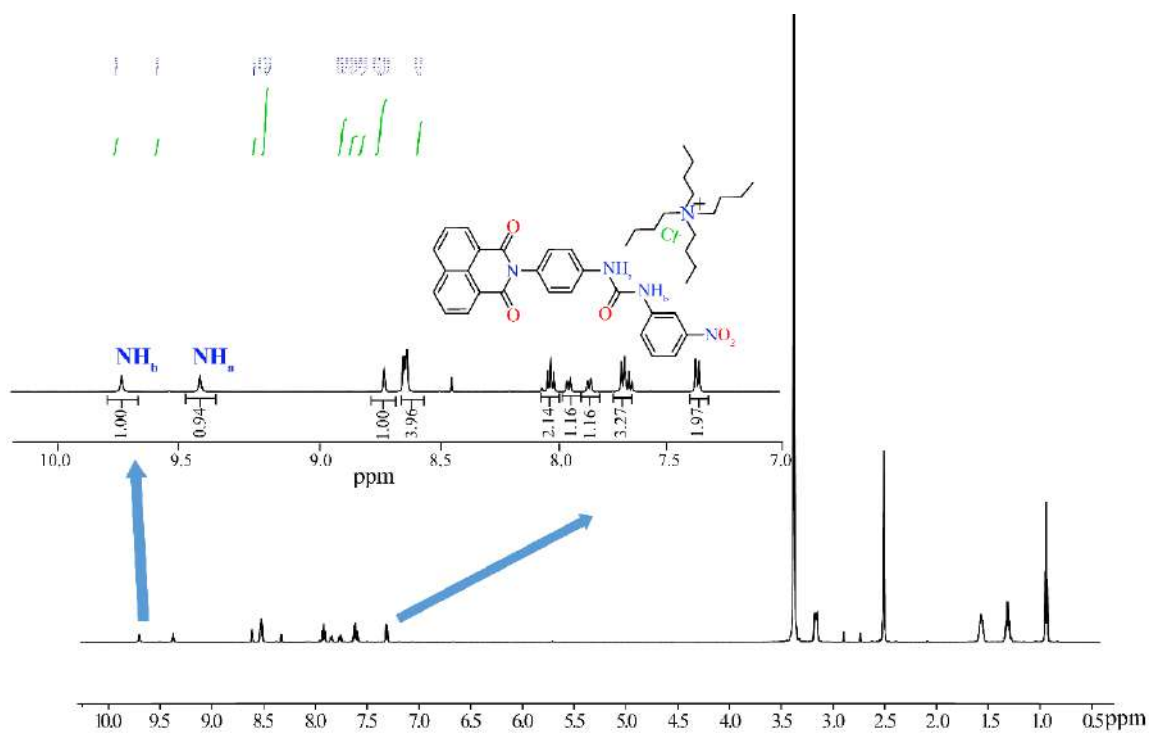


Figure A 2.31 ^1H NMR spectrum of complex **5c** in $\text{DMSO-}d_6$ at 25°C .

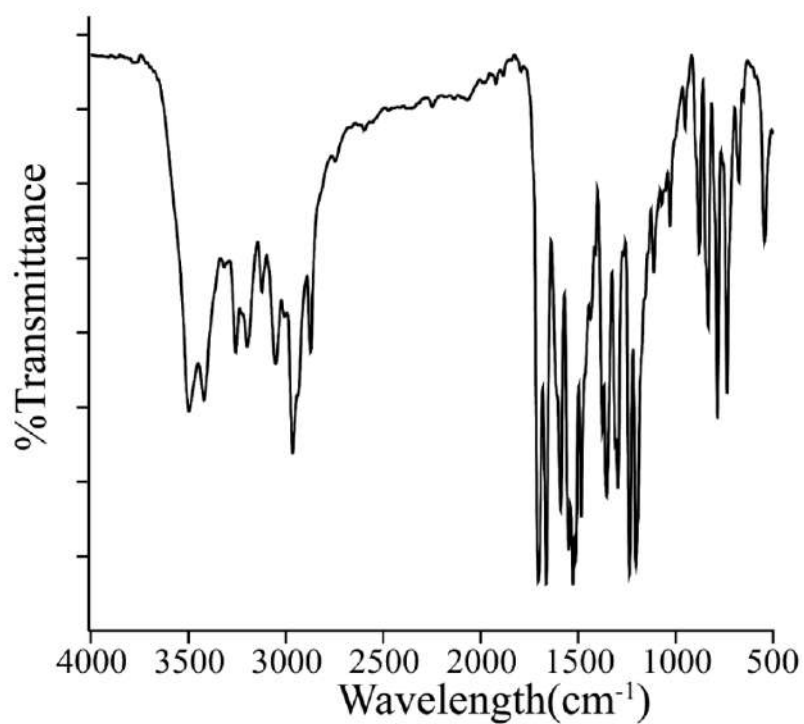


Figure A 2.32 FT-IR spectrum of **5c** recorded in KBr pellet at 25°C .

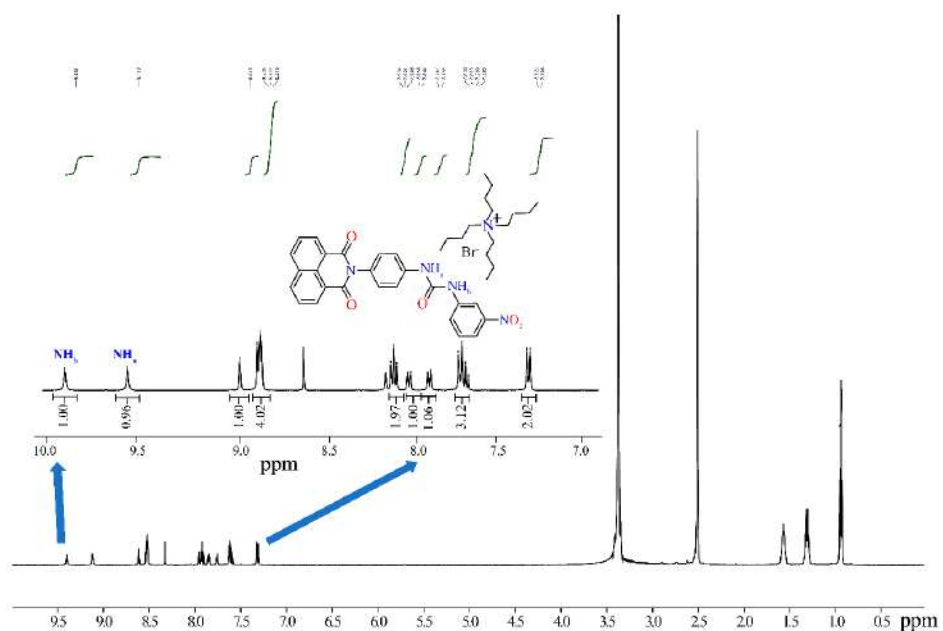


Figure A 2.33 ^1H NMR spectrum of complex **5d** in $\text{DMSO-}d_6$ at 25°C .

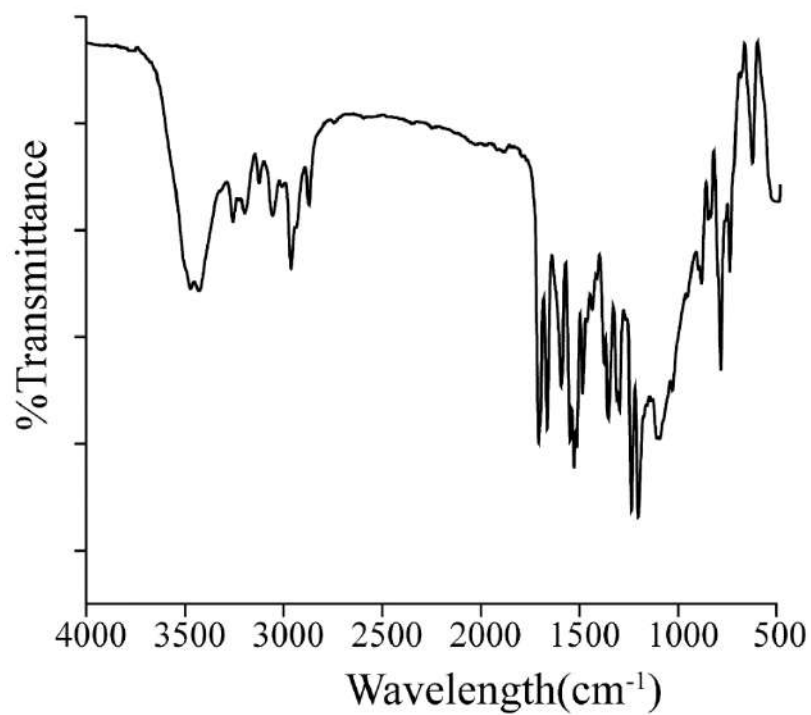


Figure A 2.34 FT-IR spectrum of **5d** recorded in KBr pellet at 25°C .

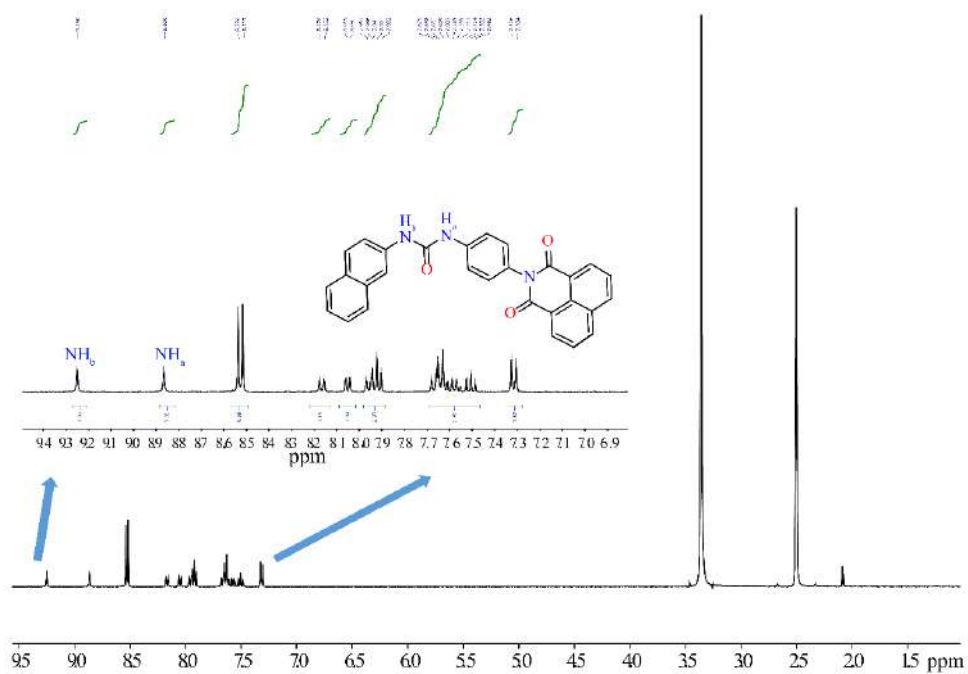


Figure A 2.35 ^1H NMR spectrum of receptor **L6** in $\text{DMSO-}d_6$ at 25°C .

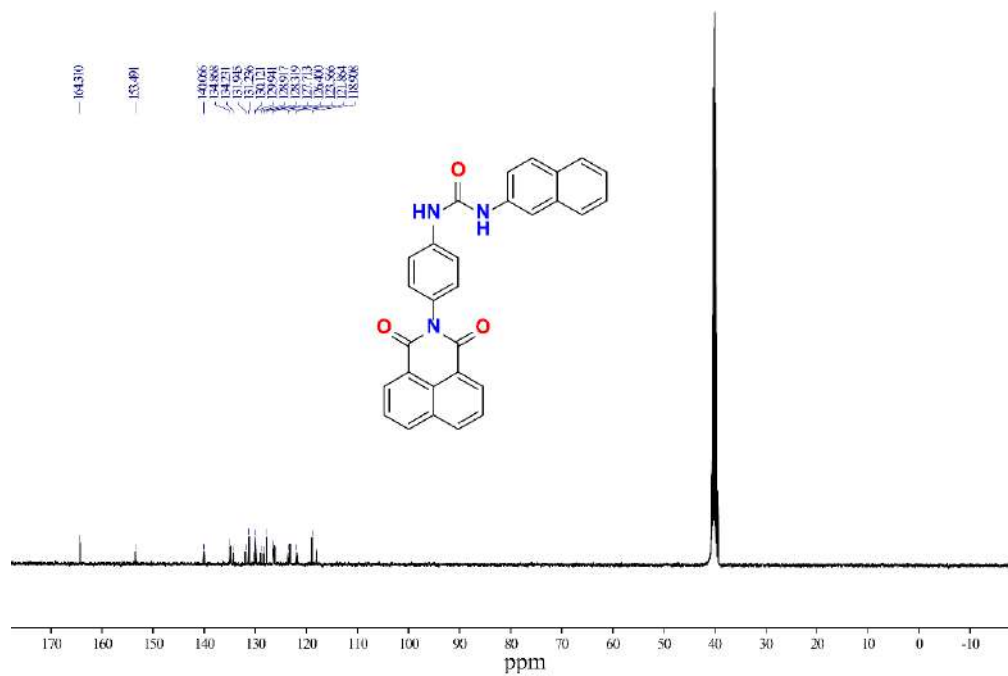


Figure A 2.36 ^{13}C NMR spectrum of receptor **L6** in $\text{DMSO-}d_6$ (Varian-100 MHz) at 25°C .

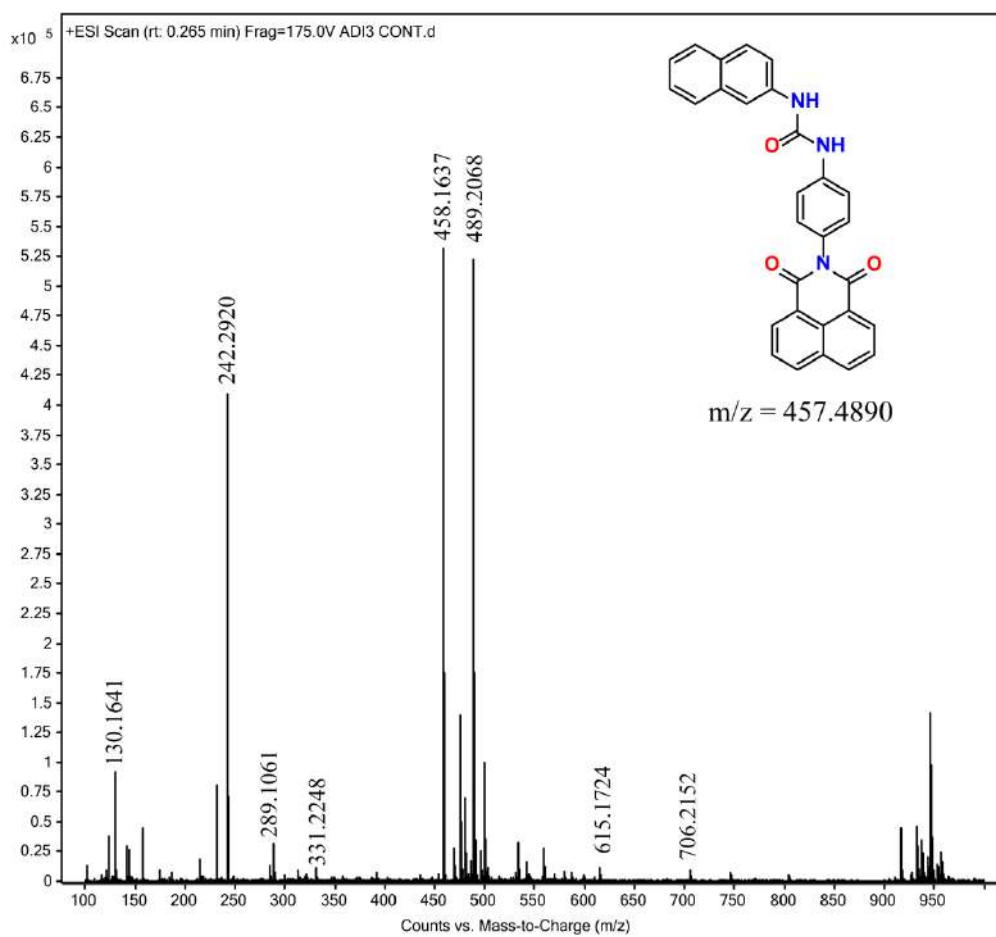


Figure A 2.37 ESI-Mass spectrum of receptor L₆ (positive mode).

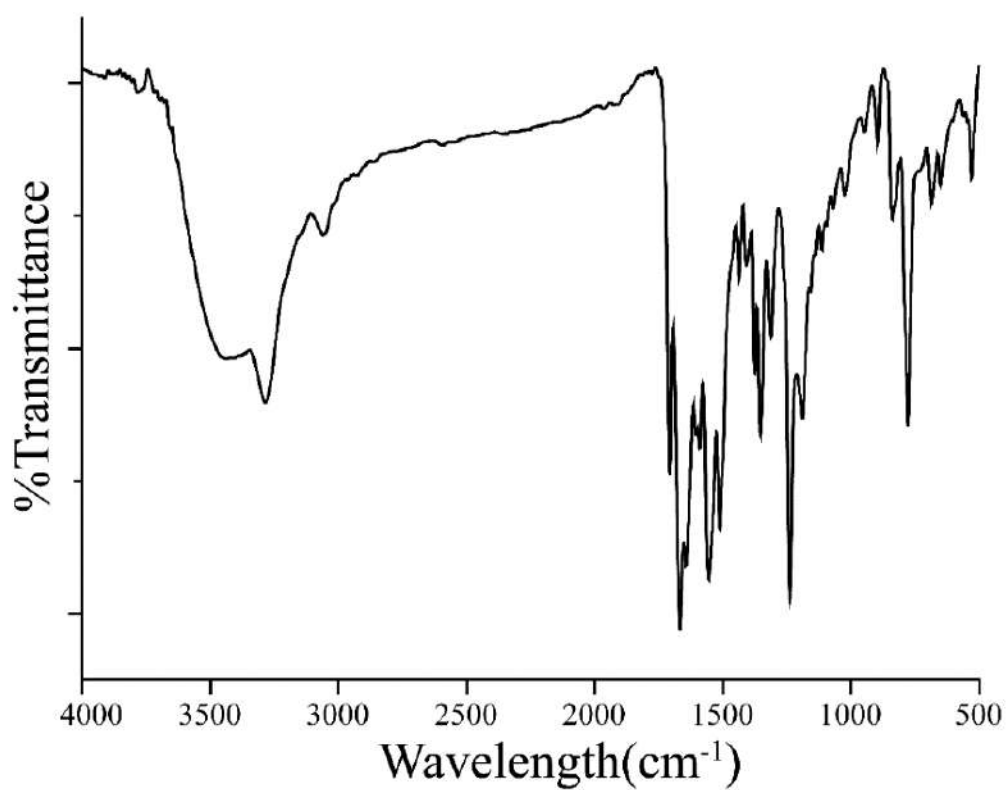


Figure A 2.38 FT-IR spectrum of receptor L₆ recorded in KBr pellet at 25°C.

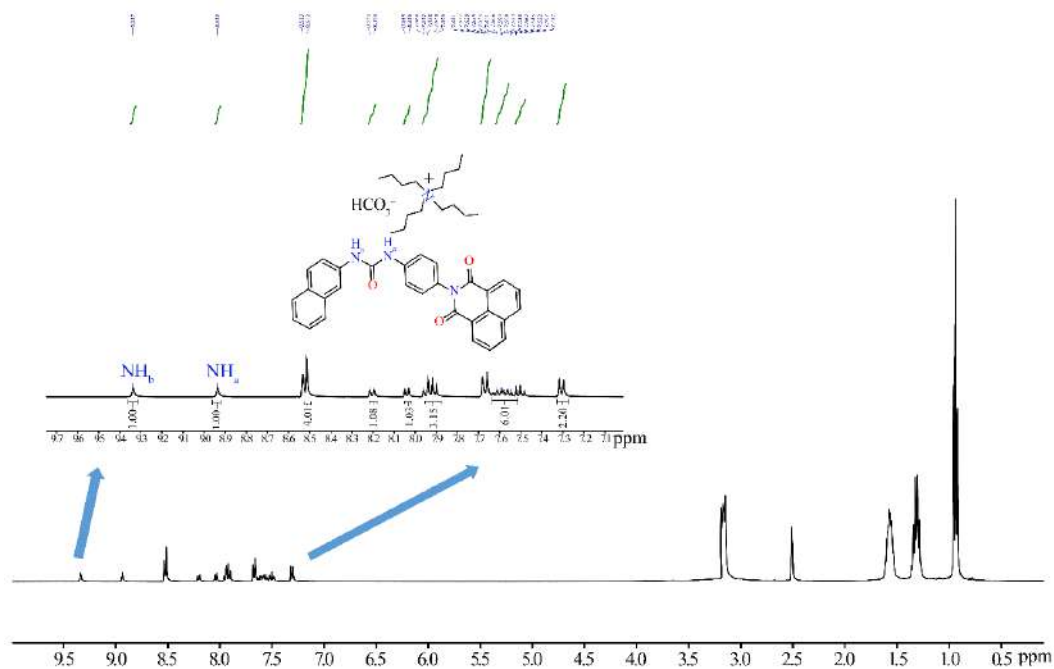


Figure A 2.39 ^1H NMR spectrum of complex **6a** in $\text{DMSO-}d_6$ at 25°C .

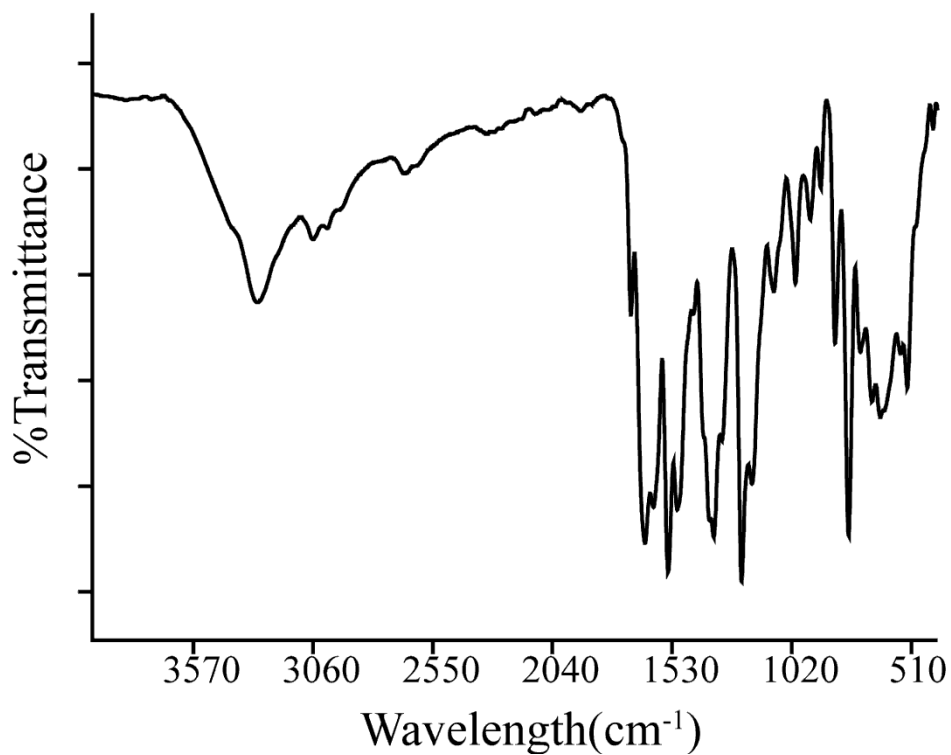


Figure A 2.40 FT-IR spectrum of **6a** recorded in KBr pellet at 25°C .

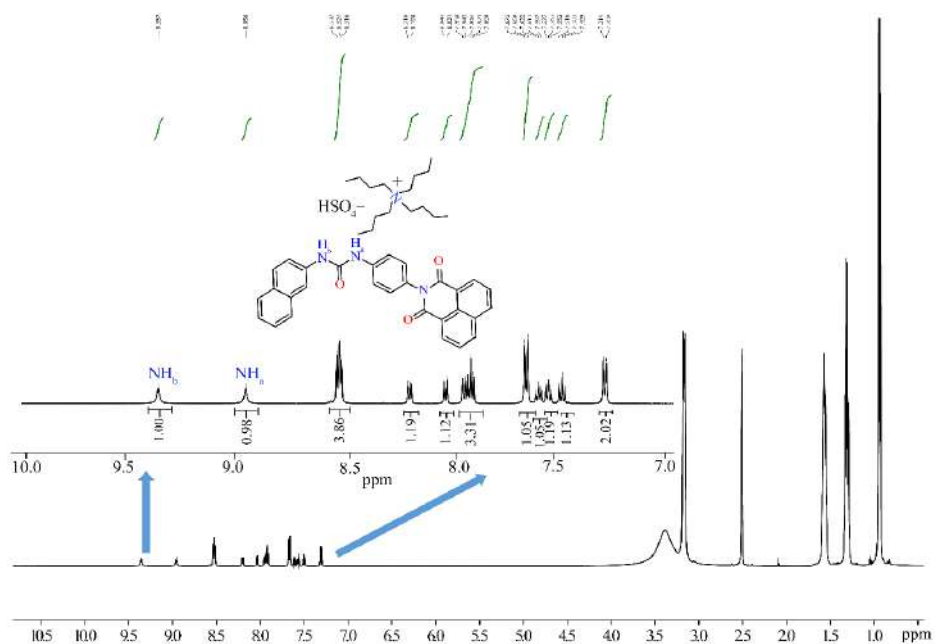


Figure A 2.41 ^1H NMR spectrum of complex **6b** in $\text{DMSO-}d_6$ at 25°C .

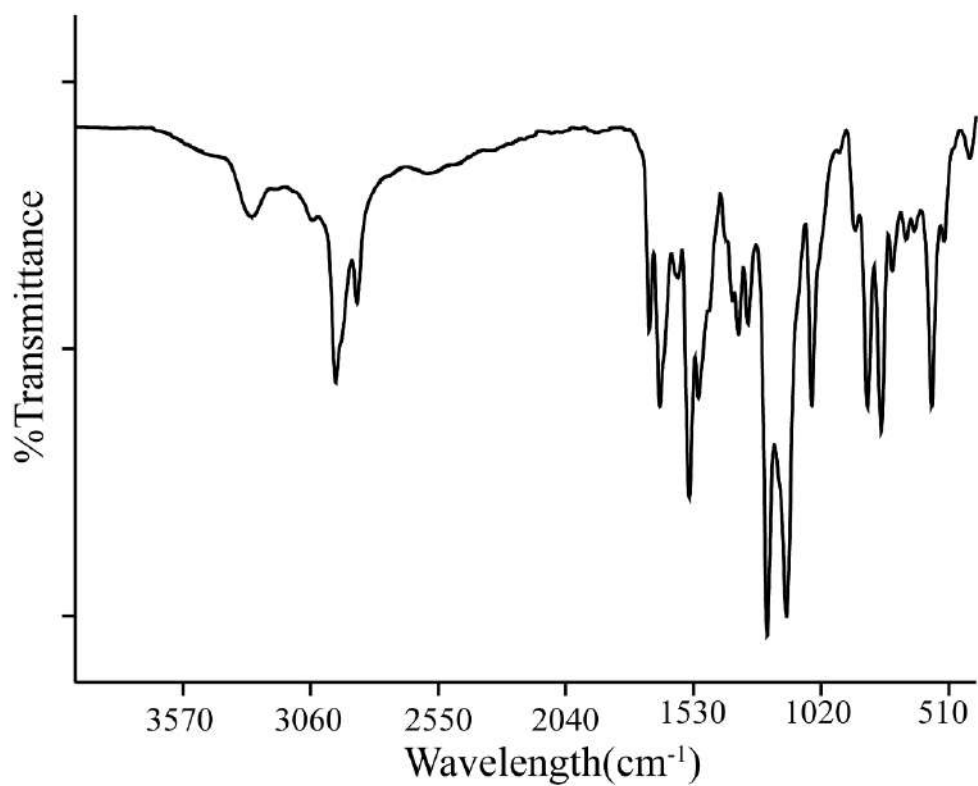


Figure A 2.42 FT-IR spectrum of **6b** recorded in KBr pellet at 25°C .

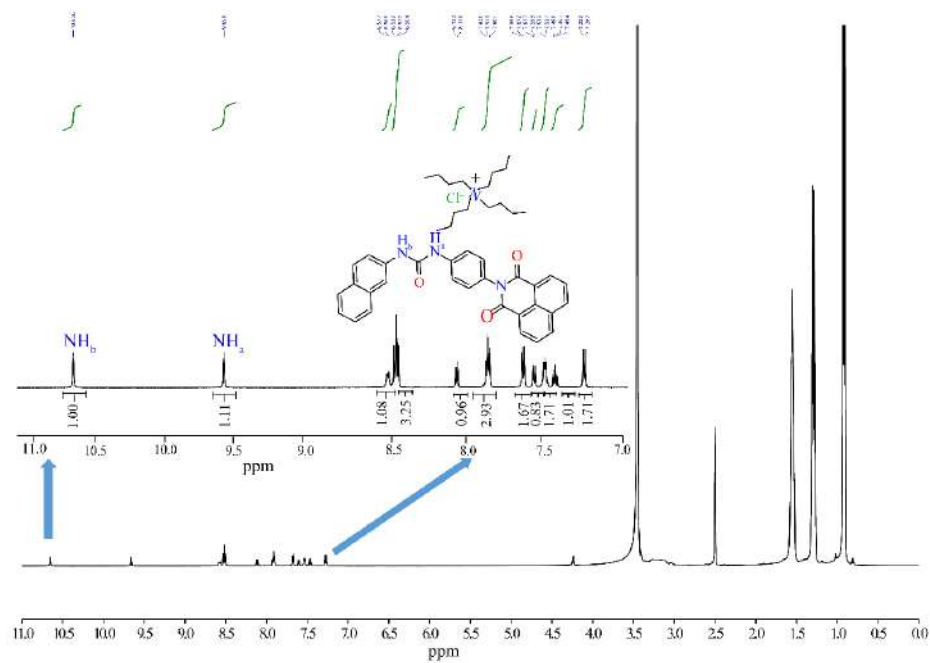


Figure A 2.43 FT-IR spectrum of **6c** recorded in KBr pellet at 25°C in DMSO-*d*₆.

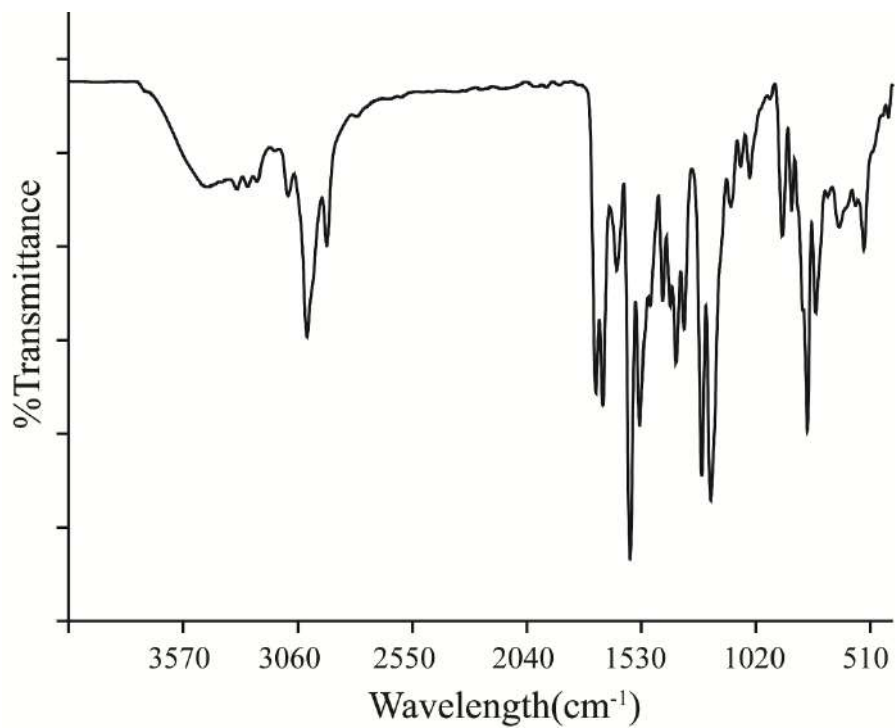


Figure A 2.44 FT-IR spectrum of **6c** recorded in KBr pellet at 25°C.

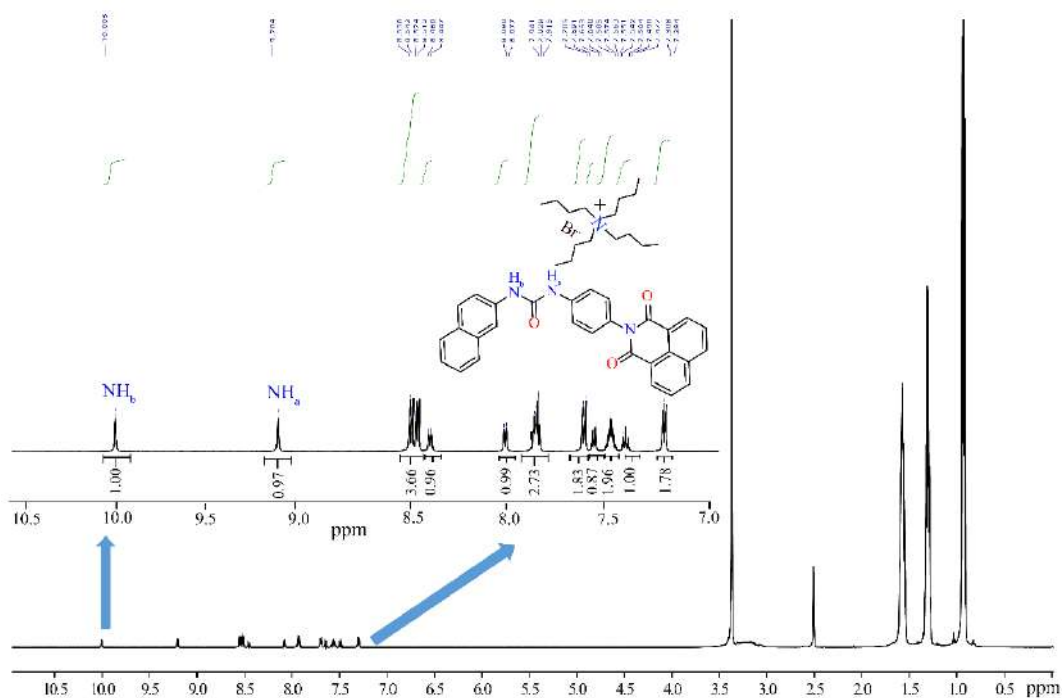


Figure A 2.45 FT-IR spectrum of **6d** recorded in KBr pellet at 25°C in DMSO-*d*₆.

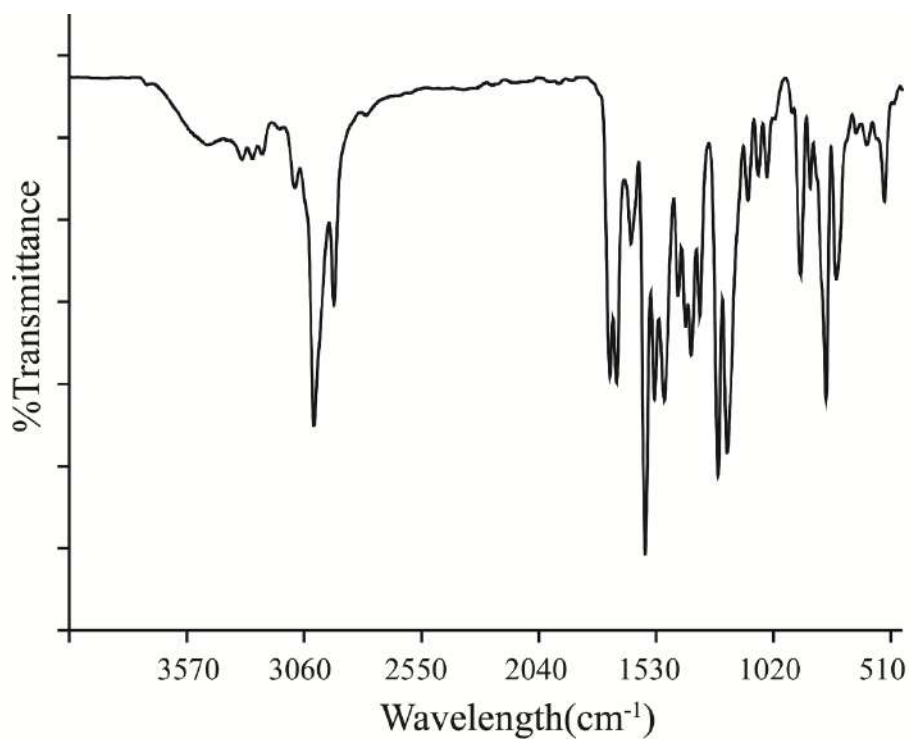


Figure A 2.46 FT-IR spectrum of **6d** recorded in KBr pellet at 25°C.

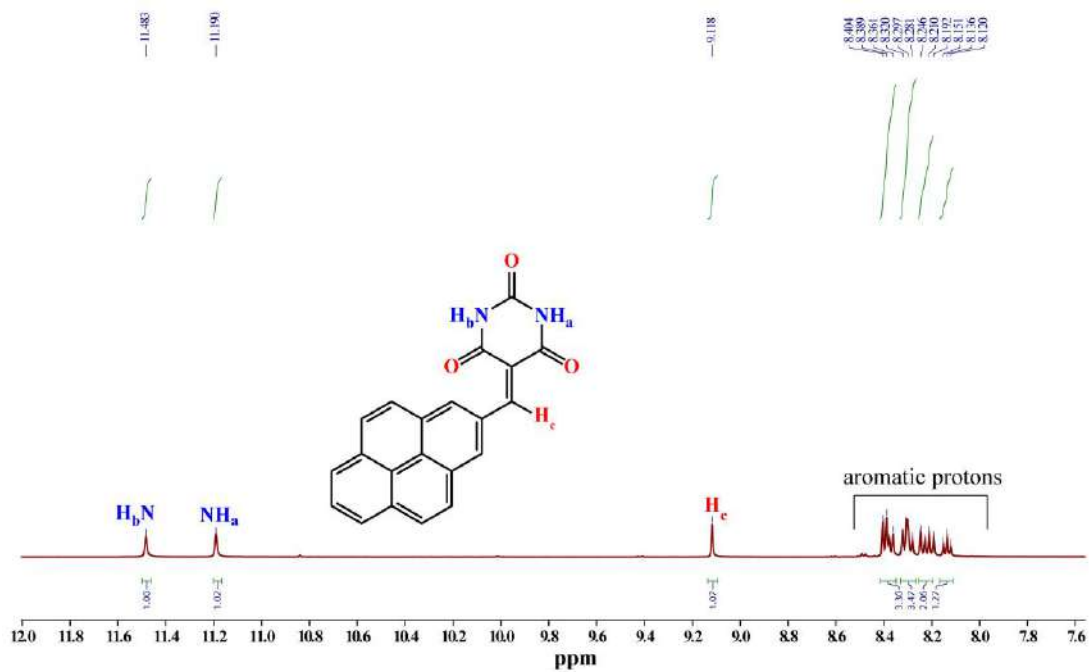


Figure A 2.47 1H NMR [500 MHz, d_6 -DMSO, TMS] of **L7** at 25°C.

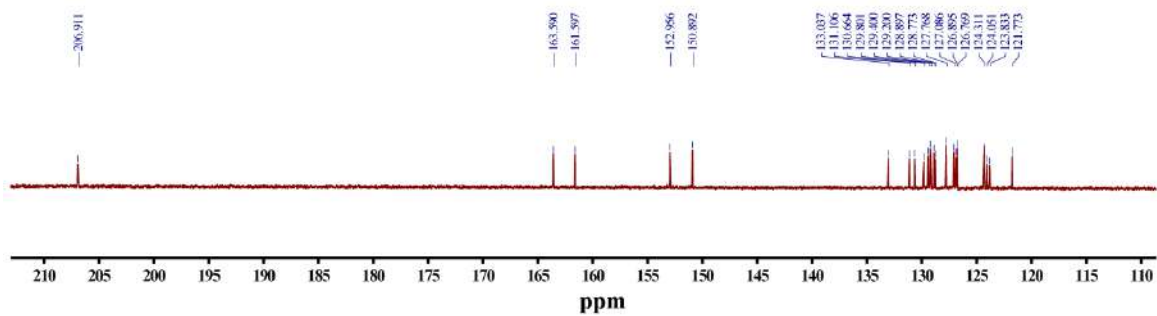


Figure A 2.48 ^{13}C NMR [126 MHz, d_6 -DMSO, TMS] of **L7** solution at 25°C.

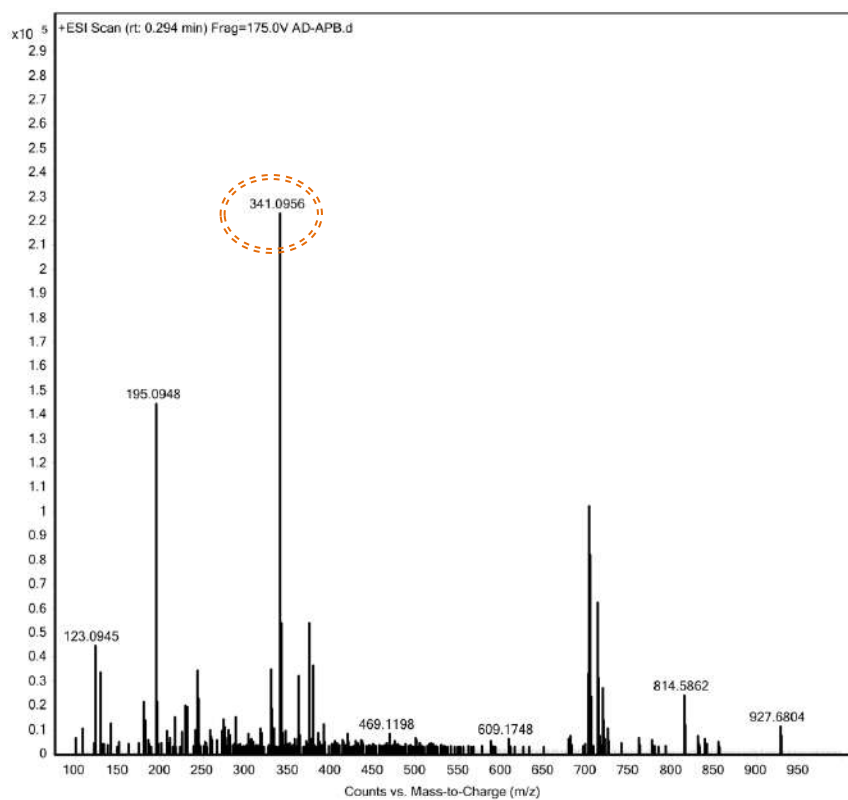


Figure A2.49 Mass spectrum of L_7 , calculated $[L_7 + H]^+ = 340.0848$, Found 341.0956. (Mass spectrum obtained in positive mode).

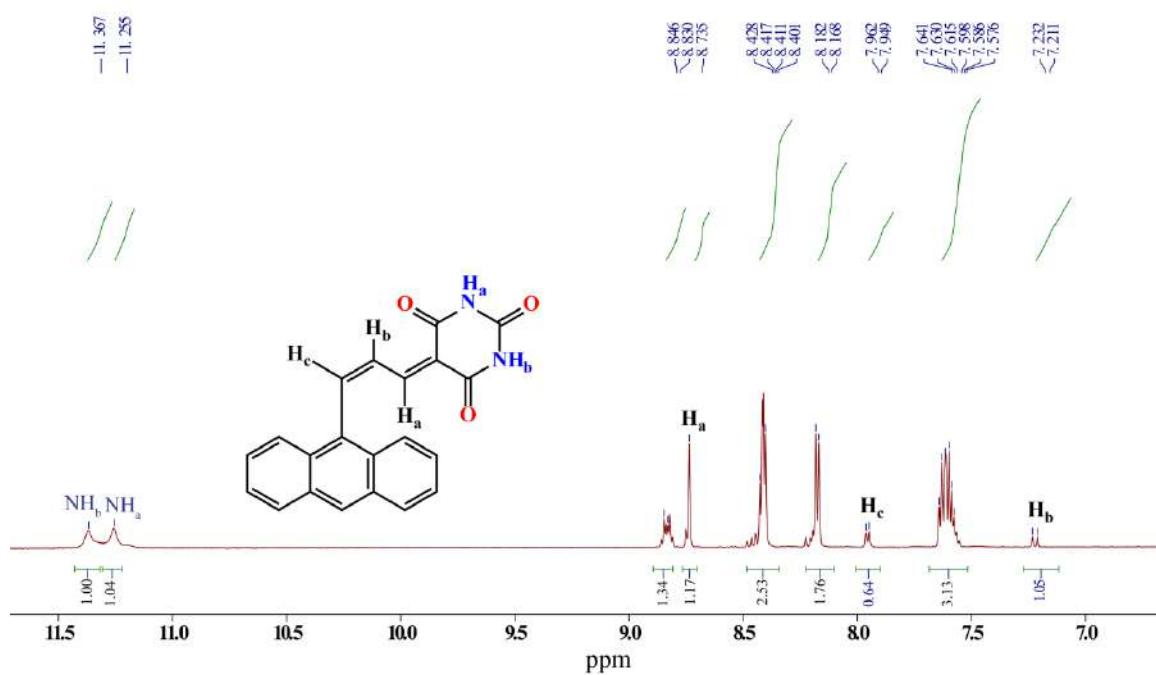


Figure A 2.50 1H NMR [500 MHz, d_6 -DMSO, TMS] of L_8 at 25°C.

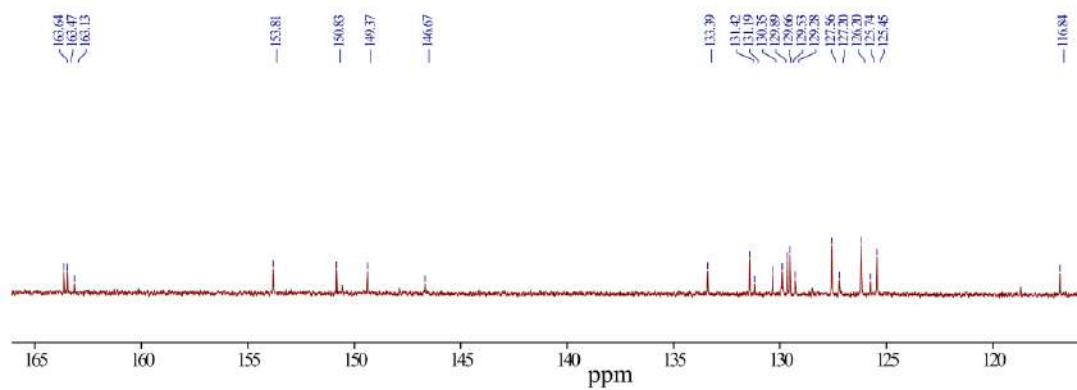


Figure A 2.51 ^{13}C NMR [126 MHz, d_6 -DMSO, TMS] of L_8 solution at 25°C.

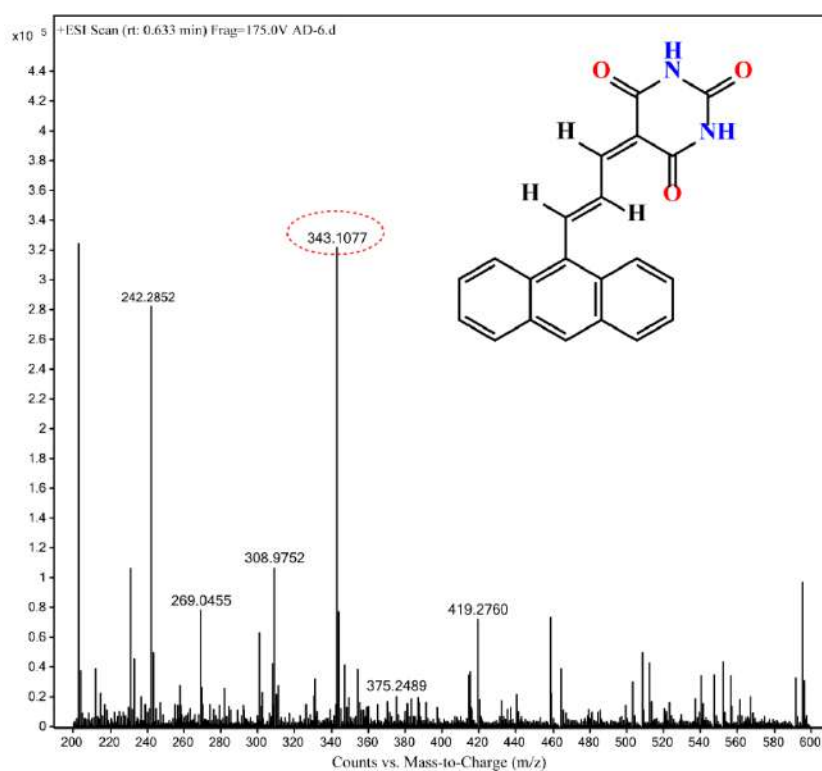
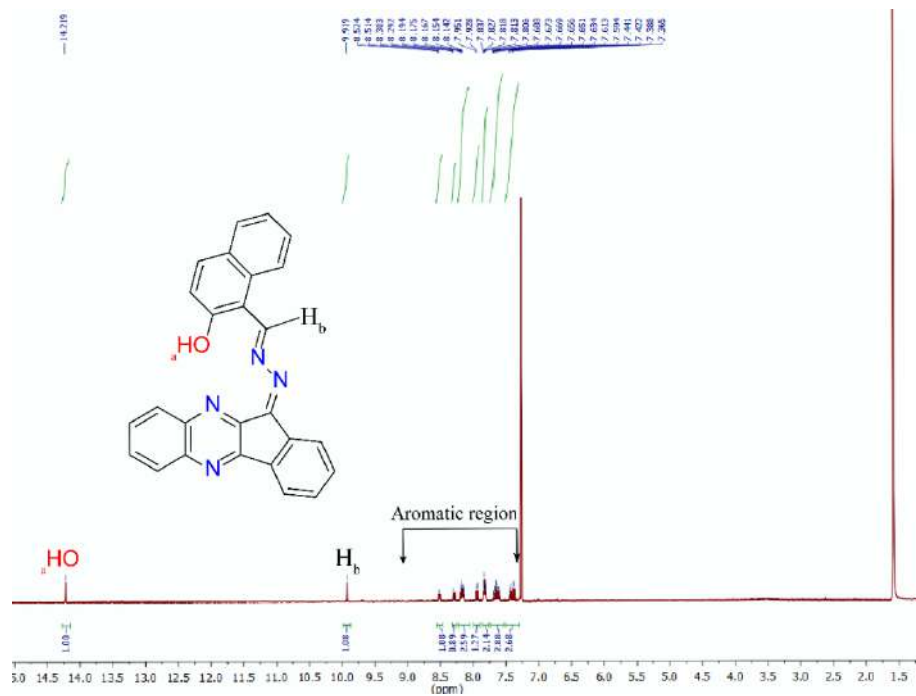
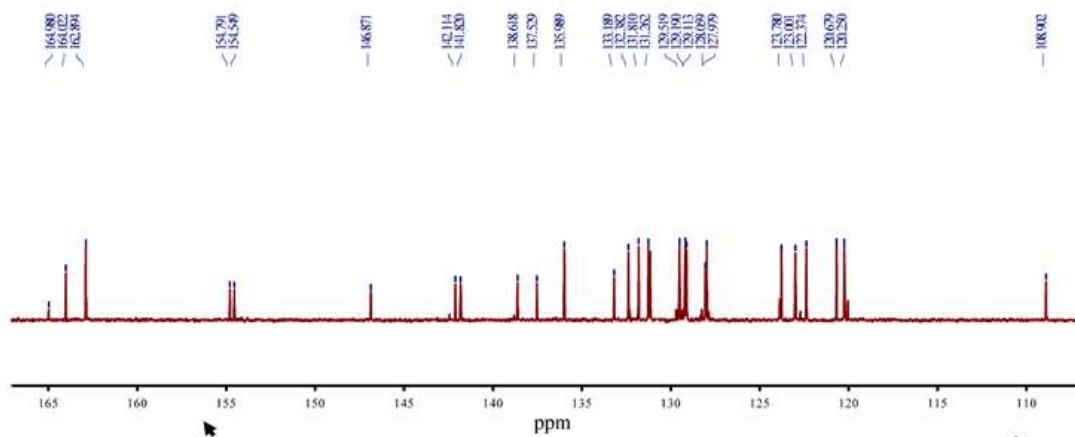


Figure A 2.52 Mass spectrum of L_8 , calculated $[\text{L}_8+\text{H}]^+ = 342.1004$, Found 343.1077. (Mass spectrum obtained in positive mode)

Figure A 2.53 ^1H NMR [400 MHz, CDCl_3 , TMS] of L_9 at 25°C .Figure A 2.54 ^{13}C NMR [100 MHz, CDCl_3 , TMS] of L_9 solution at 25°C .

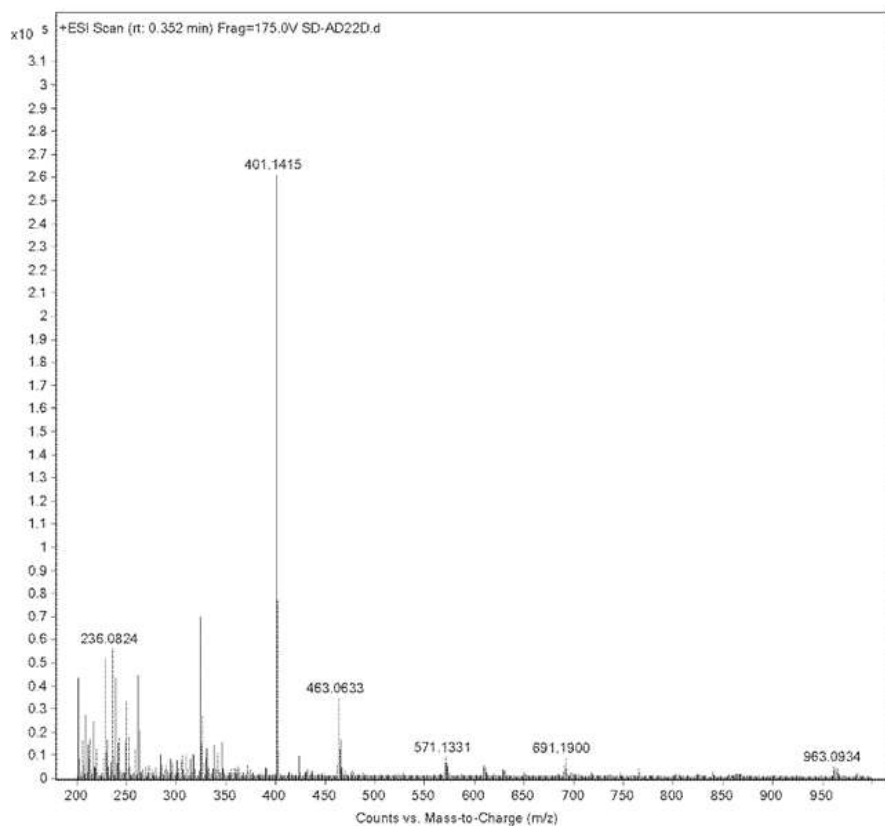


Figure A 2.55 Mass spectrum of L_9 , calculated $[L_9 + H]^+ = 401.1402$, Found 401.1415. (Mass spectrum obtained in positive mode).

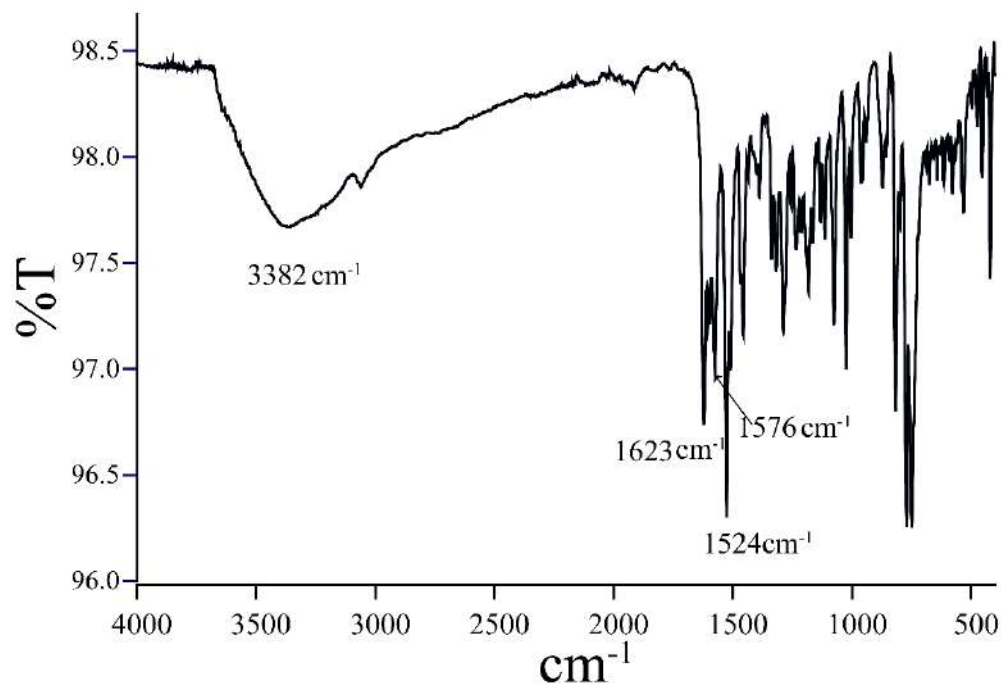


Figure A 2.56 FT-IR [KBr , $\nu\text{ cm}^{-1}$] Spectrum of Receptor L_9 .

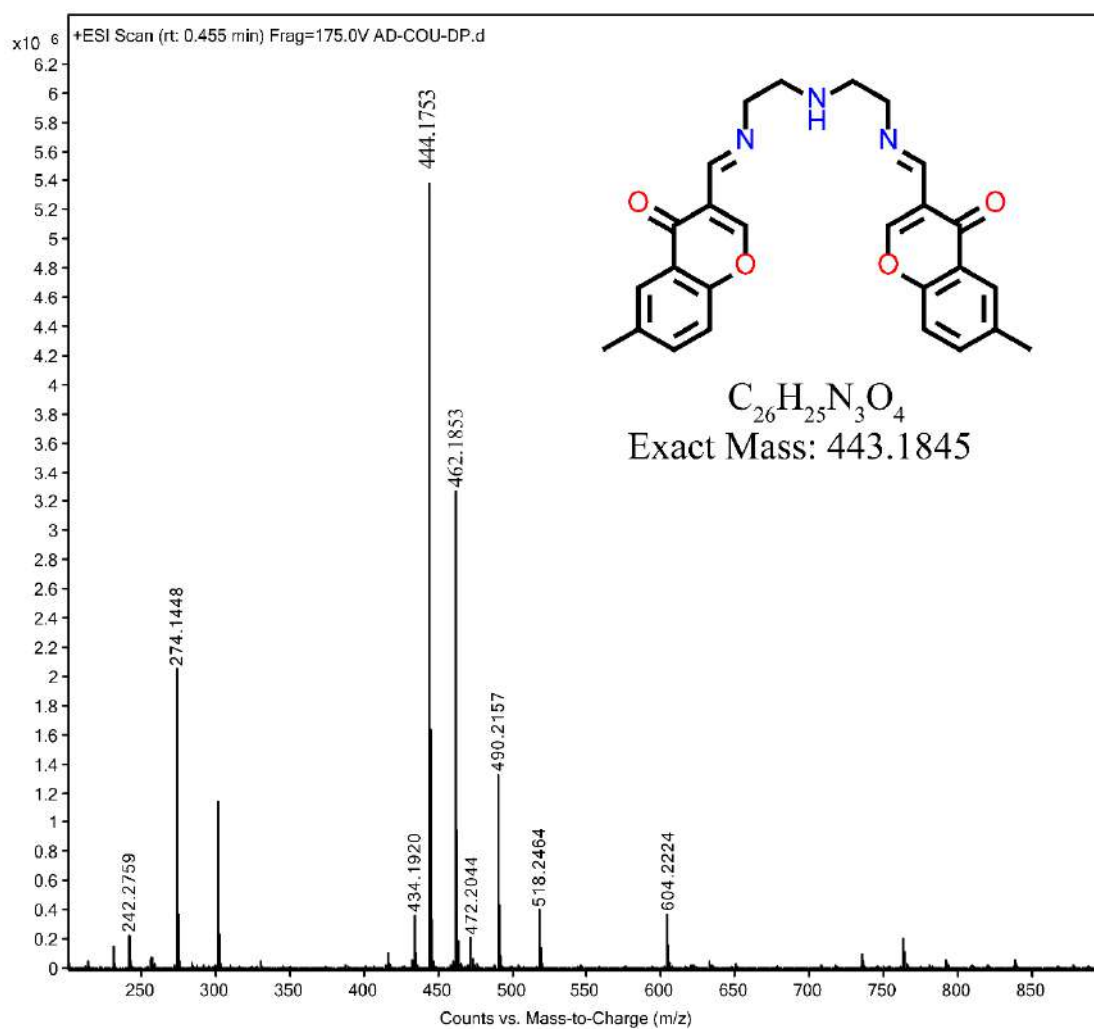


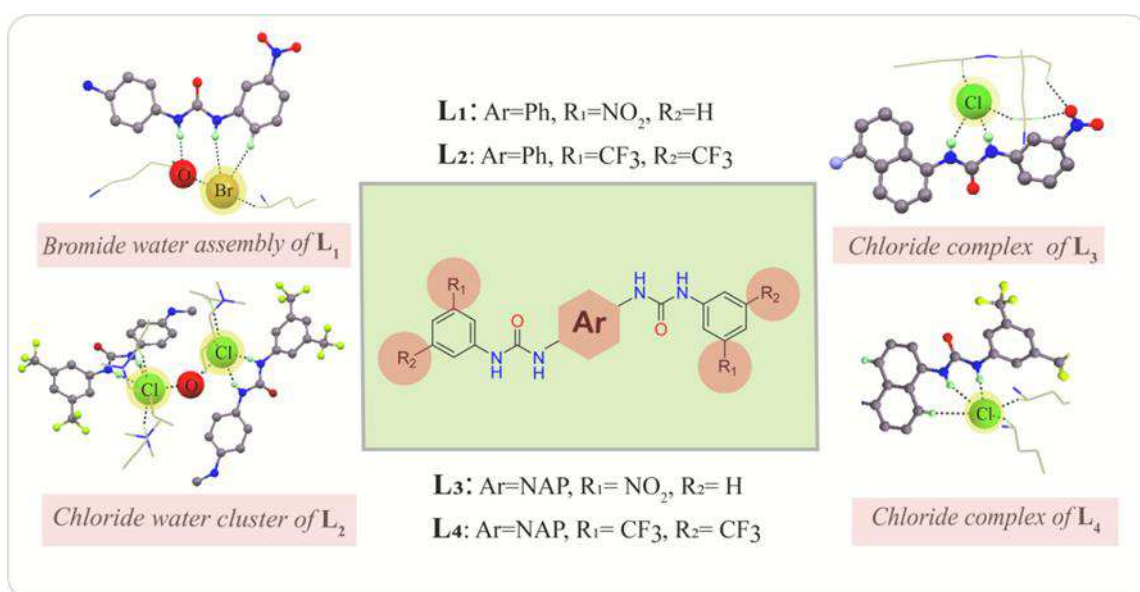
Figure A 2.57 Mass spectrum of **L₁₀**, calculated $[L_{10} + H]^+ = 443.1845$, Found 444.1753. (Mass spectrum obtained in positive mode).

References

- 2.1 F. Du, Y. Zheng, W. Yuan, G. Shan, Y. Bao, S. Jie and P. Pan, *J. Polymer Sci., Part A*: 2019, **57**, 90.
- 2.2 U. Manna, A. Das and G. Das, *Cryst. Growth Des.*, 2018, **18**, 6801.
- 2.3 O. Ando, K. Endo, N. Takahashi and Masako Takeuchi, *Jpn. Kokai Tokkyo Koho.*, 1997, CODEN: JKXXAF; JP09160300.
- 2.4 Q. Lin, X. W. Guan, Y. Q. Fan, J. Wang, L. Liu, J. Liu, H. Yao, Y. M. Zhang and T. B. Wei, *New J. Chem.*, 2019, **43**, 2030-2036.
- 2.5 A. Gogoi and G. Das, *RSC Adv.*, 2014, **4**, 55689-55695.
- 2.6 S. Samanta, S. Goswami, Md. N. Hoque, A. Ramesh, and G. Das, *Chem. Commun.*, 2014, **50**, 11833-11836.
- 2.7 CrysAlisPro, version 1171.33.34d; Oxford Diffraction Ltd. [release 27-02-2009 CrysAlis 171. NET]
- 2.8 SMART, SAINT, and XPREP; Siemens Analytical X-ray Instruments Inc.: Madison, WI, 1995.
- 2.9 G. M. Sheldrick, SADABS, Program for Area Detector Adsorption Correction; Institute for Inorganic Chemistry; University of Göttingen: Germany, 1996.
- 2.10 G. M. Sheldrick, *Acta Crystallogr., Sect. C: Struct. Chem.*, 2015, **3**, 71.
- 2.11 Mercury 4.1.3, supplied with Cambridge Structural Database; CCDC, Cambridge, U.K., 2001-2019.
- 2.12 P. Van der Sluis and A. L. Spek, PLATON/SQUEEZE, *Acta Crystallogr., Sect. A: Found. Crystallogr.*, 1990, **46**, 194–201.
- 2.13 A. H. Benesi, H. J. Hildebrand, *J. Am. Chem. Soc.*, 1949, **71**, 2703- 2707.
- 2.14 R. Wang, Z. Yu, *Acta Physico-Chimica Sinica*, 2007, **23**, 1353- 1359.
- 2.15 S. Johnson, B. T. Couch, A. Meyer, and B. Heller, *Bull. Am. Phys. Soc.*, 2018, **7**, 015004.
- 2.16 M. J. Frisch, G. W. Trucks, H. B. Schlegel, G. E. Scuseria, M. A. Robb, J. R. Cheeseman, G. Scalmani, V. Barone, B. Mennucci, G. A. Petersson, H. Nakatsuji, M. Caricato, X. Li, H. P. Hratchian, A. F. Izmaylov, J. Bloino, G. Zheng, J. L. Sonnenberg, M. Hada, M. Ehara, K. Toyota, R. Fukuda, J. Hasegawa, M. Ishida, T. Nakajima, Y. Honda, O. Kitao, H. Nakai, T. Vreven, J. A. Montgomery, Jr. J. E. Peralta, F. Ogliaro, M. Bearpark, J. J. Heyd, E. Brothers, K. N. Kudin, V. N. Staroverov, R. Kobayashi, J. Normand, K. Raghavachari, A. Rendell, J. C. Burant, S. S. Iyengar, J. Tomasi, M. Cossi, N. Rega, J. M. Millam, M. Klene, J. E. Knox, J. B. Cross, V. Bakken, C. Adamo, J. Jaramillo, R. Gomperts, R. E. Stratmann, O. Yazyev, A. J. Austin, R. Cammi, C. Pomelli, J. W. Ochterski, R. L. Martin, K. Morokuma, V. G. Zakrzewski, G. A. Voth, P. Salvador, J. J. Dannenberg, S. Dapprich, A. D. Daniels, O. Farkas, J. B. Foresman, J. V. Ortiz, J. Cioslowski and D. J. Fox, Gaussian 09, Revision A.1. Gaussian, Inc.; Wallingford CT: 2009
- 2.17 A. K. Mahapatra, S. S. Ali, K. Maiti, S.K. Manna, R. Maji, S. Mondal, M. R. Uddin, S. Mandal and P. Sahoo, *RSC Adv.*, 2015, **5**, 81203

Chapter 3

Design and Synthesis of Neutral Acyclic Receptors: A Case Study to Verify the Effect of Substitution on Halide/Hydrated Halide Binding



3.1 Background and Focus of the Chapter

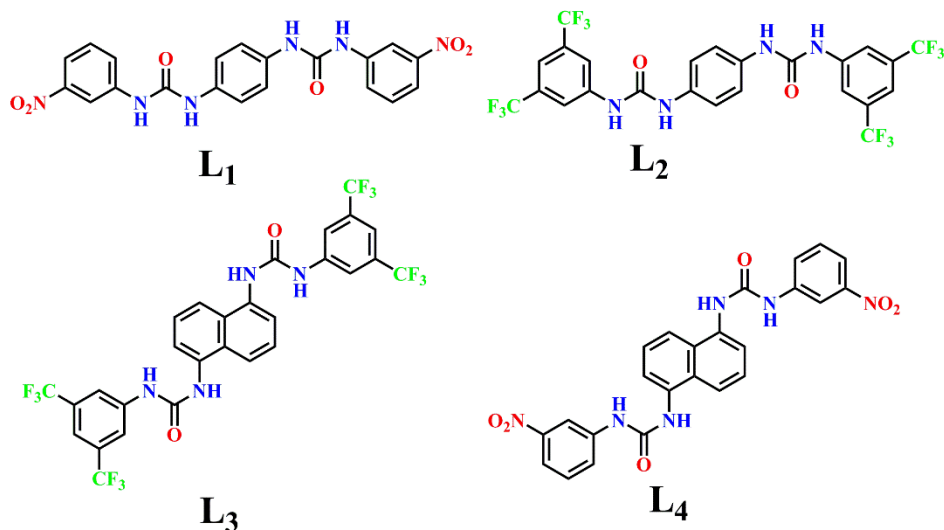
In past years the development of anion recognition was slow, but in recent years the extensive development of anion coordination chemistry within the self-assembled construction of neutral host molecules becomes an essential field.^{3.1-3.3} Anions have a considerable impact on our lives. As anions have a vital and significant impact on living organisms as well as in a range of medical, biological, industrial, and environmental processes the encapsulation of anionic species by various non-covalent interactions within the multi-armed host receptor has appeared to be a principal area in supramolecular chemistry.^{3.4-3.6} Among anionic guests of varied dimensions, encapsulation of spherical halides by synthetic artificial receptors has been of vast importance. It is crucial to study the supramolecular chemistry of hydrated halides due to the abundance and significance of hydrated halides $X^- (H_2O)_n$ in nature.^{3.7-3.11} Among all the halides, Chloride is essential due to its crucial role in the biological area like signal transduction, transport of organic substances through cell membranes. Bromide is necessary for post-translational modification for tissue development and architecture found within the collagen IV scaffold of basement membranes (BMs).^{3.12-3.13} In our continuing effort to understand the binding behaviour of the hydrated/solvated anionic entity by the synthetic receptors^{3.14-3.18} herein, we report the Chloride and Bromide recognition by the substituted thiourea receptors *via* 2:1 anion-receptor interactions in solid-state. In this work, we have presented four neutral hosts **L**₁ – **L**₄ (Scheme 3.1). These receptors recognize Chloride and Bromide through various significant H-bonding interactions. After careful investigation of the anion complexes, it has been observed that all the neutral receptors form halide or hydrated halide-bridged architecture through the involvement of strong $N-H \cdots X^-$ and as well as moderate aromatic $C-H \cdots X^-$ H-bonding interactions (where $X = Cl^-$ and Br^-). It is interesting to note that our group has previously shown that one of the linear bis-urea receptors (**L**₁) can readily form bicarbonate dimer $(HCO_3)_2$ in the solid-state by fluoride- or hydroxide-induced atmospheric CO_2 fixation. This receptor has also been found to self-assemble with divalent sulphate (SO_4^{2-}) and polymeric dihydrogen-phosphate $(H_2PO_4)_n$ *via* non-cooperative hydrogen-bonding interactions. In the present work, we have found that the receptor (**L**₁) can also form complexes with spherical Chloride and Bromide ions in solution as well as solid phases too. Along with **L**₁, three neutral dipodal receptors (**L**₂, **L**₃, and **L**₄) have also been purposefully designed and synthesized by varying the substituents from phenyl to naphthyl moiety to investigate the anion coordinating activities of bis urea receptors. Crystal structure investigation of the complexes correctly validates the fact that the receptors **L**₁-**L**₄ form halide as well as hydrated halide complexes. Most interestingly in complex **2a**, the phenyl based neutral

bis urea receptor **L**₂ binds with two Chloride via participation of N-H...Cl⁻ interaction from adjacent urea group and aromatic C-H...Cl⁻ interaction along with the construction of a halide-water-halide bridged architecture supported by another. Whereas another phenyl-based urea receptor **L**₁ binds to one Bromide (**1b**) which is coordinated with two water molecules (from the lattice) forming a suitable 2:1 anion-receptor interaction. In all cases, the coordinated -NH protons from adjacent urea moieties play an important role in terms of coordination are oriented in trans-fashion concerning the core substituent. The transformation from phenyl to naphthyl ring shows a clear distinction on halide binding which is very much consistent with the size as well as hydrophobic nature of the substituent.

3.2 Design principle of the dipodal receptors **L**₁-**L**₄ and structural aspect of anion coordination

The highly electron-rich naphthyl and phenyl groups have been separately used as a core building block to design four dipodal bis-urea receptors **L**₁-**L**₄. Each receptor has been synthesized by the reaction between either *p*-phenylenediamine or 1, 5-diaminonaphthalene, and 2.0 equiv. of either 3-nitrophenyl isocyanate or 3, 5-bis (trifluoromethyl) phenyl-isothiocyanate in acetonitrile medium with a good yield. The purposeful insertion of urea groups in highly organized dipodal scaffolds becomes useful to determine the binding discrepancies of anionic guests *via* several non-covalent interactions. Receptors **L**₁- **L**₄ show symmetric orientation central aryl core (naphthyl and phenyl) and each of them contains suitable architecture to bind with various anions. **L**₁-**L**₄ includes highly electron-withdrawing groups that form an ordered dipodal void that becomes suitable for anion coordination through effective hydrogen bonding. The presence of electron-withdrawing groups (-CF₃ and -NO₂) moderately enhances the acidity of the bis-urea receptors that satisfactorily help the urea arms to bind the halides by properly orienting themselves adjacent urea moieties of all the rigid receptors adjust their orientation in anti-fashion in most of the cases such as in free receptors or halide complexes and they interact through non-cooperative H-bonding interactions with either adjacent receptors or anions respectively. Efforts were made to study the solid-state binding properties of **L**₁-**L**₃ with various halide ions in different crystallization conditions, by charging excess quaternary ammonium (*n*-TBA/TEA) anion salts to the individual solutions of receptors in aprotic solvents like DMF, DMSO, or a mixture of both. The single-crystal X-ray analysis followed by typical crystallization techniques of free receptors and their halide/hydrated-halide complexes has

always given the comprehensive structural elucidation that indicates the discrepancies of their binding phenomena.



Scheme 3.1 Chemical structures of the receptors L₁ – L₄.

3.2.1. Structural analysis of halide bound complexes of receptors L₁, L₂, L₃, and L₄

Single-crystal XRD analyses of receptor-bound neutral halide complexes as well as studying binding interactions of the receptors with the halide, hydrated-halides of varied shapes are majorly based on either the effect of core substitution or terminal functionalization of synthesized receptors or the size of anionic species.

3.2.1.1 Comparative Structural Analysis Chloride complex [(*n*-TBA)₂{(L₁) (Cl)₂}] (**1a**) and [(*n*-TBA)₂{(L₂) (Cl)₂(H₂O)}] (**2a**):

Suitable single crystals of Chloride/Hydrated-Chloride entrapped neutral complexes **1a/2a**, respectively, were found from either DMF or DMSO solutions of receptor L₁/L₂ or excess of *n*-TBACl salts (Fig. 3.1). The X-ray studies disclosed that Chloride complex **1a** crystallized through monoclinic space group *P* 2₁/*c* (*Z*= 2), whereas the hydrated Chloride complex **2a** crystallized through monoclinic space group *C* 2/*c* (*Z*= 4). In complex **2a**, water oxygen lies on a twofold axis in their asymmetric unit.

In complex **1a**, Chloride is stabilized from the participation of four hydrogen bonds concerning two –NH protons from the host side, and three aliphatic–CH protons from two close-by tetrabutylammonium units which form 2:1 anion-receptor interactions (Fig. 3.1a-c). In addition, the extra C_{TBA}-H···O_{Urea} interaction (Fig. A3.1) from local aliphatic groups delivering additional stability to the complex.

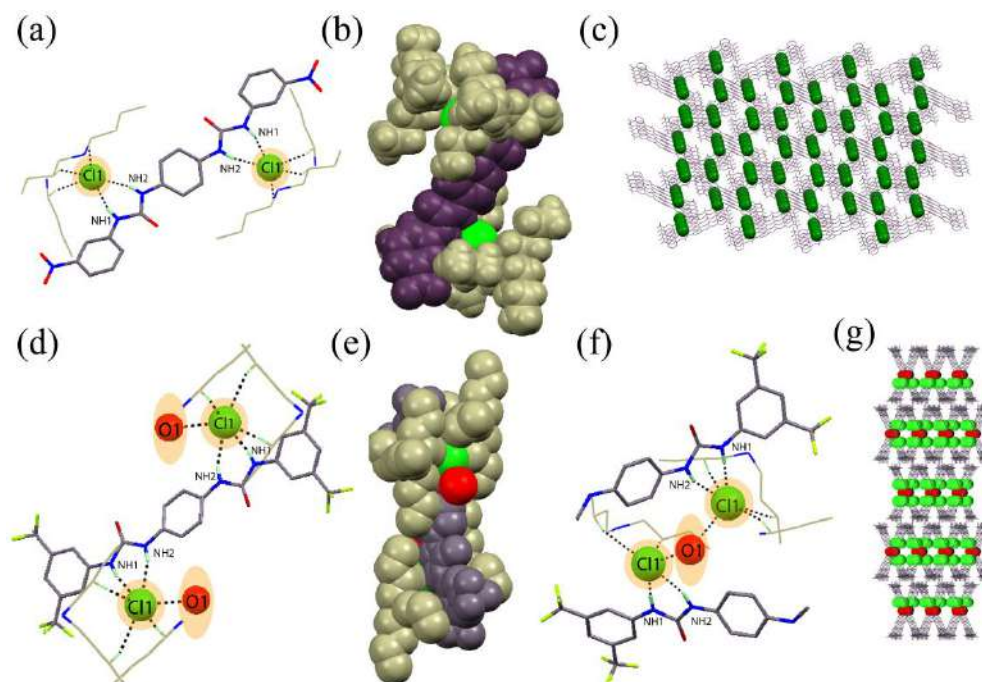


Figure 3.1 X-ray structures revealing (a) an H-bonding interaction created around of Chloride-coordinated ligands, in complex **1a**, (b) space-filling view of TBA cation potted Chloride-receptor shown in complex **1a**, (c) 3D packing diagram of complex **1a**. Single-crystal portraying (d) complex **2a** showing H-bonding coordination surrounding Chloride-coordinated ligands, (e) space-filling view demonstrates of TBA cation potted Chloride-receptor complex in **2a**, (f) the water Chloride hydrogen-bonding interactions in a different way are also pictured clearly for complex **2a**, (g) 3D packing diagram of complex **2a**. Dashed lines indicate the hydrogen-bonding interactions in both cases.

In the case of **2a**, the total interactions with the anion come from the receptor and adjacent tetrabutylammonium groups that are believed to be governed by the hydrogen bonding effectively clearly designed shown in (Fig. 3.1d-g) with numbering the atom scheme. Interestingly, the water molecule serves like a hydrogen-bonded triangle-like structural design by using two coordinated anions forming a $[\text{Cl}_2\text{H}_2\text{O}]^{2-}$ triangle-like architecture with a $\text{Cl}^- - \text{O} - \text{Cl}^-$ angle of 114.5° , and here the $\text{Cl}^- - \text{Cl}^-$ separation is 6.443\AA . By closer inspection, we found that the donor-acceptor distances ($\text{N} \cdots \text{Cl}^-$) fall in the range $2.59\text{--}3.01\text{ \AA}$, which shows moderate Hydrogen bond nature in electrostatic manner.^{3.19-3.23}

Structural examination of the complex (**2a**) discloses that Chloride (1) get stabilized by using five hydrogen bonds involving two $-\text{NH}$ protons from the host, one $-\text{OH}$ proton which mainly comes from lattice water, and the last one coming from two aliphatic $-\text{CH}$ protons from two immediate tetrabutylammonium units (Fig. A3.2). Like complex **1a**, complex **2a** also gains stability by the participation of two $\text{C}_{\text{TBA}} - \text{H} \cdots \text{O}_{\text{Urea}}$ interactions, and here the coordination number of Chloride in complex **1a** is 5 and in complex **2a** are 6.

3.2.1.2. Comparative Structural Analysis Bromide complex $[(n\text{-TBA})_2\{(\text{L}_1) (\text{Br})_2(\text{H}_2\text{O})_2\}]$ (**1b**) and $[(n\text{-TBA})_2\{(\text{L}_2) (\text{Br})_2\}]$ (**2b**)

Suitable single crystals of Bromide/Hydrated-Bromide entrapped neutral complexes **1b/2b** respectively have been found from DMF or DMSO solutions of receptor L_1/L_2 and in the presence of an excess of $n\text{-TBABr}$ salts (Fig. 3.2). The X-ray study exposes that Bromide complex **1b** crystallizes in monoclinic space group $P 2_1/c$ ($Z=2$), whereas the Bromide complex **2b** crystallizes in triclinic space group $P -1$ ($Z=1$).

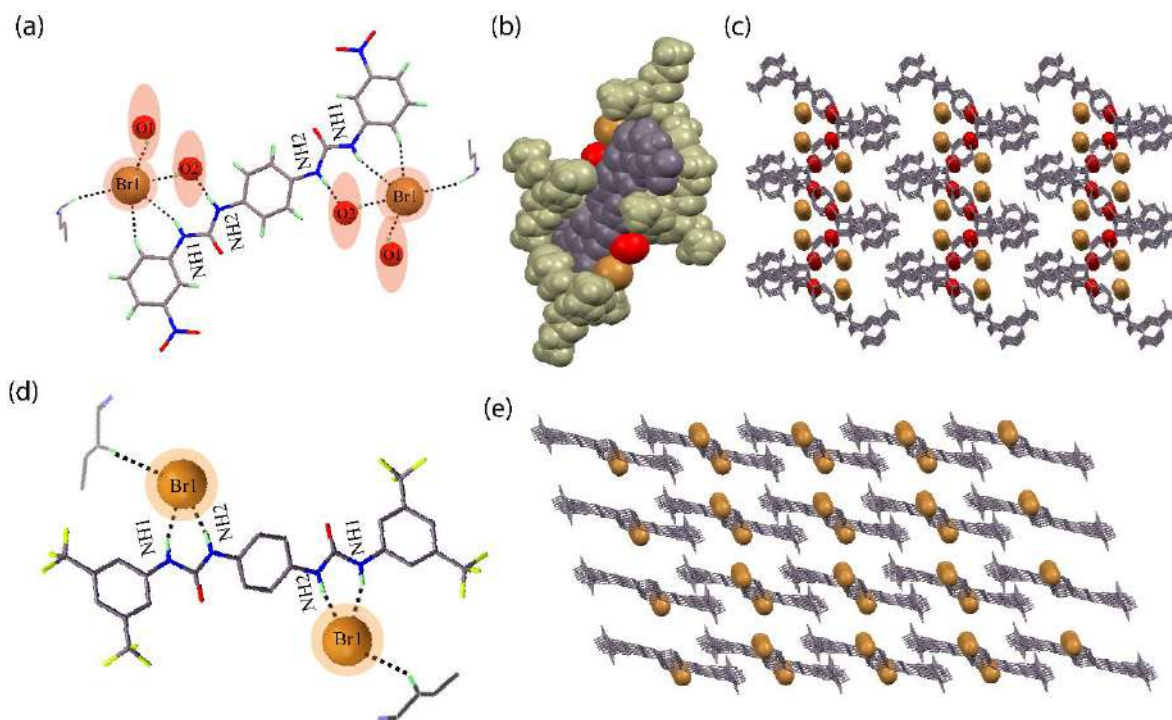


Figure 3.2 (a) complex **1b** showing an H-bond interaction around of Bromide-coordinated ligands, The water Bromide hydrogen-bonding interactions in a different way are also pictured clearly in the complex (b) space-filling view of TBA cation potted Bromide-receptor in complex **1b**, (c) 3D packing diagram of complex **1b**. Single-crystal X-ray structures portraying (d) showing an H-bond interaction around Bromide-coordinated ligands in complex **2b**, (e) 3D packing diagram of complex **2b**. Dashed lines indicate the hydrogen-bonding interactions in both cases.

Interestingly in the case of complex **1b**, the larger Bromide gets stabilized from the participation of four hydrogen bonds concerning one $\text{N-H}_{\text{Urea}} \cdots \text{Br}^-$ interaction (N1H), and one aryl. $\text{C-H}_{\text{Benzene}} \cdots \text{Br}^-$ interaction, two $\text{O-H} \cdots \text{Br}^-$ interactions (O1H and O2H , from lattice water where the H-atoms connected to water molecule O_4 has been identified in the difference map), and one aliphatic $\text{C-H} \cdots \text{Br}^-$ interaction from neighbouring tetrabutylammonium unit forming 2:1 anion-receptor interactions (Fig. 3.2a-c). Most interestingly, the water molecule serves as a hydrogen-bonded triangle-like structural design between one coordinated anion forming a $[\text{Br}$

$(\text{H}_2\text{O})_2]^-$ like assembly with a Br^- -O distance of 3.19 Å. The donor-acceptor distances in $\text{N}\cdots\text{Br}^-$ bond resides in the range of 3.00–4.01 Å, which shows moderate Hydrogen bonding nature. The complex also gets extra stability from two $\text{C}_{\text{Aliphatic}}-\text{H}\cdots\pi_{\text{benzene}}$ interactions and one aliphatic $\text{C}_{\text{Aromatic}}-\text{H}\cdots\text{O}_{\text{Urea}}$ interaction (Fig. A3.3).

But conventionally, in the complex **2b**, the larger Bromide is stabilized by two strong hydrogen bonding from the host via $\text{N}-\text{H}_{\text{Urea}}\cdots\text{Br}^-$ interaction (N1H) through usual 2:1 anion-receptor interactions (Fig. 3.2d-e). Here the coordination number of Bromide in complex **1b** is 5 and unusually 3 for complex **2b** (Fig. A3.4). From the crystallographic data, it is cleared that hydrogen-bond distances for Bromide complexes (**1b** and **2b**) are slightly higher than those of the Chloride complex (**1a** and **2a**). The observation may be recognized with the lower basicity and higher polarizability of Bromide that reduce H-bonding ability.

3.2.1.3 Comparative Structural Analysis Chloride complex $[(n\text{-TBA})_2\{(\text{L}_3) (\text{Cl})_2\}]$ (**3a**) and $[(n\text{-TBA})_2\{(\text{L}_4) (\text{Cl})_2\}]$ (**4a**)

Suitable single crystals of Chloride entrapped neutral complexes **3a/4a**, respectively have been found from either DMF or DMSO solutions of receptor L_3/L_4 and excess of $n\text{-TBACl}$ salts (Fig. 3.3). The X-ray investigation states that Chloride complex **3a** crystallizes in triclinic space group $P\bar{1}$ ($Z=1$), whereas the Chloride complex **4a** crystallizes in monoclinic space group $C2/c$ ($Z=4$).

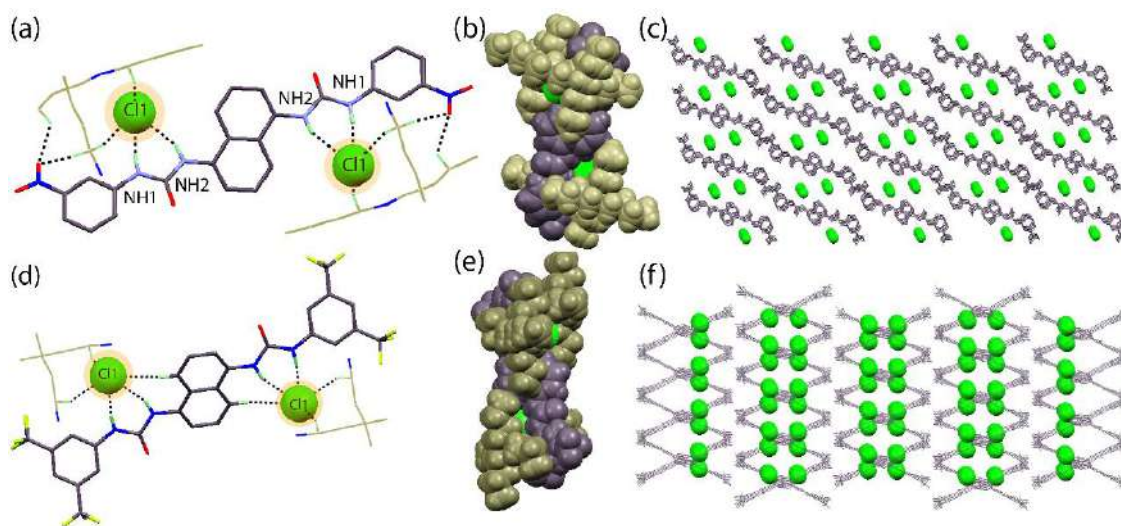


Figure 3.3 Portraying (a) an H-bond interaction around Chloride-coordinated ligands in complex **3a**, (b) space-filling appearance of TBA cation potted Chloride-receptor in complex **3a**, (c) packing diagram of complex **3a**. Single-crystal X-ray structures demonstrating (d) an H-bonding interaction about Chloride-coordinated ligands in complex **4a**, (e) space-filling view of TBA cation potted Chloride-receptor complex in **4a**, (c) packing diagram of complex **4a**. Dashed lines indicate the hydrogen-bonding interactions in all cases.

In the case of complex **3a**, Chloride is stabilized by two robust $\text{N-H}_{\text{urea}}\cdots\text{Cl}^-$ interactions and weak aliphatic $\text{C-H}_{\text{TBA}}\cdots\text{Cl}^-$ interactions from neighbouring two tetrabutylammonium units forming 2:1 anion-receptor interactions (Fig. 3.3a). The extra stability of that complex attained by the cooperation of two aliphatic CH- groups with oxygen and three aliphatic $\text{C-H}\cdots\text{O}_{\text{urea}}$ interactions is shown in (Fig. A3.5). But in the case of complex **4a**, Chloride is stabilized by two strong $\text{N-H}_{\text{urea}}\cdots\text{Cl}^-$ interactions along with two weak aliphatic $\text{C-H}_{\text{TBA}}\cdots\text{Cl}^-$ interactions from neighbouring two tetrabutylammonium units forming 2:1 anion-receptor interactions (Fig. 3d-f) and one aryl $\text{C-H}_{\text{Benzene}}\cdots\text{Cl}^-$ interaction effectively. Moreover, the complex gets extra stability by two aliphatic $\text{C-H}\cdots\text{O}_{\text{urea}}$ interaction (Fig. A3.6). Here the coordination number of Chloride in complex **3a** is 4, and for in complex **4a** is 5.

3.2.1.4 Comparative Structural Analysis Bromide complex $[(n\text{-TBA})_2\{(\text{L}_3) (\text{Br})_2\}]$ (**3b**) and $[(n\text{-TBA})_2\{(\text{L}_4) (\text{Br})_2\}]$ (**4b**)

Single crystal of Bromide enclosed neutral complexes **3b/4b** respectively have been synthesized from either DMF or DMSO solutions of receptor **L3/L4** and excess of *n*-TBA⁺Br⁻ salts (Fig. 3.4). The single-crystal X-ray analysis clearly explains that Bromide complex **3b** crystallizes in triclinic space group *P* 1 (*Z*=1). Whereas the space group of complex **4b** is found to be monoclinic *C* 2/*c* (*Z*=4). In the case of complex **3b** larger size, Br⁻ get stabilized by two moderately strong $\text{N-H}_{\text{urea}}\cdots\text{Br}^-$ interactions and three weak aliphatic $\text{C-H}\cdots\text{Cl}^-$ interactions from neighboring two tetrabutylammonium units forming 2:1 anion-receptor complex (Fig. 3.4a-c). The extra stability of that complex attained by the interaction of two aliphatic CH- groups with oxygen and three aliphatic $\text{C-H}\cdots\text{O}_{\text{urea}}$ interactions is shown in (Fig. A3.7).

But in complex **4b**, the larger Bromide is stabilized by two tetrabutylammonium units forming a 2:1 anion-receptor complex (Fig. 3.4d-f). But here the water molecule stays in coordination lattice without any participation in bonding. Here the coordination number of complex **3b** is 5 and for in complex **4b** is 4. The extra stability of the complex **3b** may be attained by the interaction of three aliphatic $\text{C-H}\cdots\text{O}_{\text{urea}}$ interactions shown in (Fig. A3.8). In all individual anion complexes, the scatter plot that includes the $\text{N-H}\cdots\text{Anion}$ angles vs. $\text{H}\cdots\text{Anion}$ distances (Fig. 3.9) also confirms that these interactions are mostly governed by various strong H-bonding interactions summarized in Table A3.2.

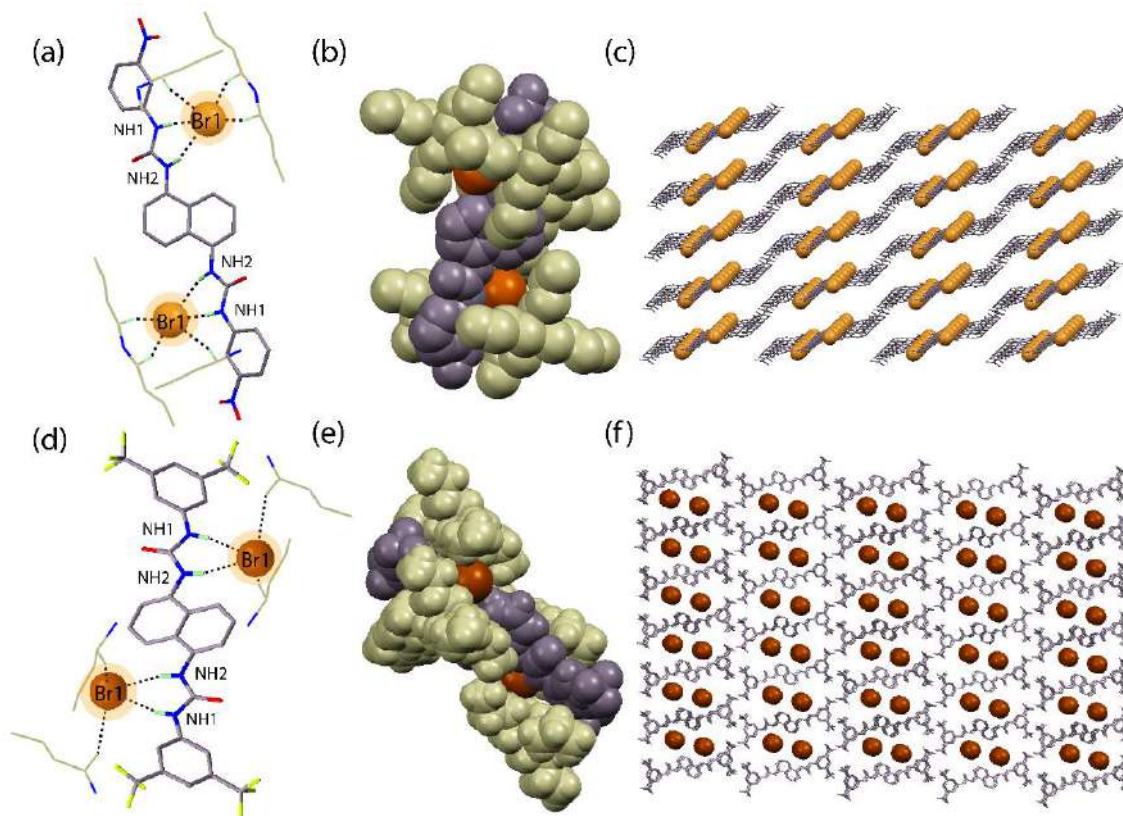


Figure 3.4 describes (a) an H-bond interaction around Bromide-coordinated ligands for complex **3b**, (b) a space-filling view of TBA cation potted Bromide-receptor in complex **3b**, and (c) a packing diagram of complex **3a**. (d) Showing an H-bonding coordination environment of Bromide-coordinated ligands in complex **4b**, (e) space-filling demonstration of TBA cation potted Bromide-receptor complex in **4b**, (f) showing a packing diagram of complex **4b**. Dashed lines indicate the hydrogen-bonding interactions in all complexes.

3.3 ^1H NMR study of dipodal complexes in solution

The qualitative experiment by ^1H NMR in (DMSO-d_6) by using the quaternary ammonium (n-TBA) salts of the anions with free receptors **L**₁–**L**₄ has been performed. The isolated anion complexes **1a**, **1b**, **2a**, **2b**, **3a**, **3b**, **4a**, and **4b** have been done which shows the most significant changes of the urea –NH protons, (Fig. 3.5b) represents the maximum amount of chemical shift changes observed in the presence of different types of halides. The change of the chemical shift values is consistent with the effect of electronegativity and the effect of conjugation along with the change of core substituent. ^1H NMR analysis of the free **L**₁ receptor shows the chemical shift values of ($\delta\text{-NH}_a = 8.745$ ppm; $\delta\text{-NH}_b = 9.169$ ppm) but protonated **L**₁ shows a significant change in the chemical shift after entrapment of Chloride and Bromide. For Chloride the average downfield shift of $\Delta\delta = 0.357$ ppm ($\Delta\delta\text{-NH}_a = 0.306$ ppm; $\Delta\delta\text{-NH}_b = 0.357$ ppm) and for Bromide the average downfield shift of $\Delta\delta = 0.049$ ppm ($\Delta\delta\text{-NH}_a = 0.041$; $\Delta\delta\text{-NH}_b = 0.057$ ppm) which are clearly depicted in (fig. 3.5b). The **L**₂ receptor shows the chemical shift values

of ($\delta\text{-NH}_a = 8.897$ ppm; $\delta\text{-NH}_b = 9.341$ ppm), but protonated **L**₂ shows a significant change in the chemical shift after entrapment of Chloride and Bromide. For Chloride the average downfield shift of $\Delta\delta = 0.345$ ppm ($\Delta\delta\text{-NH}_a = 0.253$ ppm; $\Delta\delta\text{-NH}_b = 0.437$ ppm) and for Bromide the average downfield shift of $\Delta\delta = 1.071$ ppm ($\Delta\delta\text{-NH}_a = 1.033$; $\Delta\delta\text{-NH}_b = 1.110$ ppm) respectively shown by NH protons (fig. 3.5c). ¹H NMR analysis of the free **L**₃ receptor shows the chemical shift values of ($\delta\text{-NH}_a = 8.637$ ppm; $\delta\text{-NH}_b = 8.932$ ppm), but significant change in the chemical shift after entrapment of Chloride and Bromide was observed in protonated **L**₃. For Chloride the average downfield shift of $\Delta\delta = 0.557$ ppm ($\Delta\delta\text{-NH}_a = 0.355$ ppm; $\Delta\delta\text{-NH}_b = 0.760$ ppm) and for Bromide the average downfield shift of $\Delta\delta = 0.555$ ppm ($\Delta\delta\text{-NH}_a = 0.348$; $\Delta\delta\text{-NH}_b = 0.762$ ppm) respectively shown by NH protons (Fig. 3.5d). ¹H NMR analysis of the free **L**₄ receptor shows the chemical shift values of ($\delta\text{-NH}_a = 8.932$ ppm; $\delta\text{-NH}_b = 9.569$ ppm) but protonated **L**₄ shows a significant change in the chemical shift after entrapment of Chloride and Bromide. For Chloride the average downfield shift of $\Delta\delta = 0.780$ ppm ($\Delta\delta\text{-NH}_a = 0.474$ ppm; $\Delta\delta\text{-NH}_b = 1.087$ ppm) and for Bromide the average downfield shift of $\Delta\delta = 1.144$ ppm ($\Delta\delta\text{-NH}_a = 1.084$; $\Delta\delta\text{-NH}_b = 1.205$ ppm) (fig. 3.5e). It is clear that for all these cases we have noticed that Chloride complexes of all the receptors show a comparatively more downfield shift in chemical shift values. This may be attributable to the higher charge density, more basicity, and lesser polarizability of Chloride compare to Bromide^{3,24}. The change in the chemical shift is inconsistent with an overall electron density of the receptor via the combined effect of the terminal substituents as well as the core. The anion binding properties of receptor **L**₁ in solution were studied by qualitative as well as quantitative ¹H NMR experiments in DMSO-d₆ using the quaternary ammonium (*n*-TBA) salt of Chloride and Bromide as evidenced from the solid-state. The most significant change has been observed for the urea -NH protons which are expected because of the -NH function of urea moiety act as a primary site for halide binding. The chemical shift changes were observed upon the gradual addition of TBACl in DMSO-d₆ solution to the solutions of **L**₁. It showed an average downfield shift of $\Delta\delta = 1.014$ ppm ($\Delta\delta\text{-NH}_b = 1.139$ ppm; $\Delta\delta\text{-NH}_a = 0.889$ ppm) followed by broadening of the NH signals (Fig. A3.10A). But upon gradual addition of TBABr in DMSO-d₆ solution of **L**₁ showed an average downfield shift of $\Delta\delta = 0.566$ ppm ($\Delta\delta\text{-NH}_b = 0.635$ ppm; $\Delta\delta\text{-NH}_a = 0.497$ ppm) (Fig. A3.11A).

A similar study has been performed with receptor **L**₂. The gradual addition of TBACl in DMSO-d₆ solutions of **L**₂ showed an average downfield shift of $\Delta\delta = 1.057$ ppm ($\Delta\delta\text{-NH}_b = 1.318$ ppm; $\Delta\delta\text{-NH}_a = 0.797$ ppm) with the broadening of the NH signals (Fig. A3.12A). However, gradual

addition of TBABr in DMSO- d_6 solution of L_2 showed an average downfield shift of $\Delta\delta = 0.6$ ppm ($\Delta\delta\text{-NH}_b = 0.778$ ppm; $\Delta\delta\text{-NH}_a = 0.422$ ppm) (Fig. A3.13A). We have attempted a similar experiment with L_3 and L_4 , however, due to poor solubility of the ligand in DMSO- d_6 , we were unable to perform the NMR titration studies.

The Bind-fit^{3.25} model was used to fit the NMR titration data to a 1:1 host-guest stoichiometry (Fig. A3.10-3.14B), which yielded the stability constants of the receptors with each anion. Both receptors (L_1 and L_2) show a higher binding constant with Chloride rather than Bromide. However, the solid-state binding stoichiometry is different from the value obtained from the NMR titration studies. The discrepancy is rather common in literature and it may be attributed to the more compact and organized anion binding by several numbers of non-covalent interactions with the receptors in the solid-state.

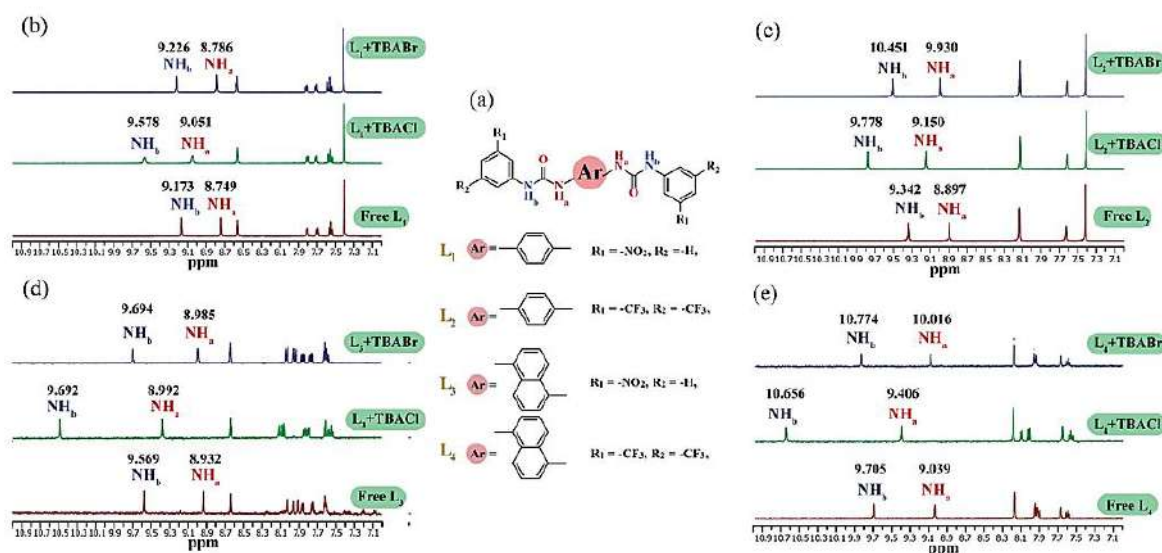


Figure 3.5 (a) Depiction of $-NH_a$ and $-NH_b$ protons from urea side in neutral bis urea scaffolds L_1 / L_2 / L_3 / L_4 (b) expanded view of partially stacked 1H NMR spectra in DMSO- d_6 of L_1 with Chloride and Bromide, (c) expanded view of partially stacked 1H NMR spectra of L_2 with Chloride and Bromide, (d) expanded partial stacked 1H NMR spectra of L_3 with Chloride and Bromide, (e) expanded view of partially stacked 1H NMR spectra of L_4 with Chloride and Bromide.

3.4 Conclusion

In this work, we have systematically examined the halide binding with *p*-phenylenediamine and 1,5-diamino naphthalene based on four bis-urea neutral receptors (L_1 – L_4). Crystal structure analysis reveals that all the complexes form 2:1 anion-receptor architecture in solid-state. Crystal structure analysis reveals that the urea groups within a receptor bind the halide ions in an anti-fashion through $N-H\cdots X$ hydrogen bonding. The solid-state structure is formed by the

various interactions of halides with the receptors in the presence of tetrabutyl ammonium cation. From solid-state structural analysis, it also appears that the receptor lies about an inversion center in the respective complexes. The binding pattern of the halide gets affected as we move from smaller phenyl core into larger and rigid naphthyl ring. ^1H NMR titration study reveals that efficient binding interaction observed for Chloride than Bromide which may be concluded from the binding constant in solution state which is consistent with their solid-state binding data. The binding interaction with halides reveals that the adjacent urea moieties orient themselves in *anti*-fashion in solid-state. The change in the electronic nature of the terminal substituents and the core part of the receptors has made the difference in binding both in the solid and solution phase. The results obtained will help us to design new receptors for efficient binding of anions from solution.

References

- 3.1 B. J. Calnan, B. Tidor, S. Biancalana, D. Hudson and A. D. Frankel, *Science*, 1991, **252**, 1167.
- 3.2 P. Chakrabarti, *J. Mol. Biol.*, 1993, **234**, 463.
- 3.3 M. Cametti and K. Rissanen, *Chem. Soc. Rev.*, 2013, **42**, 2016.
- 3.4 M. Wenzel, J. R. Hiscock and P. A. Gale, *Chem. Soc. Rev.*, 2012, **41**, 480.
- 3.5 B. P. Hay, *Chem. Soc. Rev.*, 2010, **39**, 3700.
- 3.6 F. P. Schmidtchen, *Chem. Soc. Rev.*, 2010, **39**, 3916.
- 3.7 C. Caltagirone and P. A. Gale, *Chem. Soc. Rev.*, 2009, **38**, 520.
- 3.8 P. Weis, P. R. Kemper, M. T. Bowers and S. S. Xantheas, *J. Am. Chem. Soc.*, 1999, **121**, 3531.
- 3.9 D. D. Kemp and M. S. Gordon, *J. PhysChem. A.*, 2005, **109**, 7688.
- 3.10 C. P. Kelly, C. J. Cramer and D. G. Truhlar, *J. Phys. Chem. B.*, 2006, **110**, 16066.
- 3.11 S. Lima, B. J. Goodfellow, J. J. Teixeira-Dias and C. J. Inclusion Phenom, *Mol. Recognit. Chem.*, 2006, **54**, 35.
- 3.12 Krik and L. Kenneth, *Biochemistry of the Elemental Halogens and Inorganic Halides*, Ed. Plenum Press: New York, 1991.
- 3.13 A. S. McCall, C. F. Cummings, G. Bhave, R. Vanacore, A. Page-McCaw and B. G. Hudson, *Cell.*, 2014, **157**, 1380.
- 3.14 A. Gogoi and G. Das, *Supramol. Chem.*, 2013, **25**, 819.
- 3.15 A. Basu and G. Das, *Chem. Commun.*, 2013, **49**, 3997.
- 3.16 M. N. Hoque and G. Das, *CrystEngComm.*, 2014, **16**, 4447.
- 3.17 U. Manna, R. Chutia and G. Das, *Cryst. Growth Des.*, 2016, **16**, 2893.
- 3.18 U. Manna, A. Das, and G. Das, *Cryst. Growth Des.*, 2018, **18**, 6801.
- 3.19 H. Ohtaki and T. Radnai, *Chem. Rev.*, 1993, **93**, 1157.
- 3.20 D.T. Richens, *The Chemistry of Aqua Ions*, Wiley, Chichester., 1987.
- 3.21 S. K. Dey and G. Das, *Chem. Commun.*, 2011, **47**, 4983.
- 3.22 S. K. Dey, Ojha, B, and G. Das, *CrystEngComm.*, 2011, **13**, 269.
- 3.23 A. Pramanik and G. Das, *Tetrahedron.*, 2009, **65**, 2196.

3.24 M. Savastano, C. Bazzicalupi, C. García-Gallarín, C. Giorgi, M. D. López de la Torre, F. Pichierri, A. Bianchi and M. Melguizo, *Dalton Trans.*, 2018, **47**, 3329.

3.25 D. Brynn Hibbert and P. Thordarson, *ChemCommun.*, 2016, **52**, 12792.

Annexure 3

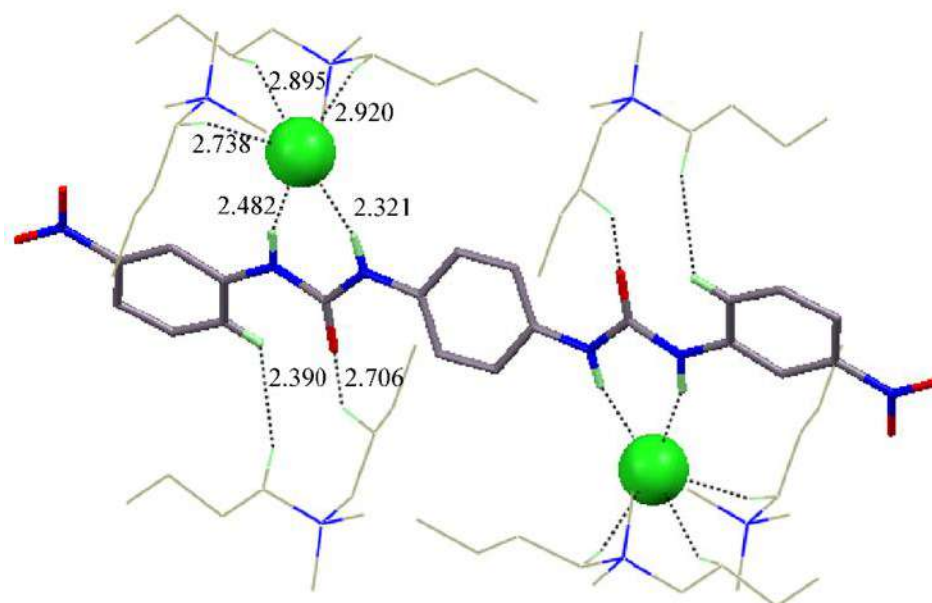


Figure A3.1 X-ray structure analysis of complex **1a** showing coordination environment of anion as well as extra stabilization through $C-H_{\text{aliphatic}} \cdots O_{\text{urea}}$ and $C-H_{\text{aliphatic}} \cdots \pi_{\text{aromatic}}$ interaction with proper bond distances in Angstrom.

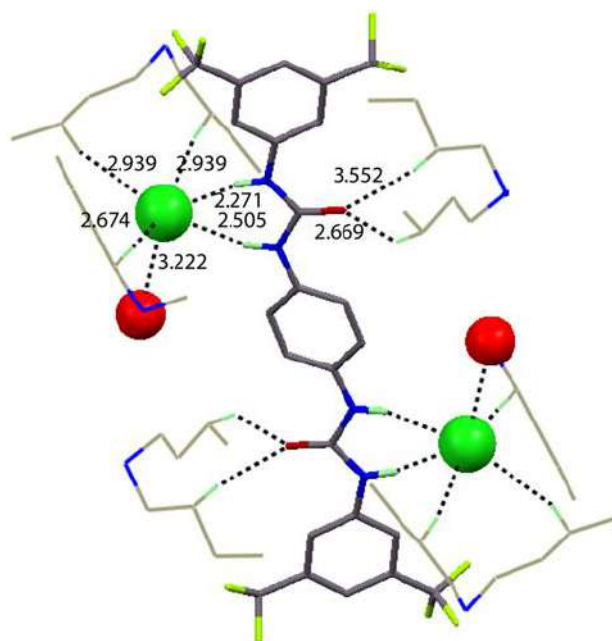


Figure A3.2 X-ray structure analysis of complex **2a** showing coordination environment of anion as well as extra stabilization through two $C-H_{\text{aliphatic}} \cdots O_{\text{urea}}$ with proper bond distances in Angstrom.

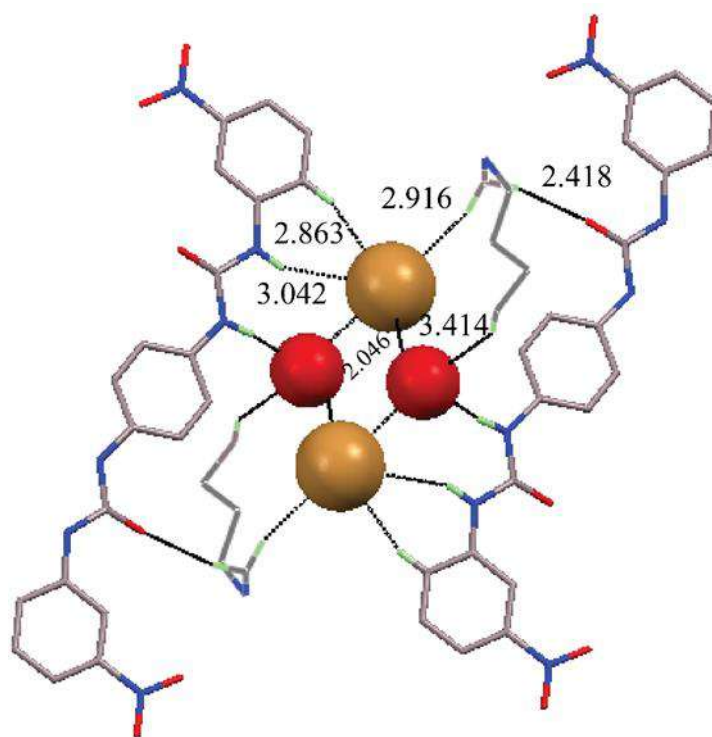


Figure A3.3 X-ray structure analysis of complex **1b** showing coordination environment of anion as well as extra stabilization through C-H_{aliphatic}...O_{urea}, C-H_{aliphatic}...π_{aromatic}, C-H_{aliphatic}...O_{water} interaction with proper bond distances in Angstrom.

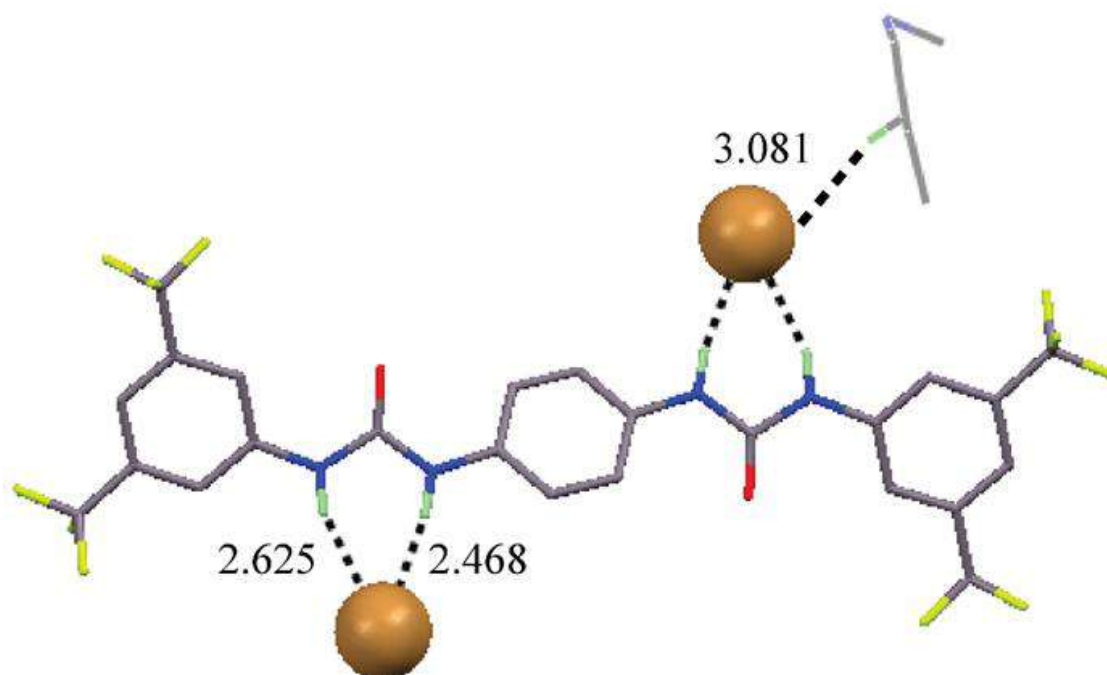


Figure A3.4 X-ray structure analysis of complex **2b** showing coordination environment of anion as well as extra stabilization through C-H_{aliphatic}...O_{urea}, with proper bond distances in Angstrom.

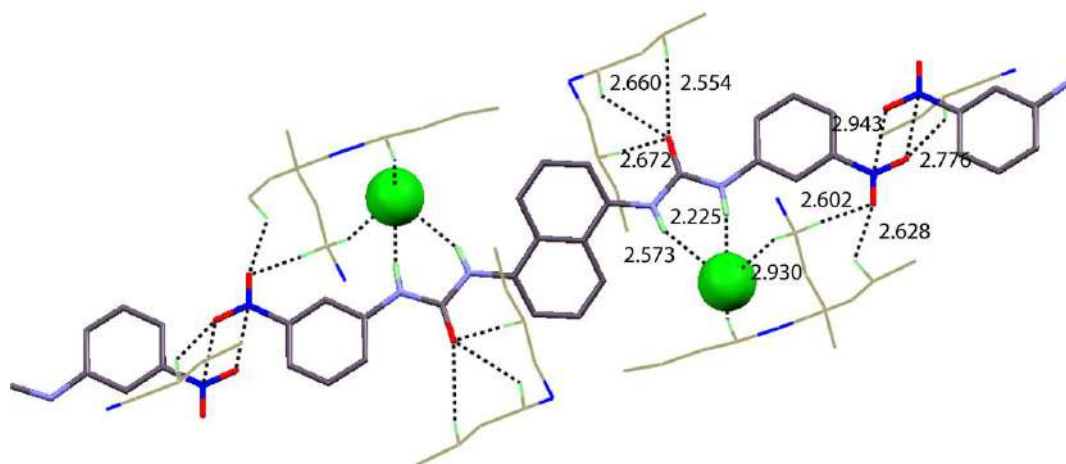


Figure A3.5 X-ray structure analysis of complex **3a** showing coordination environment of anion as well as extra stabilization through three C-H_{aliphatic}...O_{urea}, four C-H_{aliphatic}...O interaction from two different oxygen of substituted NO₂ group and one cross connected parallel C-H...O interaction between two NO₂ groups of each host site with proper bond distances in Angstrom.

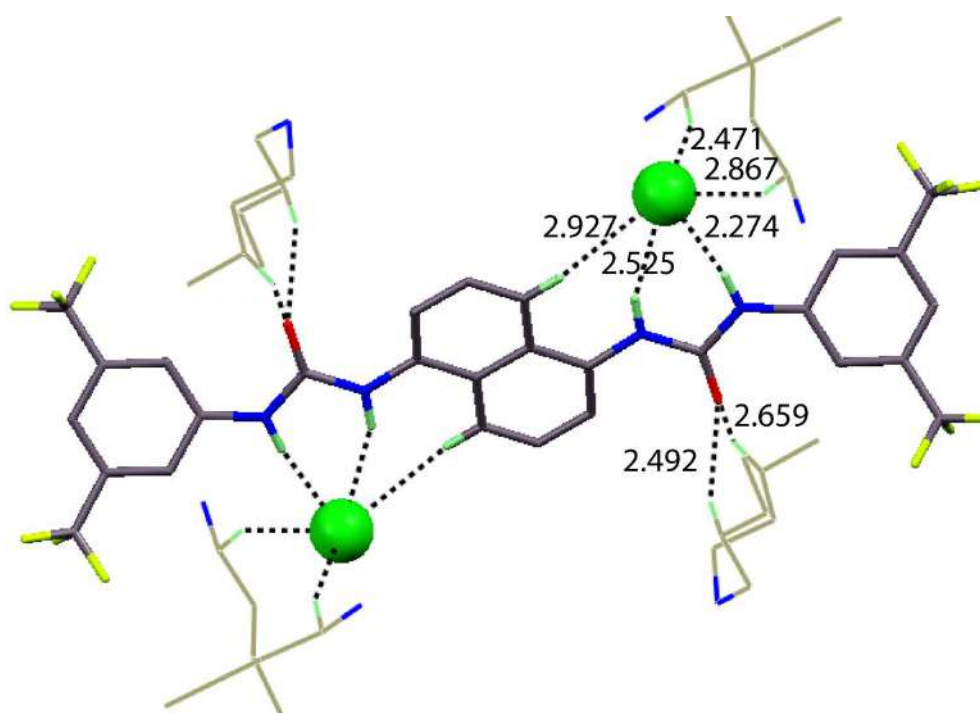


Figure A3.6 complex **4a** showing coordination environment of anion as well as extra stabilization through two C-H_{aliphatic}...O_{urea} interaction with proper distances in Angstrom.

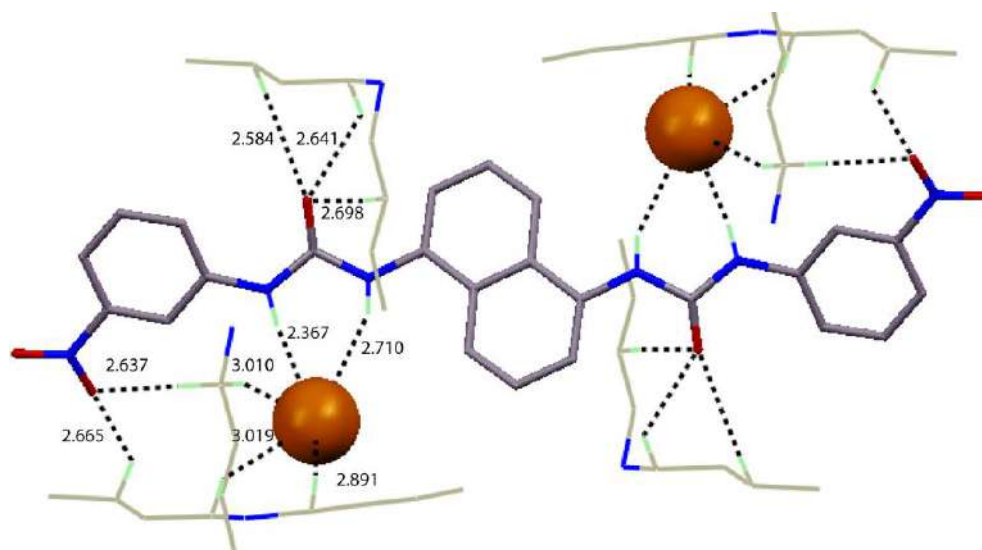


Figure A3.7 X-ray structure analysis of complex **3b** showing coordination environment of anion as well as extra stabilization through three C-H_{aliphatic}...O_{urea}, two C-H_{aliphatic}...O interaction involving one oxygen atom of substituted NO₂ group with proper bond distances in Angstrom.

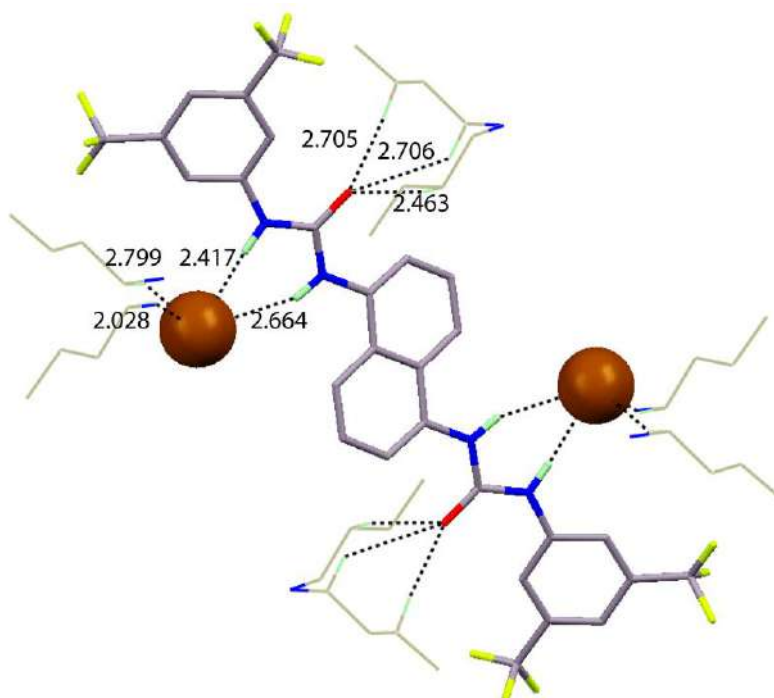


Figure A3.8 X-ray structure analysis of complex **4b** showing coordination environment of anion as well as extra stabilization through three C-H_{aliphatic}...O_{urea} interaction with proper distances in Angstrom.

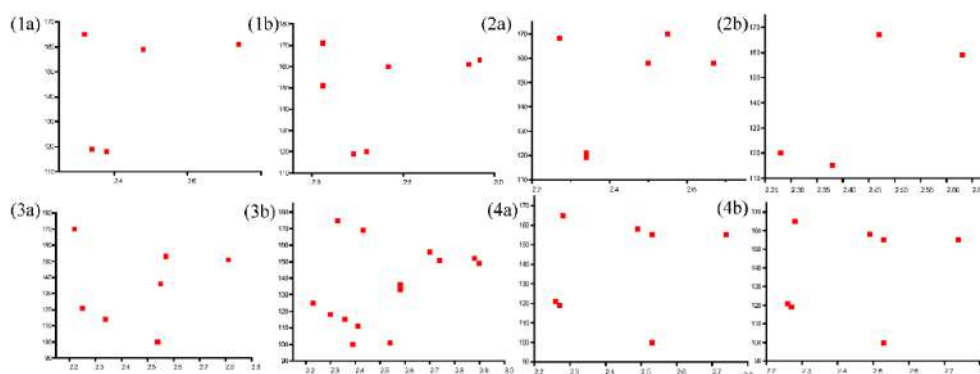


Figure A3.9 The scatters plot of N–H···A angle vs. H···A distance of the hydrogen bonds in the complexes (1a, 1b, 2a, 2b, 3a, 3b, 4a and 4b).

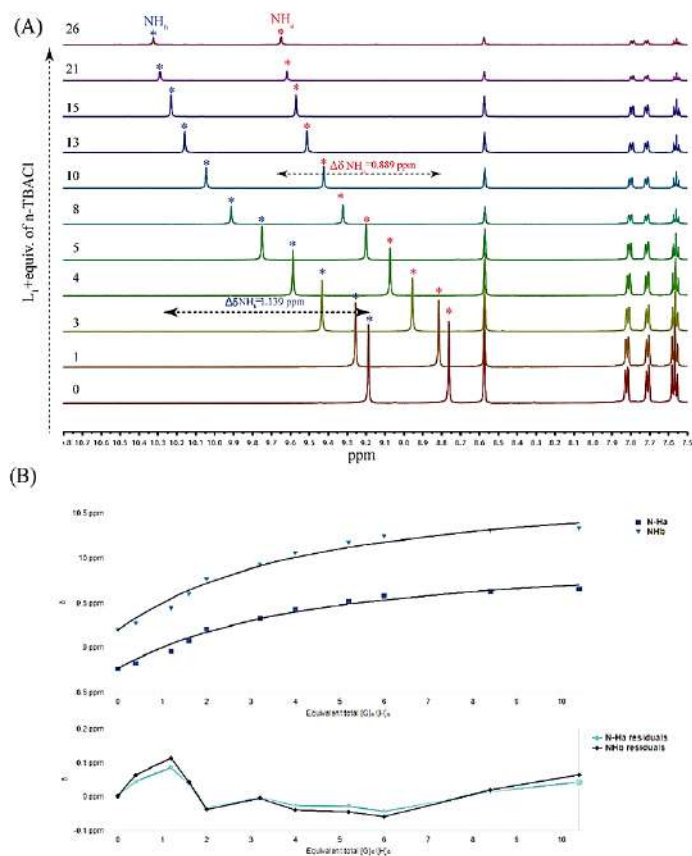


Figure A3.10 (A) Expanded partial ^1H NMR spectra of L_1 upon titration with $n\text{-TBACl}$ in DMSO-d_6 . (B) Showing the raw vs. fitted data (fitted to 1:1 NMR binding data) (top) and the corresponding residual plot (bottom). Binding constant (K) = 24.36 M^{-1} (Ref. 3.25) (<http://app.supramolecular.org/bindfit/view/a04aa7b4-1b10-4ec4-b62a-004488bc153d>)

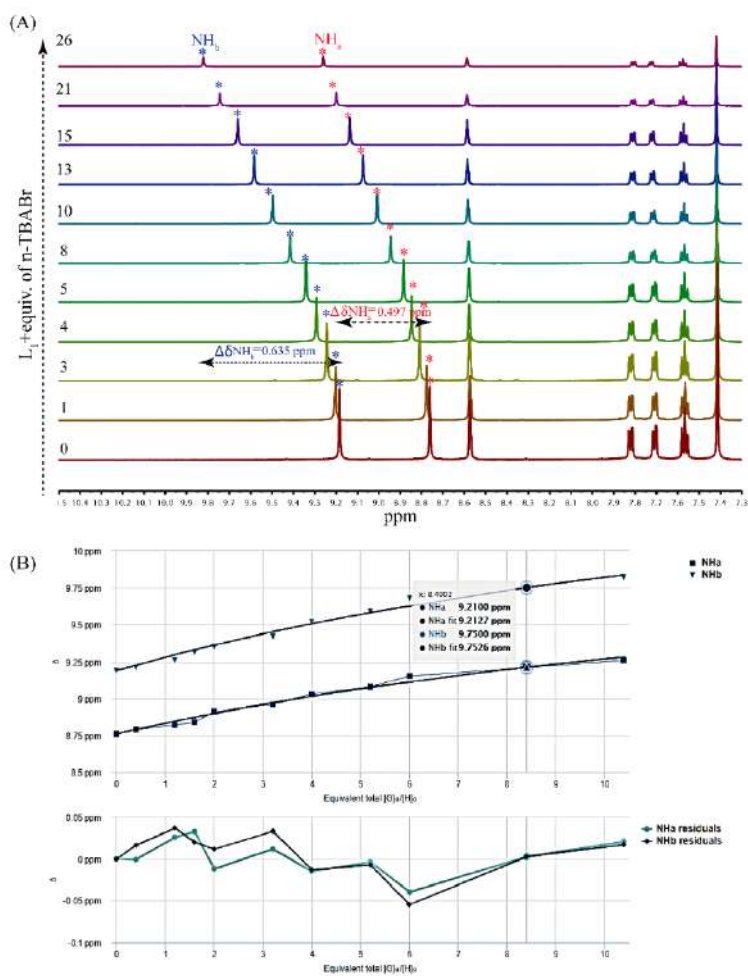


Figure A3.11(A) Expanded partial ^1H NMR spectra of L_1 upon titration with $n\text{-TBABr}$ in DMSO-d_6 . (B) Showing the raw vs. fitted data (fitted to 1:1 NMR binding data) (top) and the corresponding residual plot (bottom). Binding constant (K) = 2.85 M^{-1} (Ref 3.25). (<http://app.supramolecular.org/bindfit/view/2f704e70-704c-4c4a-b586-861ec75747dc>)

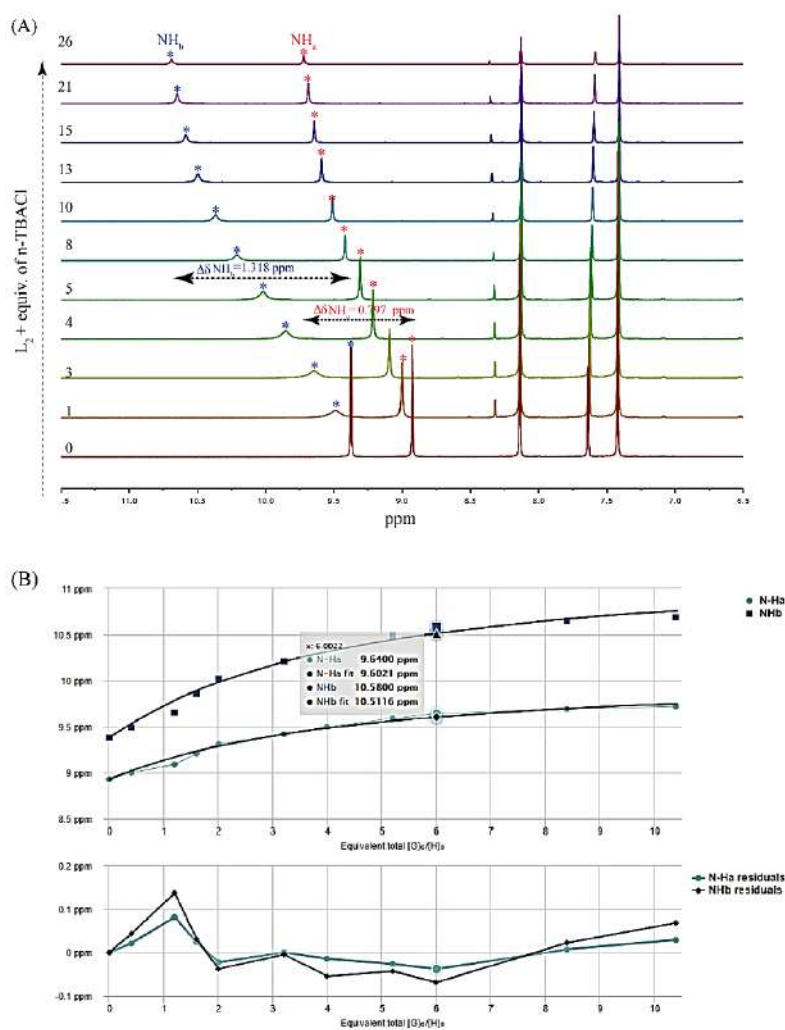


Figure A3.12(A) Expanded partial ^1H NMR spectra of L_2 upon titration with n-TBACl in DMSO-d_6 . (B) Showing the raw vs. fitted data (fitted to 1:1 NMR binding data) (top) and the corresponding residual plot (bottom). Binding constant (K) = 24.43 M^{-1} (Ref 3.25). (<http://app.supramolecular.org/bindfit/view/ee741007-4a26-4279-9860-6c57eaca46fb>)

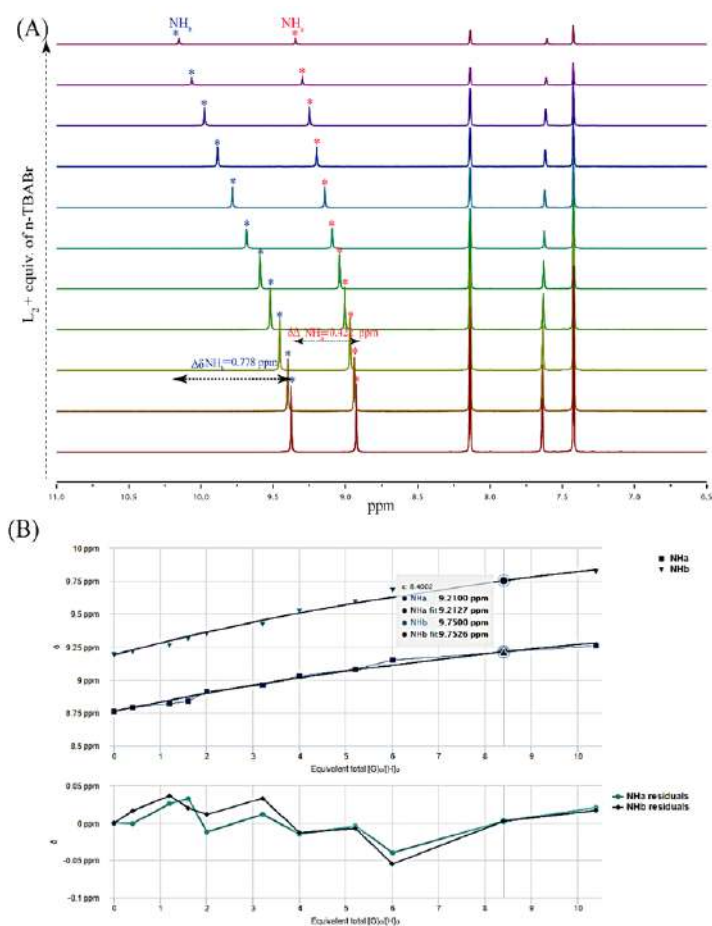


Figure A3.13(A) (A) Expanded partial ^1H NMR spectra of L_2 upon titration with n-TBABr in DMSO- d_6 . (B) Showing the raw vs. fitted data (fitted to 1:1 NMR binding data) (top) and the corresponding residual plot (bottom). Binding constant (K) = 2.72 M^{-1} (Ref 3.25). (<http://app.supramolecular.org/bindfit/view/c24e85bf-7407-49e2-87cb-19270479e6fd>)

Table A3.1 Crystallographic parameters and refinement details of anion complexes of receptors **L1- L4**

Parameters	1a	1b	2a	2b	3a	3b	4a	4b
Formula	C ₅₂ H ₈₈ Cl ₂ N ₈ O ₆	C ₅₂ H ₉₂ Br ₂ N ₈ O ₈	C ₅₆ H ₈₈ Cl ₂ F ₁₂ N ₆ O ₃	C ₅₆ H ₈₆ Br ₂ F ₁₂ N ₆ O ₂	C ₅₆ H ₉₀ Cl ₂ N ₈ O ₆	C ₅₆ H ₉₀ Br ₂ N ₈ O ₆	C ₆₀ H ₉₀ N ₆ F ₁₂ Cl ₂ O ₃	C ₆₀ H ₉₀ N ₆ F ₁₂ Br ₂ O ₃
Fw	992.20	1117.14	1192.21	1263.11	1042.26	1131.16	1242.26	1331.16
Crystal system	monoclinic	monoclinic	monoclinic	triclinic	triclinic	triclinic	Monoclinic	monoclinic
Space group	<i>P</i> 21/ <i>c</i>	<i>P</i> 21/ <i>c</i>	<i>C</i> 2/ <i>c</i>	<i>P</i> -1	<i>P</i> -1	<i>P</i> -1	<i>C</i> 2/ <i>c</i>	<i>C</i> 2/ <i>c</i>
a/Å	10.125(9)	16.393(9)	38.195(3)	9.143(7)	8.517(7)	8.647(7)	40.030(2)	39.833(18)
b/Å	15.271(13)	11.487(5)	8.7032(7)	13.492(14)	10.178(5)	10.270(9)	8.676(6)	8.844(4)
c/Å	18.764(2)	16.227(13)	19.5870(17)	14.1248(16)		18.554(9)	19.164(14)	19.364(8)
					8.6475(10)			
α/°	90.00	90.00	90.00	72.228(9)	95.052(4)	94.548(5)	90.0	90.00
β/°	91.183(8)	92.402(7)	90.426(9)	72.109(9)	90.100(5)	90.103(5)	92.331	93.005
γ/°	90.00	90.00	90.00	85.995(8)	112.025(6)	111.809(7)	90.0	90.00
V/Å ³	2900.7(5)	3053.3(3)	6510.9(9)	1578.6(3)	1491.76(17)	1524.4(2)	6650.5(8)	6813.1(5)
Z	2	2	4	1	1	1	4	4
D _c /g cm ⁻³	1.136	1.215	1.214	1.329	1.160	1.232	1.239	1.296
μ Mo K _α /mm ⁻¹	0.163	1.380	0.117	1.362	0.161	1.381	0.176	1.267
F000	904	1256	2520	658	564.0	600	2624.0	2768.0
T/K	298(2)	298(2)	298(2)	298(2)	298(2)	298(2)	298(2)	298(2)
θ max.	24.995	25.000	25.046	25.000	28.873	25.046	25.000	28.940
Total no. of reflections	10732	10042	7469	10471	11303	10092	12245	13986
Independent reflections	5100	5334	4554	5443	6780	5401	5857	7799
Observed reflections	2027	1875	3908	3598	4111	3898	3218	3658
Parameters refined	312	324	361	356	330	329	379	379
R ₁ , I > 2σ(I)	0.0887	0.0840	0.0913	0.0672	0.0624	0.0489	0.0891	0.0792
wR ₂ , I > 2σ(I)	0.1755	0.1887	0.1783	0.1189	0.1859	0.0701	0.1820	0.2283
GOF (F ²)	1.087	0.971	1.188	0.898	0.978	1.188	1.236	0.932
CCDC No.	1937116	1937113	1937114	1937117	1937120	1937119	1937118	1937115

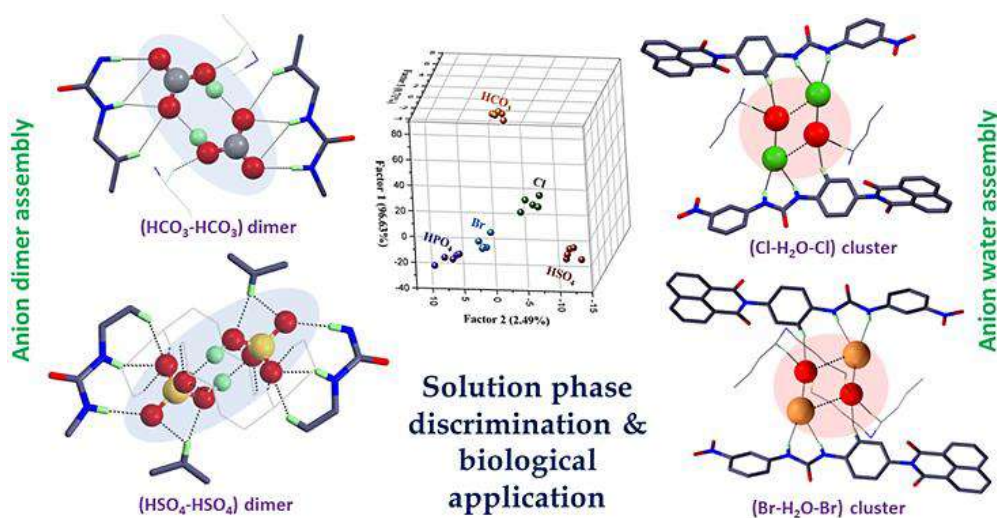
Table A3.2 Details of Hydrogen Bonding contacts in the anion complexes of receptors L1-L2

Complex	D-H...A	d(D...H)/Å	d(H...A)/Å	d(D...A)/Å	∠ D-H...A/°	Symmetry codes
1a	N2-H2N...C11	0.86	2.48	3.299(5)	159	1-x,1/2+y,1/2-z
	N3-H3N...C11	0.86	2.32	3.159(5)	165	1-x,1/2+y,1/2-z
	C6-H6...O3	0.93	2.34	2.901(9)	119	x, y, z
	C10-H10...O3	0.93	2.38	2.934(9)	118	x, y, z
	C16-H16B...O1	0.97	2.61	3.515(1)	154	x, y, z
	C15-H15A...C11	0.97	2.92	3.861(7)	163	x, y, z
	C11-H11A...C11	0.97	2.74	3.669(7)	161	x, y, z
	C20-H20B...C11	0.97	2.89	3.748(8)	147	x, y, z
1b	N2-H2N...Br1	0.86	2.06	3.838(6)	151	-x,1-y,-z
	N3-H3N...O4	0.86	2.05	2.898(8)	170	1-x,1-y,-z
	C4-H4...Br1	0.93	2.86	3.753(8)	161	x,y,z
	C6-H6...O3	0.93	2.23	2.798(8)	119	x,y,z
	C10-H10...O3	0.93	2.29	2.867(9)	119	x,y,z
	C18-H18A...O3	0.97	2.42	3.348(10)	161	x,-1+y,z
	O4-H4A...Br1	0.85	2.70	3.413(7)	143	x,y,z
	O4-H4B...Br1	0.85	2.37	3.206(6)	167	1-x,1-y,-z
	C18-H18B...Br1	0.97	2.92	3.851(10)	162	x,y,z
2a	N1-H1...C11	0.86	2.27	3.115(6)	168	x,y,z
	N2-H2...C11	0.86	2.50	3.317(6)	158	x,y,z
	C8-H8...O1	0.93	2.34	2.908(7)	119	x,y,z
	C12-H12...O1	0.93	2.34	2.929(7)	121	x,y,z
	C14-H14B...O1	0.97	2.55	3.510(8)	170	x,1-y,1/2+z
	C24-H24A...C11	0.97	2.67	3.589(6)	158	x,y,z
2b	N1-H1N...Br1	0.86	2.63	3.441(4)	159	x,y,z
	N2-H2N...Br1	0.86	2.47	3.312(4)	167	x,y,z
	C6-H6...O1	0.93	2.28	2.855(6)	120	x,y,z
	C11-H11...O1	0.93	2.38	2.894(6)	115	x,y,z
3a	N1-H1N...C11	0.86	2.57	3.360(2)	153	x,y,z
	N2-H2N...C11	0.86	2.22	3.076(2)	170	x,y,z
	C4-H4...O1	0.93	2.25	2.850(3)	121	x,y,z
	C9-H9...O1	0.93	2.34	2.854(3)	114	x,y,z
	C11-H11...N1	0.93	2.54	2.850(3)	100	1-x,1-y,1-z
	C14-H14A...O1	0.97	2.55	3.318(4)	136	x,y,z

	C20-H20B...C11	0.97	2.81	3.691(4)	152	x,-1+y,z
3b	N2-H2N...Br1	0.86	2.36	2.367(4)	173	1+x,1+y,z
	N3-H3N... Br1	0.86	2.70	2.709(5)	154	1+x,1+y,z
	C16-H16...Br1	0.97	2.89	3.767(3)	150	1+x, y, z
	C22-H22B...O3	0.97	2.58	2.584(2)	134	x, y, z
	C22-H22A...O2	0.97	2.66	3.334(5)	126	x, y, z
	C23-H23A...O1	0.97	2.66	3.534(3)	149	x, y, z
	C24-H24A...O3	0.97	2.64	3.394(4)	134	x, y, z
	C27-H27A...O3	0.97	2.69	3.666(4)	175	x, y, z
	C28-H28A...O2	0.97	2.63	3.522(4)	151	x, y, z
4a	N1-H1N...C11	0.86	2.28	3.115(4)	165	x,y,z
	N2-H2N...C11	0.86	2.53	3.326(4)	155	x,y,z
	C7-H7...O1	0.93	2.27	2.835(6)	119	x,y,z
	C11-H11...O1	0.93	2.26	2.852(6)	121	x,y,z
	C13-H13...N2	0.93	2.53	2.841(5)	100	-x,1-y,-z
	C17-H17A...O1	0.97	2.49	3.414(6)	158	x,1-y,1/2+z
	C22-H22B...C11	0.97	2.74	3.642(5)	155	x,y,z
4b	N10-H10N...Br1	0.86	2.67	3.472(4)	157	x,y,z
	N17-H17N...Br1	0.86	2.42	3.258(4)	166	x,y,z
	C5-H5...O25	0.93	2.29	2.856(7)	119	x,y,z
	C24-H24...O25	0.93	2.26	2.851(8)	121	x,y,z
	C28-H28B...O25	0.97	2.47	3.390(9)	159	x,1-y,1/2+z
	C29-H29A...Br(1)	0.97	2.93	3.803(6)	151	x,1+y,z
	C35-H35A...Br(1)	0.97	2.80	3.702(6)	155	x,y,z
	C57-H57...N10	0.93	2.53	2.841(7)	100	x,y,z

Chapter 4

Centro-Symmetric Dimeric Oxyanion Assembly Supported by multi-arm Hydrogen Bonds (HBs): A Case Study in Linear Discriminant Analysis and as Antibacterial Agents

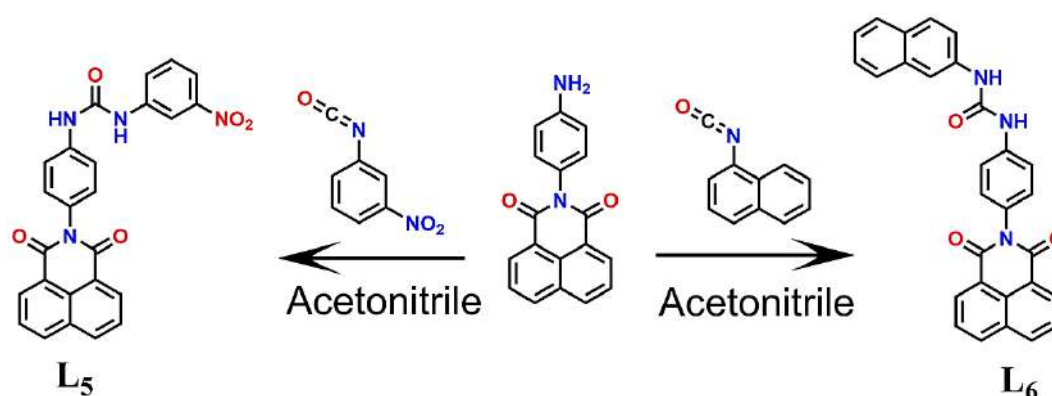


4.1 Background and Focus of the Chapter

In recent years, anion recognition *via* the formation of the self-assembled architecture of neutral hosts has turned into an emerging discipline in supramolecular chemistry due to its significant impact on the environment and therapeutics along with vast application in the field of membrane transport, molecular sensing, catalysis and so on.^{4.1-4.3} Among the interactions involved in the anion recognition, hydrogen bonding plays an important role due to its high strength. It has always been challenging to capture the biologically important oxyanions (e.g. bicarbonate, bisphosphate, and bisulphate) for their high solvation enthalpies (e.g., ΔG_{hyd} of H_2PO_4^- , SO_4^{2-} , and CO_3^{2-} , are -465, -1080, and -1315 kJ mol^{-1} , respectively) and their complicated geometries. It has been suggested that urea- or thiourea-based neutral receptors can form chelated complexes with spherical anions through classical and non-classical bifurcated H-bonding with high directionality. Nowadays, anthropogenic activities such as heavy use of fossil fuels and industrial agriculture are known to cause the release of a high level of carbon dioxide (CO_2) into the atmosphere.^{4.4} So, eventually, the efficient entrapment and activation of CO_2 as bicarbonate anion, using neutral synthetic receptors, has an impactful demand in the fixation of the environmental CO_2 .^{4.5} On the other hand, tetrahedral sulphate (SO_4^{2-}) anions have adverse effects on the nuclear waste recovery process, while eutrophication, etc., is responsible for the accumulation of tetrahedral phosphate anions in aquatic habitats.^{4.6} Bisulphates also are known to affect human health by causing breathing difficulties, burning pain in the mouth, chest pain, burning of the oesophagus, diarrhoea etc. To date, various neutral, and protonated anion receptors, having multiple NH units, have been reported with topological complementarities in their molecular assemblies.^{4.7-4.9} In this regard, tactically synthesized urea-derived polytopic neutral receptors seem to be potentially significant to the researchers for complete encapsulation or trapping of monomeric, dimeric, or polymeric oxyanions. In the area of supramolecular chemistry, of late, the roles of hydrogen bonds (HBs), which facilitate favourable hydrogen bonds between anions, have gained much attention. It is believed that both the hydrogen bonding interactions inside the dimeric assembly and the attractive interaction between the host and guest molecules overcome the repulsive force between the anion-anion dimer. This mechanism imparts a substantial impact to form stable dimers in solid-state.^{4.10}

In our continuing effort to encapsulate anion/hydrated anion assembly by urea-based receptors^{4.11-4.14} herein, we report two naphthalimide based linear monourea receptors (**L**₅ and **L**₆) (Scheme 4.1) which exhibit anion (oxyanions and halides) binding ability in solid- and solution-states. **L**₅ could render fluoride/hydroxide-induced aerial CO_2 fixation and form a cylindrical dimer assembly of the anion with $\text{R}_2^2(8)$ arrangement. The assembly of anion is

stabilized *via* short-range hydrogen bonding characterised as hydrogen bonds (HBs) in solid-state. Besides, HBs based cyclic dimeric assembly of bisulphate anion sealed by the linear tetrameric assembly of host molecule was also evidenced from solid-state architecture. Upon addition of excess chloride and bromide anion, **L**₅ linearly assembled to capture a cyclic chloride-water and bromide-water tetrameric cluster backed up by various solid-state H-bonding interactions. The ligands (**L**₅ and **L**₆) were capable of discriminating five relevant anions with 100% classification accuracy in aqueous media based on multivariate pattern analysis. Interestingly, the ligands **L**₅ and **L**₆ displayed notable bactericidal activity against the Gram-ve pathogen *E. coli* MTCC 433 and were non-toxic to cultured human embryonic kidney (HEK 293) cells.



Scheme 4.1 Chemical structures of the receptors **L**₅ and **L**₆.

4.2 Structural aspects of anion binding with **L**₅-**L**₆

An appropriate receptor to coordinate with the anionic species of various dimensions, it should, in principle, hold a particular supramolecular architecture comprising directional hydrogen-bond donors organized on a proper platform/framework. Introducing nitrophenyl (**L**₅) (electron-deficient) and naphthyl (**L**₆) (electron-rich) substituents to the core of the urea functionality, we have generated diversity in electronic properties as well as hydrophobicity of these receptors. Both the receptors **L**₅ and **L**₆ consist of urea -NH donor sites which can receive guests of different charges and sizes *via* the formation of cooperative/non-cooperative host-guest assemblies despite having a linear, rigid molecular framework. Here, receptor **L**₅ was purposefully decorated with a -NO₂ group with a strong -I effect to impart greater acidity to the urea NH protons. However, in receptor **L**₆, the acidic nature of the NH protons was sufficiently reduced, compared to **L**₅, by replacing the nitrophenyl unit with the naphthyl group. Unfortunately, we failed to obtain solid-state crystal structures for **L**₆ despite many careful attempts. From the crystal structure analysis of **L**₅, it was clear that two symmetry-equivalent DMSO molecules were encapsulated inside the hexamer cleft (average terminal aromatic

centroid distance of 12.802 Å) of six inverse symmetric receptor molecules through twelve hydrogen bonding interactions (**Fig. 4.1a**). Out of these interactions, four are strong bifurcated urea N–H···O_{DMSO} (with a mean donor-to-acceptor distance of 2.840 Å), the other four are intermolecular C–H···O_{NO₂/NAP} (with a mean donor-to-acceptor distance of 2.585 Å) and the rest are two weak C–H···π interactions (with a mean distance of 3.653 Å). Each penta-coordinated DMSO molecule gained stabilization by forming a stable 3:1 guest: solvent model evidenced from the solid-state crystal structure. The dihedral angle between the central aromatic unit and the terminal naphthalimide/meta-nitro phenyl moieties was found to be 78.21°/23.04° for the free receptor molecule. It was also evident that the receptor molecule adjusts opposite orientation with respect to each other to favour various cooperative interactions with the host molecules. In this context, Table 4.1 summarises the results of SC-XRD analysis of oxyanion and halide complexes of neutral monourea receptors, **L₅** and **L₆**.

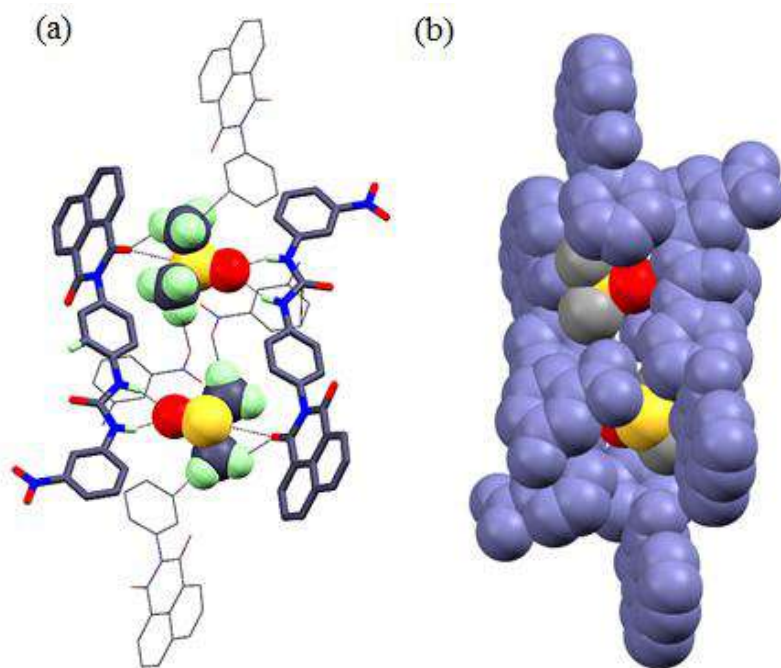


Figure 4.1 X-ray (partial) structures representing (a) various C–H···O, N–H···O and C–H···π interactions in DMSO-solvated receptor **L₅** and (b) Encapsulation of solvent molecule by hexameric receptors assembly.

4.2.1 Solid-state evidence of HBs based anion···anion dimer formation

The single-crystal structure of the anion-anion dimers is well known in solid-state chemistry for a long time. The negatively charged pole of the dimeric assembly should satisfy all the electrostatic interactions involved in the formation of HBs. The O_{donor}···O_{acceptor} distance falls in the narrow range of 1.52–3.04 Å.^{4,15} A closer examination indicated that the shortest O···O contact was found to be 2.681 Å for the bicarbonate dimer (Fig. 4.2a) while the longest contact was observed for bisulphate dimer with a value of 2.911 Å (Fig.4.2b) which was almost similar

to, or marginally shorter than the O...O distances observed in the carboxylic acid dimer. Indeed, there is no noticeable connection between acidity and contact distance generally.

Table 4.1 Key observations on halide- and oxyanion-binding of receptors L_5 and L_6

Anions (Size and Shape)	Neutral receptor–anion complexes	Mode of binding and conformation of the receptor	Observation	
Oxyanions	Planar bicarbonate (HCO_3^-)	Consistent and conventional homodimer of planar HCO_3^- anion entrapped within a linear association of L_5 (complex 5a) insisted <i>via</i> atmospheric CO_2 fixation	Self-complementary and linear (the average terminal aromatic centroid distance 13.004 Å) arrangement for L_5	The ability to form various types of H-bonding interactions (HBs for oxyanions) depends on the electronic effects associated with the terminal aromatic substituents of the receptors.
	Tetrahedral bisulphate (HSO_4^-)	Familiar inter-ionic assembly of tetrahedral HSO_4^- ion sealed by tetrameric linear encapsulation of L_5 (complex 5b)	Self-assembled and linear (the average terminal aromatic centroid distance 12.987 Å) for L_5	
Halides	Spherical chloride (Cl^-)	A stable tri-coordinated cyclic chloride-water cluster of L_5 forming 1:1 guest-host entrapped complex (5c)	Cooperative and pillar (average terminal centroid distance of 12.960 Å in L_5)	
	Spherical bromide (Br^-)	Monomeric tri/polymeric hexa-coordinated hydrated bromide/ bromide-entrapped complexes (5d) and (6d) of L_5 and L_6 respectively	Cooperative (the average terminal centroid distance of 12.973 Å) for L_5 and non-cooperative for L_6 (average terminal centroid distance of 13.551 Å)	

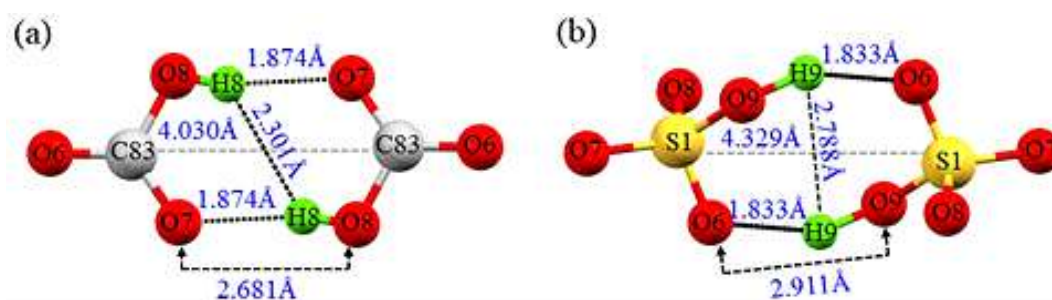


Figure 4.2 HBs contacts in (a) bicarbonate and (b) bisulphate dimer (magnified view of intra-hydrogen bonding).

The planar HCO_3^- ion, being less acidic ($\text{pK}_a \sim 10.3$) exhibited the shortest O...O contact leading to slightly stronger interactions as compared to more acidic HSO_4^- ion ($\text{pK}_a \sim 1.9$)^{4,16}. But one could expect that the acidic moieties (i.e. greatest hydrogen bond donors) would establish the shortest interactions in general. In reality, the poor basicity ($\text{pK}_b \sim 17$) of HSO_4^- ion makes it a poorer H-bond acceptor which leads to forming longer hydrogen bond interaction compared to bicarbonate ion. Additionally, the $\text{C83}\cdots\text{C83}$ (smaller in size) distance in the bicarbonate dimer was found to be 4.030 Å but in the case of bisulphate anion, the $\text{S1}\cdots\text{S1}$

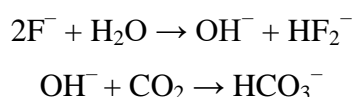
(larger in size) distance has a value of 4.329 Å. Based on the above crystallographic data, it may be assumed that the relatively planar association of bicarbonate dimer acquires more perfect centrosymmetric assembly while the tetrahedral bisulphate dimer remains a little distorted or tilted as evidenced from the (solid-state) structure of the crystal.

4.2.2 Structural analysis of anion bound complexes of receptors **L₅** and **L₆**

Single-crystal XRD analyses of receptor-bound neutral complexes and consistent as well as discriminating binding behavior of receptors toward di-anionic associations or hydrated-anions of varied shapes are heavily reliant on either the effect of terminal functionalization of the mono-podal receptors or the size of anionic guests.

4.2.2.1 A comparative structural analysis of complexes **5a** and **5b**

The encapsulation of individual bicarbonate or bisulphate ions are broadly discussed in MOF based cage but an encapsulation of dimeric assembly by synthetic receptors provide sufficient space for di- anions in both acidic and neutral form, are scantily reported. So, in this context, we have a good opportunity to investigate the production of hybrid anion–anion clusters utilizing hydrogen sulphate or bicarbonate molecules. The brown coloured **L₅**. F/OH⁻ DMSO/DMF solution was kept in the open air for a few days and as a consequence of exposure of the mother solution in the open-air condition resulted in the formation of [HCO₃⋯HCO₃]²⁻ dimer-sealed 1:1 host-guest assembly of receptor **L₅**. The process involves spontaneous fixation of aerial CO₂ near to the air/solvent interface as bicarbonate anion maintaining the following simple mechanism,



This is not unusual in literature and has already been reported by Gale and *et. al.*^{4.17, 4.18} and Ghosh *et al.*^{4.19} and from our group.^{4.20} R₂²(8) arrangement of [HSO₄⋯HSO₄]²⁻ dimer (between pairs of 2⁻ anions) i.e. complex **5b** (achieved from monovalent tetrahedral HSO₄⁻ anions) was obtained from colourless **L₅**.HSO₄ DMSO solution after keeping the mother liquor for several days in an open-air system. X-ray analysis suggested that the asymmetric unit of **5a** have one **L₅** receptor unit, one guest anion (HCO₃⁻) and its relevant counter cation (*n*-TBA⁺). The dimer was trapped inside the dimeric void of the two receptor units enclosed by the hydrophobic atmosphere of two external tetrabutylammonium cations constructing an overall 2:2:2 binding stoichiometry. But in the case of **5b**, the asymmetric unit contained one **L₅** receptor moiety, one guest anion (HSO₄⁻) and corresponding counter cation (*n*-TBA⁺).

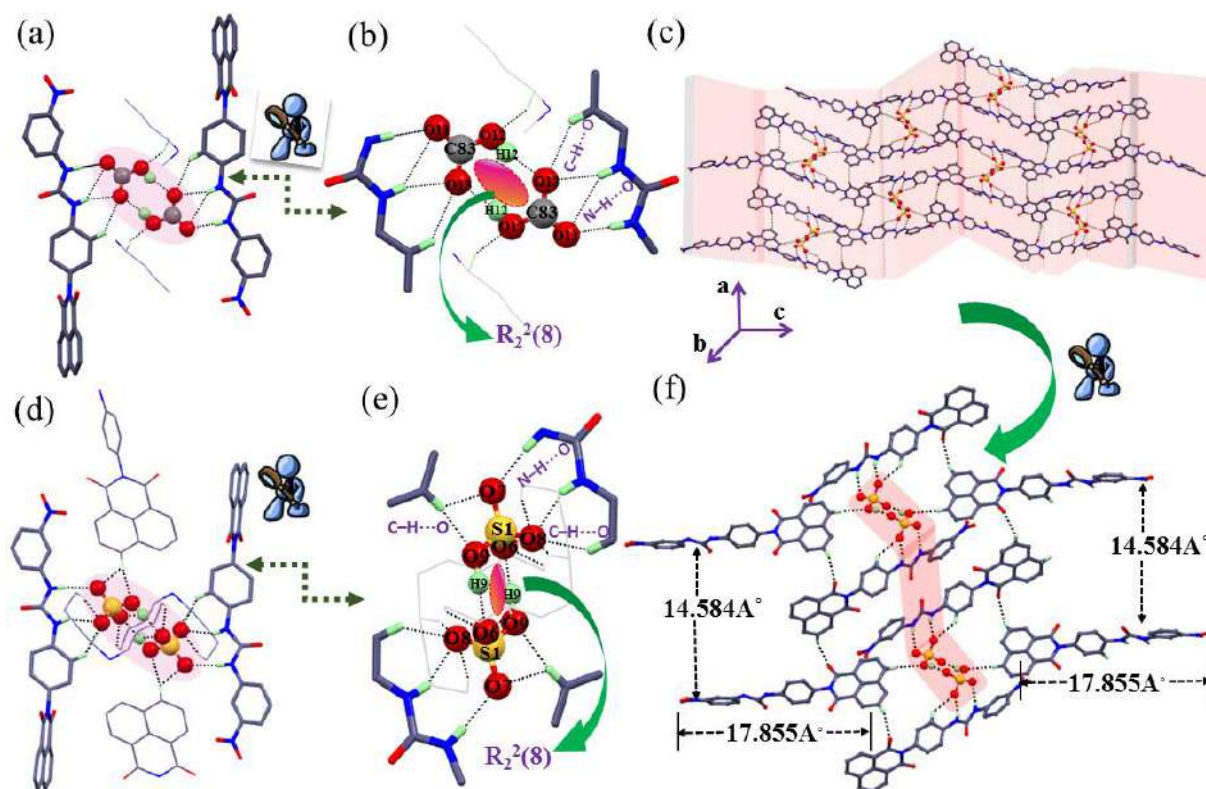


Figure 4.3 (a) H-bonded dimer bicarbonate assembly (**5a**) supported by *n*-TBA cations; (b) $R_2^2(8)$ arrangement of $(\text{HCO}_3)_2$ in complex **5a**; (c) ‘open book’ like a polymeric extension of the complex **5b**; (d) H-bonded $(\text{HSO}_4)_2$ assembly in complex **5b**; (e) $(\text{HSO}_4)_2$ dimer adopting ‘cylindrical assembly and (f) polymeric framework of the complex **5b** with relevant polymeric distances.

The homodimer was embedded inside the tetrameric assembly of the receptor molecules surrounded by two exterior tetrabutylammonium cations making an overall 2:4:2 binding stoichiometry. Presumably, due to the planar organization of the bicarbonate anion in the dimeric association, the receptor molecule does not undergo any structural variation in solid-state architecture. But for **5b**, a slightly distorted arrangement of tetrahedral bisulphate anion in the dimeric entity forces the receptor molecule to adopt a bent orientation to facilitate the formation of the complex. In both cases, the NO_2 group present at the terminal aromatic unit remains anti oriented relative to the urea moiety in the free receptor molecule, but the same rotate to a *cis*-position upon complexation with subjected anions (HCO_3^- , HSO_4^-) to facilitate various types of favourable non-covalent interactions. Crystal structure elucidation revealed that for both complexes, two symmetry-identical anions are dimerized via hydrogen bonding interactions (HBs) with a close donor and acceptor oxygen ($\text{O}\cdots\text{O}$) distance of 2.681 Å (bicarbonate dimer) and 2.911 Å (bisulphate dimer), within the range observed for other bicarbonate/bisulphate dimers that are already well known in the literature. Detailed investigation of the crystal structure of **5a** revealed that linear entrapment of cylindrical shaped

(HCO₃)₂ dimeric capsules was stabilized via participation of a total of twelve C–H···O and N–H···O type effective and strong hydrogen-bonding interactions. Out of these, four are strong trifurcated N–H_{urea}···O_{bicarbonate} interactions with a mean donor-to-acceptor distance of 2.038 Å, two are effective C–H_{ortho-aryl}···O_{bicarbonate} connections with a mean donor-to-acceptor distance of 2.574 Å and the rest two are moderate C–H_{TBA}···O_{bicarbonate} contacts having an average distance of 2.503 Å (Fig. 4.3a). Each of the symmetrically identical bi-carbonate anion in the dimeric assembly is coordinated via three strong trifurcated N–H_{urea}···O_{bicarbonate}, two strong self-complementary intermolecular O–H···O and two moderate C–H···O H-bonding interactions satisfying a coordination number of seven each (Fig. 4.3b). Interestingly, after a detailed study of complex **5b**, it was observed that the two symmetry-identical (HSO₄)₂ anions reside inside the tetrameric linear association of the receptor molecules where the dimeric association of such large tetrahedral anions is stabilized by a total number of twenty N–H_{urea}···O_{bisulphate} and C–H_{ortho-aryl}···O_{bisulphate} type cooperative H-bond and electrostatic interactions. These kinds of noncovalent interactions overcome the anion-anion repulsive interactions between the dimer and make them suitable inside the cavity, which stabilizes the dimer by a total number of twenty N–H_{urea}···O and C–H_{ortho-aryl}···O_{bisulphate} type cooperative hydrogen-bonding interactions. A detailed investigation suggested that the linear entrapment of the di-anions was backed up by the involvement of four strong N–H_{urea}···O_{bisulphate} interactions possessing a mean donor-to-acceptor distance of 2.094 Å, six effective C–H_{ortho-aryl}···O_{bisulphate} contacts with a mean donor-to-acceptor distance of 2.412 Å, eight moderate C–H_{TBA}···O_{bisulphate} contacts having an average distance of 2.554 Å (Fig. 4.3d). Interestingly, upon two-dimensional extension of the dimeric unit, it adopted an open book-like polymeric framework (Fig. 4.3c, f). Moreover, the formation of supramolecular network encouraged by anion-anion association is quite rare and only a few are reported. Previously, Flood has discovered such anion-anion dimer induced polymers by phosphate monomer where the cyanostar macrocycle stabilized each of the anion^{4.21-4.22}. An individual unit of bisulphate ion in the dimeric assembly is showing a coordination number of 11 with two urea –NH, three aromatic C–H, four aliphatic C–H and two self-complementary O–H (in dimeric unit) interactions (Fig. 4.3e). Like **5a**, the bisulphate dimer (complex **5b**) was also stabilized through various weak C–H···O[–] type effective interactions originating from *n*-TBA cations and naphthalimide units (Fig. A4.1a-A4.2a). The function of naphthalimide units present in the receptor **L**₅ could be justified based on the crystal structure of the complex and free receptor. In both cases, the X-ray analysis disclosed that the inter-anionic complexes (**5a**, **5b**) are endowed with a pair of self-complementary face-to-face electrostatic hydrogen bonds with an

average O–H···O[−] contact distance of 1.874 and 1.833 Å for bicarbonate and bisulphate anion, respectively.

4.2.2.2 Structural analysis of cyclic hydrated-chloride complex (**5c**)

Various entrapments or encapsulations of cyclic/acyclic halide/hydrated halide cluster $[(X^-)_2(H_2O)_2]$ ($X = F, Cl, Br$) based on various types of cooperative and non-cooperative interactions with di- or tripodal synthetic receptors have been described previously.^{4,23} But simple mono urea-based synthetic receptor (**L₅**), showing the ability to form cyclic (chloride)₂(water)₂ assembled complex (**5c**) is certainly very rare in literature. The crystal structure of **5c** involves one receptor molecule **L₅**, a chloride ion, a water molecule and an *n*-TBA⁺ in its asymmetric unit. Unlike the free receptor molecule, the NO₂ group of corresponding receptor units in complex **5c** also orient itself to a *cis* position (concerning the urea moiety) to offer various favourable cooperative hydrogen-bonding interactions to form a stable complex in the presence of receptor molecule. Detail study of the crystal structure of **5c** disclosed that two identical receptors (with two urea arms) associated in an anti-parallel fashion, enclosing two symmetry-equivalent chloride anions and two molecules of water in the crystal lattice structure. The cyclic ‘chloride-water-chloride’ cluster is stabilized by the participation of a total of ten intra as well as intermolecular hydrogen bond comprising of urea N–H, aryl C–H and water O–H interactions. Each chloride ion in the assembly is associated with two strong bifurcated N–H_{urea}···Cl[−] interactions (with a mean donor-acceptor distance of 2.452 Å), one O–H_{lattice water}···Cl[−] interaction (with a mean distance of 3.167 Å). Additionally, the hydrated chloride complex was also supported by one C–H_{TBA}···O (exterior *n*-TBA⁺) and one C–H_{ortho-aryl}···O[−] (from the adjacent symmetry-equivalent receptor) hydrogen-bonded interactions with a very strong distance of 2.481 Å and 2.497 Å respectively (Fig. 4.4a, b). The encapsulation of cyclic chloride-water-chloride assembled system inside the hydrophobic cation-enclosed milieu is shown in Fig. 4.4c. Herein, each pair of chloride-water assembly is sharing only one receptor molecule with a coordination number three for individual chloride ions. Whereas each lattice water molecule also shows a coordination number of three in the solid-state complex. The complex **5c** was also stabilized through various weak C–H···O[−] contacts supported by *n*-TBA cations and naphthalimide units in the crystal structure (Fig. A4.3a). Though the receptor **L₆** formed a complex with an excess amount of tetrabutylammonium chloride (*n*-TBACl) salt from the DMF medium, the single-crystal structure could not be solved due to the poor crystal quality.

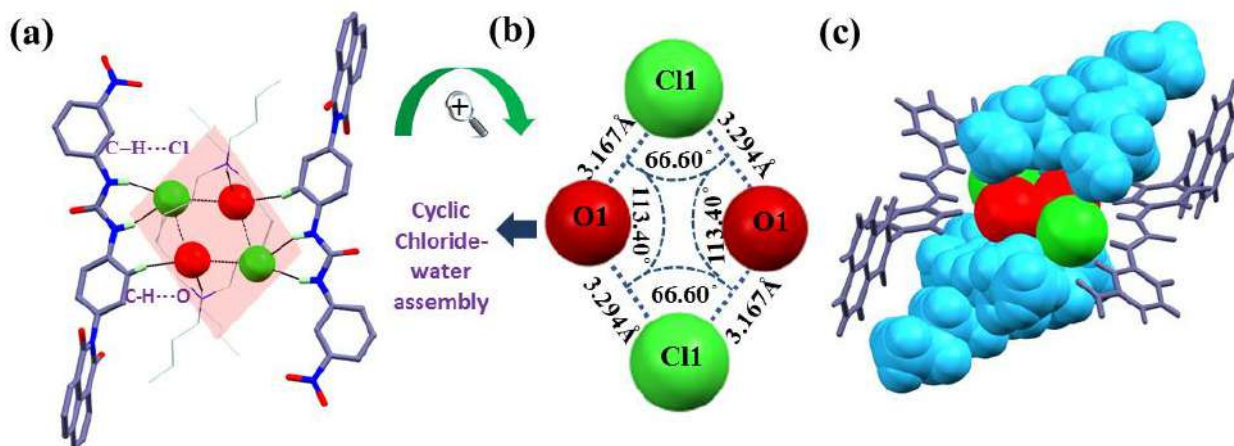


Figure 4.4 (a) Cyclic chloride-water assembly in **5c**; (b) magnified view of hydrogen bonding in the cyclic chloride-water assembly of **5c** (c) encapsulation of cyclic chloride-water assembly in the *n*-TBA cation-sealed environment.

4.2.2.3 Cooperative vs. non-cooperative binding in Bromide complexes (**5d**, **6d**)

Single crystal study revealed that in complex **5d**, the receptor **L₅** adopted a linear orientation to render a 1:1 host-guest bound cyclic bromide-water-bromide assembly through cooperative H-bonding interactions involving the urea –NH groups (of two adjacent symmetric receptors), the symmetry-equivalent bromide ions, and water molecules in the crystal lattice. As the urea group arranged in *syn*-fashion like in the free receptor (**L₅**), it was H-bonded to the same type of cyclic bromide–water clusters (Fig. 4.5d). Whereas, in complex **6d**, the receptor **L₆** produced a familiar 1:1 host-guest complex through non-cooperative interactions of urea protons leading to the formation of a one-dimensional polymeric chain of anionic association (Fig. 4.5b). For complex **5d**, the receptor-bromide cyclic association stabilized *via* involvement of strong cooperative N–H_{urea}···Br[−] bi-furcated H-bonding interaction (with a mean donor-acceptor distance of 2.553 Å) and O–H···Br[−] intramolecular H-bonding interactions (with an average distance of 3.255 Å). Interestingly oxygen atoms in water molecules formed bifurcated H-bonds with the adjacent Br1 of receptor **L₅**. This type of H-bonds within the observed average distance of 3.276 Å are very common in biological processes. Each water molecule in the assembly further stabilized the hydrated bromide cyclic complex via one C–H_{TBA}···O (exterior *n*-TBA⁺) and one C–H_{ortho-aryl}···O (from the adjacent symmetry-equivalent receptor) H-bonded interaction by maintaining a conventional H-bond with an average distance of 2.457 Å (Fig. 4.5a, d). Moreover, each bromide ion in the hydrated bromide assembly exhibited a coordination number of three, including two –NH units and one water oxygen molecule connected *via* H-bonding interactions. Various C–H···O type favourable interactions could assist in the formation of the receptor-stabilized bromide-water cluster (Fig. A4.4a).

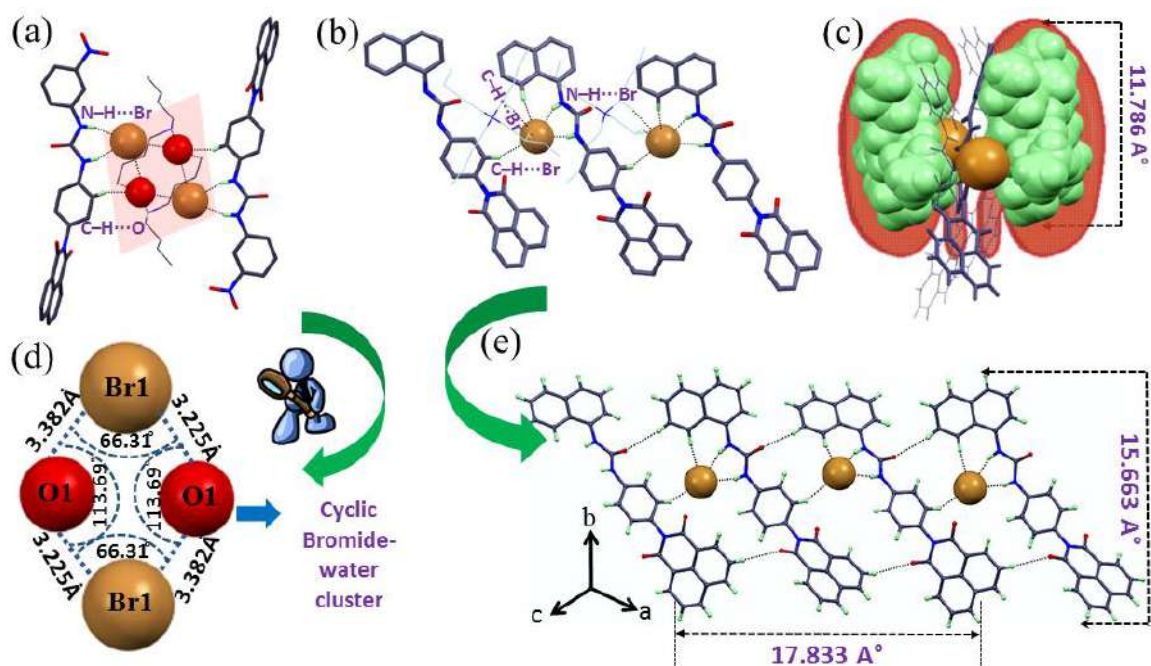


Figure 4.5 (a) Cyclic bromide-water association in **5d**; (b) non-cooperative H-bonding interactions between bromide ion and linear receptor molecule decorated with *n*-TBA cation in **6d**; (c) ‘Human-kidney’-like encapsulation of bromide ion by the hydrophobic environment of *n*-TBA cation in **6d**; (d) magnified interpretation of H-bonding interactions in cyclic bromide-water assembly of **5d** and (e) 1D polymeric chain of receptor-bromide complex (**6d**) along crystallographic *b*-axis.

Unlike complex **1d**, in complex **2d**, despite having a linear and rigid arrangement, receptor **L₂** stabilized with spherical bromide ion through the participation of two strong bifurcated N–H_{urea}···Br[−] (with a mean donor-acceptor distance of 2.528 Å), one intra/intermolecular C–H_{ortho-aryl}···Br[−] (with a mean donor-acceptor distance of 2.926 Å and 2.969 Å respectively) and four exterior C–H_{TBA}···Br[−] interactions (with a mean donor-acceptor distance of 2.962 Å) around single monovalent anion. Fig. 4.5c depicts the encapsulation of Br[−] by the hydrophobic surroundings of the organic cation, generating a ‘human-kidney’-like shaped structural design, whereas Fig. 4.5e demonstrates a chain-like polymeric anionic association of Br[−] ion, supported *via* two N–H_{urea}···Br[−] and two C–H_{aromatic}···Br[−] donor-acceptor interactions around a single spherical bromide ion within the arrays of non-cooperative host (**L₆**) assemblies.

Each bromide ion in its asymmetric motif exhibited a coordination number of six within the individual linear non-cooperative self-assemblies between host and guest. Additionally, the receptor-stabilized bromide complex was captured with the aid of four effective π–π stacking (with an average distance of 3.375 Å), four C–H···O, two C–H···π interactions (Fig. A4.5a). Unlike **L₅**, more hydrophobicity in **L₆** may be resistant to the formation of a hydrated complex with bromide ion whereas, in the case of complex **5d**, we observe a suitable hydrated bromide assembly within a self-complementary H-bonded network. However, the binding diversity of

two electrochemically different receptors **L**₅ and **L**₆ towards bromide anion may be ascribed to the electrochemical variation in their aromatic substitution, sterically less hindered urea groups of receptor **L**₅ are more exposed to provide a cooperative binding mode, while in contrary, in receptor **L**₆ the urea arms suffer more steric environment to assemble its urea -NH units for a non-cooperative binding interaction.

4.2.2.4 Effect of electronic substitution on anion coordination

Both the receptors, **L**₅ and **L**₆, supposedly possess anion-recognizing ability in solid- and solution-states through the urea -NH units *via* H-bonding interactions which, in turn, rest on the electronic nature of the substituents, which can be varied to tune the electron availability of the coordinating site of the receptors. Here, receptor **L**₅ was purposefully decorated with a -NO₂ group with a strong -I effect to impart greater acidity to the urea NH protons. So, as a result, **L**₅ exhibited multiple H-bonding contacts with the bound oxyanions (and halides) in the solid phase. However, in receptor **L**₆, the acidic nature of the NH protons was sufficiently reduced, compared to **L**₅, by replacing the nitrophenyl unit with the naphthyl group. Unfortunately, we failed to obtain solid-state crystal structures for **L**₆ with the corresponding anions (except Br⁻) despite many careful attempts.

On the contrary, the ¹H NMR studies of the solution-state interactions between either of the receptors and the anions demonstrated that, while **L**₅ showed remarkable changes in the chemical shifts of the urea -NH protons in the presence of HCO₃⁻, no significant changes were observed as such in case of **L**₆ with other anions. This bolsters the fact that in both solid- and solution-states, receptor **L**₆ did not involve any kind of major H-bonding interactions. Both the receptors formed halide- or hydrated halide-bound complexes as evident from the solid-state structures. So, the purpose of introducing different electronic environments within these receptors might be justified based on their versatile nature of coordination with the given anions.

4.2.2.5 Comparative anion interaction studies of the complexes in solution state

To obtain additional insights into the mode of the competitive binding with anions in the solution, comparative ¹H NMR studies were performed with the aforementioned ligands and the corresponding anions. As expected, in all the cases, the most acidic urea -NH protons exhibit significant downfield chemical shifts, depending on the strengths of the H-bonds between urea -NH protons and the subjected anions. The comparison among the relevant NMR spectra along with the urea -NH protons of the corresponding receptors and complexes are shown in Fig. 4.6a, b with the chemical shift values listed in Table A2. In the concentration-dependent ¹H NMR

titration, **L**₅ showed the highest (average) downfield shift ($\Delta\delta = 3.020$ ppm) in the case of -NH_a and -NH_b protons for the planar CO₃²⁻/HCO₃⁻, among the given anions (Fig A4.6). This indicated the potentially strong participation of -NH_b and -NH_a protons in bonding in the solution-state. The receptor-anion association is efficiently stabilised in the solid-state by various types of effective non-covalent interactions while the receptor and anions have much looser orientations in the solution phase.

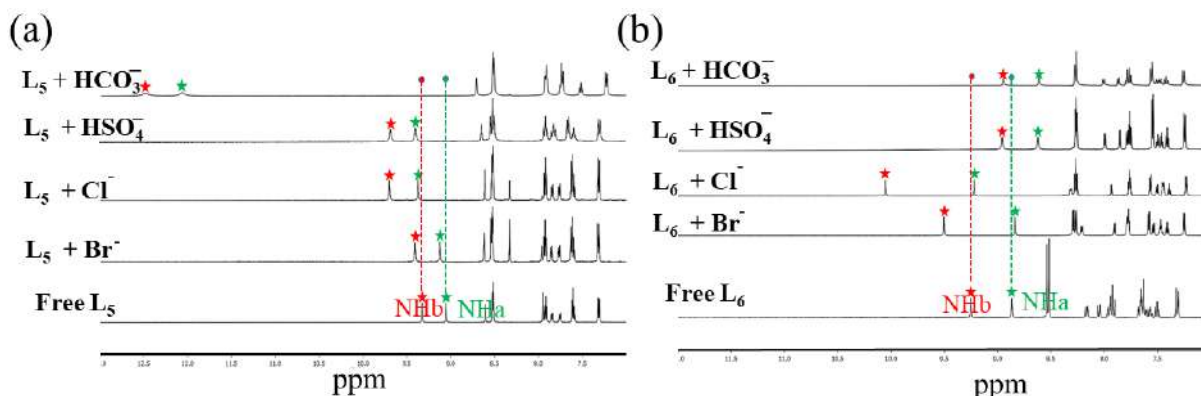


Figure 4.6 Solution phase comparative ¹H NMR studies of (a) free **L**₅ and (b) free **L**₆ (5 mM each) along with different anions (10 equivalents each) of *n*-TBA salts of interest w.r.t. the ligand concentration in DMSO-*d*₆.

The presence of such a strong interaction was also bolstered by the crystal structure data regarding the solid-state coordination of the receptor with CO₃²⁻/HCO₃⁻ with the mean distance between donor and acceptor (N-H_{urea}...O_{bicarbonate}) is being 2.038 Å. Similarly, the binding of HCO₃⁻ anion in the solution phase with the receptor **L**₆ has also been supported by the ¹H NMR experiment (Fig. A2.39). Quite similar to the case with CO₃²⁻/HCO₃⁻, incremental addition of SO₄²⁻/HSO₄⁻ to a solution of **L**₅ resulted in a lower mean downfield shift ($\Delta\delta = 0.577$ ppm) associated with the urea -NH protons presumably due to the smaller magnitude of H-bonding contact between the N-H proton and the O_{bisulphate} (the average solid-state N-H_{urea}...O_{bisulphate} distance = 2.083 Å). The greater alteration in the chemical shift of the urea NH protons for **L**₅ could be because of the less dispersed negative charge on the oxygen of planar CO₃²⁻/HCO₃⁻ than that of distorted tetrahedral SO₄²⁻/HSO₄⁻. The systematic ¹H NMR titration analysis (Fig A4.7) suggested almost equal and moderate involvement of -NH protons towards SO₄²⁻/HSO₄⁻ recognition. Similarly, **L**₆ exhibited very small $\Delta\delta$ -NH_{av} (= 0.081 ppm), upon the addition of an excess amount of SO₄²⁻/HSO₄⁻ to the **L**₆ solution (Fig. A2.41).

For the complexes of **1a** and **1b**, the systematic titration was also conducted using UV-vis spectroscopy (Figure A4.8-4.9). The hydrated complexes of **L**₅, for the spherical chloride ions, displayed moderate $\Delta\delta$ -NH_{av} = 0.350, with the average (solid-state) N-H_{urea}...Cl distance = 2.452 Å alongside a similar trend in case **L**₆. Likewise, for the hydrated complex of **L**₅ as well

as **L**₆, for the spherically shaped bromide ions, $\Delta\delta$ further decreased (0.128 for **L**₅ and 0.548 for **L**₆). In its ¹H NMR result (Fig. A2.31, A2.33) the halide or hydrated halide complexes of **L**₅ display an insignificant average downfield change in comparison to the oxyanions for the urea -NH protons. We have also examined the affinity of the receptors (**L**₅, **L**₆) towards a variety of basic anions (such as fluoride, hydroxide and various phosphate analogues) through ¹H NMR spectroscopic analyses due to the excellent binding ability of urea -NH protons for the same. In general, electron-pulling substituents attached to the urea moieties tend to enhance the polarisation of the N-H bonds and its H-bond donating propensities. Consequently, the potential interactions between highly basic negative ions and highly acidic urea moieties are expected to take place in solution, *via* an acid-base mechanism, through proton transfer from urea to the anion.^{4.24} Owing to this, we have performed ¹H NMR experiments upon administration of excess (~10 equiv.) amounts of X⁻ (H₂PO₄⁻, PO₄³⁻, F⁻ and OH⁻) to both the receptor solutions. Upon addition to an excess of X⁻, for the more basic anions, both the receptors displayed massive downfield chemical shifts with broadening of the peaks corresponding to the urea -NH protons along with its complete disappearance in few cases (Fig. A4.10- A4.13), interestingly, in case of **L**₅, the polarisation of the N-H bond led to urea deprotonation and formation of the [HF₂]⁻, whose stability was dependent on the basicity of the anion. In this context, it is important to note that, whether the addition of excess X⁻ induced deprotonation or not, relied on both the intrinsic acidity of the urea-containing receptor and the stability of the [HX₂]⁻ complex.

4.2.2.6 Hirshfeld Surface Analyses

Hirshfeld Surface (HS) analysis is expected to be a significant method to establish the characteristics associated with the surface of the molecules based on several non-covalent interactions which involve the presence of high-strength N-H...A (anion) bonds along with several weak C-H...Cl/Br, C-H...O, C-H... π contacts.^{4.25} It can provide a distinctive interpretation of intermolecular interactions by the colour intensity which defines the strength (in a relative sense) of the probable contacts. The two-dimensional fingerprint plots (2D FPs) that are obtained from Hirshfeld surfaces analysis, quantitatively describe the fundamental aspects of the intermolecular interactions, plays a crucial role in a specific crystalline molecule, generally called “contact contribution”.^{4.26} The contribution percentages of the interaction of the d_{norm} surface area of the free ligand and corresponding complex segments are given in Table A3. The bright red spot on the d_{norm} surface represents the N-H...O interactions of high strength, involving the N-H_{urea} donors and the oxygen atom of dimethyl sulfoxide-solvated receptor molecule **L**₅, and the strong N-H...A (anion) hydrogen bonds between urea N-H donors of

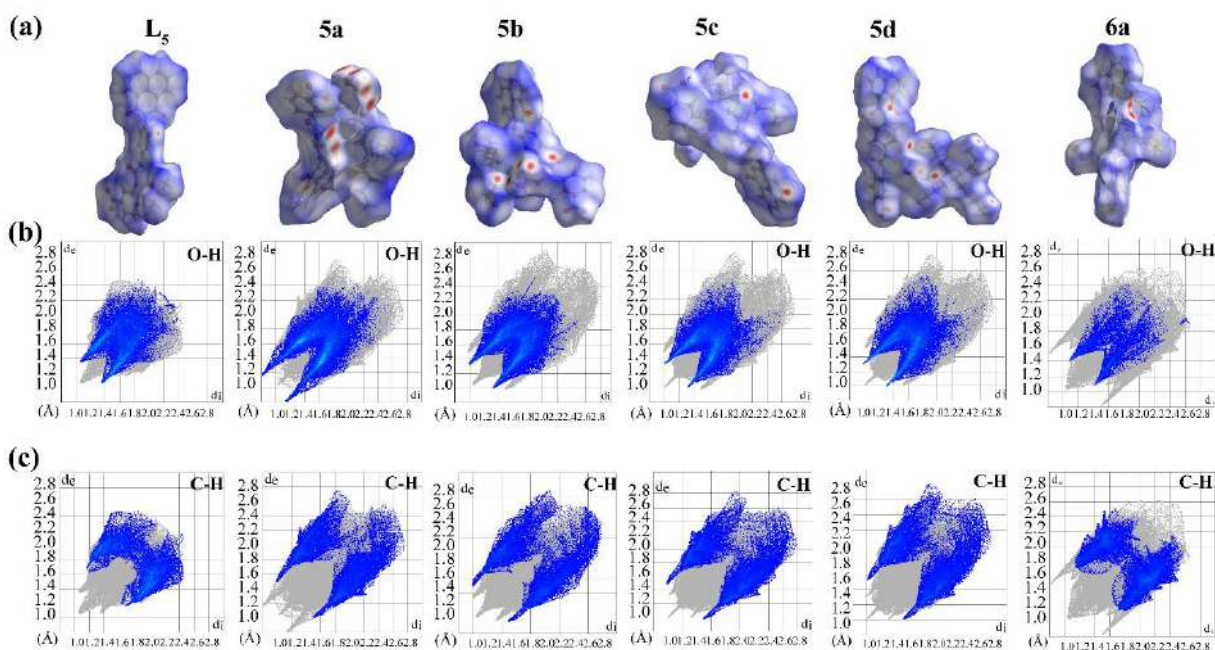


Figure 4.7 Hirshfeld surface analysis depicting (a) the corresponding d_{norm} surfaces of negatively charged ion-bound monopodal segments of the DMSO solvated receptor **L₅** and the corresponding complexes **5a**, **5b**, **5c**, **5d** and **6d**, (b) relevant 2D FPs having O···H interactions marked in colour includes N–H···O or C–H···O close contacts and (c) corresponding 2D FPs with the C···H interactions highlighted in colour contacts involved in C–H··· π or C–H···O contacts.

receptors and O atom of oxyanions in the above-mentioned complexes, while the other important contacts like C–H··· π and C–H···O, appears as faded reddish spots which involve the nearby receptor molecules or the subjected anions and an *ortho*-aryl group of receptors or interactions between the anions and *n*-tetrabutylammonium cation in the crystal structure (Fig. 4.7a). From the HSs experiment, the corresponding 2D fingerprint plot of the oxyanions and halide complexes are depicted in Fig. 4.7b, c with sharp “spikes” positioned in the lower right and upper left on the plot which sometimes reveals as pseudo symmetry in some cases on both sides of the diagonal arrangement ($d_e = d_i$). The plots describe the H···O (contact contribution of 25.9%, 30.0%, 26.2%, 24.0%, 24.1% and 7.3% for **L₅**, **5a**, **5b**, **5c**, **5d** and **6d** respectively) and C···H (contact contribution having a value of 21.1%, 17.6%, 19.1%, 18.6%, 18.3% and 17.7% for the complexes **L₅**, **5a**, **5b**, **5c**, **5d** and **6d**, respectively) close contacts. The interactions data reveals that H···O and C···H contact in all the anions bound complexes, as well as receptor molecule, show relatively higher contribution; compare to the N···H contacts (average value of 2.03%). This discrepancy may be owing to a greater number of C–H···O or N–H···O contacts associated with the oxyanion-bound coordinated structures of the neutral receptor segments. Hence, the interaction spots including C–H···O or N–H···O H-bonding contacts are observed prominently on the crystal structure surface. As a result, the solid-state results obtained from

SCXRD studies are validated by these data or information collected from Hirshfeld surfaces and the relevant 2D FPs of free ligand segments and negatively charged ion-bound receptor complexes.

4.2.2.7 Discrimination among anions using multivariate analysis

The subtle yet unique absorption spectra in the presence of the studied anions (oxyanions such as: HCO_3^- , HSO_4^- and Cl^- , Br^-) along with HPO_4^{2-} (taken as an interesting phosphorylated oxyanion) made us curious to investigate if they can be discriminated separately using the ligands as probes (Fig. A4.14-A4.15). Hence, to check the qualitative discriminatory ability of the probes among the anions, the absorbance of L_5 and L_6 (10 μM each) were recorded after the addition of 10 Equiv. of the analyte in water (**Table A4**). Thus the shifts in the absorption intensities at different wavelengths enabled the differentiation among the analyte through the examination of distinctive optical fingerprints (**Table A5**). The absorption patterns, thus generated, were subjected to linear discriminant analysis (LDA), the multivariate pattern analysis technique, to differentiate among them (See Annexure).

The two-dimensional canonical score plots for both L_5 and L_6 displayed a conspicuous separation among each of the oxyanions and halides with no clustering in close proximity (**Fig. 4.8a, e**). As another factor was introduced to the score plot, it further improved the separation among the observables in the 3D LDA plot (Fig. 4.8b, f). Interestingly, based on a strong interaction between L_5 and HCO_3^- , as evident from NMR and crystal structure, HCO_3^- became the most distinctly separated ion in 2D as well as 3D plots.

The information content could be further improved by applying hierarchical clustering analysis (HCA) to categorize all the test trials into the same group in the case of each anion and separate the ions into various groups (Supporting information). In the resultant dendrograms it could be seen that, while all the anions were mostly separated and clustered for L_5 , the ions were scattered, in the case of L_6 , with obvious grouping (Fig. 4.8c, g). Although the differentiation was difficult in univariate analysis, the multivariate studies exhibited distinct discrimination with 100% classification accuracy (**Fig. 4.8d, h**). The high efficacy of both the ligands as probes for the anions could be deciphered from the heat maps (Fig. A4.16). Thus, the LDA mapping unmistakably suggested that ligands-turned probes could discriminate among the anions. As for all the absorbance data used in the generation of the aforementioned plots, both the ligands were taken in 10 μM concentration and each anion added was 10 Equiv. w.r.t. the ligand concentration. The charges of the anions labelled along the vertical axes are omitted for clarity.

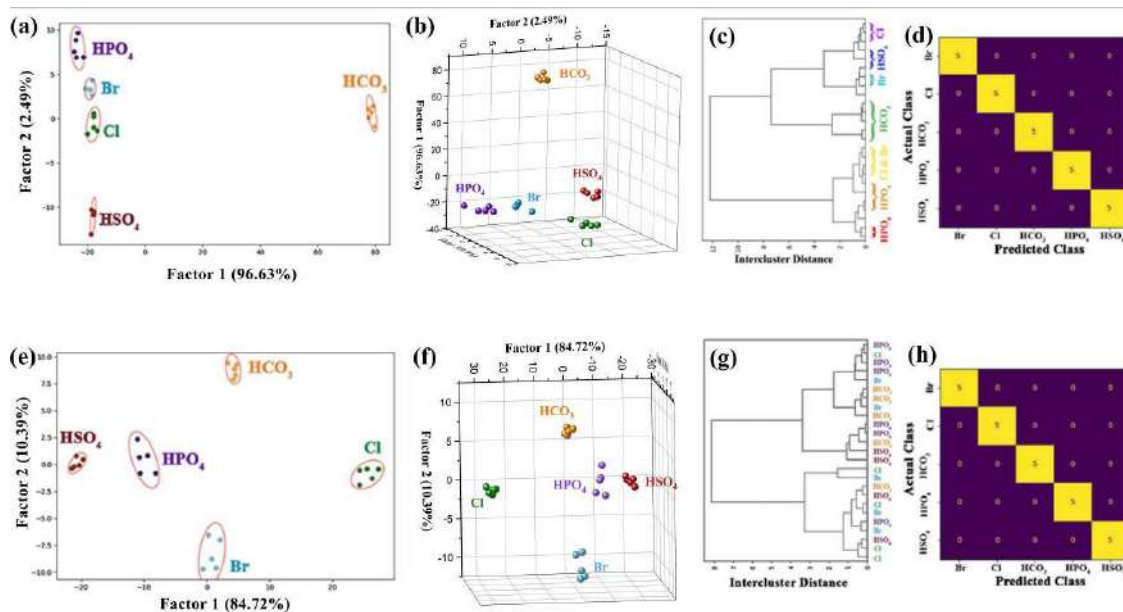


Figure 4.8 Two-dimensional LDA score plots for (a) L_5 and (e) L_6 as single sensor elements discriminating anions in aqueous solution. Three-dimensional LDA plots for (b) L_5 and (f) L_6 as single sensors under the same conditions. The confidence ellipsoids represent 95% probability. The percentage values shown between the parentheses after each of the factor axes denote the weightage contribution of the factor towards the total information content. The dendrograms associated with the HCA for the anions interacting with (c) L_5 and (g) L_6 . The confusion matrices (signifying the classification accuracy based on LDA classifier) are trained on the full data set for (d) L_5 and (h) L_6 .

4.2.2.8 Antibacterial and Cytotoxic Potential

The persistence of antibiotic-resistant pathogenic bacteria is a grave concern in the domain of healthcare.^{4.27-4.28} Pathogenic bacteria are known to evade the host defence mechanism and defy the action of major frontline therapeutic antibiotics^{4.29}. This predicament demands the discovery of synthetic antibacterials that can hold therapeutic potential against antibiotic-resistant pathogens. Literature reports seem to suggest that naphthalimide-appended ligands hold potential as antibacterial agents^{4.30-4.31}. Based on this tenet, our endeavour was to evaluate the antibacterial activity of the ligands L_5 and L_6 and their respective complexes against representative bacterial pathogens. A notable observation was that the ligands L_5 and L_6 seem to exhibit bactericidal activity against both the Gram -ve pathogen *E. coli* MTCC 433 as well as the Gram +ve pathogen *S. aureus* MRSA 100 in a concentration-dependent manner (Fig. 4.9A, Fig. A4.17). The presence of teichoic acid in Gram-positive bacteria and lipopolysaccharide in Gram-negative bacteria is known to render a negative charge to bacterial cells^{4.32-4.33}. Hence, the anion binding ligands L_5 and L_6 are likely to interact efficiently with bacterial cells. It is also plausible that the ligands L_5 and L_6 engage in hydrogen bond interaction with

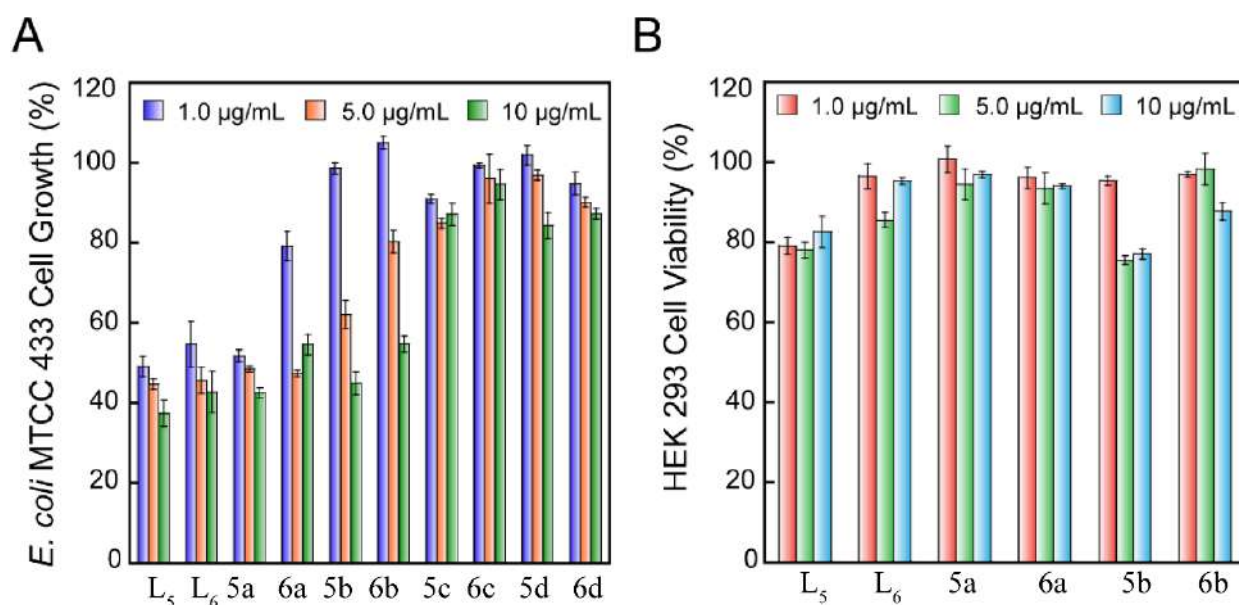


Figure 4.9 (A) Antibacterial activity of ligands L_5 and L_6 and their complexes against *E. coli* MTCC 433. (B) Evaluation of the cytotoxic effect of ligands L_5 and L_6 and their complexes on HEK 293 cells determined by MTT assay. Each data point represents mean \pm standard deviation from six samples.

phosphoryl and carboxyl groups, which are typically present in bacterial membrane phospholipids, which in turn, may facilitate efficient interaction of the ligands with the bacterial cell surface, as reported earlier for some antibacterials.^{4.34-4.36} Notably, the degree of bactericidal activity for the ligands was higher against *E. coli* MTCC 433 as compared to *S. aureus* MRSA 100. For instance, at a concentration of 1.0 $\mu\text{g/mL}$, 5.0 $\mu\text{g/mL}$ and 10 $\mu\text{g/mL}$ of L_5 , growth of *E. coli* MTCC 433 cells was estimated to be around 37%, 44% and 49%, respectively, while in the case of *S. aureus* MRSA 100, the growth of the cells was observed to be approximately 64%, 66% and 74%, respectively (Table A6). It is possible that the presence of a thick peptidoglycan layer in the cell wall of the Gram-positive MRSA strain may act as a barrier and render a certain degree of protection to the cells. In future, it would be interesting to validate this notion. In case of *E. coli* MTCC 433, it was also apparent that all the complexes (**5a-6d**) unequivocally displayed lower bactericidal activity as compared to the corresponding ligands L_5 and L_6 (Fig 4.9A, Table A6). This suggested that hydrogen bond interaction of the ligands with phosphoryl and carboxyl groups present in membrane phospholipids of the target bacteria is perhaps critical for antibacterial activity as complexation of the ligands seems to reduce their bactericidal potency against *E. coli* MTCC 433. However, in the case of *S. aureus* MRSA 100, this general trend of the ligands being more potent than the complexes was not observed (Fig. A4.17, Table A6). Overall, the heterogeneity with regard to the growth suppression of *E. coli* MTCC 433 and *S. aureus* MRSA 100 cells in response to treatment with the ligands or their complexes also indicates an innate difference in the resistance mechanism present in the target pathogens. A

more detailed structure-activity study in future can perhaps provide a mechanistic insight into this phenomenon. Further, in the case of *E. coli* MTCC 433, the highest growth inhibition was rendered by the ligand **L₅** at a concentration of 10 µg/mL (around 37% growth), whereas in the case of *S. aureus* MRSA 100, the complex **5a** rendered the highest growth inhibition at a concentration of 10 µg/mL (around 55% growth) (Table A6). It may be mentioned here that at concentrations exceeding 10 µg/mL, the ligands and their corresponding complexes tend to precipitate rapidly in solution. Hence, antibacterial assays with the ligands and their corresponding complexes could not be performed at concentrations higher than 10 µg/mL. Despite this limitation, reasonably significant growth inhibition of the pathogen *E. coli* MTCC 433 observed in presence of 10 µg/mL of the ligands **L₅** and **L₆** (around 37% and 42% growth, respectively) (Table A6) is encouraging and in future it would be worthwhile to explore these ligands as adjuvants in combination with therapeutic antibiotics in a combinatorial treatment regimen to mitigate *E. coli* mediated infections. Interestingly, the ligands and their corresponding complexes were essentially non-toxic to cultured HEK 293 cells, with the cell viability being around 80% and above at the tested concentrations (Fig. 4.9B). This observation also augers well for potential therapeutic applications of the ligands as an adjuvant for combating *E. coli* infections.

4.3 Conclusion

The monopodal urea-based receptors (**L₅**, **L₆**) with different hydrophobicity were designed to interact with different anions/hydrated anions. $R_2^2(8)$ arrangement of centrosymmetric and cylindrical $[\text{HCO}_3 \cdots \text{HCO}_3]^{2-}$ dimer (fluoride/hydroxide induced) was identified. In a similar fashion, distorted cylindrical $[\text{HSO}_4 \cdots \text{HSO}_4]^{2-}$ assembly of anion homodimers formed via strong H-bonding interactions between the anions (O \cdots O distances are 2.681 Å for planar bicarbonate dimer and 2.911 Å for tetrahedral bisulphate dimer). Another notable outcome of this report involves the formation of a cyclic halide-water cluster within the hydrophobic linear assembly of receptor molecules. LDA analysis revealed that both the receptors were able to effectively discriminate, as evident from the 2D and 3D score plots, a set of five anions comprising oxyanions and halide ions. NMR titration experiments corroborate the LDA results. Interestingly, the ligands displayed antibacterial activity against model bacterial pathogens, rendering notable growth inhibition in the case of *E. coli* MTCC 433 and were non-toxic at their working concentrations. Future studies focussing on the structure-activity relationship and adjuvant activity can expand the therapeutic prospect of the ligand against pathogenic bacteria.

References

- 4.1 N. Busschaert, C. Caltagirone, W. V. Rossom and P. A. Gale, *Chem. Rev.*, 2015, **115**, 8038.
- 4.2 Themed issue: Supramolecular chemistry of anionic species, *Chem. Soc. Rev.*, 2010, **39**, 3581.
- 4.3 P. R. Edwards, J. R. Hiscock, P. A. Gale and M. E. Light, *Org. Biomol. Chem.*, 2010, **8**, 100.
- 4.4 E. A. Quadrelli, G. Centi, J. L. Duplan and S. Perathoner, *Chem. Sus. Chem.*, 2011, **4**, 1194.
- 4.5 R. Custelcean, *Chem. Commun.*, 2020, **56**, 10272.
- 4.6 A. S. McCall, C. F. Cummings, G. Bhave, R. Vanacore, A. P. McCaw and B. G. Hudson, *Cell*, 2014, **15**, 1380.
- 4.7 U. Manna and G. Das, *Cryst. Growth Des.*, 2018, **18**, 3138.
- 4.8 N. Busschaert, C. Caltagirone, W. Van Rossom and P. A. Gale, *Chem. Rev.*, 2015, **115**, 8038.
- 4.9 U. Manna and G. Das, *Cryst. Eng. Comm.*, 2019, **21**, 65.
- 4.10 W. Zhao, A. H. Flood and N. G. White, *Chem. Soc. Rev.*, 2020, **49**, 7893.
- 4.11 A. Das, B. Nayak and G. Das, *Cryst. Eng. Comm.*, 2020, **22**, 2197.
- 4.12 U. Manna and G. Das, *Cryst. Eng. Comm.*, 2017, **19**, 5622.
- 4.13 U. Manna, R. Chutia and G. Das, *Cryst. Growth Des.*, 2016, **16**, 5, 2893.
- 4.14 A. Basu and G. Das, *Chem. Commun.*, 2013, **49**, 3997.
- 4.15 Nicholas G. White, *Cryst. Eng. Comm.*, 2019, **21**, 4855.
- 4.16 All pKa data are taken from: J. Bjerrum, G. Schwarzenbach and L. G. Sillen, Stability constants of metal-ion complexes, Chemical Society, London, 1958.
- 4.17 S. J. Brooks, S. E. Garcia-Garrido, M. E. Light, P. A. Cole and P. A. Gale, *Chem. - Eur. J.*, 2007, **13**, 3320.
- 4.18 S. J. Brooks, P. A. Gale and M. E. Light, *Chem. Commun.*, 2006, 4344.
- 4.19 I. Ravikumar and P. Ghosh, *Chem. Commun.*, 2010, **46**, 1082.
- 4.20 U. Manna, S. Kayal, S. Samanta and G. Das, *Dalton Trans.*, 2017, **46**, 10374.
- 4.21 W. Zhao, B. Qiao, J. Tropp, M. Pink, J. D. Azoulay and A. H. Flood, *J. Am. Chem. Soc.*, 2019, **141**, 4980.
- 4.22 W. Zhao, J. Tropp, B. Qiao, M. Pink, J. D. Azoulay and A. H. Flood, *J. Am. Chem. Soc.*, 2020, **142**, 2579.
- 4.23 B. Nayak, U. Manna and Gopal Das, *ChemistrySelect.*, 2018, **3**, 3548.
- 4.24 M. Boiocchi, L. D. Boca, D. E. Gómez, L. Fabbri, M. Licchelli and E. Monzani, *Chem. Eur. J.*, 2006, **11**, 3097-3104.
- 4.25 J. A. McKinnon, S. Mitchell and M. A. Spackman, *Chem. – Eur. J.*, 1998, **4**, 2136.
- 4.26 T. E. Clark, M. Makha, A. N. Sobolev and C. L. Raston, *Cryst. Growth Des.*, 2008, **8**, 890.
- 4.27 A. Petchiappan, D Chatterji, *ACS Omega*, 2017, **2**, 7400.
- 4.28 R. J. Fair and Y. Tor, *Perspect. Medicin. Chem.*, 2014, **25**.
- 4.29 H. Nikaido, *Annu. Rev. Biochem.*, 2010, **78**, 119.
- 4.30 Y. Y Zhang and C. H. Zhou, *Bioorg. Med. Chem. Lett.*, 2011, **21**, 4349.
- 4.31 Y. Y. Chen, L. Gopala, R. R. Y. Bheemanaboina, H. B. Liu, Y. Cheng, R. X. Geng and C. H. Zhou, *ACS Med. Chem. Lett.*, 2017, **8**, 1331.
- 4.32 C. Weidenmaier and A. Peschel, *Nat. Rev. Microbiol.*, 2008, **6**, 276.
- 4.33 T. Gutschmann and U. Seydel, *Eur. J. Cell Biol.*, 2010, **89**, 11.
- 4.34 S. French, D. Puddephatt, M. Habash and S. Glasauer, *Crit. Rev. Microbiol.*, 2013, **39**, 196.
- 4.35 S. Cho, Q. Wang, C. P. Swaminathan, D. Hasek, M. Lee, G. J. Boons, S. Mobashery and R. Mariuzza, *Proc. Natl. Acad. Sci. U. S. A.*, 2007, **104**, 8761.

4.36 D. F. Suárez, J. Consuegra, V. C. Trajano, S. M. L. Gontijo, P.P.G. Guimarães, M. E. Cortés and A. L. Denadai, R. D. Sinisterra, *Colloids Surf. B: Biointerfaces.*, 2014, **118**, 194.

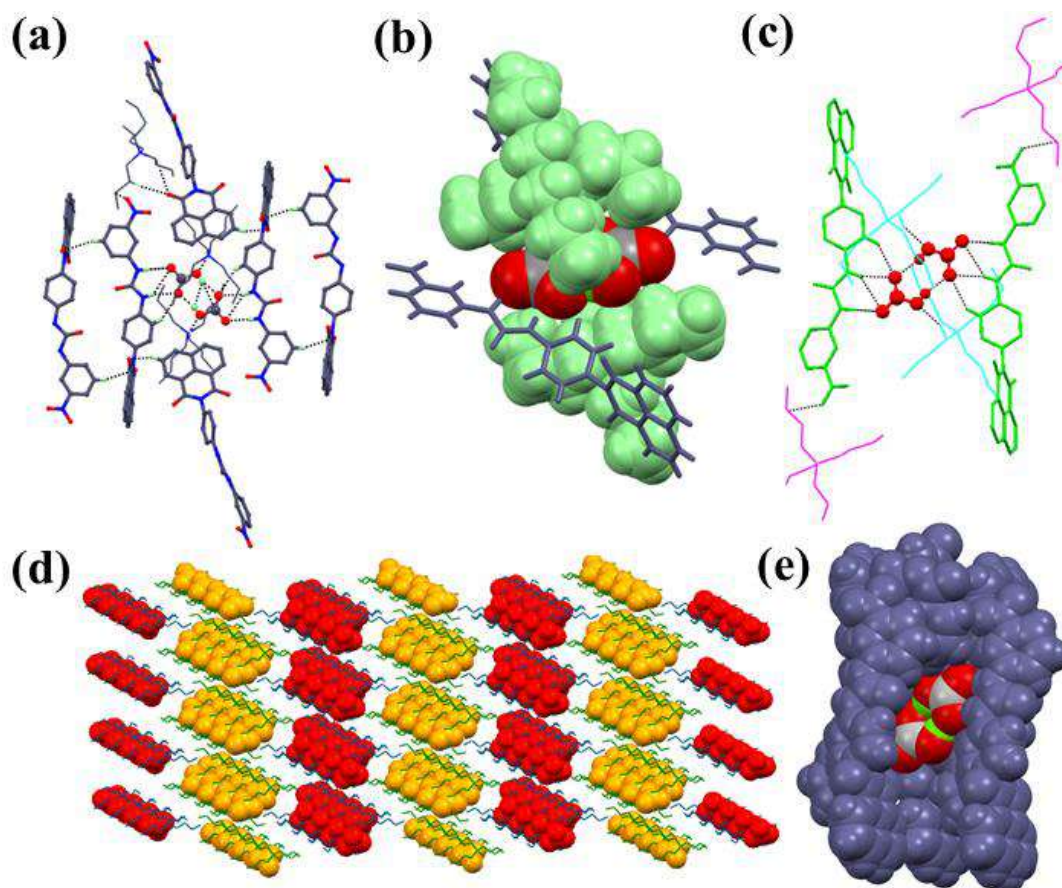
Annexure 4

Figure A4.1 X-ray of complex **5a** revealing (a) all types of non-covalent interactions (b) *n*-TBA cation-sealed full entrapment of the dimeric assembly (space-fill) (c) symmetry equivalent arrangement of receptor-anion stabilized dimer (d) packing arrangement of complex **5a** showing trapping of the cation-sealed environment as viewed from crystallographic b-axis and (e) full entrapment of the bicarbonate dimer linear-shaped assembly of host molecules of the **L₅** (space-fill representation). For (a), (b) and (e), in the receptor-bound bicarbonate structure, carbon, oxygen and hydrogen atoms are represented by grey, red and green colours respectively.

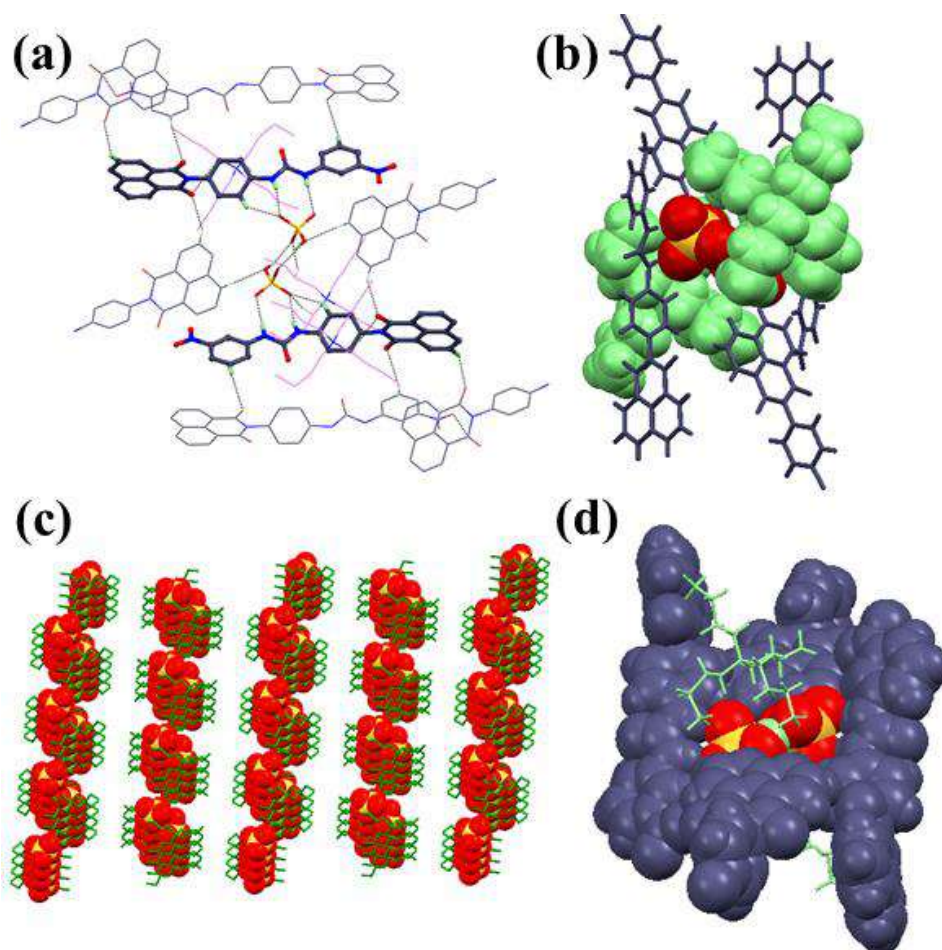


Figure A4.2 X-ray of complex **5b** revealing (a) all types of non-covalent interactions (b) *n*-TBA cation-sealed full entrapment of the dimeric assembly (space-fill) (c) symmetry equivalent arrangement of receptor-anion stabilized dimer (d) packing arrangement of anion trapping of the cation-sealed environment as viewed from crystallographic *b*-axis and (e) full entrapment of the bicarbonate dimer linear-shaped assembly of host molecules of the L_5 (space-fill representation). For (a), (b) and (d), in the receptor-bound bisulphate structure, sulphur, oxygen and hydrogen atoms are represented by yellow, red and green colours respectively.

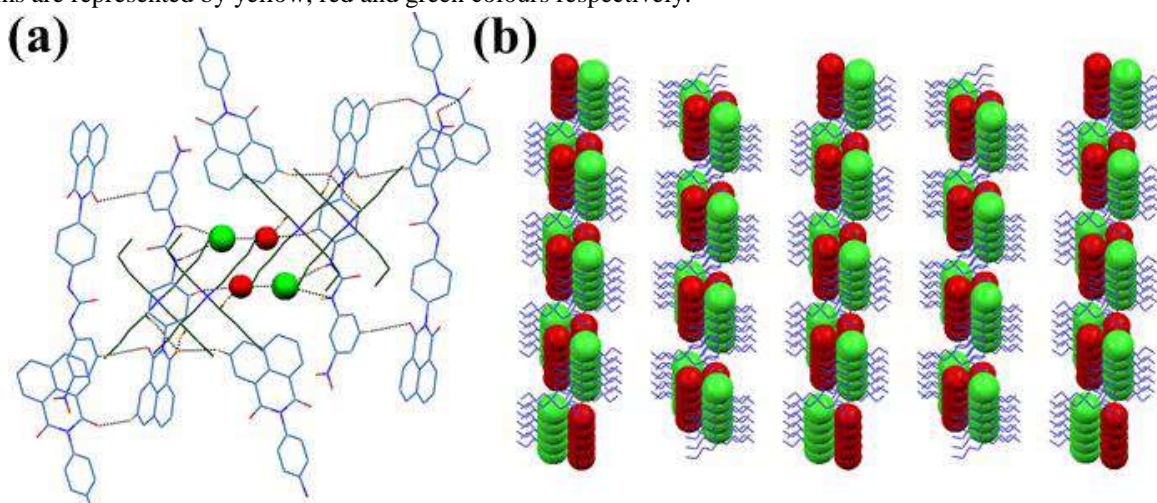


Figure A4.3 X-ray of complex **5c** revealing (a) all types of non-covalent interactions and (b) packing arrangement of hydrated anion trapping of the cation-sealed environment as viewed from crystallographic *b*-axis. The receptor-bound chloride ions and the oxygen atoms of lattice water molecules are represented by green and red colours respectively.

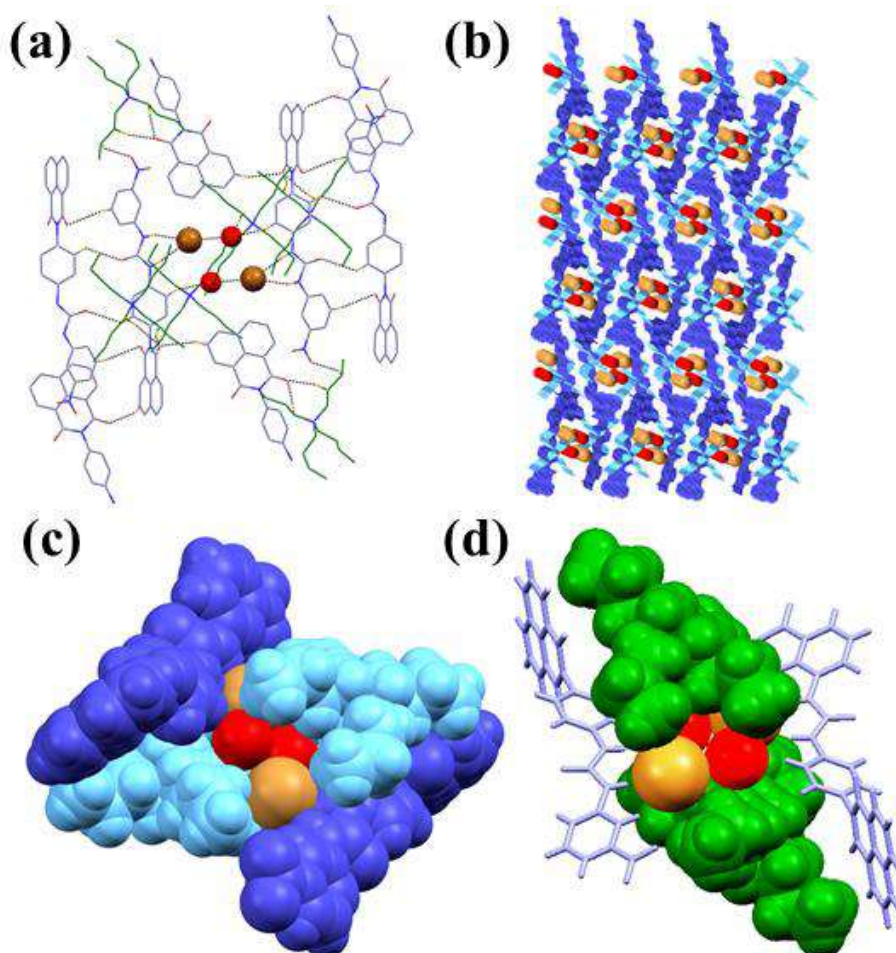


Figure A4.4 X-ray of complex **5d** revealing (a) all types of non-covalent interactions (b) molecular packing of the hydrated guest inside cleft of host molecule enclosed by the fully cation-sealed environment as viewed down along the crystallographic *c*-axis (c) space-fill view of hydrated bromide complex fully surrounded by the host molecules involving and *n*-TBA cations and (d) *n*-TBA cation-sealed full entrapment of the bromide water assembly (space-fill). The receptor-bound bromide ions and the oxygen atoms of lattice water molecules are represented by brown and red colours respectively.

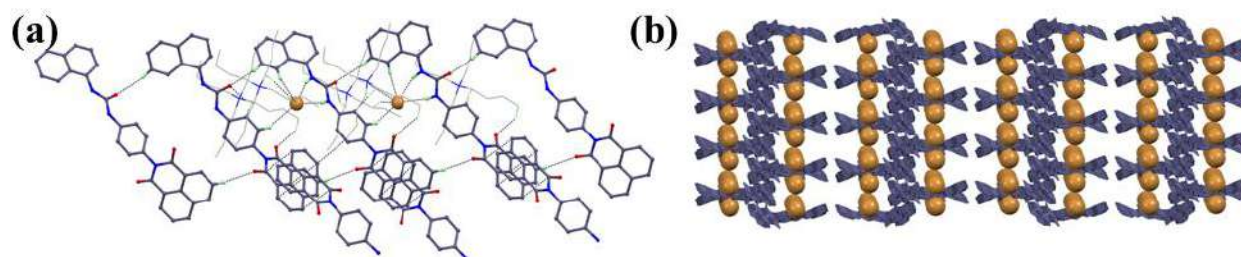


Figure A4.5 X-ray of complex **6d** revealing (a) all types of non-covalent interactions and (b) packing arrangement of spherical halide trapping of the cation-sealed environment as viewed from crystallographic *b*-axis. The receptor-bound bromide ions are represented by brown colour.

¹H NMR (titration) studies: A 5 mM solution of **L**₁ was prepared in 500 μL of DMSO-*d*₆ for ¹H NMR titration studies. Aliquots of *n*-TBAHCO₃ and *n*-TBAHSO₄ solutions prepared in DMSO-*d*₆ were gradually added to the ligand solution in various proportions up to 2 equiv., and 7 equiv., respectively, with respect to the ligand concentration.

UV-vis (titration) studies: A stock solution of L_1 (5 mM) was prepared in DMSO. From this stock solution, a 50 μ M solution of L_1 was prepared in 2 mL of water for UV-vis spectroscopic studies. Aliquots of bicarbonate and bisulphate solutions prepared in Milli-Q water were added to the ligand solution in various proportions up to 2 Equiv. with respect to the ligand concentration. All the data were taken in water at pH 7.0 buffered with HEPES (1 mM) at 25 $^{\circ}$ C.

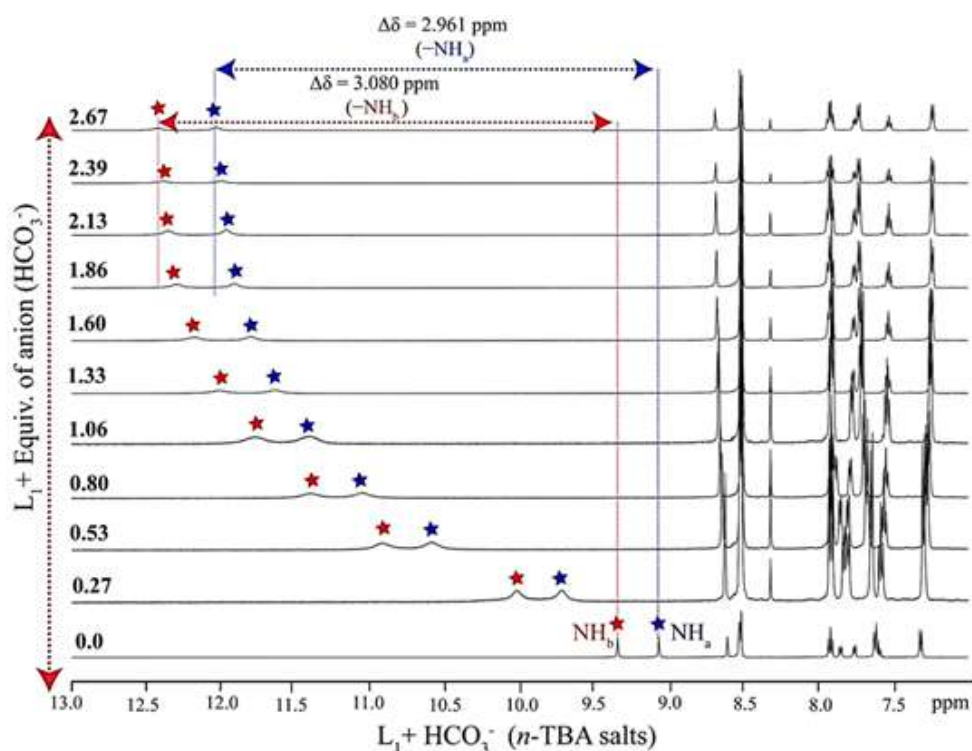


Figure A4.6 Expanded partials ^1H NMR (600 MHz) titration spectra of L_1 (5 mM) upon gradual addition of (0-2.67 equiv.) $n\text{-TBAHCO}_3$ in DMSO-d_6 .

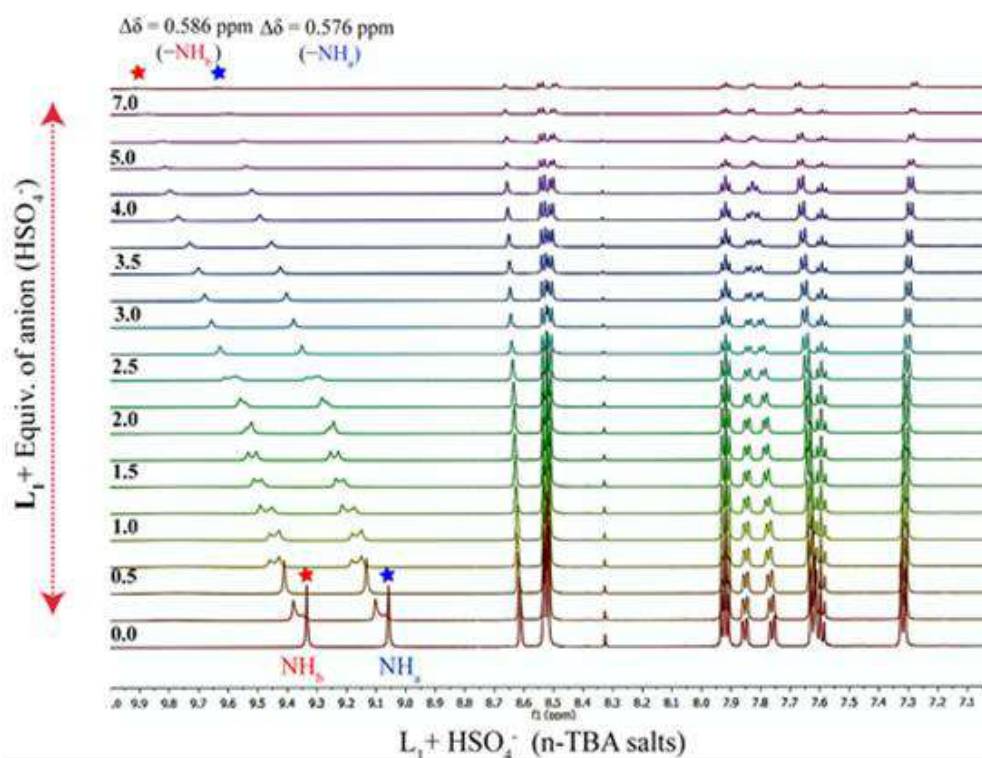


Figure A4.7 Expanded partials ^1H NMR (600 MHz) titration spectra of L_1 (5 mM) upon incremental addition of (0-7.8 equiv.) $n\text{-TBAHSO}_4$ in DMSO-d_6 .

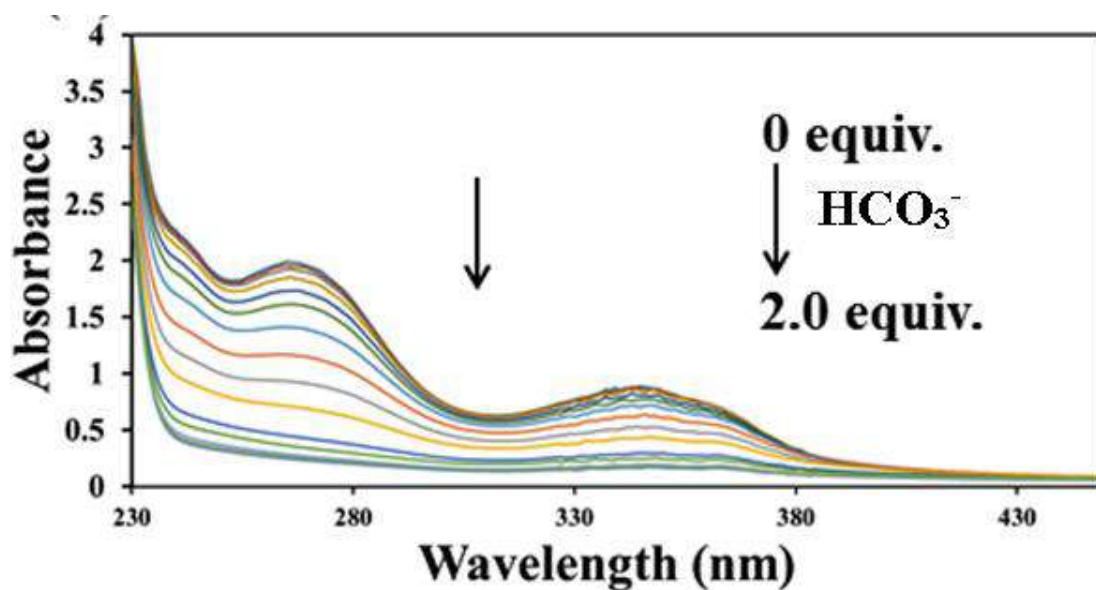


Figure A4.8 Changes in the absorption spectra of L_1 ($50\ \mu\text{M}$) with incremental addition of $n\text{-TBAHCO}_3$ (0-2 equiv.) in water at pH 7.0 buffered with HEPES (1 mM) at $25\ ^\circ\text{C}$.

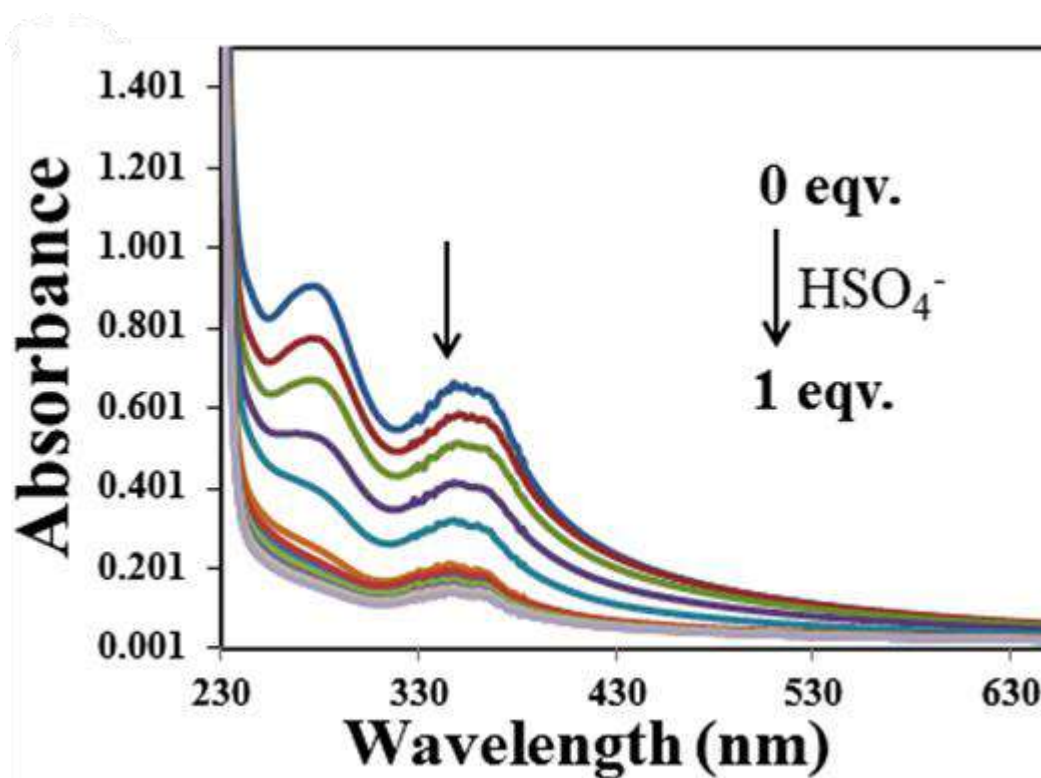


Figure A4.9 Changes in the absorption spectra of L_1 ($50\ \mu\text{M}$) with incremental addition of $n\text{-TBAHSO}_4$ (0-1 equiv.) in water at pH 7.0 buffered with HEPES (1 mM) at $25\ ^\circ\text{C}$.

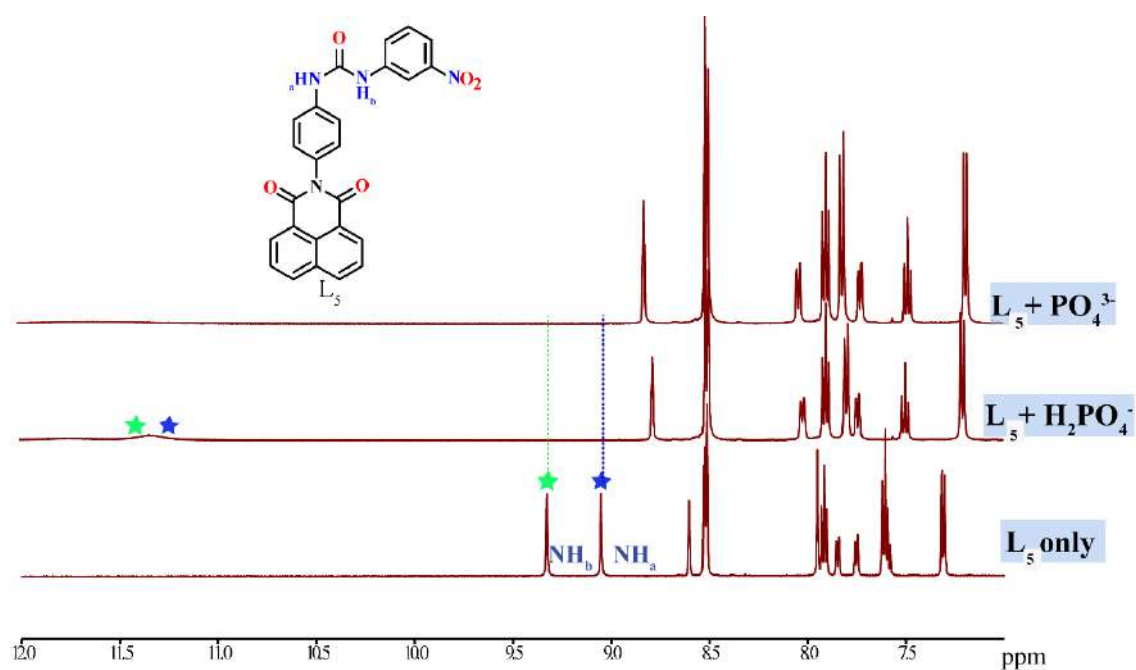


Figure A4.10 Solution phase comparative (partial) ^1H NMR studies of L_1 (5 mM) along with H_2PO_4^- and PO_4^{3-} (10 equiv. each) of *n*-TBA salts of interest w.r.t. the ligand concentration in $\text{DMSO-}d_6$.

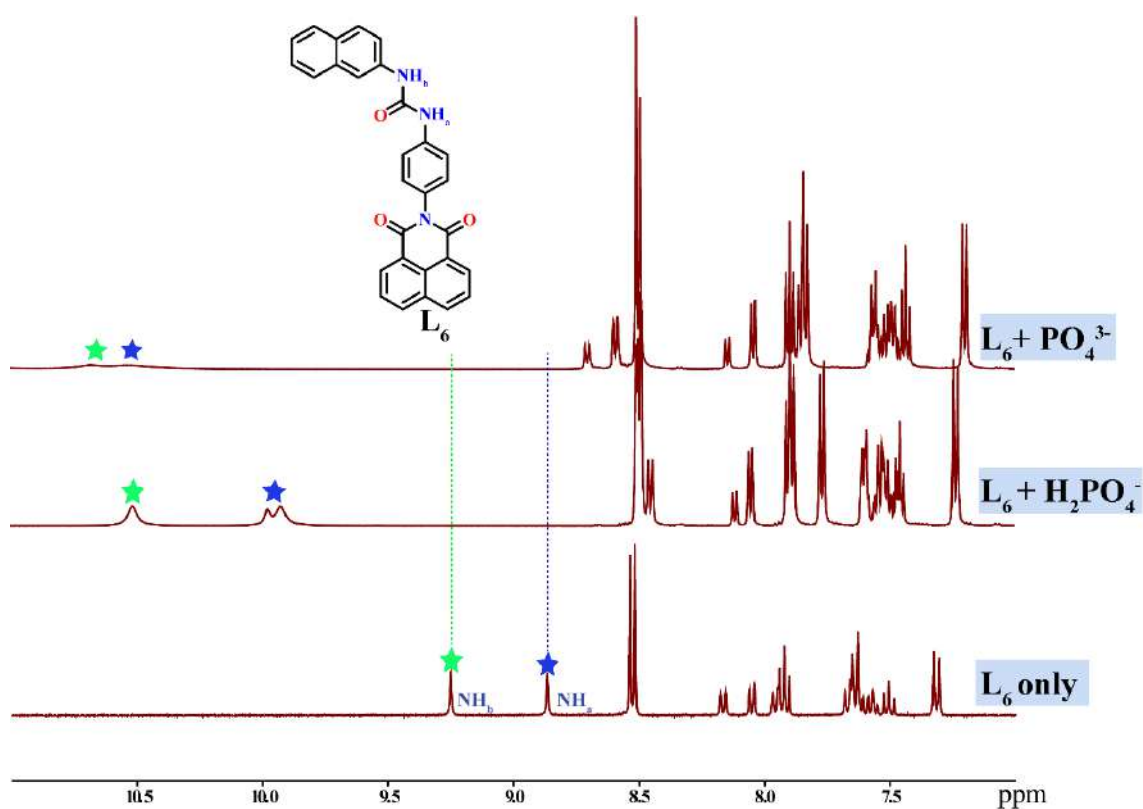


Figure A4.11 Solution phase comparative (partial) ^1H NMR studies of L_2 (5 mM) along with H_2PO_4^- and PO_4^{3-} (10 equiv. each) of *n*-TBA salts of interest w.r.t. the ligand concentration in $\text{DMSO-}d_6$.

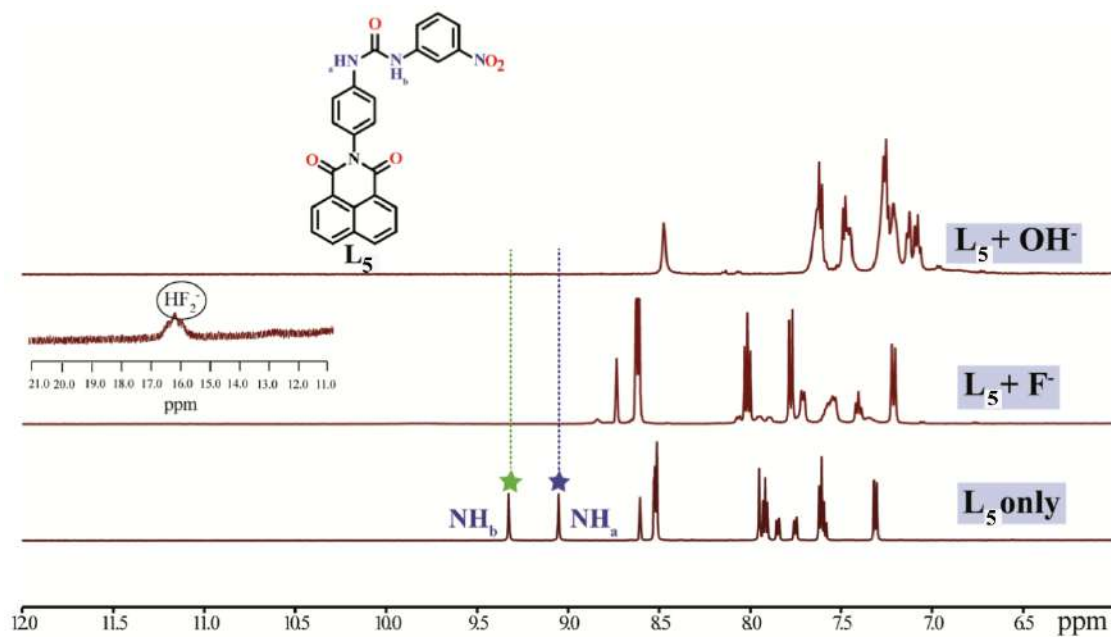


Figure A4.12 Solution phase comparative (partial) ^1H NMR studies of L_1 (5 mM) along with F^- and OH^- (10 equiv. each) of *n*-TBA salts of interest w.r.t. the ligand concentration in $\text{DMSO-}d_6$.

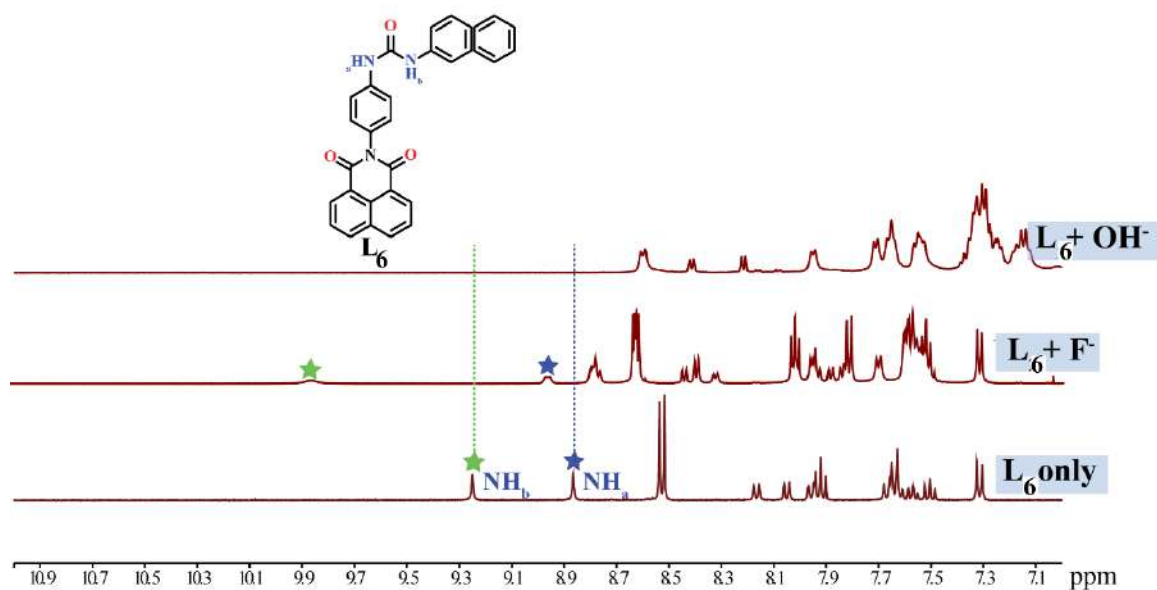


Figure A4.13 Solution phase comparative (partial) ^1H NMR studies of L_2 (5 mM) along with F^- and OH^- (10 equiv. each) of *n*-TBA salts of interest w.r.t. the ligand concentration in $\text{DMSO-}d_6$.

Table A2 Chemical shift values (δ) of the receptors and their complexes obtained from the ^1H NMR studies of L_1 and L_2 (5 mM each) along with different anions (10 equivalents each) of n -TBA salts of interest w.r.t. the ligand concentration in $\text{DMSO-}d_6$.

	NH_a (ppm)	NH_b (ppm)	$\Delta\delta$ - NH_a		$\Delta\delta$ - NH_b	$d_{\text{av}}(\text{N-H}_{\text{urea}} \cdots \text{X}_{\text{anion}})/\text{\AA}$ (From crystal data)
Free L_5	9.059	9.335	–		–	–
$\text{L}_5+n\text{-TBAHCO}_3$	12.070	12.483	2.961		3.080	2.038
$\text{L}_5+n\text{-TBAHSO}_4$	9.393	9.677	0.577		0.578	2.083
$\text{L}_5 + n\text{-TBACl}$	9.374	9.699	0.332		0.369	2.452
$\text{L}_5 + n\text{-TBABr}$	9.119	9.401	0.132		0.124	2.553
Free L_6	8.865	9.249	–		–	–
$\text{L}_6+n\text{-TBAHCO}_3$	8.935	9.336	0.070		0.087	–
$\text{L}_6+n\text{-TBAHSO}_4$	8.956	9.657	0.075		0.088	–
$\text{L}_6 + n\text{-TBACl}$	8.956	10.654	0.091		1.405	–
$\text{L}_6 + n\text{-TBABr}$	9.204	10.005	0.339		0.756	2.528

Table A3 Contact contributions from the d_{norm} surface area of dipodal segments in free receptors and anion complexes

Contacts	L_5 . DMSO	5a	5b	5c	5d	6d
$\text{H} \cdots \text{Cl/Br}$				2.4	2.4	9.4
$\text{H} \cdots \text{O}$	25.9	30.0	26.2	24.0	24.1	7.3
$\text{H} \cdots \text{N}$	2.7	2.0	2.5	2.5	2.5	1.6
$\text{H} \cdots \text{C}$	21.1	17.6	19.1	18.6	18.3	17.7
$\text{H} \cdots \text{H}$	32.4	46.0	47.1	46.9	47.2	59.6

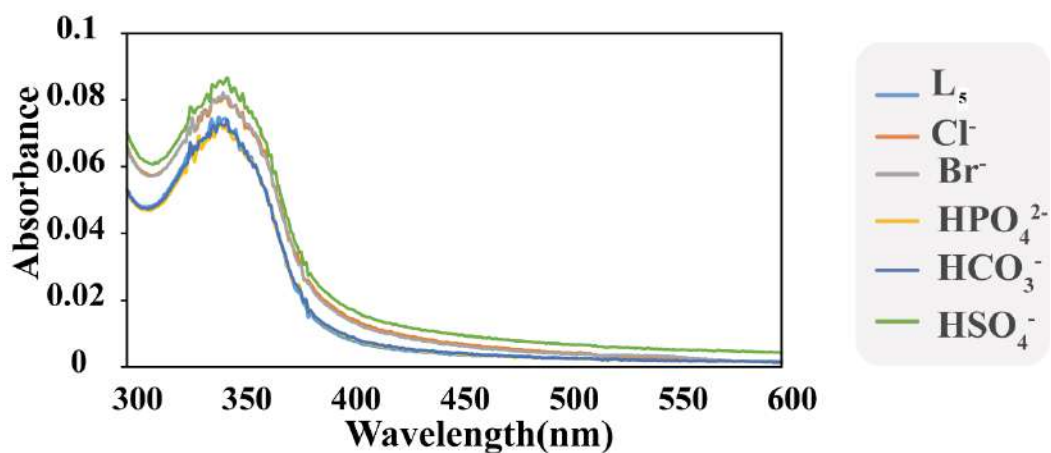


Figure A4.14 Absorption spectra of L_1 (10 μM) along with spectral changes after addition of various anions (100 μM each) in water at pH 7.0 buffered with HEPES (1 mM) at 25 $^\circ\text{C}$.

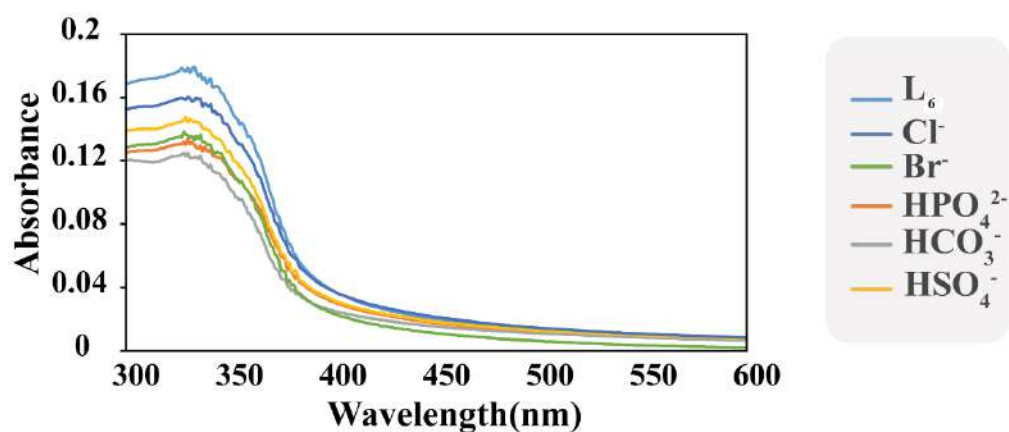


Figure A4.15 Absorption spectra of L_2 (10 μM) along with spectral changes after addition of various anions (100 μM each) in water at pH 7.0 buffered with HEPES (1 mM) at 25 $^\circ\text{C}$.

Table A4 Instrumental variables (features) used in the multivariate pattern analysis.

Absorption maxima (nm)								Total instrumental variables
300	305	310	315	320	330	345	354	22
	360	390	400	410	420	430	440	
	460	475	484	490	505	550	590	

The raw data matrix has 25 rows (analyte replicates) and 22 columns in total (variables), a total of 550 raw data points were obtained.

Table A5 Features and data points processed in the multivariate pattern analysis.

5 anions	5 data points per anion	= 25 total data points
1 sensor	22 variables	= 22 total variables
550 raw data points		

Multivariate data analysis: Linear discriminant analysis (LDA) was used to derive underlying patterns of information that classify the 5 ions. The aim of using LDA was to project a large dataset into a smaller subspace while keeping class-discriminatory information. LDA defines components that optimise the between-class measure (i.e. a linear combination of the observed variables from the data), while minimizing the within-class measure. The raw experimental data corresponding to the individual anions was normalised to the corresponding values calculated for the sole ligand during the pre-processing stage to remove the dependence of the discriminating capacity of the ligands on the background (ligand only) intensity. No data points were removed from the primary 550 ($=1 \times 25 \times 22$) raw data points before further analysis of LDA.

550 raw data points \rightarrow raw data read/averaged probe signal \rightarrow 550 normalized data points

Linear discriminant analysis (LDA): During this method, a new collection of variables known as factors was created that best distinguished the anions. By holding only, the best two or three variables and discarding the rest, the data dimensionality was reduced. As a result, a transformed data set was generated, which consisted of points, each of which was associated with factor scores, which were represented by a doublet or triplet of numbers. The coordinates of these factor scores were then used in a two- or three-dimensional score plot of the points under observation

Hierarchical Clustering Analysis (HCA): The HC analysis was used to see whether the anion responses were comparable and to gather as much information as possible. In that case, the anions can be grouped into a hierarchical cluster tree using the entire information content

derived from the multivariate response.¹ The dendrograms for both media systems display the results of the hierarchical classification based on Euclidean distance and Ward linkages.² HCA clearly groups all observed trials together, owing to its high repeatability, which allows for distinction even with minor signal variations.

Confusion matrix: The training data set was fitted over the training data set itself by considering the whole data set as unknown and the LDA predicted the classes based on the previously given data (which was training data only). This was basically classifying the data based on it. The classification accuracy was 100% because they are very well separated from one another.

Heat map: Heat maps were generated by processing the relative intensity data by acquiring the absorbance data on different wavelengths before and after the addition of the five anions separately. The relative absorption intensity values were calculated by subtracting the average absorbance values of the blank sample (only the probe) from those obtained after adding the anions and dividing the resultant by the "blank value."

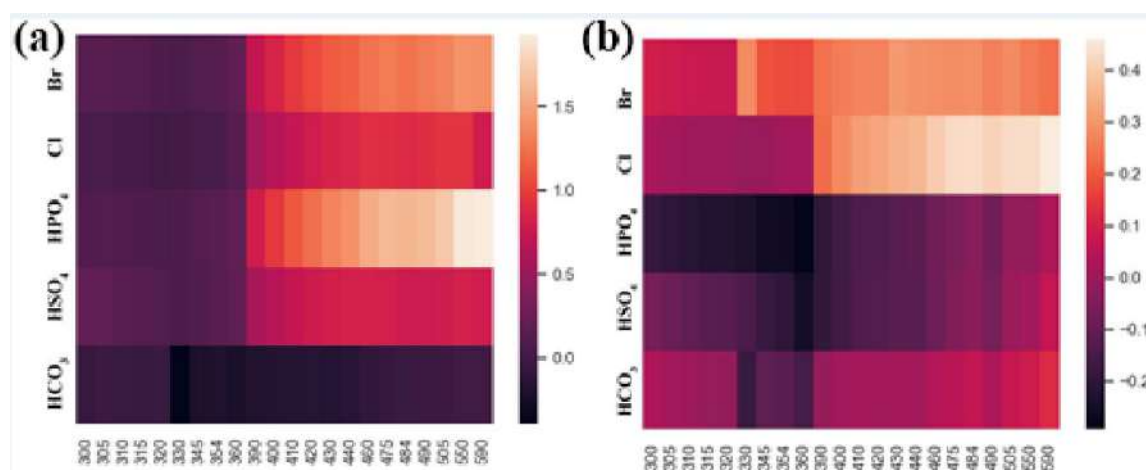


Figure A4.16 Heat maps of the optical responses of (a) L_5 and (b) L_6 toward anions in water. They display the pattern of responses of the ligands to the anions. The scale bar represents hues corresponding to relative intensity values as the optical responses.

Table A6. Effect of ligands **L₅** and **L₆** and their complexes on the growth of pathogenic bacteria *E. coli* MTCC 433 and *S. aureus* MRSA 100.

Compound	Concentration	Growth of <i>E. coli</i> MTCC 433*	Growth of <i>S. aureus</i> MRSA 100*
		(%)	(%)
L₅	1.0 µg/mL	37.46	64.67
	5.0 µg/mL	44.78	66.69
	10 µg/mL	49.13	74.97
L₆	1.0 µg/mL	42.81	76.53
	5.0 µg/mL	45.68	79.62
	10 µg/mL	54.72	90.19
5a	1.0 µg/mL	42.56	55.40
	5.0 µg/mL	48.47	64.93
	10 µg/mL	51.76	74.14
6a	1.0 µg/mL	54.56	72.34
	5.0 µg/mL	47.41	78.09
	10 µg/mL	79.21	85.74
5b	1.0 µg/mL	44.94	73.31
	5.0 µg/mL	62.07	66.63
	10 µg/mL	98.60	72.34
6b	1.0 µg/mL	54.80	79.72
	5.0 µg/mL	80.27	85.24
	10 µg/mL	105.01	89.89
5c	1.0 µg/mL	87.09	61.08
	5.0 µg/mL	84.88	63.97
	10 µg/mL	90.96	73.18
6c	1.0 µg/mL	94.57	86.97
	5.0 µg/mL	95.97	90.06
	10 µg/mL	99.34	93.58
5d	1.0 µg/mL	84.30	65.66
	5.0 µg/mL	96.87	65.43
	10 µg/mL	101.88	71.25
6d	1.0 µg/mL	87.26	81.12
	5.0 µg/mL	90.13	84.77
	10 µg/mL	94.74	90.19

* Growth of *E. coli* MTCC 433 and *S. aureus* MRSA 100 in percentage represents the average value calculated from triplicate samples.

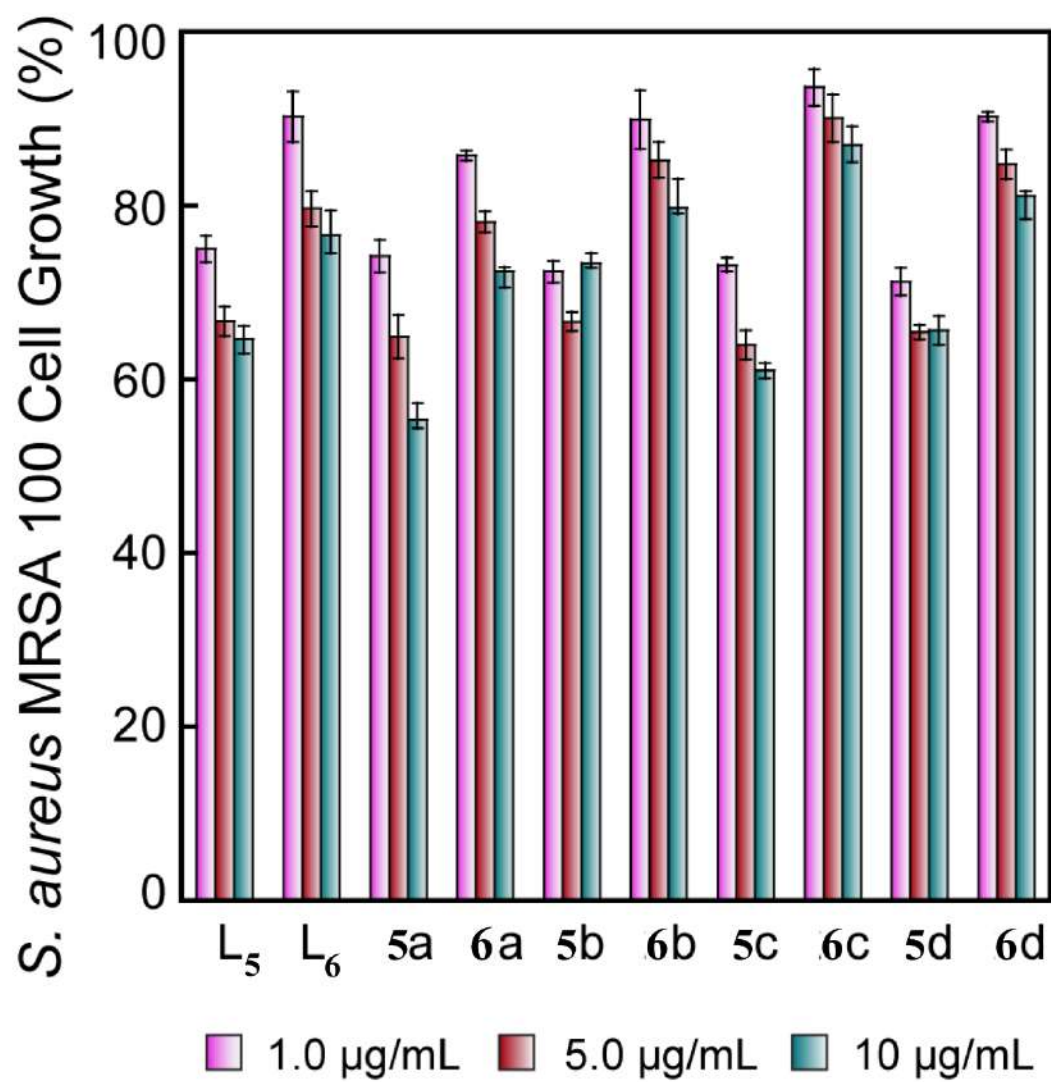


Figure A4.17 Bactericidal activity of ligands L_5 and L_6 and their complexes against *S. aureus* MRSA 100.

Table A7 Crystal parameters and refinement data of anion complexes

Parameter s	L ₅ ·DMSO	5a	5b	5c	5d	6d
Formula	C ₂₇ H ₂₂ N ₄ O ₆ S	C ₄₂ H ₅₃ N ₅ O 8	C ₄₁ H ₅₃ N ₅ O ₉ S	C ₄₁ H ₅₂ ClN ₅ O 6	C ₄₁ H ₅₂ BrN ₅ O 6	C ₄₅ H ₅₅ N ₄ BrO 5
Fw	530.55	755.89	791.94	746.33	790.78	779.83
Crystal system	Triclinic	Monoclinic	Monoclinic	Monoclinic	Monoclinic	Monoclinic
Space group	<i>P</i> -1	<i>P</i> 2 ₁ / <i>n</i>	<i>P</i> 2 ₁ / <i>n</i>	<i>P</i> 2 ₁ / <i>n</i>	<i>P</i> 2 ₁ / <i>n</i>	<i>C</i> 2/ <i>c</i>
<i>a</i> /Å	9.2795(15)	9.703(3)	9.9411(14)	9.8636(13)	9.864(3)	52.776(6)
<i>b</i> /Å	9.7556(17)	13.930(3)	14.454(2)	14.1737(19)	14.241(5)	8.7508(12)
<i>c</i> /Å	13.691(2)	29.661(8)	28.999(4)	28.934(4)	29.017(8)	17.833(2)
<i>α</i> /°	95.221(15)	90.00	90.00	90.00	90.00	90.00
<i>β</i> /°	93.741(5)	92.240(9)	97.05(5)	91.662(4)	91.357(10)	96.514(4)
<i>γ</i> /°	97.085(6)	90	90.00	90.00	90.00	90.00
<i>V</i> /Å ³	1221.1(3)	4006.0(19)	4135.3(10)	4043.4(9)	4075(2)	8182.7(17)
<i>Z</i>	2	4	4	4	4	8
<i>D</i> /g cm ⁻³	1.440	1.253	1.272	1.226	1.289	1.226
<i>μ</i> Mo K _α /mm ⁻¹	0.185	0.087	0.138	0.146	1.060	1.049
F000	548.0	1616.0	1472	1592.0	1664.0	3296.0
<i>T</i> /K	296(2)	296(2)	296(2)	296(2)	296(2)	296(2)
<i>θ</i> max.	28.09	23.92	20.87	25.09	23.10	27.70
Total no. of reflections	42038	54194	32707	75423	45668	136557
Independent reflections	6077	9553	6787	9743	7171	9815
Observed reflections	5127	4393	3656	4467	4243	5058
Parameters refined	345	501	510	482	482	482
<i>R</i> ₁ , <i>I</i> > 2σ(<i>I</i>)	0.05	0.09	0.08	0.06	0.05	0.06
w <i>R</i> ₂ , <i>I</i> > 2σ(<i>I</i>)	0.1475	0.2216	0.2099	0.1596	0.1173	0.1725
GOF (<i>F</i> ²)	0.963	1.177	1.095	0.869	1.008	1.103
CCDC no.	2075153	2075154	2077109	2075155	2075156	2075157

Table A8: Hydrogen bonding distances (Å) and Bond angles (°) in free ligand (**L₅**) and its complexes **5a**, **5b**, **5c**, **5d** and **6d**)

Ligand/Complex	D–H···A	d(D···H)/Å	d(H···A)/Å	d(D···A)/Å	<D–H···A/°	Symmetry codes
L₅ -DMSO	N2-H2N···O6	0.86	2.12	2.921(2)	154	1-x, 1-y, 1-z
	N3-H3N···O6	0.86	1.96	2.777(3)	159	1-x, 1-y, 1-z
	C7-H7···O4	0.93	2.57	3.363(2)	144	1-x, 1-y, -z
	C15-H15···O3	0.93	2.36	2.907(2)	117	x, y, z
	C21-H21···O3	0.93	2.33	2.899(2)	119	x, y, z
	C27-H27B···O2	0.96	2.50	3.245(3)	135	x, -1+y, z
5a	N2-H2N···O7	0.86	2.15	2.971(4)	158	1-x, 1-y, -z
	N3-H3N···O6	0.86	1.92	2.782(4)	177	1-x, 1-y, -z
	O8-H8O···O7	0.82	1.87	2.681(3)	168	1-x, -y, -z
	C8-H8···O1	0.93	2.42	3.251(5)	149	1/2-x, -1/2+y, 1/2-z
	C15-H15···O7	0.93	2.57	3.332(4)	139	1-x, 1-y, -z
	C17-H17···O3	0.93	2.29	2.830(4)	116	x, y, z
	C20-H20···O3	0.93	2.24	2.807(4)	118	x, y, z
	C51-H51B···O1	0.97	2.49	3.447(4)	167	1+x, y, z
	C55-H55A···O8	0.97	2.50	3.418(4)	157	x, 1+y, z
5b	N2-H2N···O8	0.86	2.11	2.899(3)	152	1/2+x, 1/2-y, 1/2+z
	N3-H3N···O7	0.86	2.08	2.924(3)	167	1/2+x, 1/2-y, 1/2+z
	O6-H6O···O9	0.82	2.30	2.921(3)	133	1-x, 1-y, -z
	C2-H2C···O2	0.93	2.55	3.341(3)	142	3/2-x, -1/2+y, 1/2-z
	C8-H8A···O2	0.93	2.43	2.781(3)	102	x, y, z
	C10-H10···O9	0.93	2.38	3.301(3)	169	x, y, z
	C15-H15···O8	0.93	2.26	3.031(3)	140	1/2+x, 1/2-y, 1/2+z
	C17-H17···O3	0.93	2.50	3.102(3)	122	x, y, z
	C23-H23···O5	0.93	2.15	2.492(2)	100	x, y, z
	C26-H26A···O8	0.96	2.59	3.542(3)	167	1-x, 1-y, -z
	C29-H29B···O8	0.97	2.57	3.451(3)	144	1-x, 1-y, -z
	C30-H30A···O1	0.96	2.36	3.168(3)	141	3/2-x, -1/2+y, 1/2-z
	C32-H32B···O5	0.97	2.48	3.432(3)	168	1-x, 1-y, 1-z
	C39-H39A···N3	0.97	2.61	3.461(3)	147	1/2-x, 1/2+y, 1/2-z
	C40-H40B···O6	0.97	2.43	3.324(3)	152	x, y, z

Contd.

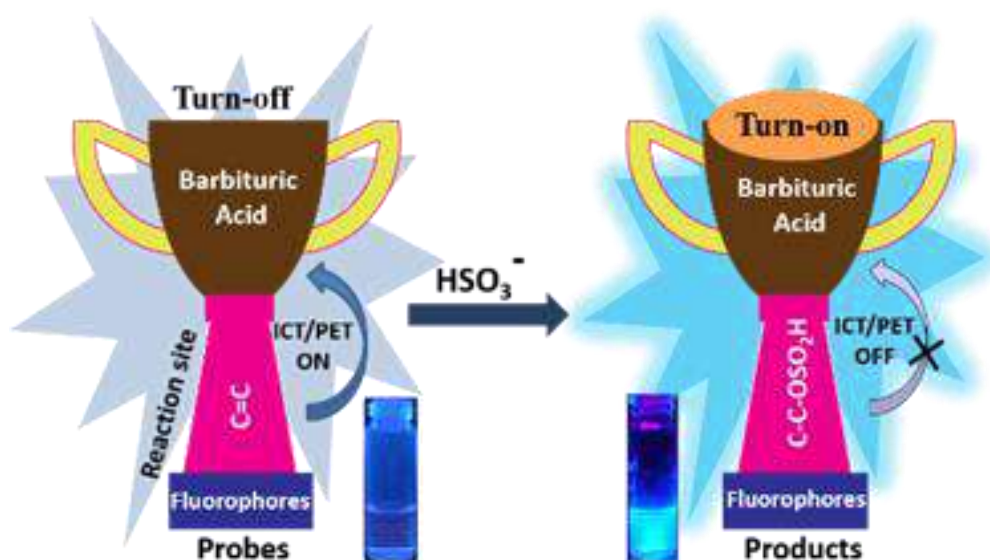
Ligand/Complex	D-H...A	d(D...H)/Å	d(H...A)/Å	d(D...A)/Å	<D-H...A/°	Symmetry codes
5c	N2-H2N...C11	0.86	2.44	3.226(4)	152	1-x, 1-y, -z
	N3-H3N...C11	0.86	2.46	3.252(4)	167	1-x, 1-y, -z
	C4-H4...O1	0.93	2.50	3.330(5)	142	1/2-x, -1/2+y, 1/2z
	C15-H15...O3	0.93	2.31	2.859(4)	102	x, y, z
	C17-H17...O6	0.93	2.50	3.397(5)	169	x, y, z
	C21-H21...O3	0.93	2.30	2.850(4)	169	x, y, z
	C36-H36A...O6	0.97	2.48	3.394(5)	169	x, y, z
	C40-H40B...O1	0.97	2.53	3.492(5)	169	1+x, y, z
5d	N2-H2N...Br1	0.86	2.44	3.347(3)	151	1-x, 1-y, -z
	N3-H3N...Br1	0.86	2.46	3.340(3)	155	1-x, 1-y, -z
	C1-H1...O2	0.93	2.50	3.381(6)	149	1/2-x, -1/2+y, 1/2-z
	C15-H15...O6	0.93	2.31	3.347(6)	160	x, y, z
	C17-H17...O3	0.93	2.50	2.878(5)	117	x, y, z
	C21-H21...O3	0.93	2.30	2.858(5)	118	x, y, z
	C29-H29A...O2	0.97	2.48	3.499(5)	171	x, y, z
	C33-H33B...O6	0.97	2.53	3.375(6)	158	1+x, y, z
6d	N2-H2N...Br1	0.86	2.46	3.295(3)	164	x, 1-y, -1/2+z
	N3-H3N...Br1	0.86	2.59	3.413(3)	159	x, 1-y, -1/2+z
	C17-H17...O3	0.93	2.33	2.884(4)	118	x, y, z
	C21-H21...O3	0.93	2.23	2.815(5)	120	x, y, z
	C26-H26... Br1	0.93	2.92	3.817(4)	161	x, 1-y, -1/2+z
	C44-H44A... Br1	0.97	2.88	3.753(5)	150	x, -1+y, z

References

- A4.1 E. M. Blalock, ed. A Beginner's Guide to Microarrays. *Springer Science & Business Media*, 2003.
A4.2 J. C. Miller, and J. N. Miller, A review. *Statistics for Analytical Chemistry*, 1988.

Chapter 5

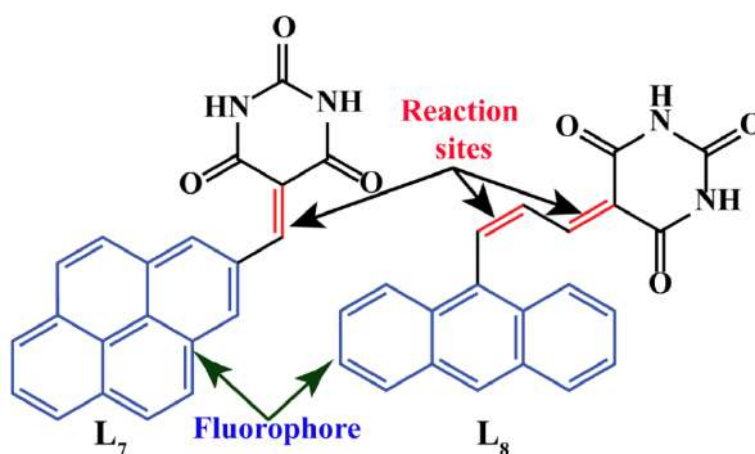
Selective Chemodosimetric 'Turn-On' Fluorescence Sensor for HSO_3^- : Comparing the Reactivity of the Exocyclic vs. Non-Exocyclic C=C Double Bond



5.1 Background and Focus of the Chapter

HSO_3^- is a well-known reducing agent, and under an acidic environment, releases SO_2 , which is one of the important air pollutants, predominant in the air, generated from extensive combustion of fossil fuels^{5.1-5.4}. In the pharmaceutical industry, it is used as an intermediate in the manufacture of metamizole sodium tablets, aminopyrine, and a popular additive in epinephrine medications to avoid adrenaline inactivation^{5.5-5.6}. It is considered to be an important food-preserving additive, which inhibits oxidation (and hence the discolouration and deterioration) by anaerobic bacterial and fungal microorganisms in fruits, seafood, meats, vegetables, and beverages^{5.7-5.8}. However, HSO_3^- is a toxic substance with detrimental (including allergic) effects such as asthma, gastrointestinal diseases, skin allergies, DNA cleavage, and chronic bronchitis. Moreover, in some cases, a higher level of HSO_3^- concentration may also be responsible for lowering blood pressure, kidney failure, etc.^{5.9-5.11} In 1986, following 13 death tolls along with ~500 reports of intense allergic reactions, mostly in the asthmatic population, arising upon the consumption of sulphite-treated food forced the U.S. Food and Drug Administration (FDA) to limit its use on various food sources^{5.12}. Concerns were also being raised over the health risk associated with the hypersensitivity of sulphite observed in children¹³. The U.S. authorities have also declared to highlight details about all the crucial products that have more than 10 mg/mL of sulfite^{5.14}. Researchers have found that an incremental uptake of NaHSO_3 (0.1-1.0%) remarkably increases the hypodermal and intramuscular toxicities of epinephrine in mice, rats, dogs, and rabbits^{5.15}. Besides, the overuse of HSO_3^- , a popular industrial material for the production of leather, dye, paper, toilet cleaners, and cosmetic formulation, for preventing corrosion in the reactor^{5.16} also causes a severe upsurge in the chemical oxygen demand (COD), taking a toll on the aquatic environment too^{5.17}. Hence, selective and efficient recognition of HSO_3^- has become a crucial direction in the research field. Although many techniques are available for HSO_3^- detection, most of them are expensive as well as prone to be affected by the presence of other sulphur products with a high chance of damage. Therefore, it is essential to develop some decent methods to recognize HSO_3^- more selectively and efficiently for further applications in the future^{5.18-5.19}. Of them, fluorescence emission-based probes provide a straightforward approach compared to other reported techniques, for its recognition even in biological species with the fast, non-invasive, selective, and sensitive process^{5.20-5.23}. Although for the detection of HSO_3^- , several fluorescence probes have been reported based on nucleophilic addition reaction^{5.24}, due to several factors (such as probe localization, pH, temperature, solubility, polarity, emission efficiency, cell thickness of the photon beam, detection limit, response time, and use of organic or mixed organic solvents system),^{5.25-5.26} new robust HSO_3^- fluorescent probes still need to be

designed and developed further. Guo *et al.* reported probes that generated a new platform for HSO_3^- detection with a mechanism based on Michael condensation.^{5.27} Thereafter, several articles have been reported on the detection of any of SO_2 derivatives with selectivity^{5.28-5.30}. In addition, some of these kinds of probes included a complicated emission response, poor selectivity with the interference of other sulphur derivatives (like H_2S , SH , bio-thiol, etc.), and variable excitation spectra along with their multiple synthetic steps and sensing mechanisms. In our continuing effort to develop probes for various anion^{5.31-5.32}, herein we designed a pair of reaction-based fluorescent π conjugated probes L_7 and L_8 for ‘turn-on’, rapid, selective, and sensitive detection of HSO_3^- in a mixed aqueous medium. While for both the probes, the fluorometric as well as colorimetric recognition operated *via* traditional PET/ICT. Probe L_7 also featured excimer formation. In addition, our focus was also to verify whether the lengthening of the π -conjugation influenced the reactivity of HSO_3^- and if it made any scope for an additional site for anion to attack. For this, while we rationally synthesized the probe L_8 , the spectroscopic and analytical techniques supported the proposed mechanism which revealed no additional effect on the extra double bond for probe L_8 . To prove the feasibility of the probe in practical applications, we used L_7 for the quantitative detection of HSO_3^- in real food as well as water samples and in real samples and in dip-stick analysis.



Scheme 5.1 Chemical structure of the probes L_7 and L_8 .

5.2 Results and discussion

5.2.1 The rationale behind designing the probes for HSO_3^- detection

In this report, the new fluorescent probes (L_7 and L_8) were synthesized *via* the traditional condensation reaction leading to form D- π -A-type structure by connecting pyrene/anthracene as an electron donor (D) and barbituric acid (BA) as an electron acceptor (A). The donor and the acceptor were connected through C=C double bond(s), which provided a probable responsive site for HSO_3^- (Scheme 5.1). This kind of D- π -A structure has been commonly used as a

fluorogenic motif to develop ICT/PET-based fluorescent probes for sensing.^{5.33-5.34} Pyrene and anthracene were picked up as fluorophore units for their outstanding photo-physical properties. The detailed synthetic procedure and characterization have been provided in the Supporting Information. According to reported literature, HSO_3^- ion can attack C=C double bonds *via* nucleophilic addition reaction and thus destroy the extended conjugation^{5.35}. Furthermore, the strong electron-withdrawing nature of BA (due to the presence of polyamide group) would increase the reactivity of the C=C double bond and provide a selective and facile site for effective nucleophilic addition by HSO_3^- .^{5.36-5.37} We have developed another probe, **L₈**, where a non-exocyclic C=C double bond was purposefully introduced to verify the reactivity, as well as selectivity towards nucleophilic addition reaction. The intent of incorporating the more unsaturation was to check how the lengthening of the conjugation affected the reactivity of an incoming HSO_3^- and whether it made any room for an additional HSO_3^- to attack.

5.2.2 The selective colorimetric response towards HSO_3^-

The anion binding properties of probes, **L₇** and **L₈** (50 μM) towards various biologically important anions such as F^- , Br^- , HSO_4^- , N_3^- , H_2PO_4^- , HPO_4^{2-} , ClO_4^- , AcO^- , CN^- , PO_4^{3-} , $\text{S}_2\text{O}_8^{2-}$, $\text{S}_2\text{O}_3^{2-}$, SH^- , OCl^- were studied which exhibited excellent optical sensing properties towards only HSO_3^- through colorimetric and fluorometric responses in aq. CH_3CN ($\text{CH}_3\text{CN}-\text{H}_2\text{O} = 7:3$ v/v, 1 mM HEPES buffer, pH = 7.4) medium. Probe **L₇** displayed three well-defined absorption bands at 319, 330, and 347 nm (presumably due to the absorption of pyrene) alongside small humps at 375 and 396 nm (seemingly due to the intra-molecular $\pi-\pi^*$ transition) with a low-energy band at 452 nm owing to the ICT transition^{5.38} (Fig. 5.1a). In contrast, probe **L₈** also showed three sharp bands in the absorption spectra at 351, 368, and 388 nm which could be attributed to the presence of anthracene moiety in the same molecule. In addition, **L₈** also has an ICT peak at 482 nm with a 20 nm red-shift compared to **L₇** (Fig. 5.1d). The absorbance at 452 for **L₇** and 482 for **L₈** nm (both ascribed to the ICT) are in good agreement with the yellow-orange colour of the probes. Fig. 5.1a displayed that only the addition of HSO_3^- caused a significant spectral shift, whilst the addition of other selected anions has no effect. This observation showed the high selectivity of **L₇** for HSO_3^- . Furthermore, to achieve a quantitative assessment for the detailed interaction between HSO_3^- and **L₇**, systematic titration was carried out with increasing concentration of HSO_3^- (0-26 equivalents) (Fig. 5.1b). The spectra revealed that the signature peaks at 319, 330, and 347 nm gradually decreased, alongside the ICT band at 452 nm. The absorption band at 375 nm and 396 nm was systematically amplified along with the formation of

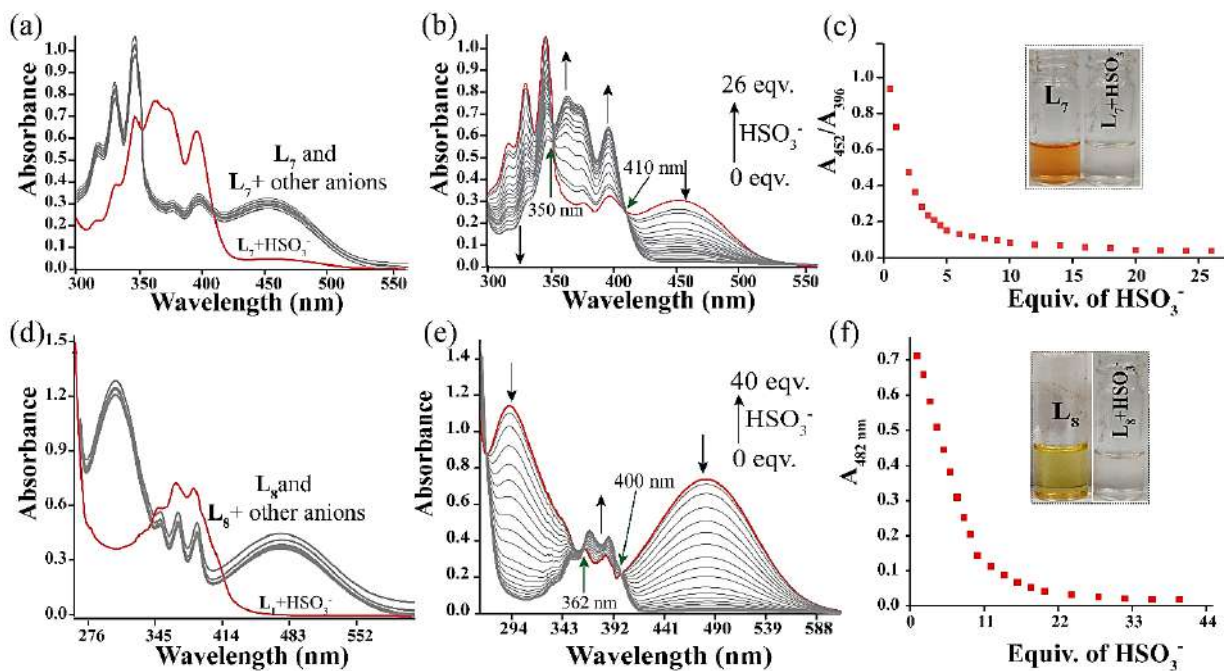


Figure 5.1 (a) and (d) Competitive absorption spectra in the presence of different anions (F^- , Cl^- , Br^- , I^- , AcO^- , N_3^- , HPO_4^{2-} , $H_2PO_4^-$, S^{2-} , HSO_4^- , ClO_4^- , CN^- , AsO_4^{3-} , SO_3^{2-} , $S_2O_3^{2-}$, SH^-) in aq. CH_3CN ($CH_3CN-H_2O = 7:3$ v/v, 1 mM HEPES buffer, pH = 7.4) and the inset shows photographs of the colour change in the presence of HSO_3^- anion, respectively for L_7 and L_8 ; (b) and (e) UV-vis absorption titration spectra in aq. CH_3CN ($CH_3CN-H_2O = 7:3$ v/v, 1 mM HEPES buffer, pH = 7.4) upon incremental addition of HSO_3^- to L_7 and L_8 ($c = 5$ mM) respectively; (c) and (f) shows the absorption intensity ($A_{452/396nm}$ for L_7 and A_{482nm} for L_8) as a function of equivalent of HSO_3^- .

a new blue-shifted band at 362 nm. Thus, the addition of 26 equivalents HSO_3^- (1300 μM) caused a prompt colour change from orange-red (L_7) to almost colourless (P_7) within seconds, detectable even with the naked eyes (Fig. 5.1c inset). Meanwhile, the formation of two prominent isosbestic points (410 and 350 nm) and hypsochromic shift in the absorption spectra hinted at some chemical interactions between L_7 and HSO_3^- . Thus L_7 portrayed the colorimetric selectivity as well as sensitivity towards HSO_3^- with a limit of detection (LOD) of 1.16 μM (0.09 ppm) (Fig. A5.1). In the case of L_8 , the selectivity was investigated from the absorbance spectra (Fig. 5.1d) which included a significant spectral shift triggered by the addition of only HSO_3^- in presence of competing analytes. To get a clear and quantitative idea about the interaction between the probe L_8 and HSO_3^- anion, systematic titration was performed with the gradual addition of HSO_3^- in the test medium (Fig. 5.1e). The titration profile revealed that upon gradual addition of HSO_3^- to L_8 , triggered a systematic diminution of absorbance at 291 nm. Akin to L_7 , the absorbance at 482 nm gradually decreased and flattens upon the addition of 40 equivalents (2000 μM) of HSO_3^- ion (Fig 5.1f), leading to the breaking of the π -conjugation in the product. In the same spectra, we have observed that the absorbance of 368 and 387 nm concomitantly

increased with a very small red-shift, making a rapid colour change from orange-yellow (**L**₈) to colourless (**P**₈) (Fig. 5.1f, inset) along with the emergence of two separate isosbestic points at 362 and 400 nm. Fig. 5.1b, e portrayed that the observed blue shift at higher wavelength presumably due to the addition reaction between the probes (**L**₇ and **L**₈) and analyte, would have reduced the displacement of π -electron density from donor sites to acceptor sites which suggested the breaking of the extended π -conjugation in the products (**P**₇ and **P**₈). As a result, the blocking of the ICT process along with the bad solubility of both the products might cause the decline of the absorbance systematically. The appearance of new isosbestic points proposed that the interaction between HSO_3^- and the probe was one-to-one conversion to form a new compound in the Electronic ground state. Thus **L**₈ represented the colorimetric selectivity as well as sensitivity towards HSO_3^- with a limit of detection of 9.4 μM (0.76 ppm) (Fig. A5.2). The UV-vis titration spectral profile, however, did not bear any sign of a second HSO_3^- addition to **L**₈ even after administration of excess (40 equiv.) of the analyte.

5.2.3 Selective Fluorescence Response towards HSO_3^-

Pyrene is considered to be one of the most used fluorophores due to its well-characterized monomer and excimer emission in the excited state. Mainly two types of excimer emission are observed: the conventional dynamic excimer and newly established static excimer. These two kinds of emission mainly rely on the effective distance between two pyrene molecules^{5,39}. We tried to investigate the nature of the excimer based on its excitation spectra. Fig. A5.3 displayed that the excitation spectra monitored at 376 and 396 nm were similar but the peak at 455 nm was ~18 nm red-shifted compared to the former two. This suggested that the chemical species corresponding to lower emission wavelengths were different from that concerning the higher wavelength.^{5,40} It could be speculated that the excitation band at ~455 nm was evident of intermolecular π - π stacking interaction resulting in the formation of the dimer consisting of two pyrene moieties in the ground state. The formation of intermolecular static excimer of **L**₇ could be supported from the above-mentioned experimental observation during the reaction with externally added analyte. Upon excitation at 345 nm, the initial intensities of monomer and excimer emission were very low in the absence of any external analyte. This could be ascribed to, the occurrence of traditional PET or weak ICT process between the pyrene and BA units along with the random alignment of pyrene molecules with respect to each other. The emission profile displayed that only the addition of HSO_3^- to **L**₇ resulted in excellent selective 'turn-on' fluorescence response relative to other competing foreign analytes (Fig. 5.2a) *via* ratiometric fluorescence approach (*vide infra*). On progressive addition of HSO_3^- (0-30 equivalents) to **L**₇

(50 μM), the increment of excimer intensity (at 455 nm with ~ 18 times enhancement) was found to be more prominent than its monomer counterpart (~ 10 nm blue-shifted at 376 nm and ~ 11 nm blue-shifted at 396 nm having ~ 20 times enhancement for both cases) (Fig. 5.2b). As a result, we speculated that Michael addition reaction between the anionic HSO_3^- and the C=C bond of L_7 led to the interruption of the PET process along with a restriction in weak dominance of intramolecular charge transfer (ICT) process initiated by the breaking of conjugation in L_7 , resulting in an excellent fluorescence ‘turn-on’ response.

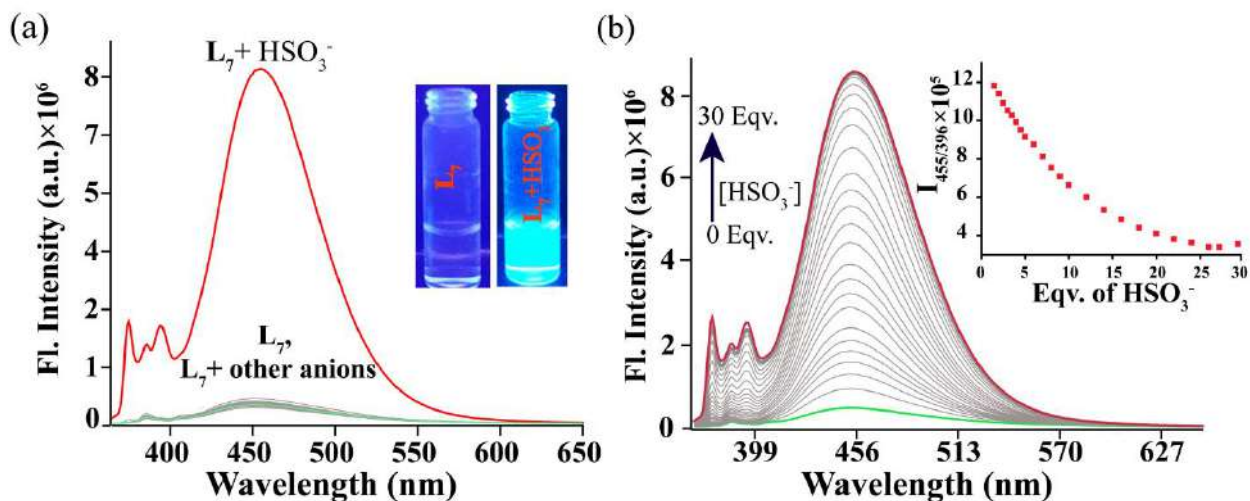


Figure 5.2 (a) Change of emission spectra with various anionic analytes (5×10^{-2} M) in mixed organic medium ($\text{CH}_3\text{CN-H}_2\text{O} = 7:3$ v/v, 1 mM HEPES buffer, pH = 7.4) and the inset shows the corresponding colour changes in the presence of HSO_3^- under UV lamp, respectively for L_7 (5×10^{-5} M); (b) Fluorescence emission titration in mixed organic medium ($\text{CH}_3\text{CN-H}_2\text{O} = 7:3$ v/v, 1 mM HEPES buffer, pH = 7.4) upon incremental addition of HSO_3^- to L_7 ($c = 5 \times 10^{-5}$ M) respectively; Inset: Shows the emission intensity ($I_{455/396}$ for L_7) as a function of the equivalent of HSO_3^- .

A sharp change in emission intensity ($I_{455/396}$) was detected up to 20 equivalents (1000 μM) of HSO_3^- . Afterward, there was no such spectral change in the emission intensity ratio of the entire system and the spectral enhancement reached a plateau after the addition of 30 equivalents (1500 μM) of HSO_3^- (Fig. 5.2b, inset). In the case of L_7 , the LOD was calculated to be 6.74 μM (0.55 ppm) (for $\lambda_{\text{em}} 376$ nm) and 0.65 nM (0.053 ppb) (for $\lambda_{\text{em}} 455$ nm) (Fig. A5.5a, A5.5b). The LOD value estimated based on the intensity at 455 nm was found to be one of the lowest in comparison with any other fluorescent probes reported in the literature. Moreover, fluorescence response time suggested that the sensing performance of L_7 was investigated ~ 3 minutes after the addition of HSO_3^- to confirm that the reaction between L_7 and HSO_3^- had reached completion of equilibrium (Fig. A5.6). Considering, pseudo-first-order kinetics, the reaction rate constants of L_7 with HSO_3^- were calculated to be 0.468 min^{-1} (Fig. A5.7). On the other hand, the fluorescence spectrum of L_8 (50 μM) in the aforementioned medium, upon excitation at 395 nm,

displayed weak emission intensity at 435 and 460 nm which are typical of the anthracene moiety (Fig. 5.2c). The initial weak emission of **L**₈ was attributed to an intra-molecular photo-induced electron transfer (PET) process operating from the excited state of the anthracene moiety (donor site) to the BA core (acceptor site). The emission spectra revealed that upon the addition of HSO₃⁻ to **L**₈, a significant ‘turn-on’ response occurred over competitive analytes (*vide infra*) (Fig. 5.2c). This observation suggested excellent selectivity of **L**₈ towards HSO₃⁻. It was assumed that upon the addition of anionic HSO₃⁻ to **L**₈, the conventional PET process operating between the anthracene and BA unit was blocked, and finally, an impressive ‘turn-on’ fluorescence emission took place at 440 nm. Upon gradual administration of HSO₃⁻ to the solution of **L**₈ (50 μM), the emission intensities at 440 and 460 nm were systematically enhanced up to the addition of 34 equiv. of HSO₃⁻ (Fig. 5.2d). The emission titration plot exhibited a linear increase up to the addition of 0-5 equiv. (0- 250 μM) of HSO₃⁻ following a small increment displayed up to 20 equiv. (1000 μM), and finally, the spectral enhancement got almost saturated at 34 equiv. (1700 μM) of HSO₃⁻ (Fig. 5.2d, inset). Primarily, it was assumed that the addition of HSO₃⁻ to probe **L**₈, led to the suppression of PET from the anthracene system and thus resulting in the rise of the fluorescence intensity originating from the anthracene motif. The fluorescence I_{440nm} was found to be linearly related to the HSO₃⁻ concentration (Fig. A5.8). The detection of limit (LOD) was found to be as low as 10.5 μM (0.85 ppm). Moreover, the emission quantum efficiency (Φ) was calculated for the probes which were found to be 0.0011 and 0.00053 respectively for **L**₇ and **L**₈. While the corresponding values have been changed to 0.0457 and 0.0185 in products **P**₇ and **P**₈ accordingly, hinting at an outstanding selectivity of the probes towards HSO₃⁻. The outcome of the experiment demonstrated that the pyrene-based probe, **L**₇, showed high sensitivity towards HSO₃⁻ compared to its anthracene analogue, **L**₈, (based on LOD values) under the same experimental conditions. Moreover, the absence of any additional discrete signature in the emission titration profile suggested that no additional chemical species seemed to form (even after the addition of 34 equiv. of HSO₃⁻) owing to the reaction associated with the non-exocyclic unsaturated C=C double bond motif present in **L**₈, which was consistent with the absorption studies.

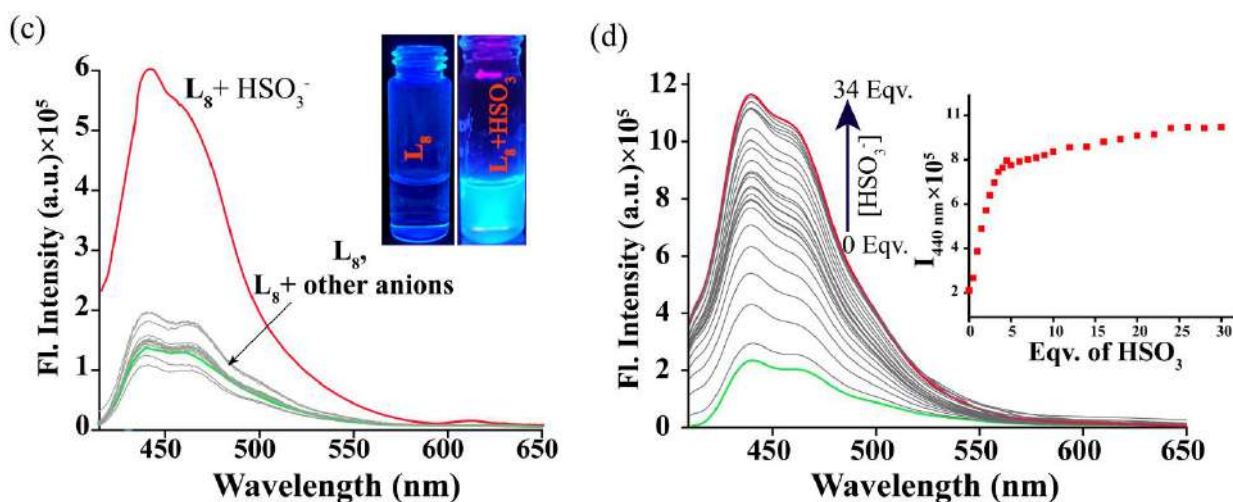


Figure 5.3 (c) Change of emission spectra with various anionic analytes (5×10^{-2} M) in mixed organic medium ($\text{CH}_3\text{CN}-\text{H}_2\text{O} = 7:3$ v/v, 1 mM HEPES buffer, pH = 7.4) and the inset shows the corresponding colour changes in the presence of HSO_3^- under UV lamp, respectively for L_8 (5×10^{-5} M); (d) Fluorescence emission titration in mixed organic medium ($\text{CH}_3\text{CN}-\text{H}_2\text{O} = 7:3$ v/v, 1 mM HEPES buffer, pH = 7.4) upon incremental addition of HSO_3^- to L_8 ($c = 5 \times 10^{-5}$ M) respectively; Inset: Shows the emission intensity ($I_{440\text{nm}}$ for L_8) as a function of the equivalent of HSO_3^- .

5.2.4 Interference studies and Effect of pH

Minimal external interference from any competing agents makes a sensor more reliable and usable for further application. Therefore, to check the selectivity, 10 equivalents of bisulphite ion was added to each of the probes in the presence of the same equivalents of other competing anions such as F^- , Br^- , HSO_4^- , N_3^- , H_2PO_4^- , HPO_4^{2-} , ClO_4^- , AcO^- , CN^- , PO_4^{3-} , $\text{S}_2\text{O}_8^{2-}$, $\text{S}_2\text{O}_3^{2-}$, SH^- , OCl^- in the aforementioned test solution. But no obvious influence was observed in the original fluorescence intensity obtained from the addition of bisulphite only (Fig. 5.4a, b) substantiating the lack of interference in the emission of the probes by the other foreign analytes (including nucleophile anions in the presence of bisulphite). To verify the influence of pH on the detecting capability of probes towards bisulphite anion, we have recorded the emission spectra of L_7 (for both monomer and excimer emission) in the presence and the absence of bisulphite anion at various pH values (Fig. A5.9). While in the absence of bisulphite anion, probe L_7 showed consistent and comparable fluorometric responses at acidic, neutral, and basic pH, in the presence of the anion, it displayed significant fluorescence ‘turn-on’ responses at acidic and neutral pH, barring the basic condition. This experiment revealed that probe L_7 was compatible in detecting bisulphite anion under low pH as well as in neutral pH.

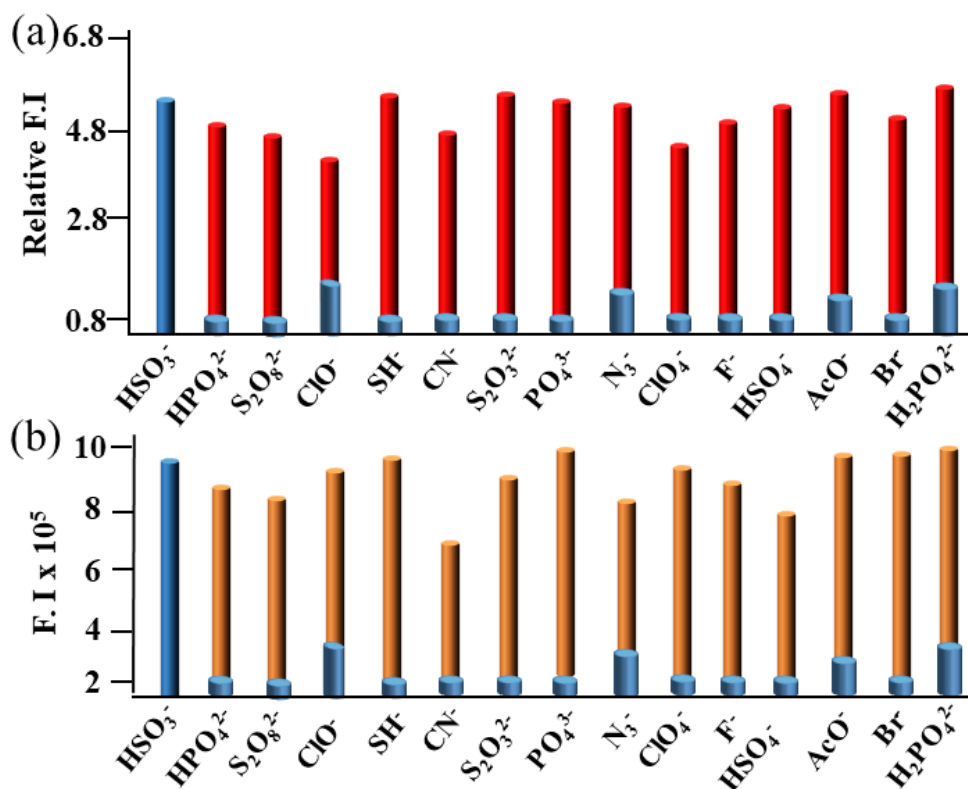


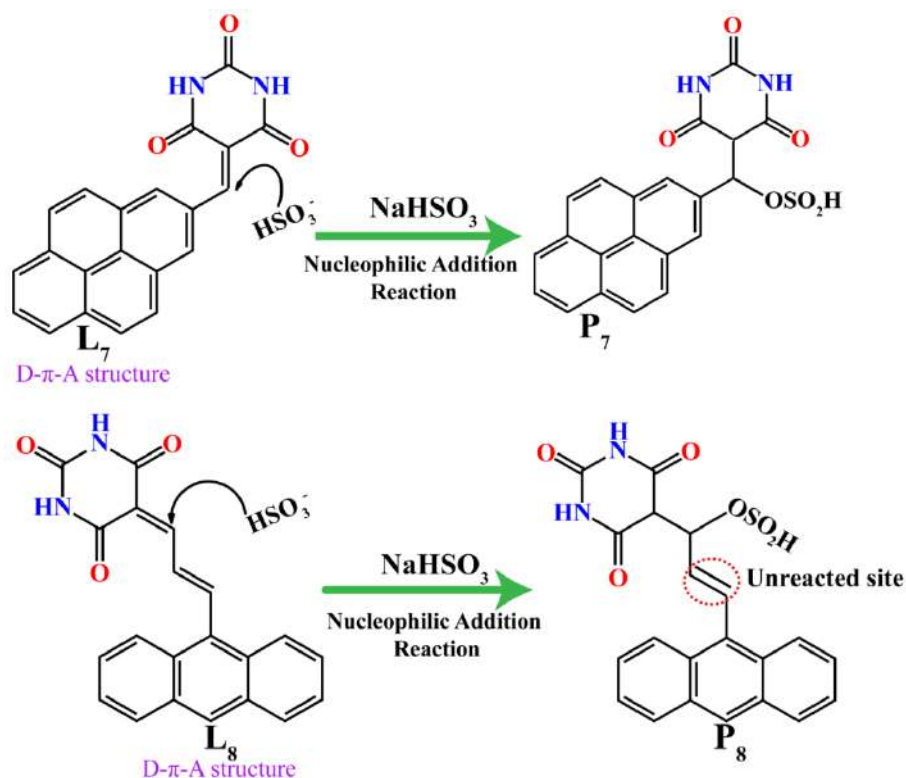
Figure 5.4 (a) and (b) depict the interference study of probe **L7** and **L8** (0.05 mM) in the presence of various competitive anions (0.5 mM) such as F⁻, Br⁻, HSO₄⁻, N₃⁻, H₂PO₄⁻, HPO₄²⁻, AcO⁻, ClO₄⁻, CN⁻, PO₄³⁻, S₂O₈²⁻, S₂O₃²⁻, SH⁻, OCl⁻ alongside HSO₃⁻ anion. The blue bar indicates probe **L7/L8** + anions and the red/brown bar shows **L7/L8** + anions + HSO₃⁻.

5.3 A plausible mechanism of bisulphite sensing

It was assumed that to attain a facile nucleophilic addition reaction by a nucleophilic anion, the BA unit played a crucial role to increase the reactivity of the C=C bond leading to a successful addition reaction upon administration of bisulphite ion (Scheme 5.2). Based on the obtained spectroscopic results so far, we envisaged that the optical changes after the addition of the anion to the probes might be associated with the bisulphite attack at the β carbon of the exocyclic C=C double bond (more electrophilic than its non-exocyclic counterpart) in a nucleophilic fashion to generate the daughter product in each case. Thus, the pyrene-based probe **L7** and anthracene-based probe **L8** reacted with HSO₃⁻ leading to the formation of the products **P7** and **P8** respectively. To get a better understanding of the reaction mechanism between the probes and anion we have performed thin layer chromatography (TLC) experiments, where the reaction mixture of the probes with HSO₃⁻ showed the presence of a new fluorescent species with higher polarity compared to the original substrate in each of the cases with probes **L7** and **L8**. The IR spectra displayed the disappearing of the C=C stretch at 1739 cm⁻¹ specifying a chemical reaction between **L7/ L8** and HSO₃⁻ (Fig. A5.12, A5.15). To explore the reaction mechanism,

mass spectra have been analysed where the probe **L**₇ exhibited a peak at m/z 341.0956 (calc. m/z

=



Scheme 5.2 The probable mechanism for the detection of HSO_3^- by the probes (**L**₇ and **L**₈).

340.0848) before NaHSO_3 addition, which resembled the $[\text{L}_7 + \text{H}]^+$ species (Fig. A2.49). Upon addition of NaHSO_3 , a peak appeared at m/z 421.0518, which corresponded to the adduct species $[\text{P}_7]^-$ (Fig. A5.11). On the other hand, before addition of HSO_3^- to **L**₈ solution, a peak was found at m/z 342.1004 (calc. = 343.1004) (Fig. A2.52), after HSO_3^- addition, two new peaks, corresponding to the $[\text{P}_8]^-$ and $[\text{L}_8 + \text{NaHSO}_3]^-$ species, showed up at $m/z = 423.0623$ (calc. $m/z = 424.0729$) and $m/z = 445.0441$, respectively (Fig. A5.14). Interestingly, the mass spectral analysis provided us with no proof of the existence of the compound supposedly formed by the nucleophilic addition at the non-exocyclic C=C double-bonded carbon (**L**₈) even in the presence of excess HSO_3^- . To confirm the reaction mechanism between the probes **L**₇ and **L**₈, systematic ^1H NMR titration analysis was performed in the absence and the presence of HSO_3^- in $\text{DMSO-}d_6$. The titration profile of **L**₇ suggested that (Fig. 5.5a), the peak at 9.1 ppm corresponding to H_b (attached with C=C bond), gradually decreased and finally completely vanished. Concurrently, the new peaks, referred to as H_a and H_b , appearing at 8.6 and 6.4 ppm, systematically increased in intensity after the probe reacted with HSO_3^- , signifying the construction of a C–C single bond between pyrene and barbituric acid moieties. In the case of **L**₈, the original peaks (H_b , H_c and, H_d) situated at 7.6 and 8.8 ppm, were systematically reduced and underwent upfield shifts after

the addition of the analyte and concomitantly the new peaks ($H_{a'}$, $H_{b'}$, $H_{c'}$ and $H_{d'}$) gradually rose in intensity at 1.3, 5.1, 6.5 and 7.1 ppm respectively, pointing to the gradual formation of P_8 (Fig. 5.5b).

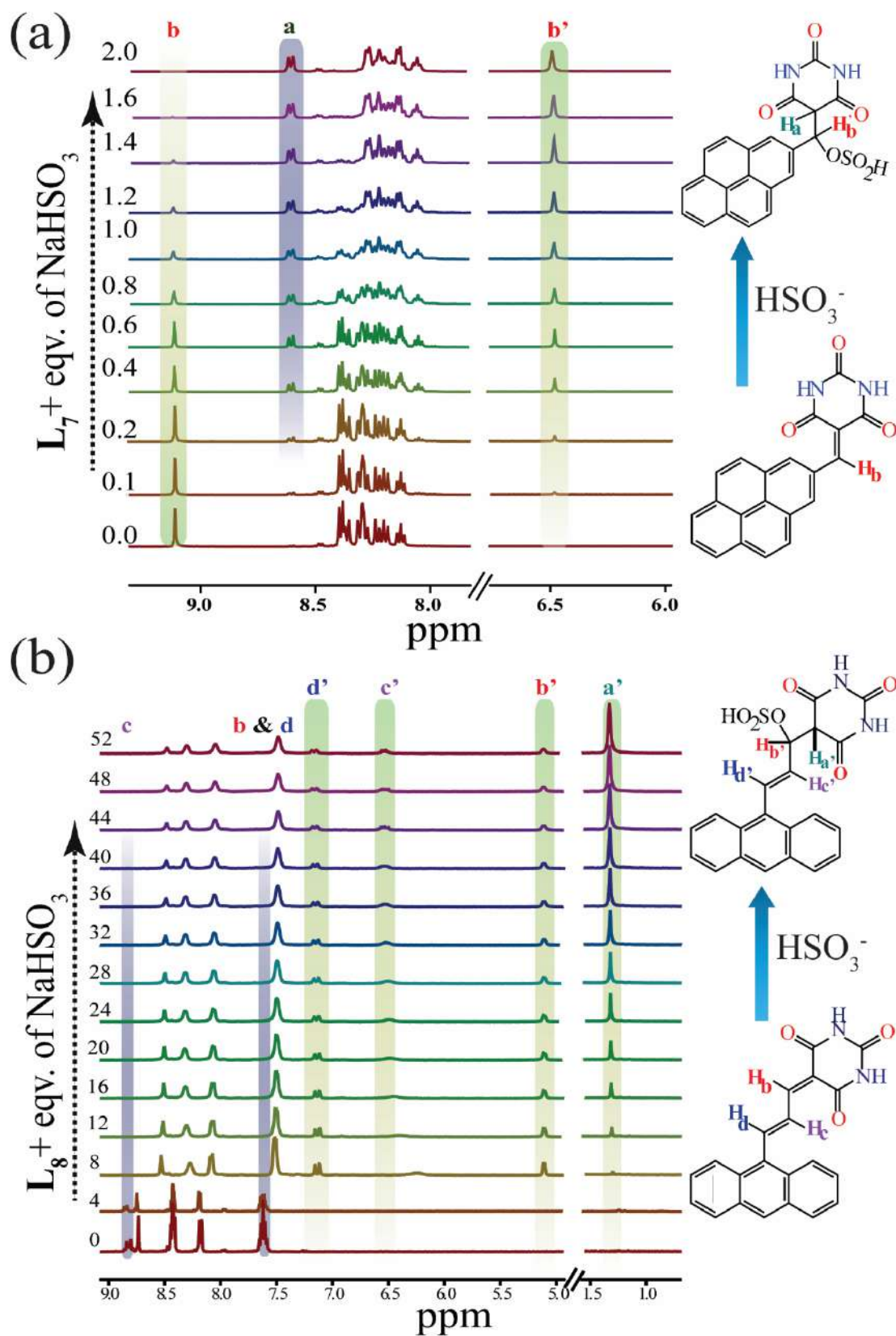


Figure 5.5 Changes in the ^1H NMR spectra of L_7 (a) and L_8 (b) upon incremental addition of HSO_3^- in DMSO-d_6 .

At this point, to verify the supposed formation of the mono- HSO_3^- product against its bis-addition analogue, we wondered if the presence of excess HSO_3^- (up to 52 equiv.) in solution could render results otherwise. The systematic $^1\text{H-NMR}$ titration profile, however, also ensured that, in the case of **L**₈, the reaction did not proceed further after the reaction with a single HSO_3^- despite the presence of excess anion presumably due to the diminished electrophilic nature of the non-exocyclic carbons. So other spectroscopic analyses like IR, mass spectra, and $^1\text{H-NMR}$ corroborated the recognition mechanism depicted in Scheme 5.2 through the confirmation of the formation of the daughter products (**P**₇ and **P**₈). So, the present investigation verified our proposition that the nucleophilic addition reaction at the exocyclic C=C double bond (present both in **L**₇ and **L**₈) was the key phenomenon for the observed ‘turn-on’ response.

5.4 DFT studies of probes and their HSO_3^- adduct

To understand the photophysical behaviour of the probes (**L**₇ and **L**₈) in terms of HSO_3^- detection, we performed DFT [b3lyp/6-31g (*d*)] calculations in Gaussian 09 program package. The optimized structures of the probes (Fig. 5.6a and 5.6c) were almost planar (C=C, sp^2 -hybridized) whereas after the addition of HSO_3^- , **L**₇ and **L**₈ were oriented in two different planes (C-C, sp^3 -hybridized). The products (**P**₇ and **P**₈) generated upon addition of HSO_3^- to the probes, ΔE of the molecular system increased (2.9101 eV to 3.1970 eV for **L**₇ and 2.6190 eV to 3.3480 eV for **L**₈). Therefore, energy transfer associated with HOMO-LUMO electronic transition becomes comparatively higher. As a result, λ_{max} of **P**₇ and **P**₈ appeared to be at relatively lower wavelength, owing to λ_{ICT} , than that for the free probes, supported by the UV-Vis spectral studies. Further, the frontier molecular orbital diagrams showed that the HOMO-LUMO electronic distribution of **L**₇ and **L**₈ was almost equal (Fig. 5.6a and 5.6c). In both cases, HOMO was located on the pyrene/anthracene unit and localized over the BA unit, whereas the electron density on LUMO was mainly located on the BA unit and also localized on the pyrene/anthracene moiety. But in **P**₇, the HOMO was exclusively located on the pyrene unit, while LUMO was entirely located on the BA unit. The outcome suggested an obvious difference in the electronic transition of compounds **L**₇ and **P**₇, leading to an observable enhancement in the fluorescence intensity *via* the ICT process [π -conjugated pyrene moiety to BA unit] upon the reaction of **L**₇ with HSO_3^- .^{5.41-5.42} However, **P**₈ displayed that both HOMO and LUMO are confined only to the fluorophore, anthracene moiety, entirely and hence, the ‘turn-on’ fluorescence response ensued *via* switching off the PET process [from electron-rich anthracene moiety to BA unit] upon the reaction of **L**₈ with HSO_3^- . These findings suggested that the

addition of HSO_3^- to the probes caused ‘turn-on’ response in the case of probe L_7 , likely to be occurred *via* ICT rather than PET process, whereas the improvement of the fluorescence intensity resulted *via* blocking of PET process in case of probe L_8 also evident from optical experiments. From the above discussion, it is quite understandable that while the higher energy transitions (376 and 396 nm) are associated with intra-molecular charge transfer, the lower energy transition (455 nm) originates from the pyrene-based π - π^* (excimer) transition^{5,39}. The above calculation (based on DFT) offered conformity with the experimental results, which proposed that the nucleophilic addition reaction between the probes (L_7 and L_8) and HSO_3^- occurred by the reaction at C=C double bond and consequently blocked the ICT/PET phenomena.

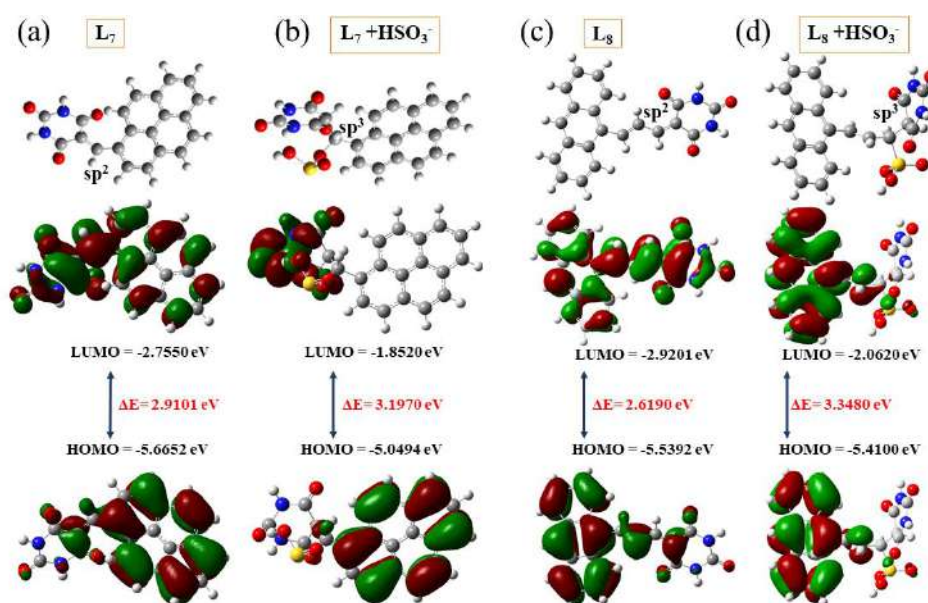


Figure 5.6 The DFT optimized geometries of the most stable form of (a) L_7 and (c) L_8 , (b) and (d) their corresponding complex with HSO_3^- . HOMO–LUMO energy levels and interfacial plots of the orbitals for L_7 and L_8 before and after reaction with HSO_3^- were calculated with the percentage of transition

5.5 Application of HSO_3^- detection in paper strips, real water sample

Furthermore, to explore the practical implication of probe L_7 , a test paper strip-based model was presented for the quick detection of HSO_3^- . Filter paper (Whatman 1, 5.5 cm × 1 cm) coated with a solution of the probe L_7 (1 mM) was air-dried for 4–6 hrs. Those paper strips were soaked with different concentrations of HSO_3^- for 4–5 min. After drying, those strips were placed under UV radiation ($\lambda = 365$ nm) (Fig. 5.7). The presence of HSO_3^- can be visualised by the change of colour from faint blue to brilliant cyan. To check the sensing ability of the probe L_7 in real water samples, the experiment was carried out using distilled water, lake water (collected from the serpentine lake in IIT Guwahati campus) and, river water (collected from the Brahmaputra river near the IIT Guwahati campus, Assam, India). Then, L_7 was treated with various known

concentrations of HSO_3^- (10, 20, and 30 μM), and the corresponding fluorescence intensity was recorded at 455 nm. The characteristic fluorescence responses at 455 nm suggested that probe **L7** showed a considerable capability to sense HSO_3^- in real water samples as well the ability to detect the HSO_3^- decreased from tap water to river water, which may be due to increased contamination in the water (Fig. 5.8).

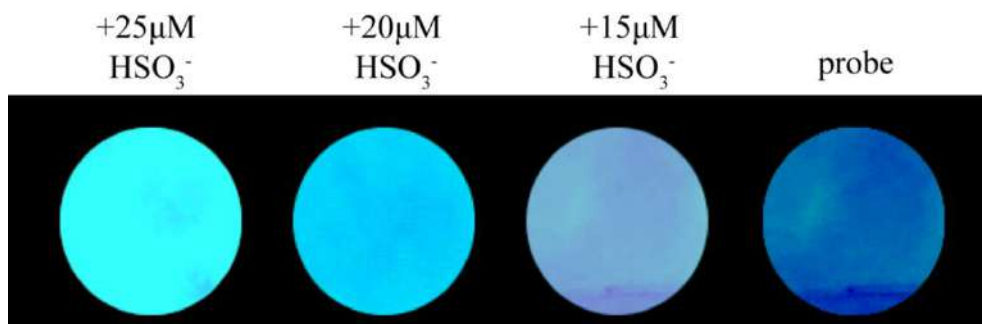


Figure 5.7 Change of colour (366 nm UV light) of probe **L7** (1.0 mM) coated paper strips upon addition of various concentrations of HSO_3^- .

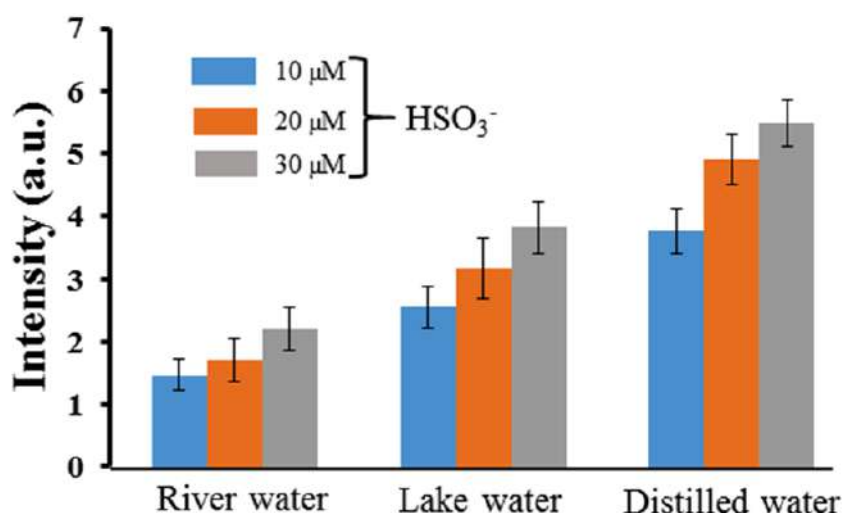


Figure 5.8 Fluorescence intensity changes of **L7** with the addition of spiked HSO_3^- in river water, lake water, and distilled water (intensity recorded at 455 nm). The error bars specify the standard deviations of three measurements.

5.6 Determination of bisulphite in real food sample

Bisulphite is well known for its uses in sugar as an antioxidant and preservative. The amounts of bisulphite in sugar sample were examined to verify the applicability of the probe towards the real sample. Sugar solutions were prepared by taking 10 g of sugar in 100 mL water. To measure the precision of the observed values obtained by using the probe, 138 μL of the stock solution of the sugar was arbitrarily taken and diluted up to 2 mL with the experimental solvent media. This solution was then spiked with HSO_3^- (2, 2.5, 3, 3.5 μM). By taking the standard calibration

curve (Fig. A5.16), HSO_3^- in sugar sample was found to be $\sim 1.7 \mu\text{M}$ in sugar solution and 20 mg kg^{-1} in the actual solid sample (Table A5.1), which were effectively lower than the maximum amount permitted to be utilized as a food additive ($< 0.1 \text{ g/kg}$)^{5.43}. In order to confirm the validity of the method, we determined bisulphite in the sample by a recognized standard method^{5.44} (iodometric titration for bisulphite). As shown in Table A5.1, the results found by the two tests were in good agreement, which defined the accuracy of probe **L7**. The recovery percentages were good enough for practical purposes. Therefore, probe **L7** could successfully determine HSO_3^- in real food samples.

5.6 Conclusions

In conclusion, a pair of simple reaction-based fluorescent probes was reported for the recognition of HSO_3^- in mixed aqueous media. These probes displayed colorimetric and fluorometric ‘turn-on’ responses toward HSO_3^- based on Michael-type addition reaction with very high selectivity and sensitivity over other anions. Both the probes have a dynamic conjugated system with pyrene/anthracene and barbituric units connected through a C=C bond-forming D- π -A structure. Upon addition of HSO_3^- to each of the probes, the disruption of the active π - π conjugation of the C=C double bond took place, leading to a fluorescence enhancement. It is proven that the extra conjugated non-exocyclic C=C double bond (in probe **L8**) did not take part in reaction with excesses HSO_3^- . This phenomenon substantiated that only the activated exocyclic C=C double bond was prone to any nucleophilic attack, owing to a more electrophilic nature compare to its non-exocyclic counterpart. Probe **L7** was proved to have a quick response time ($\sim 3 \text{ min}$) along with working capability in low and high pH as well. We have also performed various environmental application studies on probe **L7**, such as the detection ability of analytes in a real food sample, paper strips, and real water samples.

References

- 5.1 D. H. Lee, J. H. Im, S. U. Son, Y. K. Chung and J. I. Hong, *J. Am. Chem. Soc.*, 2003, **125**, 7752-7753.
- 5.2 J. L. Sessler, P. A. Gale, and W. S. Cho, *Anion receptor chemistry*; Royal Society of Chemistry, Cambridge, U.K., 2006, 1-26.
- 5.3 J. Perez and L. Riera, *Chem. Commun.*, 2008, 533-543.
- 5.4 J. Pere and L. Riera, *Chem. Soc. Rev.*, 2008, **37**, 2658-2667.
- 5.5 Y. Huang, C. Zhang, X. Zhang, and Z. Zhang, *J. Pharm. Biomed. Anal.*, 1999, **21**, 817- 825.
- 5.6 W. G. Myers and H. F. Edelhauser, *J. Cataract Refractive Surg.* 2011, **37**, 611.
- 5.7 F. Esen, A. E. Bulut, and E. Toker, *Cutaneous Ocul. Toxicol.*, 2018, **37**, 286-290.
- 5.8 H. U. Shi, R. L. Stroshine and K. Ileleji, *J. Food Prot.*, 2017, **80**, 90-95.
- 5.9 J. Xu, P. Jian, X. Jiang, C. Qin, L. Zeng, H. Zhang and J. F. Zhang, *Biosens. Bioelectron.*, 2016, **77**, 725-732.

- 5.10. E. Yokoyama, R. E. Yoder and N. R. Frank, *Arch. Environ. Health*, 1971, **22**, 389-395.
- 5.11. J. M. Skelly, *John Wiley & Sons*, 1991, 233-233.
- 5.12. <https://www.theestafrican.co.ke/tea/science-health/beware-of-meat-laced-with-lethal-chemicals-1422576>, accessed 15 September 2021.
- 5.13. W. Yang and E. Purchase, *CMAJ*. 1985, **133**, 865–867.
- 5.14. Y. Miura, M. Hatakeyama, T. Hosino and P. R. Haddad, *J. Chromatogr. A*, 2002, **956**, 77-84.
- 5.15. R. K. Richards, *J. Pharmacol. Exp. Ther.*, 1943, **79**, 111-116.
- 5.16. P. Xie, G. Gao, W. Zhang, G. Yang and Q. Jin, *J. Chem. Sci.*, 2015, **127**, 1267.
- 5.17. www.maritime-executive.com/editorials/exhaust-gas-scrubber-washwater-is-it-safe, accessed 15 September 2021.
- 5.18. A. Isaac, C. Livingstone, A. J. Wain, R.G. Compton, and J. Davis, *Trends in Anal. Chem.* 2006, **25**, 589-598.
- 5.19. L. G. D. Weever and J. C. Kraak, *Anal. Chim. Acta.*, 1997, **337**, 125-213.
- 5.20. G. Aragay, J. Pons and A. Merkok, *Chem. Rev.*, 2011, 111, 3433.
- 5.21. X. Zhang, J. Yin and J. Yoon, *Chem. Rev.*, 2014, **114**, 4918.
- 5.22. S. Samanta, S. Goswami, A. Ramesh, and G. Das, *J. Photochem. Photobiol., A*, 2015, **310**, 45.
- 5.23. S. Samanta, T. Ray, F. Haque and G. Das, *J. Lumin.*, 2016, **171**, 13-18.
- 5.24. X. Cheng, H. Jia, J. Feng, J. Qin, and Z. Li, *Sens. Actuators B Chem.*, 2013, **184**, 274-280.
- 5.25. T. Kowada, H. Maeda and K. Kikuchi, *Chem. Soc. Rev.*, 2015, **44**, 4953-72.
- 5.26. K. Kikuchi, *Chem. Soc. Rev.*, 2010, **39**, 2048.
- 5.27. Y. Q. Sun, J. Liu, J. Zhang, T. Yang and, W. Guo, *Chem. Commun.*, 2013, **49**, 2637-2639.
- 5.28. Y. Liu, K. Li, M. Y. Wu, Y. H. Liu, Y. M. Xie, X. Q. Yu, *Chem. Commun.*, 2015, **51**, 10236-10239.
- 5.29. M. X. Li, W. Y. Feng, H. Y. Zhang, and G. Q. Feng, *Sens. Actuators B Chem.*, 2017, **243**, 51-58
- 5.30. X. Pan, Y. Zhong, Y. Jiang, G. Zuo, J. Li and W. Dong, *Materials Chemistry and Physics*, 2018, **213**, 83-88.
- 5.31. S. Samanta, S. Halder, P. Dey, U. Manna, A. Ramesh and G. Das, *Analyst*, 2018, **143**, 250-257.
- 5.32. S. Samanta, P. Dey, R. Aiyagari and G. Das, *Chem. Commun.*, 2016, **52**, 10381-10384.
- 5.33. P. Jiang and Z. Guo, *Coord. Chem. Rev.*, 2004, **248**, 205-229.
- 5.34. X. He, C. Xu, W. Xiong, Y. Qian, J. Fan, F. Ding, H. Deng, H. Chen and J. Shen, *Analyst*, 2020, **145**, 29-33.
- 5.35. U. Diwan, V. Kumar, R. K. Mishra, N. K. Rana, B. Koch, M. K. Singh, K. K. Upadhyay, *Analytica. Chimica. Acta.*, 2016, **929**, 39- 48.
- 5.36. U. Tamima, M. Santra, C.W. Song, Y. J. Reo and K. H. Ahn, *Anal. Chem.*, 2019, **91**, 10779-10785.
- 5.37. M. Li, P. Cui, K. Li, J. Feng, M. Zou, and X. Yu-Chin. *Chem. Lett.*, 2018, **29**, 992-994.
- 5.38. J. Wu, L. Jiang, P. Verwilt, J. An, H. Zeng, L. Zeng, G. Niu and J. S. Kim. *Chem. Commun.*, 2019, **55**, 9947-9950.
- 5.39. H. J. Kim, S. K. Kim, J. Y. Lee and J. S. Kim, *J. Org. Chem.*, 2006, **71**, 6611-6614.
- 5.40. S. Sarkar, S. Roy, A. Sikdar, R. N. Saha and S. S. Panja, *Analyst*, 2013, **138**, 7119-7126.
- 5.41. S. D. Padghan, L. C. Wang, W. C. Lin, J. W. Hu, W. C. Liu, and K. Y. Chen, *ACS Omega*, 2021, **6**, 5287-5296.
- 5.42. G.Y. Li and K. L. Han, *Wiley Interdiscip. Rev. Comput. Mol. Sci.* 2018, **8**, 1351-1367.
- 5.43 *J. Agric. Food Chem.*, 2017, **65**, 2883-2887.
- 5.44 *J. Agric. Food Chem.*, 2014, **62**, 3405-3409.

Annexure 5

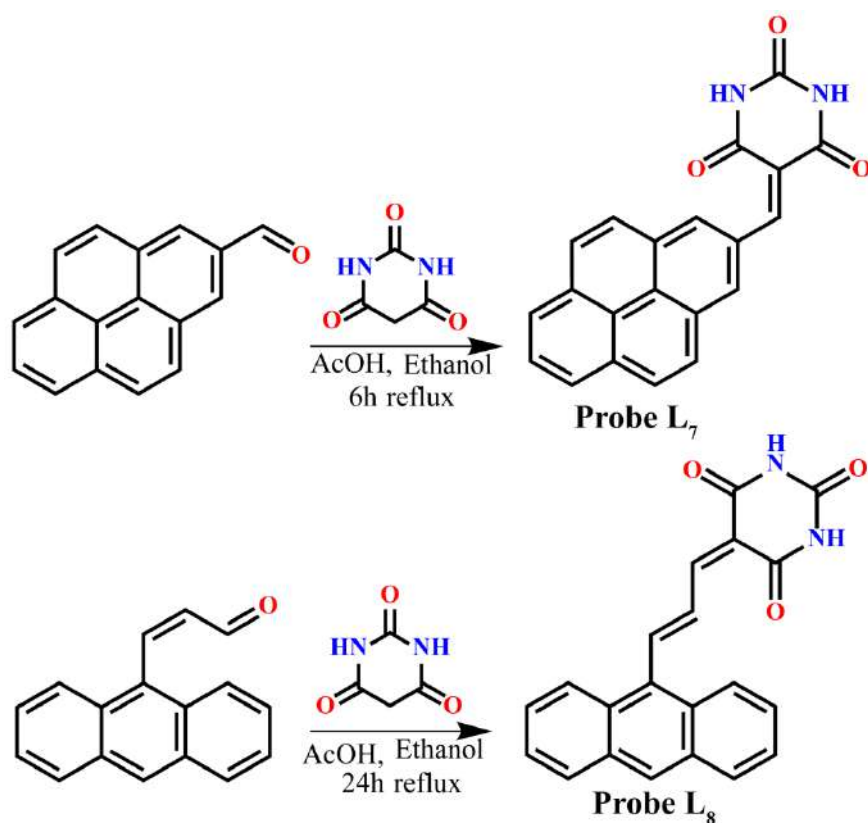
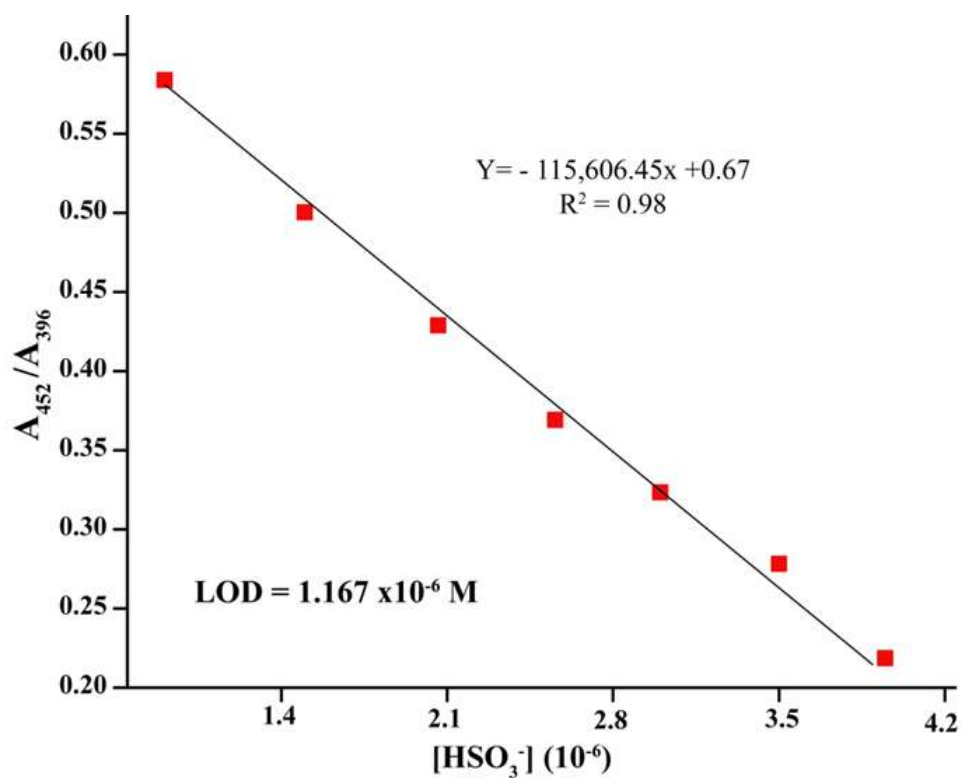
Scheme A5.1. Synthesis of the probe **L₇** and **L₈**

Figure A5.1 Linear relationship between the absorbance ratio (A_{452}/A_{396}) of **L₇** (50 μM) and the concentration of HSO_3^- for the detection limit (LOD) calculation.

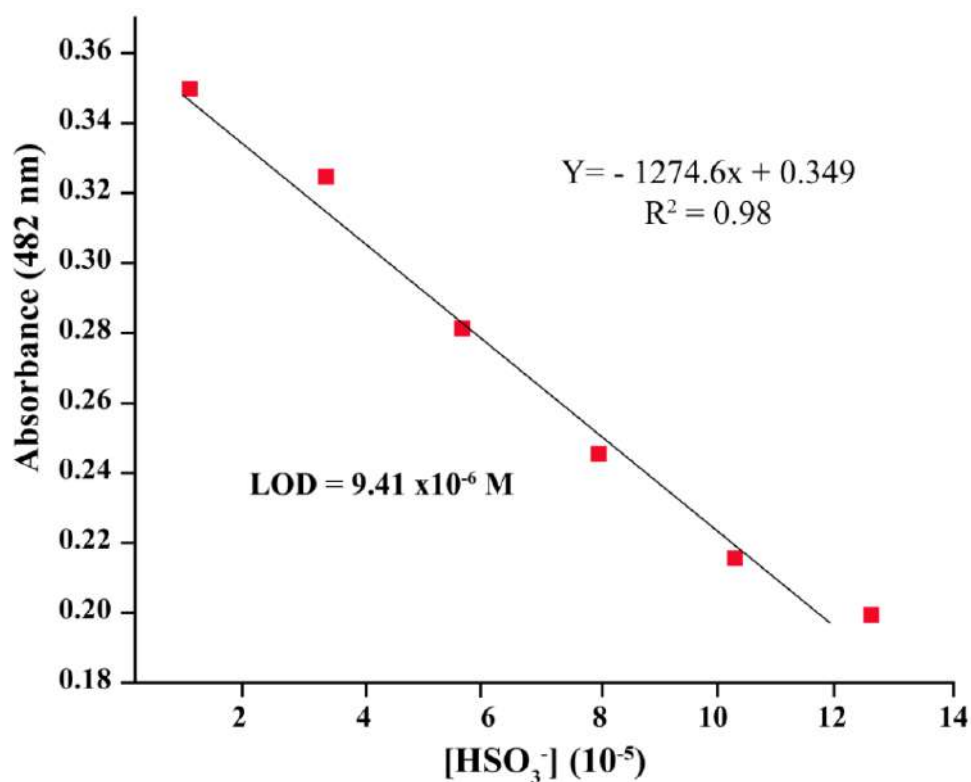


Figure A5.2 Linear relationship between the absorbance of L_8 (50 μM) and the concentration of HSO_3^- (M) at 482 nm for the detection limit (LOD) calculation.

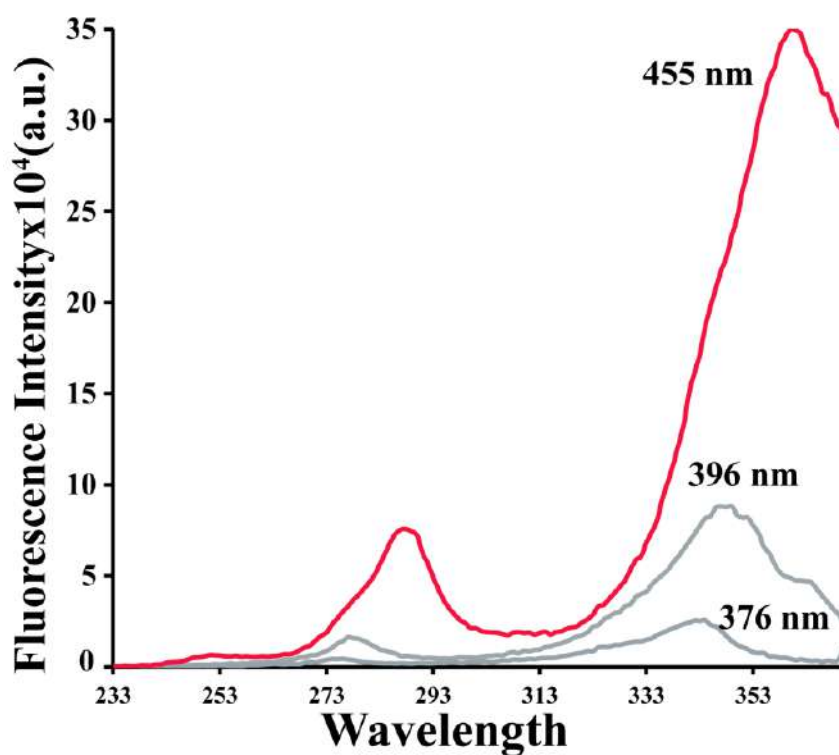


Figure A5.3 Excitation spectra of $L_7\text{-HSO}_3^-$ observed at 376 nm, 396 nm, and 455 nm.

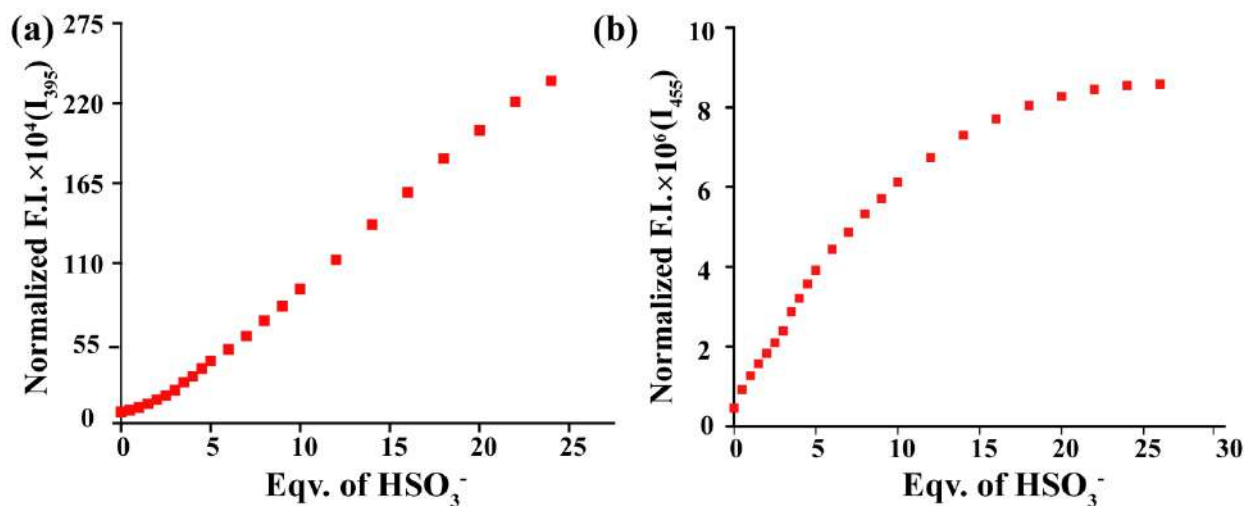


Figure A5.4 The emission intensity change of L_7 (50 μM) (a) at $I_{395\text{nm}}$ for monomer and (b) at $I_{455\text{nm}}$ for excimer emission, as a function of the equivalent of HSO_3^- .

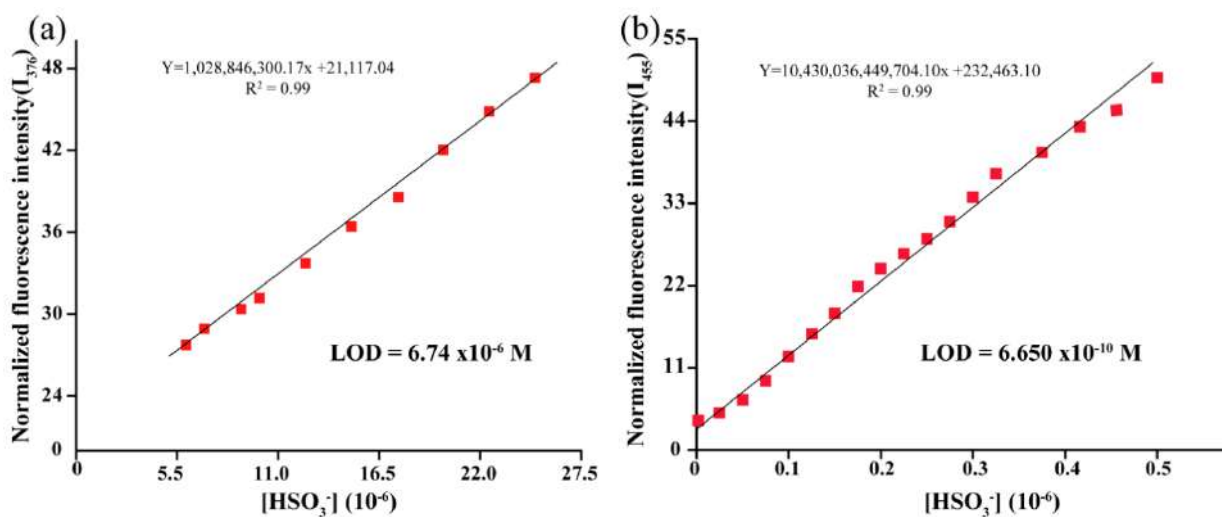


Figure A5.5 Linear relationship between the normalized fluorescence intensity (a) at 376 nm and (b) at 455 nm of L_7 (50 μM) and the concentration of HSO_3^- for the detection limit (LOD) calculation.

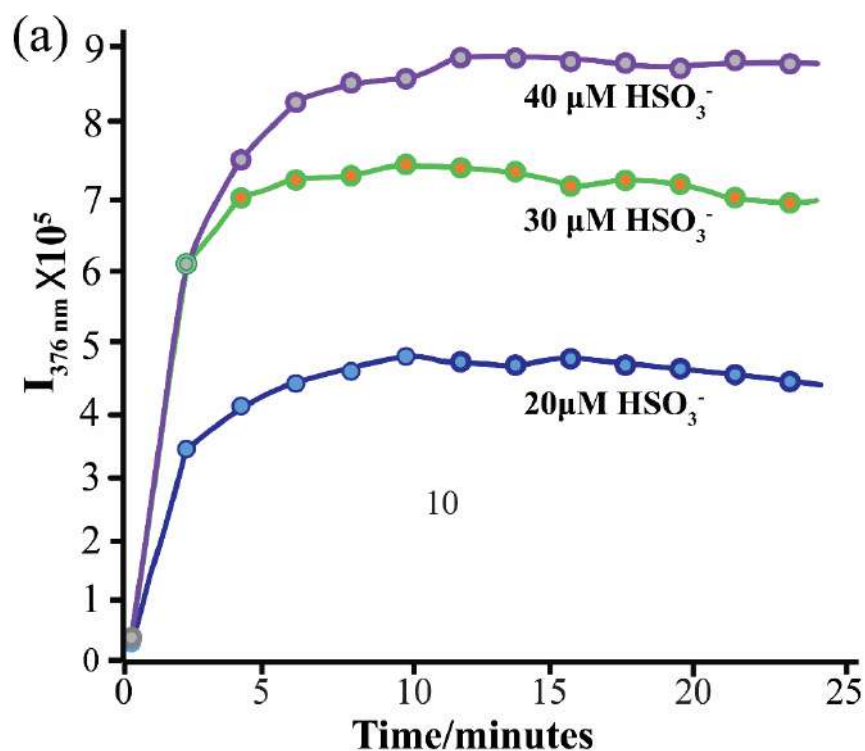


Figure A5.6 Time-dependent fluorescence intensity (at 376 nm) of probe L7 (50 μM) in the presence of HSO₃⁻ (20, 30, and 40 μM) in the test solution.

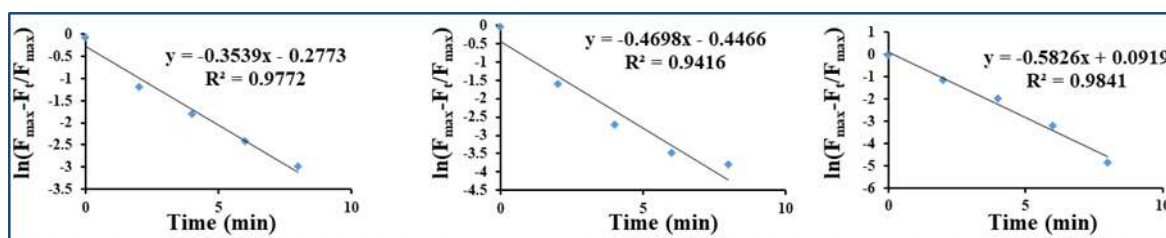


Figure A5.7 Changes in the fluorescence intensity (normalized) along with time (min), plotted using the first-order rate equation, for L7 upon reaction with bisulphite monitored at 376 nm (monomeric emission). Data have been averaged over three trials (from left to right).

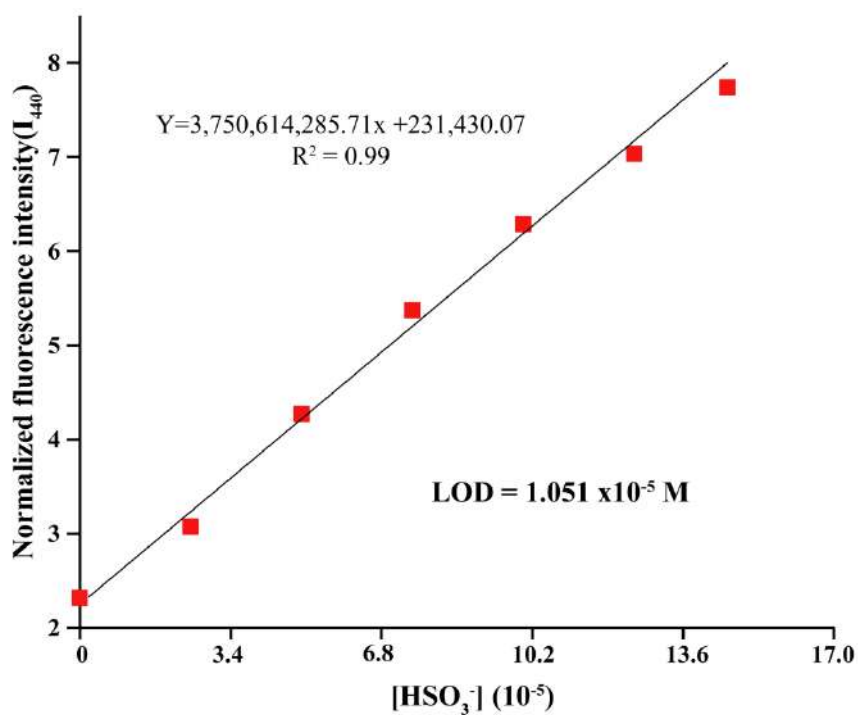


Figure A5.8 Linear relationship between the normalized fluorescence intensity ($I_{440\text{nm}}$) of L_8 ($50 \mu\text{M}$) and the concentration of HSO_3^- for the Detection limit (LOD) calculation.

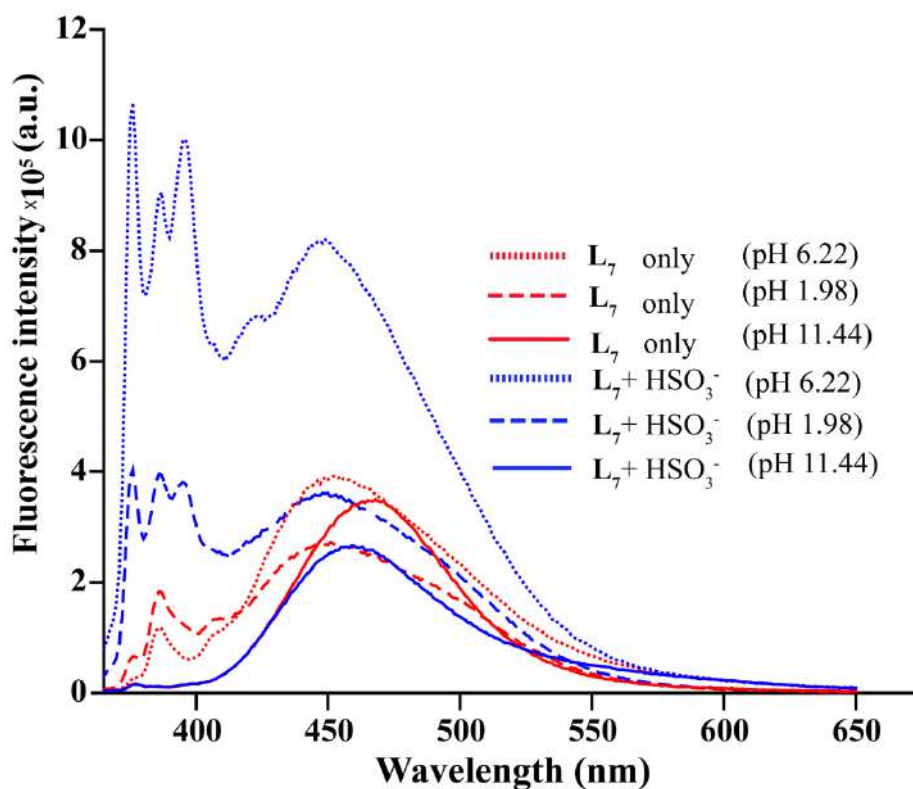


Figure A5.9 Fluorescence response of the probe L_7 ($50 \mu\text{M}$) in the absence or presence of HSO_3^- ($500 \mu\text{M}$) upon variation of pH in an experimental solution, each spectrum was recorded after 2 min.

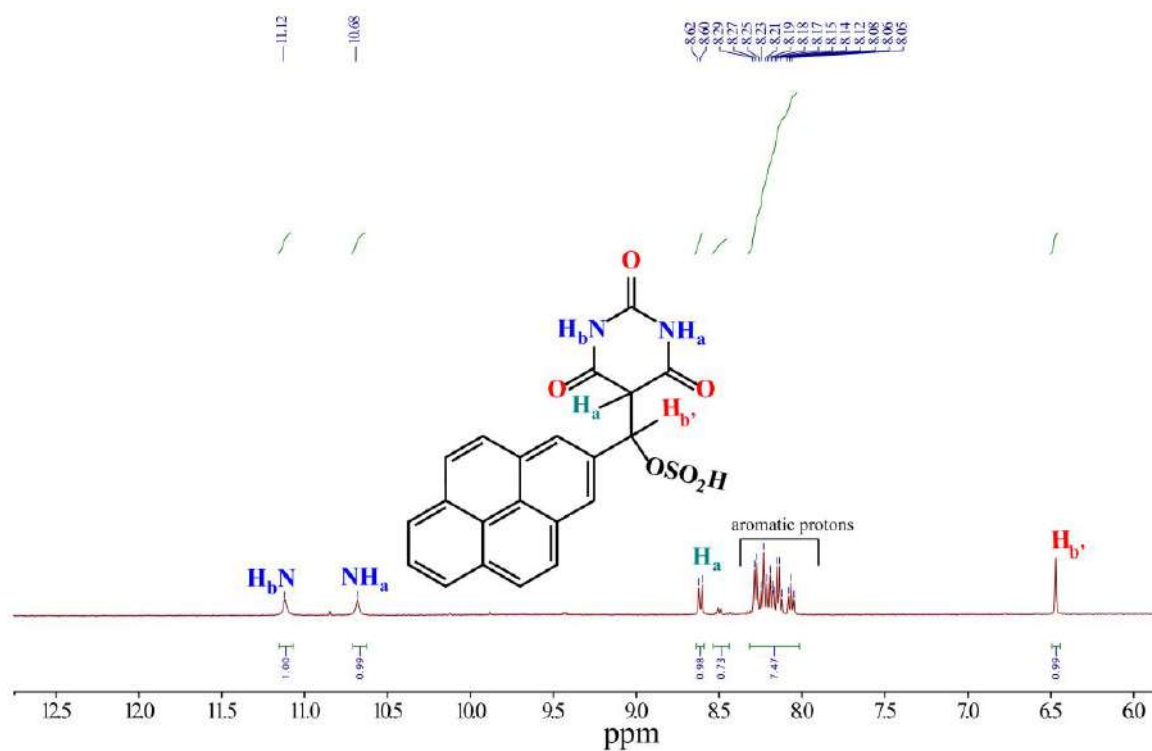


Figure A5.10 ^1H NMR spectra of [500 MHz, CDCl_3 , TMS] **L7** with HSO_3^- in DMSO-d_6 .

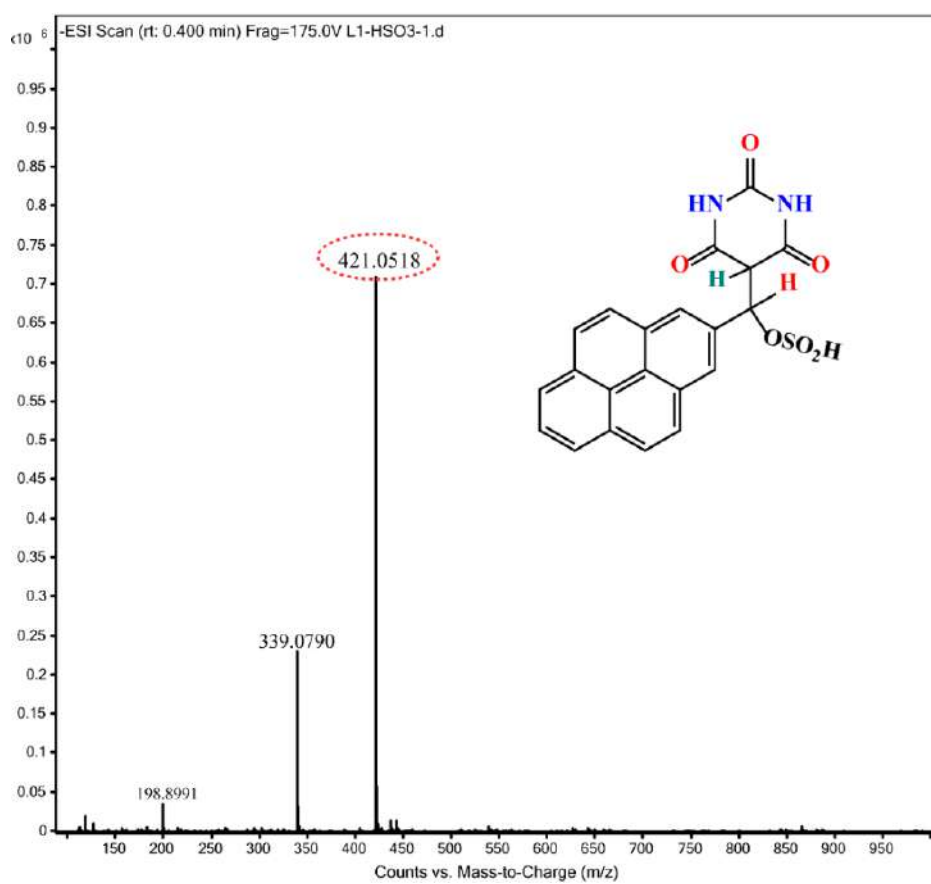


Figure A5.11 Mass spectrum of **L7** with HSO_3^- . calculated $[\text{L}_7\text{-HSO}_3^-] = 422.0573$, Found 421.0518. (Mass spectrum obtained in negative mode).

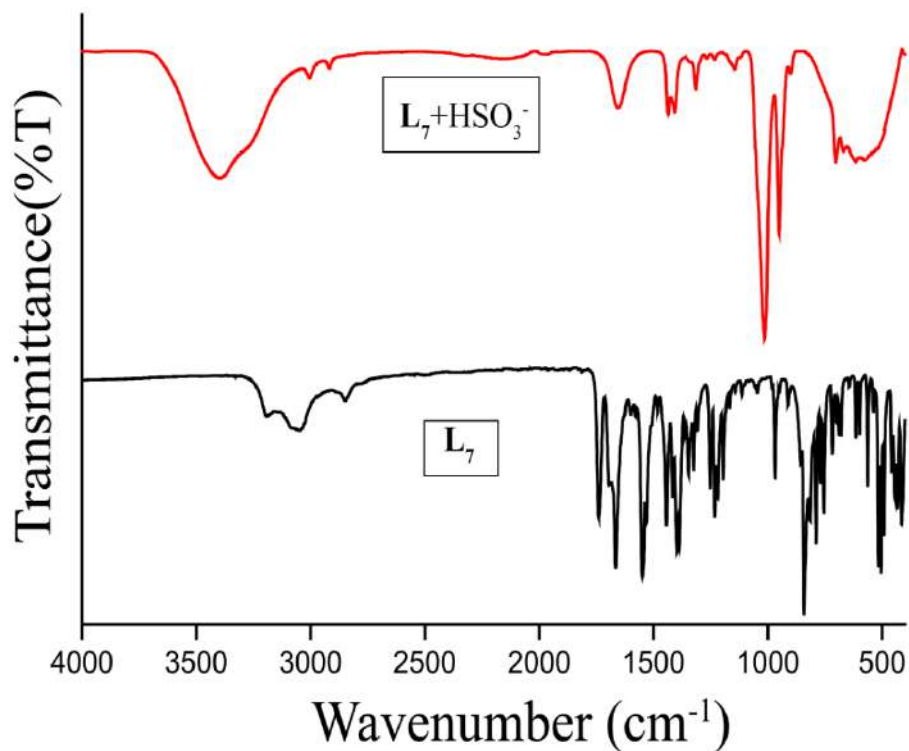


Figure A5.12 FT-IR spectra of probe L₇ in absence and presence of HSO₃⁻.

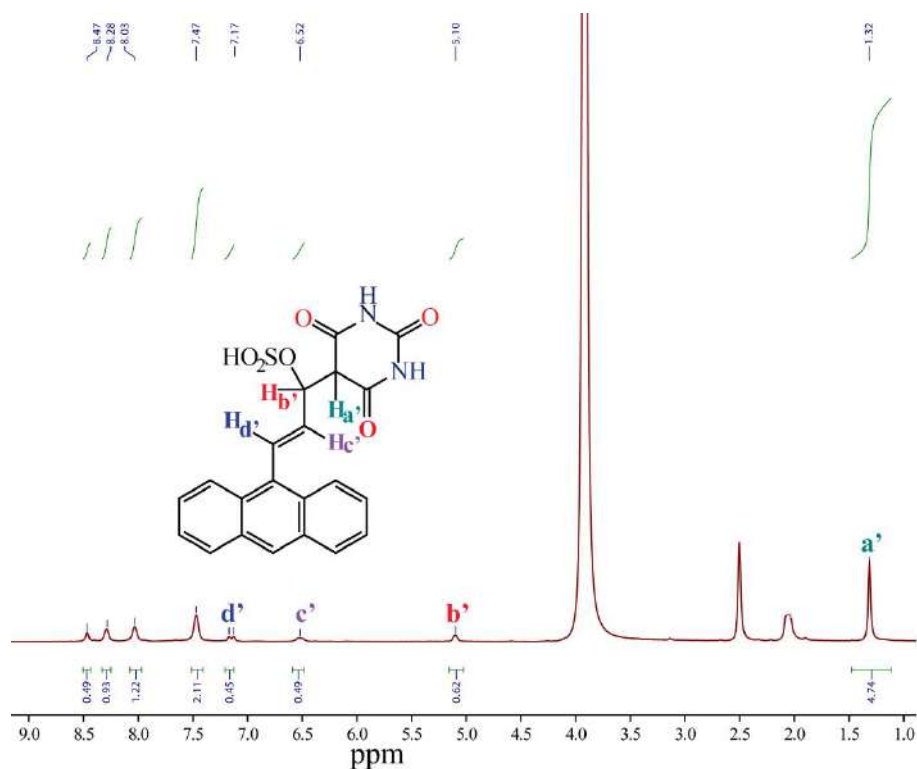


Figure A5.13 ¹H NMR spectra of [500 MHz, CDCl₃, TMS] L₈ with HSO₃⁻ in DMSO-d₆.

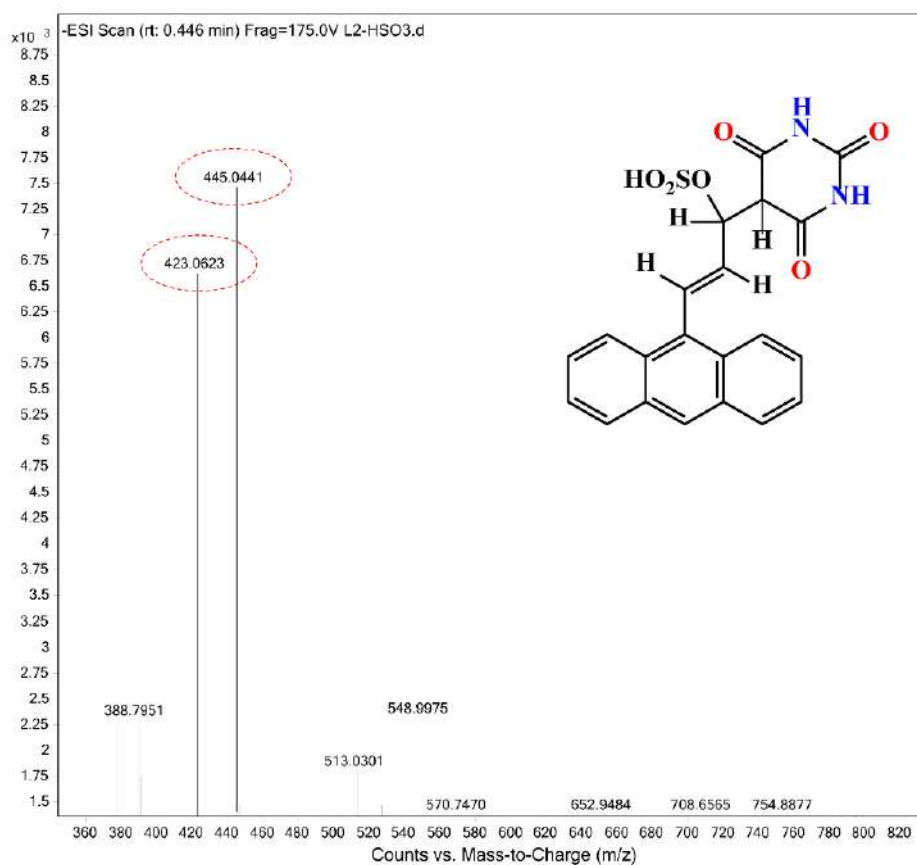


Figure A5.14 Mass spectrum of **L₈** with HSO_3^- , calculated $[\text{L}_8 - \text{HSO}_3]^- = 424.0729$ and $[\text{L}_8 + \text{NaHSO}_3]^-$ Found 423.0623 and 445.0441. (Mass spectrum obtained in negative mode).

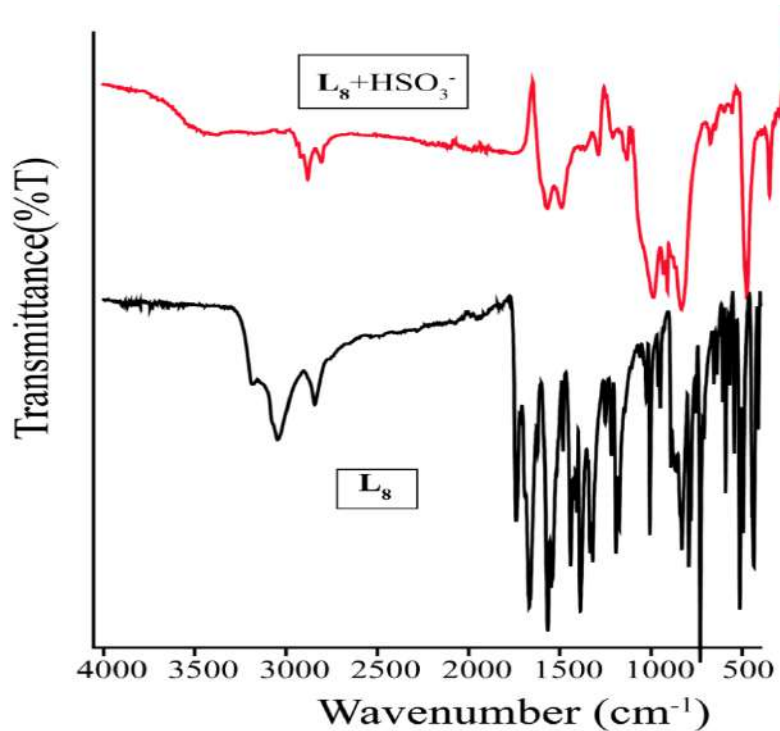


Figure A5.15 FT-IR spectra of probe **L₈** in absence and presence of HSO_3^- .

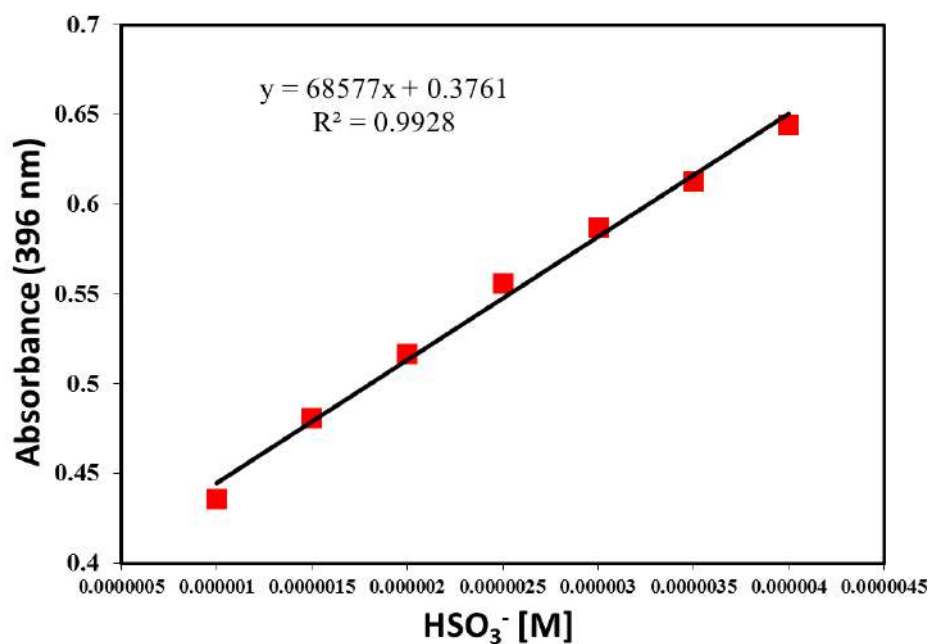


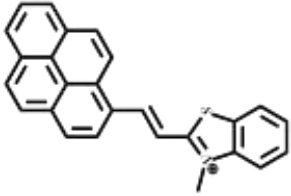
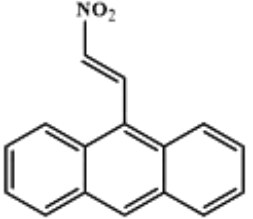
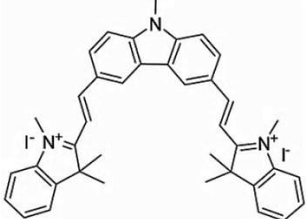
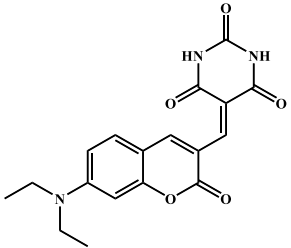
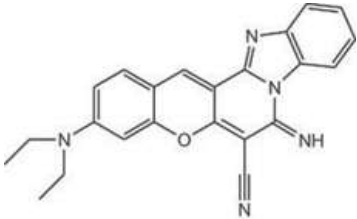
Figure A5.16 Calibration curve for detection of bisulphite in food sample by probe L7.

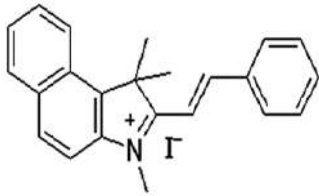
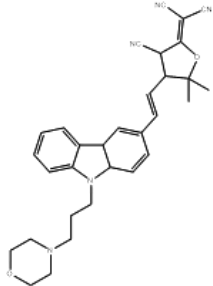
Table A5.2 Determination of HSO₃⁻ in food sample by L7 and titration method.

Added (μM)	Found (μM)	Determined (μM)	Recovery %	Titration Method (μM)
0	1.71	1.71	-----	1.78
2	3.69	1.69	99.24	1.76
2.5	4.19	1.69	98.7	1.74
3	4.69	1.69	98.54	1.71
3.5	5.24	1.74	101.81	1.76

Table A5.1 Comparison of some reported bisulphite probes with the present work.

Probe	Response type	Detection limit	Solution	Reference

<p style="text-align: center;">Present work</p>	<p style="text-align: center;">Fluorescence emission</p>	<p style="text-align: center;">0.55 ppm & 0.053 ppb (L₁), 0.85 ppm (L₂)</p>	<p style="text-align: center;">Aqueous CH₃CN (1 mM HEPES buffer, pH = 7.4, CH₃CN–H₂O = 7:3 v/v)</p>	<p style="text-align: center;">This work</p>
	<p style="text-align: center;">Fluorescence emission</p>	<p style="text-align: center;">89 nM</p>	<p style="text-align: center;">Aqueous buffer (0.01 M HEPES, pH=7.4, Water/DMF; 7:3 v/v)</p>	<p style="text-align: center;">Analytica Chimica Acta, 2016^{A5.1}</p>
	<p style="text-align: center;">Fluorescence emission</p>	<p style="text-align: center;">6.30 μM</p>	<p style="text-align: center;">Na₂HPO₄ citric acid buffer at pH 5.0.</p>	<p style="text-align: center;">Spectrochim Acta A, (2015) ^{A5.2}</p>
	<p style="text-align: center;">Fluorescence emission</p>	<p style="text-align: center;">30 μM</p>	<p style="text-align: center;">PBS buffer (pH 7.4, 10 mM)</p>	<p style="text-align: center;">RSC Adv, 6 (2016) ^{A5.3}</p>
	<p style="text-align: center;">Fluorescence emission</p>	<p style="text-align: center;">105 nM</p>	<p style="text-align: center;">water a solution containing 1% DMSO</p>	<p style="text-align: center;">J. Agric. Food Chem. 2020^{A5.4}</p>
	<p style="text-align: center;">Fluorescence emission</p>	<p style="text-align: center;">1.76 μM</p>	<p style="text-align: center;">Na₂HPO₄ citric acid buffer at pH 5.0</p>	<p style="text-align: center;">Sens. Actuators, B-Chem (2013) ^{A5.5}</p>

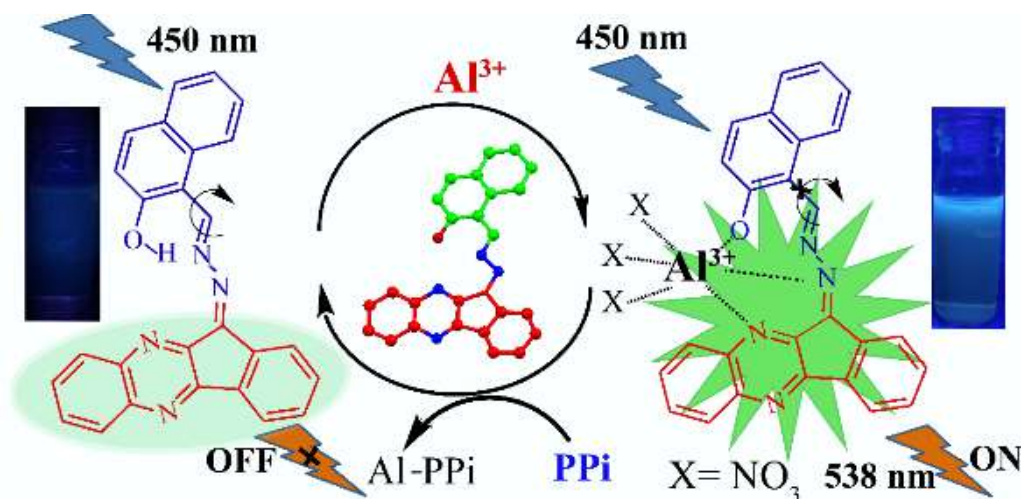
	Fluorescence emission	0.38 μM	PBS buffer (pH 7.4, 10 mM, containing 30% DMF)	Sens. Actuators, B, (2014) A5.6
	Fluorescence emission	2.08 μM	PBS : DMF = 1 : 1 buffer (pH 6.0)	New J. Chem., 2017 ^{A5.7}

References

- A5.1 U. Diwan, V. Kumar, R. K. Mishra, N. K. Rana, B. Koch, M. K. Singh and K. K. Upadhyay *Analytica. Chimica. Acta.*, 2016, **929**, 39- 48
- A5.2 J. B. Chao, Y. H. Liu and Y. Zhang, *Spectrochim Acta. A*, 2015, **146**, 33-37.
- A5.3 G. Wang, H. Chen, X. L. Chen and Y. M. Xie, *RSC Adv.*, 2016, **6**, 18662.
- A5.4 X. He, W. Xu, F. Ding, C. Xu, Y. Li, H. Chen, and J. Shen, *J. Agric. Food Chem.*, 2020, **68**, 11774–11781.
- A5.5 J. Chao, Y. Zhang, H. Wang, Y. Zhang, F. Huo, C. Yin, L. Qin and Y. Wang, *Sens. Actuators B Chem.*, 2013, **188**, 200-206.
- A5.6 Y. Sun, S. Fan, S. Zhang, D. Zhao, L. Duan and R. Li, *Sens. Actuators B Chem.*, 2014, **193**, 173 -177.
- A5.7 J. Luo, G. Song, X. Xing, S. Shen, Y. Ge and X. Cao, *New J. Chem.*, 2017, **41**, 3986-3990.

Chapter 6A

'CHEF'-based Sensing of Al(III) and Inorganic Pyrophosphate through OFF-ON-OFF Emission along with "Naked-eye" Detection of Cu(II)



6A.1 Background and Focus of the Chapter

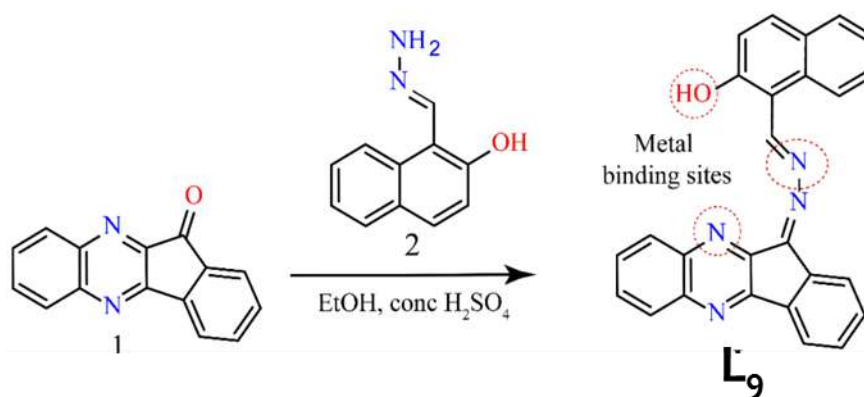
The design and development of artificial and innovative chromofluorogenic probes, which can effectively recognize various guests, has still been an evolving area in supramolecular chemistry due to the potential role in the fields of biochemistry, medicine, and environment^{6A.1-6A.6}. The development of probes for the quick and selective detection of Al^{3+} has generated great scientific interest among chemists due to their essential contribution to the biosphere and human health. The identification and quantification of Al^{3+} have remained troublesome due to the high hydration enthalpy of Al^{3+} , leading to its reduced coordination ability compared to the transition metals^{6A.7-6A.10} with a minimal emission quantum efficiency and short emission lifetime. Naphthalene can be made to play as a model platform of a fluorescence probe. Schiff bases, a competent donor site, are well-documented to be a suitable chelating agent^{6A.11-6A.12}. In addition, the phenolic OH group, appended with the naphthalene unit, is recognized by the existence of the (internal) $\text{OH}\cdots\text{N}$ hydrogen bonding, which is an indispensable prerequisite for excited-state intramolecular proton transfer (ESIPT) process. The process is associated with the proton transfer mechanism between hydrogen bond donor groups (OH, NH_2) and hydrogen bond acceptor units ($-\text{C}=\text{O}$, $-\text{N}=\text{}$) through hydrogen-bonding interactions. The interaction between the probe and Al^{3+} hinders the ESIPT process, and thus, as a result of deprotonation of the OH group, substantial OFF-ON fluorescence can be detected.^{6A.13-6A.14} Weak fluorescence (OFF state) is observed because of the photo-induced electron transfer (PET) from the unshared pair of electrons of the O donor atom towards the quinoxaline motif in the molecular structure of the probe. Owing to the effects of chelation-enhanced fluorescence (CHEF), a particular cation can bind through N and O donor sites and the $>\text{C}=\text{N}$ moiety, which, in turn, constrains these deactivation processes (PET, ESIPT), leading to the increment of the emission intensity.^{6A.15} Multiple Schiff base-derived optical chemo-receptors have recently been reported for Al^{3+} ion-selective chelation.^{6A.16} The optical sensing of Al^{3+} has always been important as the detection of Al^{3+} is challenged by its high hydration enthalpy and the tendency to form insoluble $\text{Al}(\text{OH})_3$. Inorganic pyrophosphate (PPi), among other interfering phosphorylated anions, is the most crucial member of the phosphate family. Besides having its biological and environmental impacts, its detection can be utilized as a real-time DNA sequencing tool.^{6A.17} The identification of PPi has also evolved as a hot topic in cancer research,^{6A.18} and other diseases. For example, the accumulation of the Ca^{2+} -PPi complex in the joint fluid suggests a disease generally referred to as calcium pyrophosphate deposition disease (CPDD). Hence, over the years, PPi detection has become a key motivation for research.^{6A.19} Among other approaches, the most efficient tactic

for detecting PPI is the use of the metal complex as a binding site owing to the strong affection of Al^{3+} toward phosphates.

In our ongoing efforts to design and prepare innovative molecular sensors, on the basis of the above argument, herein we propose a naphthyl-appended ninhydrin-based probe, 1-((*E*)-(((*Z*)-11H-indeno[1,2-*b*] quinoxaline-11-ylidene) hydrazone) methyl) naphthalene-2-ol (**L₉**) with a potential of detecting multiple analytes. Firstly, this probe was proved to be a highly selective and sensitive 'turn-on' fluorescence sensor for Al^{3+} . Besides, it was found to be specific also toward Cu^{2+} and was investigated in detail through colorimetric (or naked-eye) detection. The *in situ* produced **L₉**- Al^{3+} complex was found to be solely selective for phosphate ions, especially pyrophosphate (PPI), among the other studied anions. As for biological applications, we have also investigated the DNA tracking ability of the ensemble mentioned above.

6A.2 Structural aspects of the chemosensor **L₉**

The chemosensor is decorated with a signaling unit (chromophore/fluorophore) and a metal coordination site (binding part) connected via a conventional imine bond. The naphthalene moiety has increased the conjugation of the entire system and the quinoxaline is also used as a good chelating site for metal ions (Scheme 6A.1).



Scheme 6A.1 Synthetic procedure of the chemosensor **L₉**.

6A.3 Crystal structure of the chemosensor **L₉**

The molecular framework of probe **L₉** was determined by single crystal X-ray crystallographic analysis with an empirical formula: $\text{C}_{27}\text{H}_{18}\text{Cl}_2\text{N}_4\text{O}$, Mw: 485.35, $T = 298 (2) \text{ K}$, with unit cell dimension of $a = 16.509 (15) \text{ \AA}$, $b = 16.509 (15) \text{ \AA}$, $c = 33.13 (3) \text{ \AA}$, $\alpha = 90^\circ$, $\beta = 90^\circ$, $\gamma = 90.00^\circ$, $V = 9029(18) \text{ \AA}^3$, $Z = 16$, $D_x (\text{g cm}^{-3}) = 1.428$, $m = 0.317 \text{ mm}^{-1}$, $F(000) = 3537$, reflections collected/unique = 25 344/4866 [$R_{\text{int}} = 0.2324$], $wR1 = 0.3296$ [$I > 2\sigma(I)$], $R1 = 0.1199$, $wR2 = 0.2929$ (all data), $\text{GOF} (F2) = 1.693$. CCDC No. 2055399.

Detailed investigation of the crystal structure reveals that the two intramolecular hydrogen bonding, O1–H1···N1 (2.843Å) and O1–H1···N3 (2.049Å) (Fig. 6A.1a), interaction plays a crucial role to assemble the framework into a *trans*-amine form. The molecule adopts a planer geometry due to shorter C–N bond distances (C22···N4 = 1.430Å, C21···N3 = 1.321Å, C20···N2 = 1.322Å) in the solid-state. Details structural elucidation discloses that the framework of the crystal structure involves various types of C–H··· π interactions (with an average distance of 3.434Å) which played an important role in stabilizing the conformation of the molecular structure in the solid-state (Fig. 6A.1b). Moreover, all the structural interpretation clearly shows that the aromatic quinoxaline moiety of **L**₉ adopts a favourable orientation to support a chelating interaction between the host and guest metal ion.

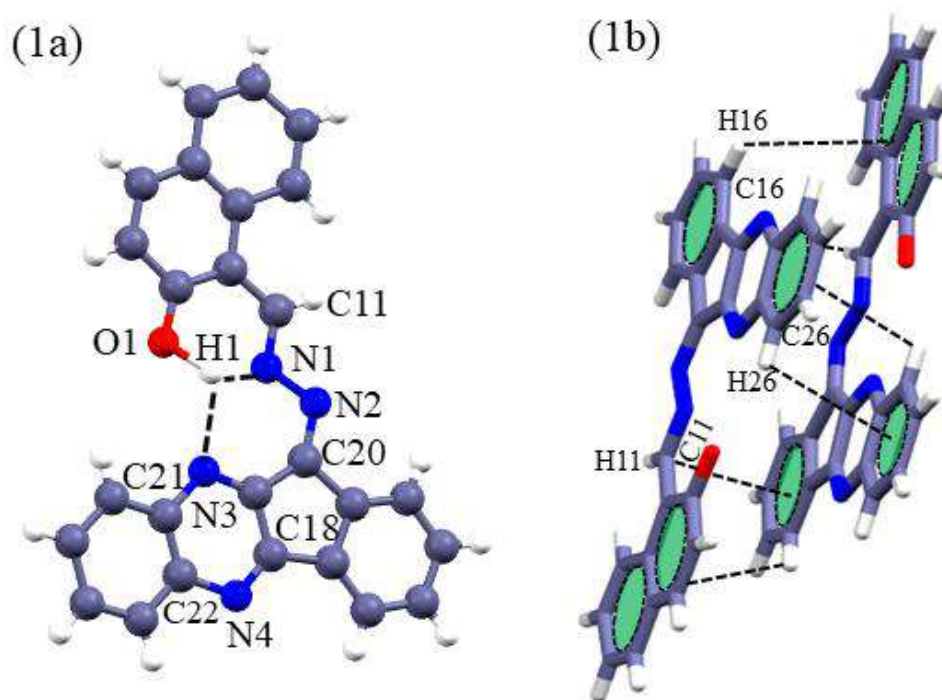


Figure 6A.1 Crystal structure of **L**₉, highlighting (a) the intramolecular H-bonding and (b) different types of effective C–H··· π interactions. Relevant bond distances: N1···H1=1.500 Å, O1···H1=1.343 Å, C21···H1=2.049 Å, C16–H16··· π = 3.506 Å, C11–H11··· π = 3.371 Å and C26–H26··· π = 3.425 Å.

6A.4 Optical studies

6A.4.1 Selective colorimetric response towards Cu²⁺ ion

Probe **L**₉ displayed a pair of broad peaks with absorption maxima ranging from 410 to 430 nm (π – π^*) and a slightly broadband at 474 nm (n – π^*) in methanol/aqueous HEPES-buffer (0.1 mM, pH~ 7.3; 9:1, v/v) solution (Fig. 6A.2a). Probe **L**₉ showed indifference toward various cations, but it exhibited a new peak at 562 nm only with Cu²⁺ ion with a concomitant vanishing of the original absorbance at 410 nm and 430 nm along with a significant 130-nm bathochromic shift (Fig. 6A.2a). It enabled us for the colorimetric naked-eye detection of Cu²⁺ ion evident

from the change of the color of the solution from faint yellow to reddish-brown color in a mixed aqueous medium^{6A.20} (Fig. 6A.2a, inset). The systematic titration experiment featured a progressive decline in the absorbance at 430 nm with a simultaneous rise in the intensity at 562 nm (Fig. 6A.2b). The distinctly sharp isosbestic point at 490 nm (assigned with dotted green lines in Fig. 6A.2b) also revealed a plausible formation of a new complex [L_9 - Cu^{2+}]. Job's plot (Fig. A6A.1), along with a detailed titration experiment, was also performed to estimate a 1:1 complex formation between L_9 and Cu^{2+} ions. The metal chelation with the naphthyl moiety aided the deprotonation of the hydroxyl group only promotes the probe to perform metal charge transfer (LMCT) as suggested by the band at 562 nm in the visible region of the spectrum. Upon careful evaluation of the B–H (Benesi–Hildebrand) plot, the binding constant associated with formation of an [L_9 - Cu^{2+}] complex was found to be $8.57 \times 10^6 M^{-1}$, revealing strong chelation between the probe and Cu^{2+} ion (Fig. A6A.2). According to the IUPAC method^{6A.21}, the detection limit was calculated to be $0.34 \mu M$ (Fig. A6A.3), which is far below the USEPA permissible Cu^{2+} limit in drinking water. Hence, based on the spectroscopic analyses, it may be suggested that the probe L_9 is potentially able to detect Cu^{2+} ions through a selective naked-eye response among all co-existing metal ions of interest.

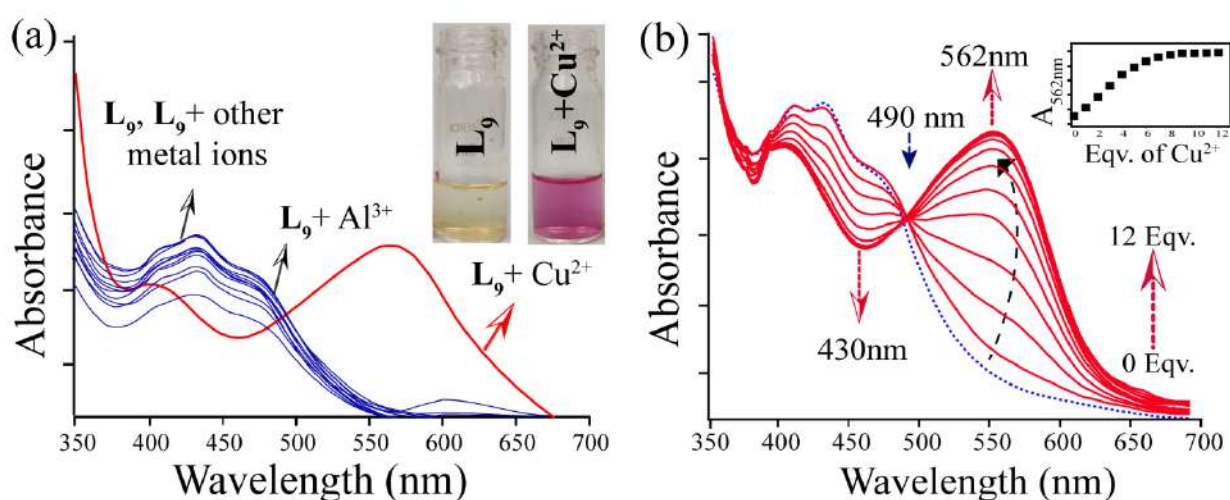


Figure 6A.2 Absorption spectra of (a) L_9 ($2 \mu M$) in presence of $100 \mu M$ each various cation (Cu^{2+} , Co^{2+} , Zn^{2+} , Mn^{2+} , Ni^{2+} , Fe^{3+} , Cr^{3+} , Hg^{2+} , Cd^{2+} , Pb^{2+} , Al^{3+}). Inset: Visual colour change of the probe in presence of Cu^{2+} under ambient light; and (b) changes in the absorption spectra of L_9 with incremental addition of Cu^{2+} . Inset: Change in absorption (562 nm) vs. [Cu^{2+} ion] in methanol/aqueous HEPES (0.1 mM ; $9:1$, v/v; pH 7.3) at $25 \text{ }^\circ\text{C}$.

6A.4.2 Selective fluorescence 'turn-on' response towards Al^{3+} ion

Probe L_9 displayed dual emission at around 519 nm and 541 nm ($\lambda_{\text{ex}} = 450 \text{ nm}$) in MeOH/aqueous HEPES (0.1 mM , pH ~ 7.3 ; $9:1$, v/v) medium. The weak emission was possibly due to the photo-induced electron transfer (PET) process supported by an extended

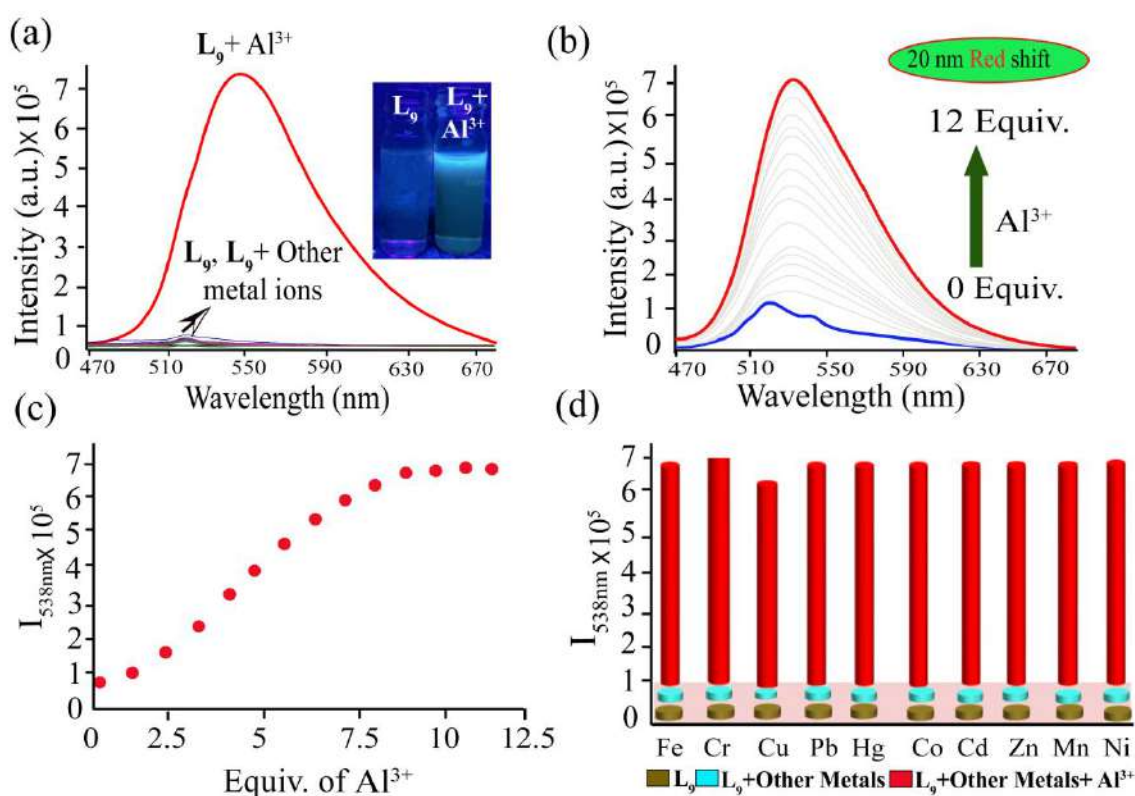


Figure 6A.3 (a) Changes in the fluorescence intensity of L_9 (2 μ M) in presence of 100 μ M each various cation (Cu^{2+} , Co^{2+} , Zn^{2+} , Mn^{2+} , Ni^{2+} , Fe^{3+} , Cr^{3+} , Hg^{2+} , Cd^{2+} , Pb^{2+} , Al^{3+}). Inset: Visual color change of the probe in the presence of Al^{3+} under 366 nm UV light; (b) changes in the fluorescence intensity of L_9 (2 μ M) with incremental addition of Al^{3+} (0-12 Equiv.); (c) fluorescence titration profile of L_9 (2 μ M) with Al^{3+} monitored at 538 nm; (d) changes in the fluorescence intensity of L_9 (2 μ M) in the presence of 100 μ M of each competitive metal ions, and the subsequent restoration of fluorescence upon addition of 100 μ M Al^{3+} in the presence of metal ions ($\lambda_{ex} = 450$ nm) in methanol/aqueous HEPES (0.1 mM; 9:1, v/v; pH 7.3) at 25 $^{\circ}C$.

delocalization of electrons from the imine nitrogen to the π -conjugated polyaromatic quinoxaline moiety through the azine (=N-N=) linkage. Of all the tested cations, only Al^{3+} showed a substantial 'turn-on' red-shifted fluorescence maximum at 538 nm with ~ 7 times enhancement in intensity (Fig. 6A.3a). Nevertheless, the other trivalent and divalent cations exhibited no sizable changes in emission response under similar conditions. Despite resemblances with Al^{3+} , even Fe^{3+} and Cr^{3+} also showed no noticeable changes in the fluorescence spectral profile of the probe. While the colored Cu^{2+} solution stayed fluorometrically indifferent, the incremental addition of Al^{3+} into L_9 caused a systematic increase in the emission intensity of L_9 with a gradual bathochromic shift of the emission maximum (Fig. 6A.3b) up to the addition of 12 Equiv. of Al^{3+} ion. A sharp rise in emission intensity was observed up to the administration of 18 μ M concentration of Al^{3+} ion (Fig. 6A.3c), and afterward, the spectral enhancement reached a plateau. Again, a linear relationship (up to the addition of 9 equiv. of Al^{3+}) between the emission intensity at 538 nm (I_{538nm}) and Al^{3+} concentration (Fig. 6A.3c) indicated that the probe L_9 could

be employed to estimate the Al^{3+} ion concentration with great precision. The LOD determined from the systematic titration experiment (Fig. A6A.4) was $1.97 \mu\text{M}$, which was very much comparable to the USEPA acceptable quantity of Al^{3+} ions in drinking water (0.05 mg L^{-1} ($1.85 \mu\text{M}$)),^{6A.22} and was compared to some other known probes in the literature (Table A6A.1). No major interference with other cations in the process of detecting Al^{3+} cation was observed (Fig. 6A.3d). Moreover, the emission quantum efficiency (Φ) of the probe **L**₉ was estimated to be 0.034, taking Rhodamine 6G as the reference. However, the quantum efficiency of the [**L**₉- Al^{3+}] complex changed to 0.090, hinting at an outstanding selectivity of the probe for Al^{3+} . The probe acted like a familiar tridentate chelating agent with 'NNO' as a coordinating unit i.e., one oxygen atom of phenol moiety, one imine nitrogen atom of the hydrazone moiety, and one aromatic nitrogen of quinoxaline unit. The proper size and high charge density of Al^{3+} and the inner-cavity of the probe allow effective interaction between the host and the corresponding guest ion.

6A.5 Plausible binding mechanism

Emission-based titration and a careful analysis of the Job's plot recommend the 1:1 binding interaction between **L**₉ and Al^{3+} (Fig. A6A.5). The binding affinity of the probe towards Al^{3+} was also attributed from the apparent binding constant (K), which was found to be $1.12 \times 10^4 \text{ M}^{-1}$ (Fig. A6A.6). The mass analysis (HRMS) also established the [**L**₉- Al^{3+}] complex in a 1:1 ratio (Fig. A6A.7) with molecular ion peak at $m/z = 612.9286$. ¹H NMR titration was performed to understand the binding mode of **L**₉ with

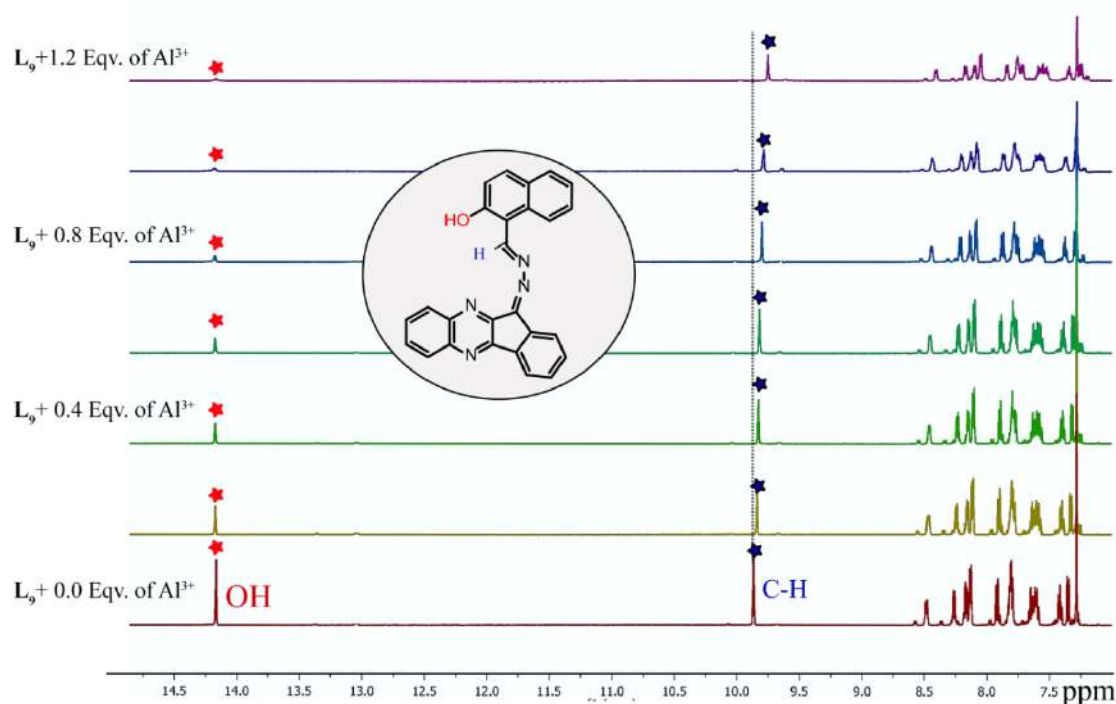


Figure 6A.4 ¹H NMR titration plot of **L**₉ upon gradual addition of Al^{3+} ion (0-120 μM).

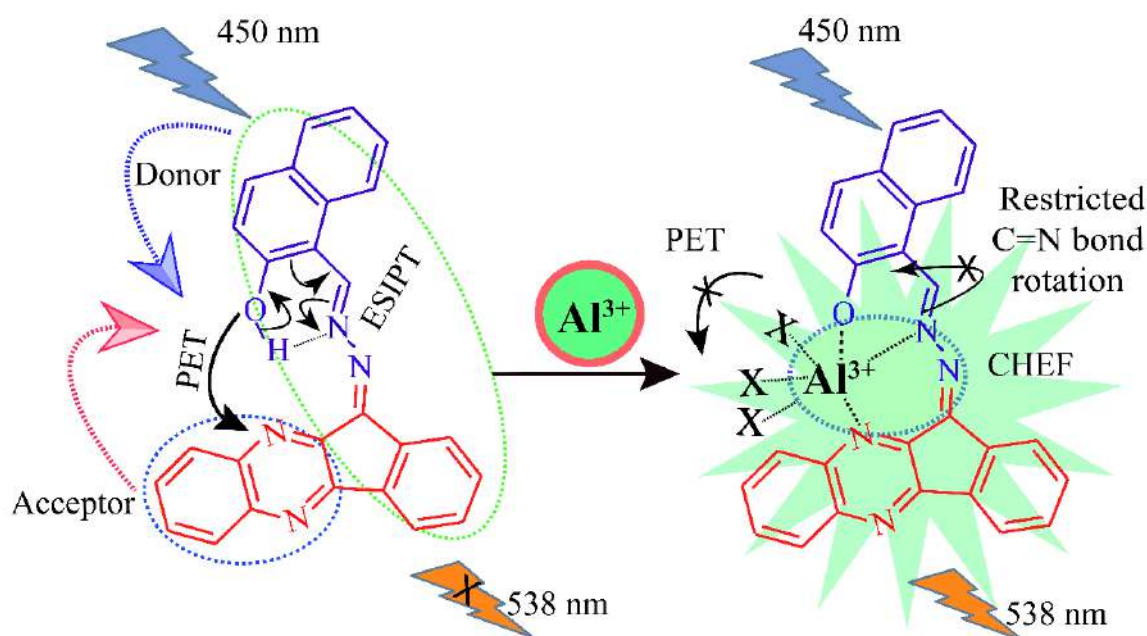
Al^{3+} (Fig. 6A.4). A substantial decrease in the peak position of the phenolic -OH proton was observed upon the addition of 0.2 to 1.2 Equiv. of Al^{3+} . Nevertheless, slight but considerable change was detected for the imine proton (-CH=N) compared to the -OH proton. Hence, the participation of the phenolic -OH unit and the imine nitrogen (-CH= N) for cation chelation was further corroborated. Quinoxaline nitrogen remains silent in the observed proton spectra, as it does not contain any hydrogen atom at any adjacent position.

6A.6 Plausible sensing mechanism

In the presence of Al^{3+} , the selective 'turn-on' emission increment accompanied by red-shifted fluorescence maximum might be owing to the abolition of PET in free **L9**, followed by the chelation-enhanced fluorescence (CHEF) process. Primarily, the low emissive nature of **L9** in experimental conditions could be due to the concomitant effect of rapid isomerization about the C=N bond and the PET process through delocalization of lone pair of electrons on imine nitrogen and the phenolic hydroxyl oxygen to the π -conjugated polyaromatic quinoxaline moiety, which is expected to act as the good acceptor^{6A.23} (Scheme 6A.2). Subsequently, as an outcome of the push-pull mechanism involved in the free **L9**, a suitable electron-withdrawing group might be available like metal ions. Accordingly, the lower wavelength band at 512 nm could be ascribed to the internal proton transfer from hydroxyl to imine nitrogen unit, giving rise to ESIPT.^{6A.24} A higher wavelength fluorescence at 532 nm was also detected (lowest in terms of intensity) because of the standard keto form of the free **L9**. However, upon the cation chelation, the electron density shifted from the naphthyl system to the electron-deficient metal-binding site. As a result, an intense magnification of the emission intensity took place *via* the coordination of Al^{3+} ions with the probe **L9**. It could be attributed to the participation of lone pair of 'N' atoms (imine unit), the 'O' atom (hydroxyl groups)^{6A.25}, and quinoxaline 'N' in the molecular structure. As the Al^{3+} ion coordinated to the hetero atom, mentioned above, the unshared pair of electrons on the relevant atoms no longer aided the PET process, leading to a fluorescence enhancement. That apart, the binding event between the cation and the ligand also imparted greater rigidity to the system, thereby resulting in an obstructed flow of vibronic energy.

Afterward, the as-formed complex interrupted the PET process and the ESIPT in the probe *via* reduction of the electron-accommodating capacity of the π -conjugated system of the aromatic rings together with the electron-giving capacity of the imine nitrogen as well as phenolic hydroxyl unit. Despite the extensive conjugation present in free receptor **L9**, the coordinating sites still may lack perfect planarity. But the formation of the stable chelate complex between the probe and Al^{3+} resulted in structural rigidity as well as more planarity of the overall system, leading to an effective chelation-enhanced fluorescence (CHEF) effect.^{6A.26-6A.27} At the same

time, the *in-situ* formed complex engendered an intense green emission at 538 nm ($\lambda_{\text{ex}} = 450$ nm). These consequences suggested turn-on fluorescence at different fluorescence wavelengths, which could be an outcome of creating a new complex between the probe and Al^{3+} . The fast isomerization of the C=N bond ceased after the addition of aluminum ions, and as a combined effect, the ensemble exhibited strong emissive properties. To substantiate that the proposed detection mechanism proceeds *via* chelation (and not by the protonation or deprotonation of L_9), the fluorescence data of the probe upon the addition of sulphuric acid (strong) and acetic acid (weak) at the particular wavelength (450 nm) were recorded. A parallel experiment was also carried out using NaOH (a strong base) and NH_4OH (a weak base). However, no noticeable enhancement was noticed in such cases, nullifying the possibility of such change of emission intensity due to the de-protonation of the phenolic group (Fig. A6A.8)



Scheme 6A.2 Proposed sensing mechanism for Al^{3+} with probe L_9 .

To comprehend the reversible nature of the probe molecule, EDTA, a well-familiar chelating agent, was added to $[\text{L}_9 - \text{Al}^{3+}]$ ensemble, causing quenching of the emission intensity through the formation of well-known stable $[\text{EDTA} - \text{Al}^{3+}]$ complex (Fig. 6A.5). After that, again, upon introducing excess Al^{3+} ion to the mixture of $([\text{L}_9 - \text{Al}^{3+}] + \text{EDTA})$, the emission intensity went upward due to creating the strongly fluorescing $[\text{L}_9 - \text{Al}^{3+}]$ ensemble *via* the displacement of EDTA from the mixture. Based on this phenomenon, it could be suggested that L_9 might act as a reversible probe for Al^{3+} with a suitable binding agent, such as EDTA.^{6A.28}

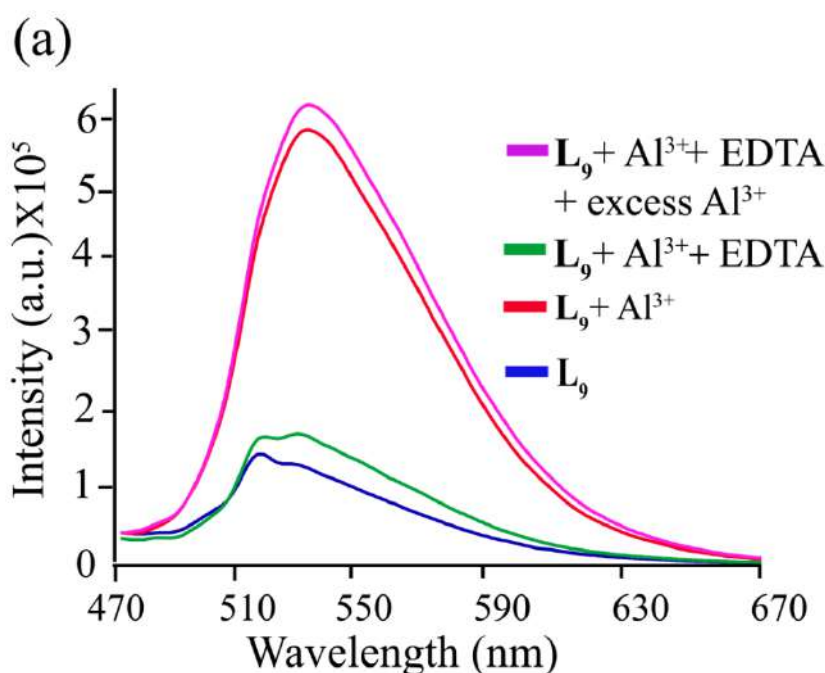


Figure 6A.5 The reversible sensing behavior of L_9 towards Al^{3+} ion. This experiment was carried out by adding Al^{3+} (100 μM) to the chemosensor solution (2 μM) followed by the addition of EDTA (100 μM). The resultant solutions were further titrated with excess Al^{3+} (>200 μM).

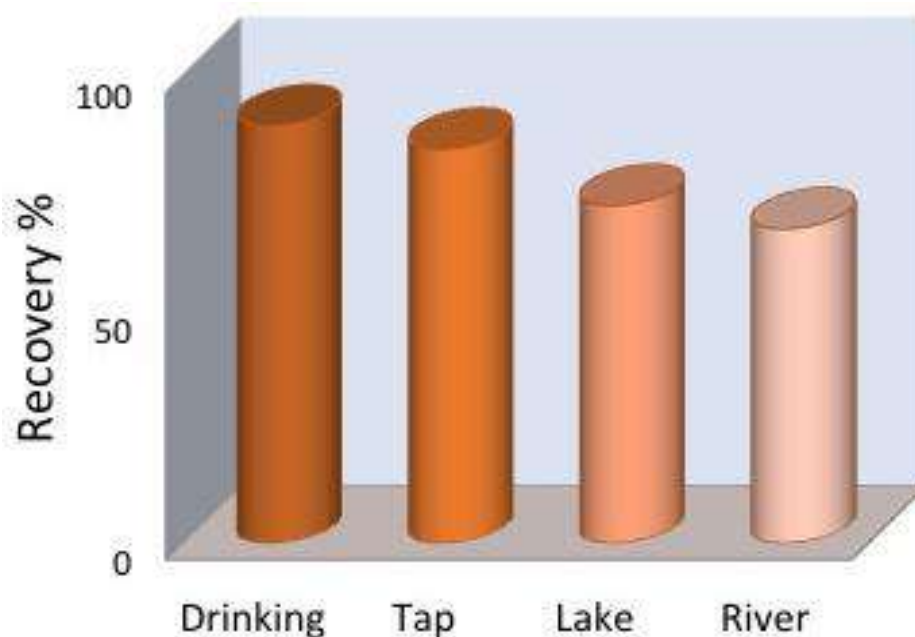
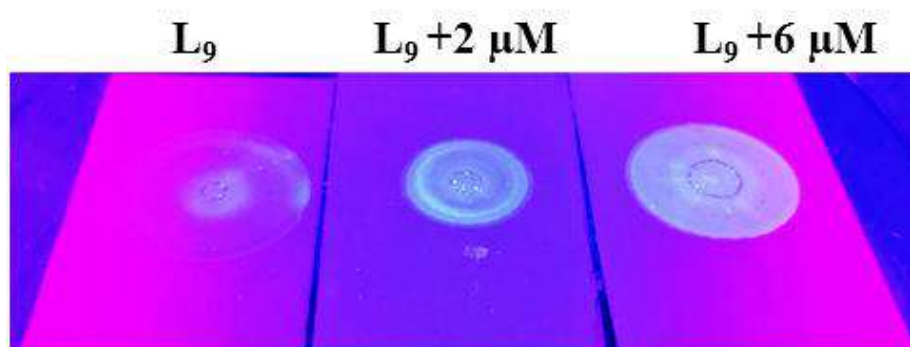
6A.7 Detection of Al^{3+} in real water samples and paper strips

A higher aluminum level in the water system may harm aquatic biocoenosis. So our focus was to detect aluminum from real natural samples by utilizing the synthesized probe L_9 . To perform the experiment, tap water, and drinking water were collected from the laboratory and the department of chemistry. IITG lake water was collected from the serpentine lake in IIT Guwahati campus. The river water was collected from the Brahmaputra River (near IIT Guwahati campus, Assam, India). All the collected real water samples were used to prepare a practical solution (methanol/water sample, 9:1, v/v). A known concentration of Al^{3+} (15 μM) was put into the experimental solutions of L_9 (2 μM), and the corresponding changes in the emission intensity at 538 nm were recorded (Fig. 6A.6). Thus, the fluorescence responses obtained after the addition of Al^{3+} to these water samples were compared. The characteristic fluorescence responses at 538 nm suggested that the probe L_9 showed the considerable ability to recognize aluminum in environmental water samples. After the addition of Al^{3+} to the probe solution, the percentage of recovery of the fluorescence intensity in the case of each of the water samples was calculated by taking deionized water as the standard (Table 6A.1).

Paper strip-based experiment has shown an important aspect for a probe to detect essential metal ions with higher selectivity.^{6A.29} Furthermore, to explore the practical significance of L_9 ; a model with test paper strips was introduced for the quick recognition of Al^{3+} .

Table 6A.1 Fluorescence detection of Al^{3+} in water samples of different sources

Water sample	Al^{3+} spiked (μM)	Recovery (%)
Drinking	15	90.00
Tap	15	85.00
Lake	15	80.35
River	15	75.00

**Figure 6A.6.** Fluorescent detection of Al^{3+} (0-15 μM) in tap water, lake water, river water, and drinking water by the probe L_9 ($\lambda_{\text{ex}} = 450 \text{ nm}$ and $\lambda_{\text{em}} = 538 \text{ nm}$).**Figure 6A.7** Paper-strip-based detection of Al^{3+} (0, 2, and 6 μM) using the probe L_9

It can be readily arranged simply by immersing the pieces of a standard filter paper in the solution of L_9 (10 μM), followed by air-drying for 1- 2 hrs. Next, the dry strips were saturated

with different concentrations of Al^{3+} ion for 2-3 min. After drying, those strips were placed into a UV chamber. Upon spraying various concentrations of Al^{3+} solution on the dried test strips, an intense 'turn-on' emission was observed under the UV ($\lambda = 365$ nm) light (Fig. 6A.7), which suggested the efficiency of the probe to detect aluminum on the paper strip. So it could have the potential ability to detect aluminum in the environment with more excellent selectivity.

6A.8 Application of the $[\text{L}_9 - \text{Al}^{3+}]$ ensemble on anion and *ct*-DNA binding studies

Given the specific detection of Al^{3+} by L_9 in physiological conditions even in a competitive milieu, it was anticipated that the generated complex could be proved to be an operative binding site for anions.^{6A.30} So, the *in situ* built $[\text{L}_9 - \text{Al}^{3+}]$ ensemble was picked up for the anion detection purpose. The positively charged metal center renders a typical environment for the interaction with the negatively charged ions. Fascinatingly, the ensemble was found to possess high selectivity toward biologically relevant anions, belonging to the inorganic phosphate (P_i) family, led to quenching emission. The phosphate and bi-phosphate showed little interference in the intensity spectra upon addition to the ensemble. Quite naturally, interest was further shifted to assess the selectivity and sensitivity of the ensemble with the inorganic pyrophosphate PP_i ($\text{P}_4\text{O}_7^{4-}$) in the aforementioned test medium. It was found that upon incremental addition of 17 equiv. of PP_i (34 μM) to the $[\text{L}_9 - \text{Al}^{3+}]$ ensemble, caused a progressive quenching in the original emission intensity of the ensemble via regenerating the original color of the solution (Fig. 6A.8a). The relative binding affinity of the $[\text{L}_9 - \text{Al}^{3+}]$ ensemble for PP_i was enumerated by a careful titration experiment with the sequential addition of PP_i and monitoring the continuous decrease in the fluorescence intensity at 538 nm (Fig. 6A.8b). Therefore, the 'OFF-ON-OFF'-type fluorescence performance of the ensemble could be substantiated by considering the strong binding affection of PP_i toward metal ions. The change of emission intensity of the ensemble ($\lambda_{\text{em}} = 538$ nm) with increasing concentrations of PP_i and the emission responses of the ensemble towards various anions are shown in Fig. 6A.8c and 6A.8d, respectively. The sequestration of Al^{3+} ions by PP_i from the ensemble and the formation of the stable $[\text{Al}^{3+} - \text{PP}_i]$ adduct triggered the liberation of the probe in the solution, rendering a high-intensity emission. Scrutiny of Job's plot revealed a 1:2 binding of PP_i with the metal ensemble (Fig. A6A.9). Based on the titration experiment, while the apparent association constant was found to be $1.05 \times 10^5 \text{ M}^{-1}$ (Fig. A6A.10), the limit of detection (LOD) of the ensemble for PP_i was calculated to be 4 μM (Fig. A6A.11). A distinct decline in the emission, indicating an outstanding selectivity and sensitivity of $[\text{L}_9 - \text{Al}^{3+}]$ ensemble toward PP_i in the buffer medium even in the presence of other competitive anions, could be ascribed to the binding of PP_i to the $[\text{L}_9 - \text{Al}^{3+}]$ complex, followed

by the appropriation of Al^{3+} in the form of an $[\text{L}_9\text{-Al}^{3+}\text{-PPi}]$ complex by releasing the free L_9 (Scheme 6A.3). So a metal ensemble-based fluorometric detection of anions can be established by the subsequent interaction of phosphate groups with the metal in the test medium. The 2:1 binding pattern between $[\text{L}_9\text{-Al}^{3+}:\text{PPi}]$ was further supported by the ESI-MS data (Fig. A6A.12). The peak at m/z 1221.9989 demonstrated the mass of the adduct of $2\text{L}_9\cdot 2\text{Al}$ and PPi ($2\text{L}_9\cdot 2\text{Al} + \text{P}_2\text{O}_7 + 3\text{Cl} + \text{MeOH} + 3\text{H}$).

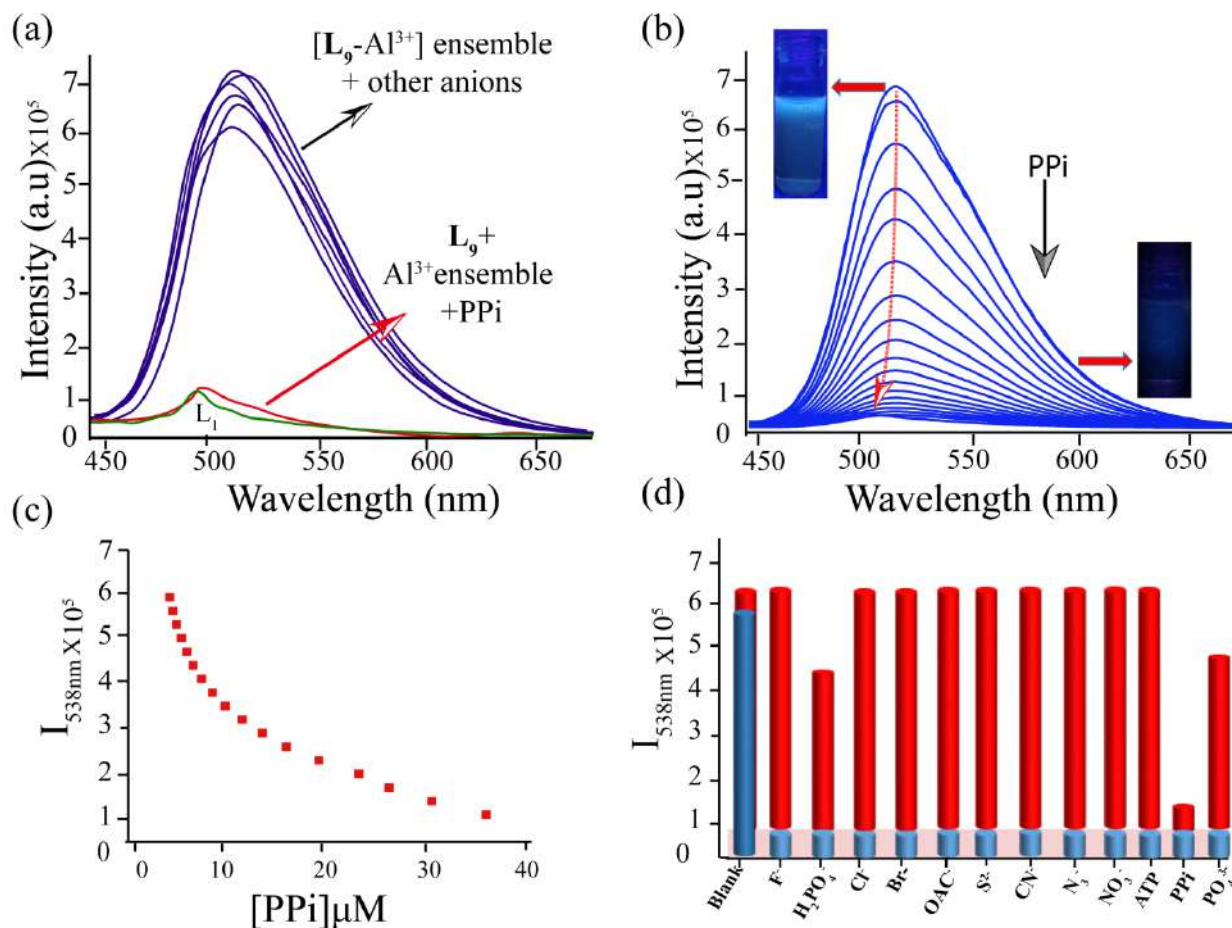
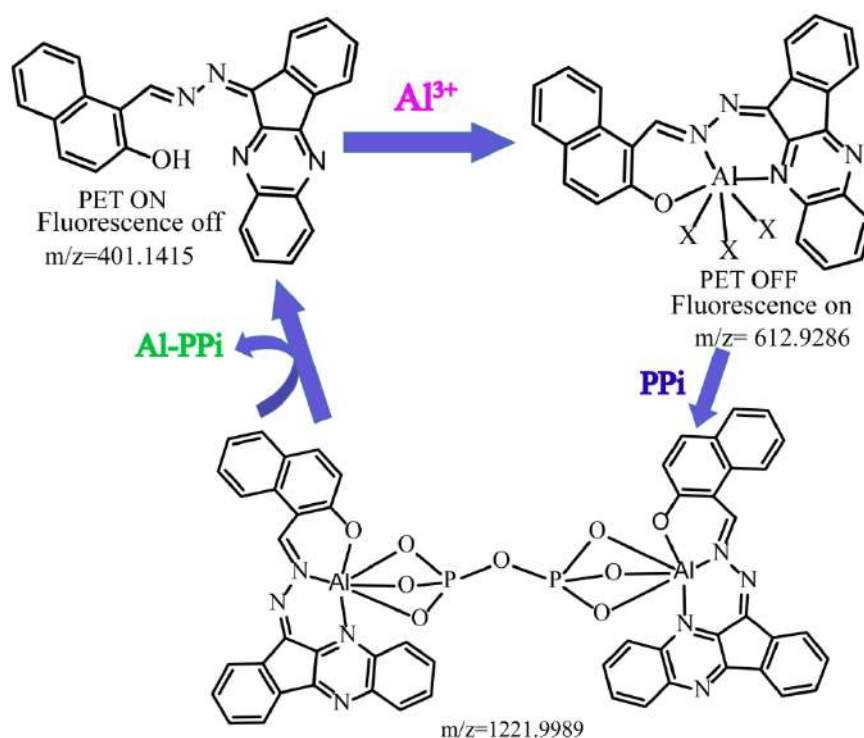


Figure 6A.8 (a) Change in fluorescence emission of $\text{L}_9\text{-Al}^{3+}$ ensemble in presence of 100 μM each various anion (F^- , Cl^- , Br^- , CN^- , N_3^- , H_2PO_4^- , PO_4^{3-} , PPi , ATP , OAc^- , NO_3^-); (b) Change in fluorescence emission of $\text{L}_9\text{-Al}^{3+}$ ensemble with incremental addition of PPi (0–34 μM). ($\lambda_{\text{ex}} = 450 \text{ nm}$); (c) Change in fluorescence emission of $\text{L}_9\text{-Al}^{3+}$ ensemble at 538 nm vs. $[\text{PPi}]$ and (d) Normalized fluorescence responses of $\text{L}_9\text{-Al}^{3+}$ ensemble towards various anions in methanol/aqueous HEPES (0.1 mM; 9:1, v/v; pH 7.3) at 25 $^\circ\text{C}$.

Further, a peak at $m/z = 262.0043$ (Fig. A6A.12) indicated complexation between the di-aluminum and PPi [$(\text{Al}_2\text{P}_2\text{O}_7(\text{OH})_2)^+$ (calculated $m/z = 261.8805$), suggesting the full release of aluminum ion from the adduct. Hence, it can be assumed that the detection of PPi is plausible due to the potential binding affinity of the PPi anion with the ensemble complex and the subsequent formation of the free L_9 , validating the formation of $[2\text{L}_9\cdot 2\text{Al}\cdot \text{P}_2\text{O}_7]$ complex. It was

envisaged that the $[L_9 - Al^{3+}]$ ensemble might undergo interaction with *ct*-DNA due to a high affinity of



Scheme 6A.3 Proposed overall interaction of the Probe with Al^{3+} and PPI.

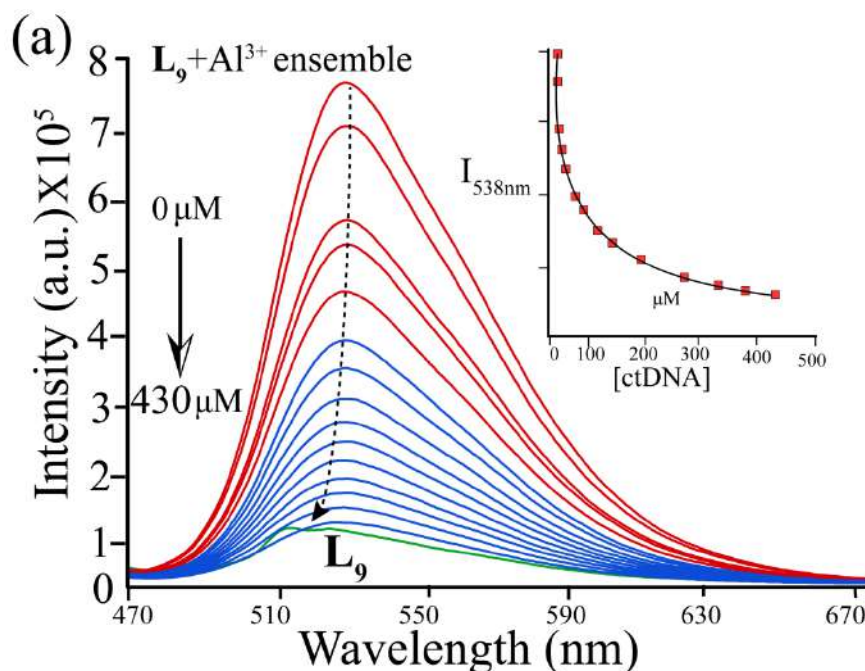


Figure 6A.9 Spectral changes of the $L_9 - Al^{3+}$ ensemble with varying concentrations of *ct*-DNA (0- 430 μM) ($\lambda_{ex} = 450$ nm). Molar concentration was calculated by dividing the absorbance of *ct*-DNA ($\lambda_{abs} = 260$ nm) with a molar extinction coefficient of *ct*-DNA per nucleotide ($\epsilon_{ct-DNA,260\text{ nm}} = 6600\text{ M}^{-1}\text{ cm}^{-1}$); Inset: Changes in the emission spectra at 538 nm with the incremental addition of *ct*-DNA.

Al^{3+} for phosphate groups. This event could be associated with drastic fluorescence changes initiated by the subsequent uncomplexation of coordinated Al^{3+} ion from the [L_9 - Al^{3+}] ensemble. Interestingly, as the calf-thymus DNA (*ct*-DNA) was slowly added to the highly emissive [L_9 - Al^{3+}] ensemble solution, there observed a subsequent decrease in the emission intensity (Fig. 6A.9). This phenomenon hints at the depletion of the [L_9 - Al^{3+}] ensemble *via* a competitive displacement of the Al^{3+} from the ensemble. It is quite reasonable to envision that the phosphate-rich *ct*-DNA likely interacted with the aluminum ensemble due to the affinity of Al^{3+} towards the phosphate backbones present in *ct*-DNA.^{6A.31-6A.32} Consequently, the L_9 - Al^{3+} ensemble got perturbed in the course of the interaction with *ct*-DNA, which, in turn, could result from favorable interaction of metal ensemble with the electron-rich phosphate anions present in the medium.

6A.9 Conclusion

In conclusion, we have rationally prepared a naphthyl-based multi-analyte probe, L_9 , which exhibited a 'turn-on' fluorescence response toward Al^{3+} and a naked-eye colorimetric response toward Cu^{2+} in a mixed aqueous medium. Interestingly, the Cu^{2+} -induced colored solution was found to be fluorescent inactive. This probe displayed its detection ability by enhancing the intensity and by causing red-shifts (~20 nm in emission for Al^{3+} and ~130 nm in absorbance for Cu^{2+}). It exhibited selective OFF-ON fluorescence signal only towards Al^{3+} (LOD 1.97 μM), presumably *via* the CHEF process. The probe was proved to be selective and sensitive for Al^{3+} over most of the biologically relevant cations. Upon undergoing chelation with Al^{3+} ions, the PET process gets hindered and improves the structural rigidity of the overall system, leading to a remarkable emission response. In addition, the [L_9 - Al^{3+}] ensemble detects PP_i anion as an ON-OFF sensor. The unique features of rapid Al^{3+} sensing and subsequent tracking of *ct*-DNA interaction have significant role in developing probes to investigate Al^{3+} -related toxicity in the future. Moreover, the present study established the utility of probe-coated dip-stick analysis with L_9 to detect Al^{3+} ions in the experimental medium.

References

- 6A.1 J. W. Steed and J. L. Atwood *Supramolecular Chemistry*, John Wiley & Sons, Ltd., New York, 2009
- 6A.2 D. Aydin, *Talanta*, 2020, **210**, 120615.
- 6A.3 A. K. K. Bhasin, P. Chauhan, and S. Chaudhary, *Sens. Actuators B Chem.*, 2021, 129328.
- 6A.4 K. Rezaeian, H. Khanmohammadi and S. G. Dogaheh, *New J. Chem.*, 2018, **42**, 2158- 2166.
- 6A.5 M. C. Aragoni, M. Arca, A. Bencini, C. Caltagirone, L. Conti, A. Garau, B. Valtancoli, F. Isaia, V. Lippolis, F. Palomba, L. Prodi and N. Zaccheroni, *Supramol. Chem.*, 2017, **29**, 912- 921.

- 6A.6 Di Wu, A. C. Sedgwick, T. Gunnlaugsson, E. U. Akkaya, J. Yoon and T. D. James, *Chem. Soc. Rev.*, 2017, **46**, 7105-7123.
- 6A.7 J. L. Ren, J. Zhang, J. Qing Luo, X.K. Pei and Z. Xi Jiang, *Analyst*, 2001, **126**, 698- 702.
- 6A.8 S. M. Ng and R. Narayanaswamy, *Anal. Bioanal. Chem.*, 2006, **386**, 1235- 1244.
- 6A.9 L. Peng, Z. J. Zhou, X.Y. Wang, R. R. Wei, K. Li, Y. Xiang, and A. J. Tong, *Anal. Chim. Acta.*, 2014, **829**, 54- 59.
- 6A.10 Y. Zhao, Z. Lin, H. Liao, C. Duan, and Q. Meng, *Inorg. Chem. Commun.*, 2006, **9**, 966- 968.
- 6A.11 B. Liu, P.F. Wang, J. Chai, X.Q. Hu, T. Gao, J. Bin Chao, T.G. Chen and B.S. Yang, *Spectrochim. Acta Part A, Mol. Biomol. Spectrosc.*, 2016, **168**, 98- 103.
- 6A.12 A. K. Manna, S. Chowdhury, and G. K. Patra, *New J. Chem.*, 2020, **44**, 10819- 10832.
- 6A.13 Y. Zhu, X. Gong, Z. Li, X. Zhao, Z. Liu, D. Cao and, R. Guan, *Spectrochim. Acta Part A: Mol. Biomol. Spectrosc.*, 2019, **219**, 202- 205.
- 6A.14 N. Yadav and A. K. Singh, *Mater. Sci. Eng. C.*, 2018, **90**, 468- 475.
- 6A.15 S. Slassi, M. Aarjane, A. Ghayoury, and A. Amine, *Spectrochim. Acta Part A: Mol. Biomol. Spectrosc.*, 2019, **215**, 348-353.
- 6A.16 E. K. Inal, *J. Fluoresc.*, 2020, **30**, 891- 900.
- 6A.17 M. Ronaghi, S. Karamohamed, B. Pettersson, M. Uhle'n and P. Nyre'n, *Anal. Biochem.*, 1996, **242**, 84-89.
- 6A.18 Xu, M. He, H. Yu, X. Cai, X. Tan, B. Lu and B. Shu, *Anal. Biochem.*, 2001, **299**, 188-193.
- 6A.19 A. K. Rosenthal and L. M. Ryan, *N. Engl. J. Med.*, 2016, **374**, 2575- 2584.
- 6A.20 A. Kumar, V. Kumar, U. Diwan, and K. K. Upadhya, *Sens. Actuators, B*, 2013, **176**, 420- 427.
- 6A.21 J. Lnczédy, T. Lengyel and A. M. Ure IUPAC Compendium of Analytical Nomenclature, Definitive Rules, 1997, web edition. IUPAC, 2002.
- 6A.22 National Secondary Drinking Water Regulations of the US EPA: Maximum Contaminant Levels, <http://water.epa.gov/drink/contaminants/secondarystandards.cfm>, accessed 15 January 2021.
- 6A.23 L. C. da Silva, E. P. da Costa, G. R.S. Freitas, M. A.F.de Souza, R. M. Araújo, V. G.Machado and F.G. Menezes, *Inorg. Chem. Commun.*, 2016, **70**, 71-74.
- 6A.24 K. Ganorkar, S. Mukherjee, S. Wankar, R. Joshi, C. Das, and S. K. Ghosh, *J. Photochem. Photobiol. A*, 2019, **371**, 81- 90.
- 6A.25 A. Saravanan, S. Shyamsivappan, N. K. Kalagatur, T. Suresh, N. Maroli, N. Bhuvaneshc, P. Koldaivel, and P. S. Mohan, *Spectrochim. Acta Part A: Mol. Biomol. Spectrosc.*, 2020, **241**, 118684.
- 6A.26 W. A. E. Omar, *J. Adv. Res.*, 2013, **4**, 525-529.
- 6A.27 S. H. Kim, H. S. Choi, J. Kim, S. J. Lee, D. T. Quang and J. S. Kim, *Org. Lett.*, 2010, **12**, 560–563.
- 6A.28 O. Ozdemir, *J. Mol. Struct.*, 2019, **1179**, 376- 389.
- 6A.29 J. Hatai, S. Pal, G. P. Jose, and S. Bandyopadhyay, *Inorg. Chem.*, 2012, **51**, 10129- 10135.
- 6A.30 S.M. Hwang, M. S. Kim, M. Lee, M. H. Lim, C. Kim, *New J. Chem.*, 2017, **41**, 15590- 15600.
- 6A.31 R. Singha, S. Samanta, P. Mullick, A. Ramesh, and G. Das, *Anal. Chim. Acta.*, (2018), **1025**, 172- 180.
- 6A.32 S. K. Sheet, B. Sena, R. Thounaojam, K. Aguan, and S. Khatua, *J. Photochem. Photobiol. A*, 2017, **332**, 101- 111.

Annexure 6A

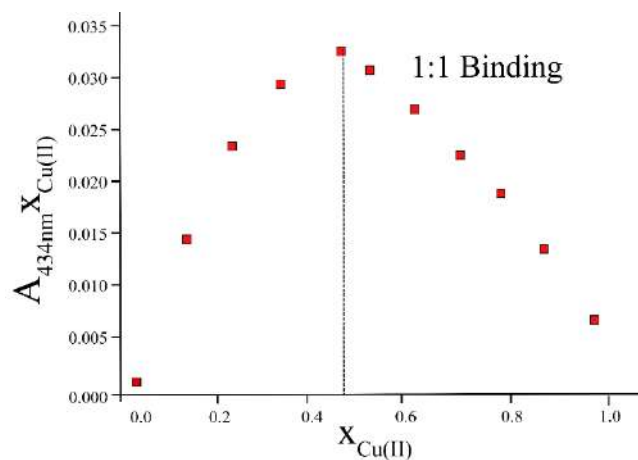


Figure A6A.1 Job's Plot for L_9 with Cu^{2+} [μM] from UV-visible spectrum. $X_{Cu(II)}$ is the mole fraction of L_9 at 434 nm in presence of the host.

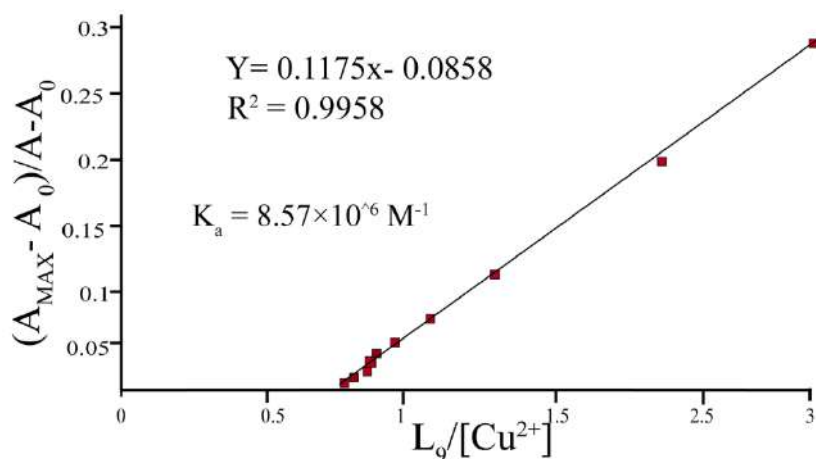


Figure A6A.2 Benesi-Hildebrand plot between L_9 and Cu^{2+} [μM] from UV-visible experiment.

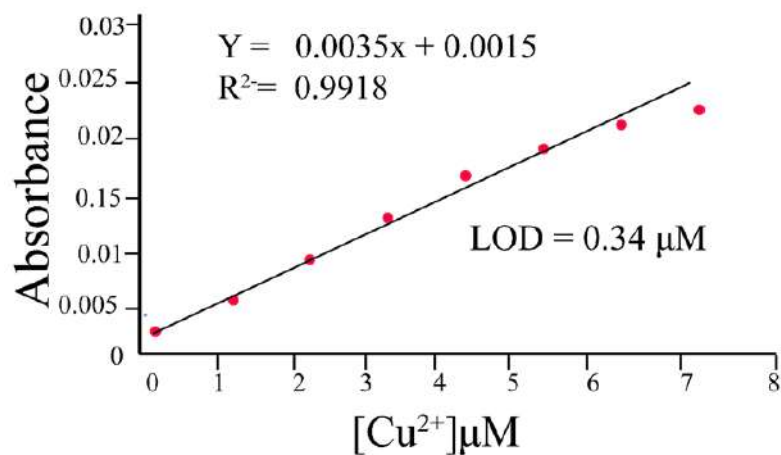


Figure A6A.3 Plot of Absorbance versus $[Cu^{2+}]$ for the detection limit calculation

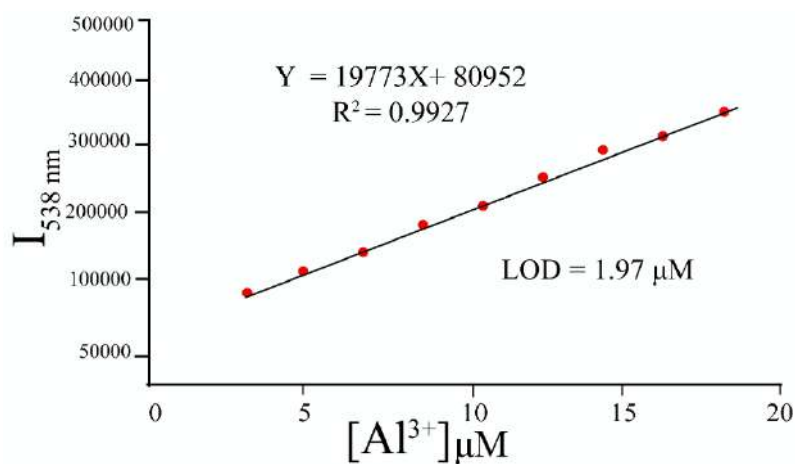


Figure A6A.4 Plot of fluorescence intensity versus $[\text{Al}^{3+}]$ for the limit of detection calculation at 538 nm.

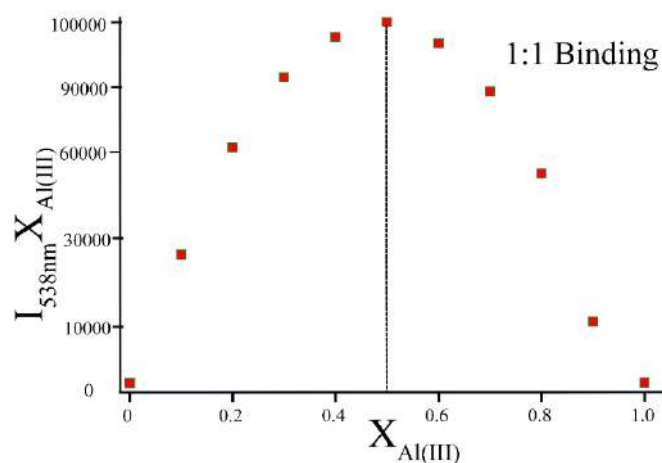


Figure A6A.5 Job's Plot for L_9 with Al^{3+} from fluorescence emission spectrum at 538 nm. $X_{\text{Al(III)}}$ = mole fraction of Al^{3+} in the presence of the guest.

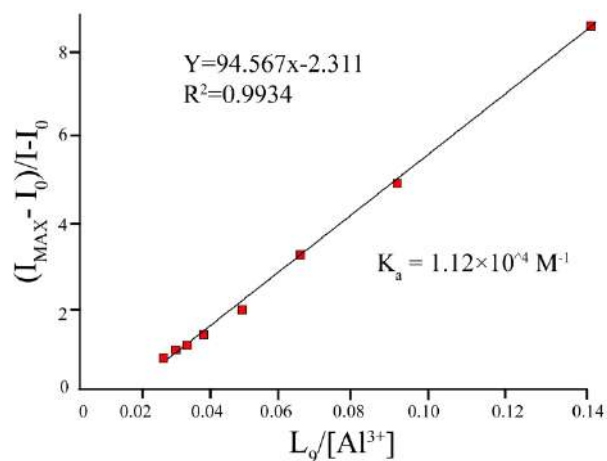


Figure A6A.6 Benesi-Hildebrand plot between L_9 and Al^{3+} [μM] (emission intensity at 538 nm).

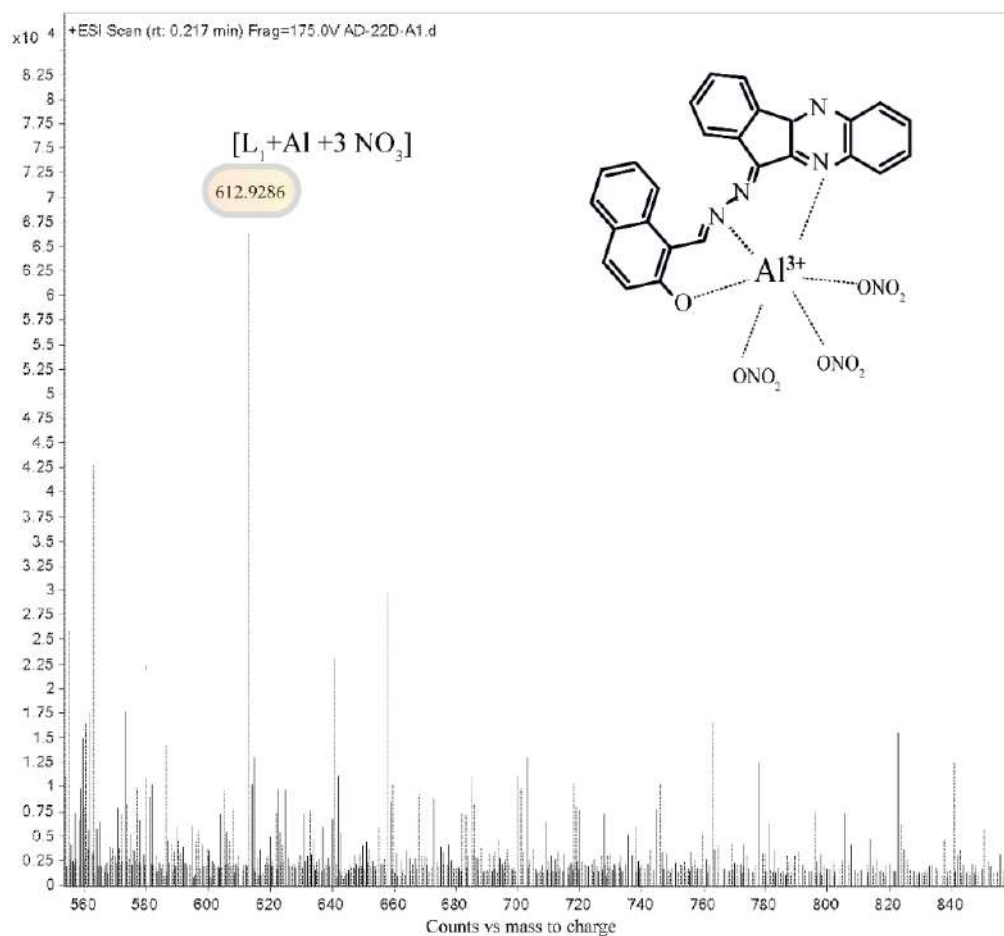


Figure A6A.7 HR- MS analysis of the solution of L_9 with $Al(NO_3)_3 \cdot 9H_2O$. (positive mode).

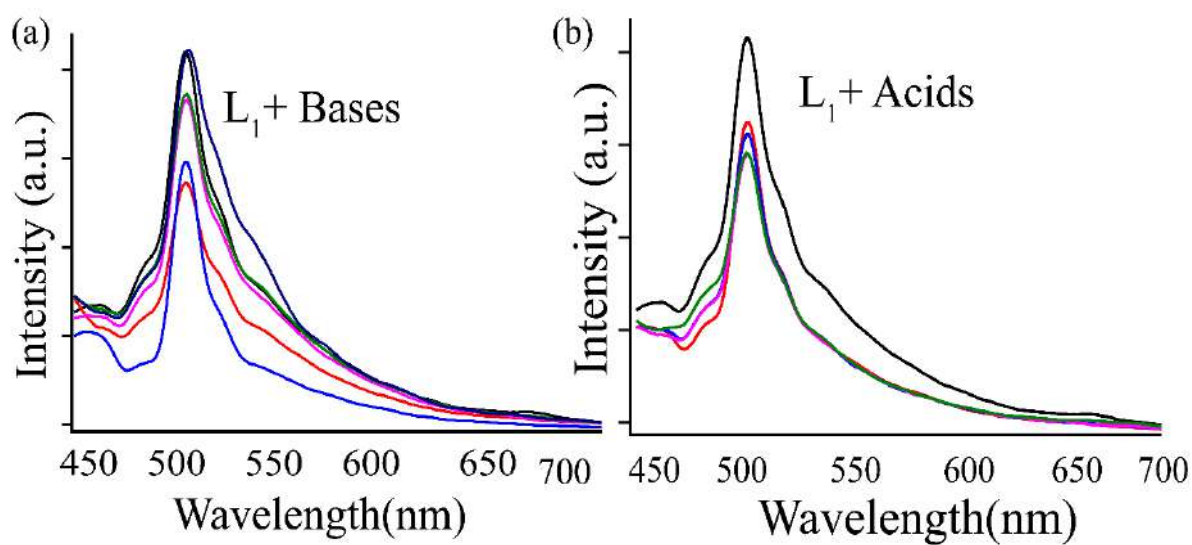


Figure A6A.8 Emission spectra to decipher the effect of the addition of (a) bases and (b) acids to L_9 in methanol-buffered mixed medium upon excitation at 450 nm.

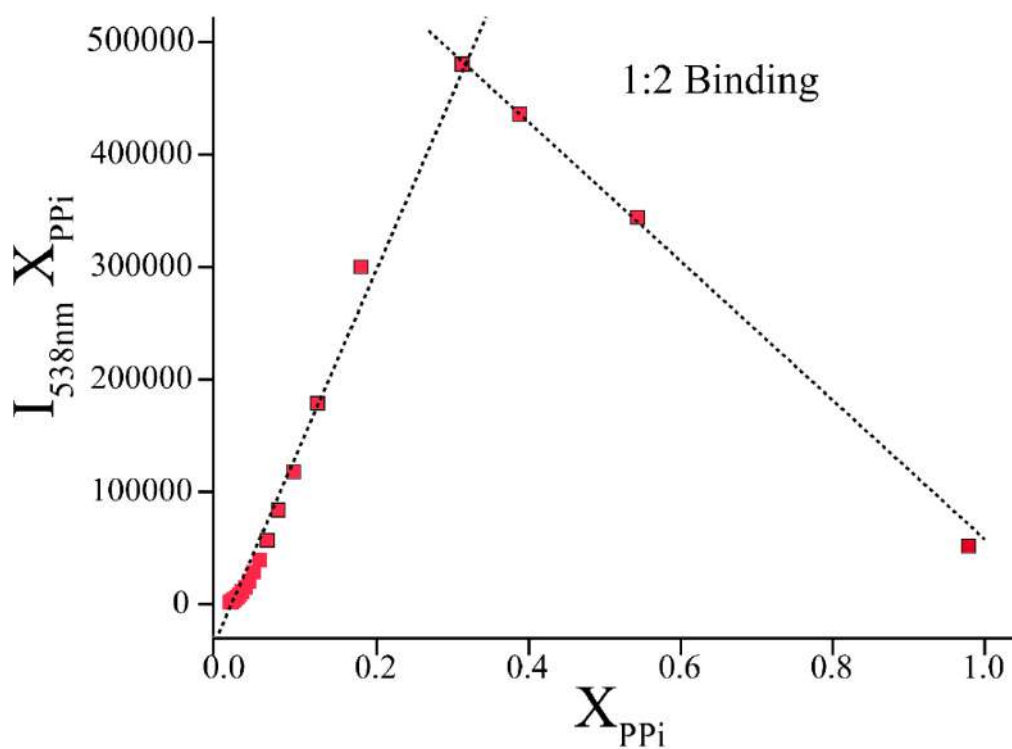


Figure A6A.9 Job's plot between $[\text{L}_9, \text{Al}^{3+}]$ complex and PPi , where X_{PPi} = the mole fraction of PPi at 538 nm.

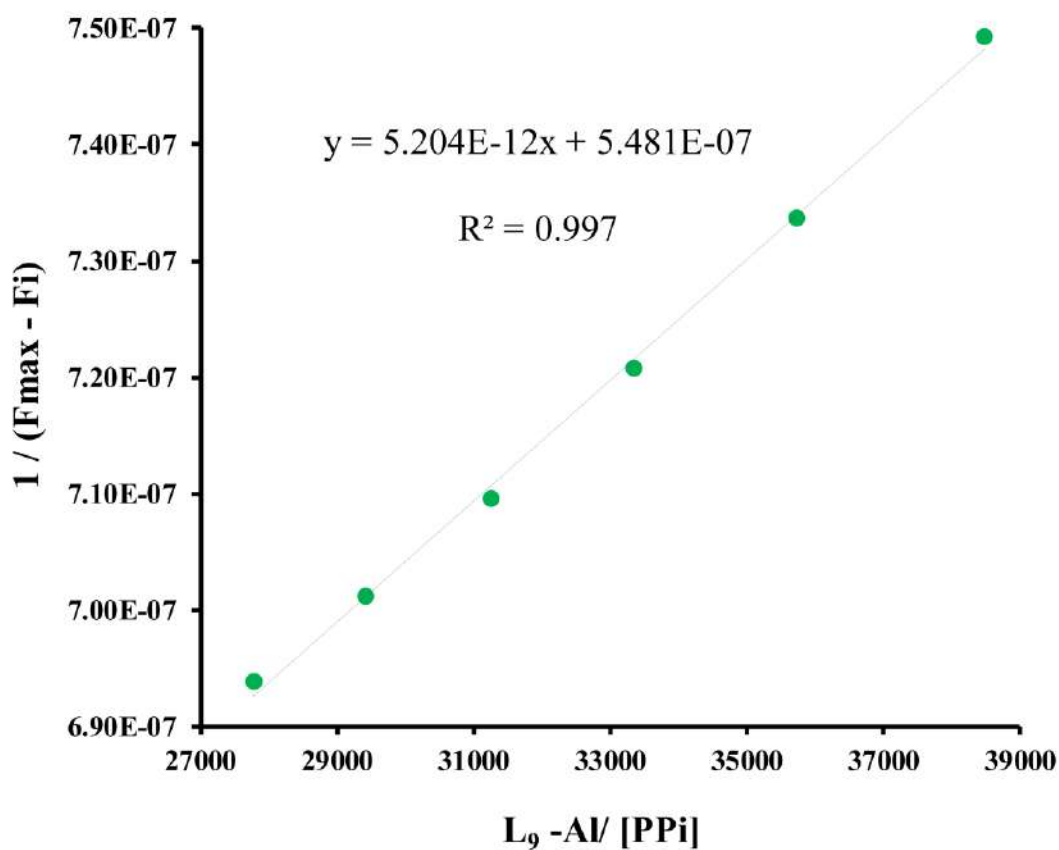


Figure A6A.10 Benesi-Hildebrand plot between $[\text{L}_9, \text{Al}^{3+}]$ complex and PPi [μM]

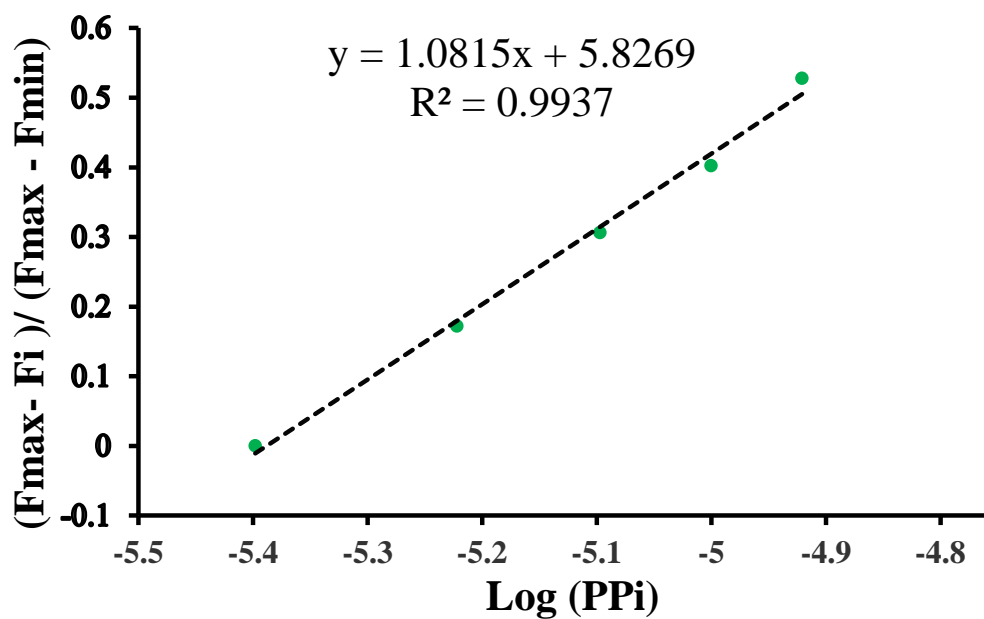


Figure A6A.11 Graph for the calculation of detection limit of PP_i towards $[L_9-Al^{3+}]$.

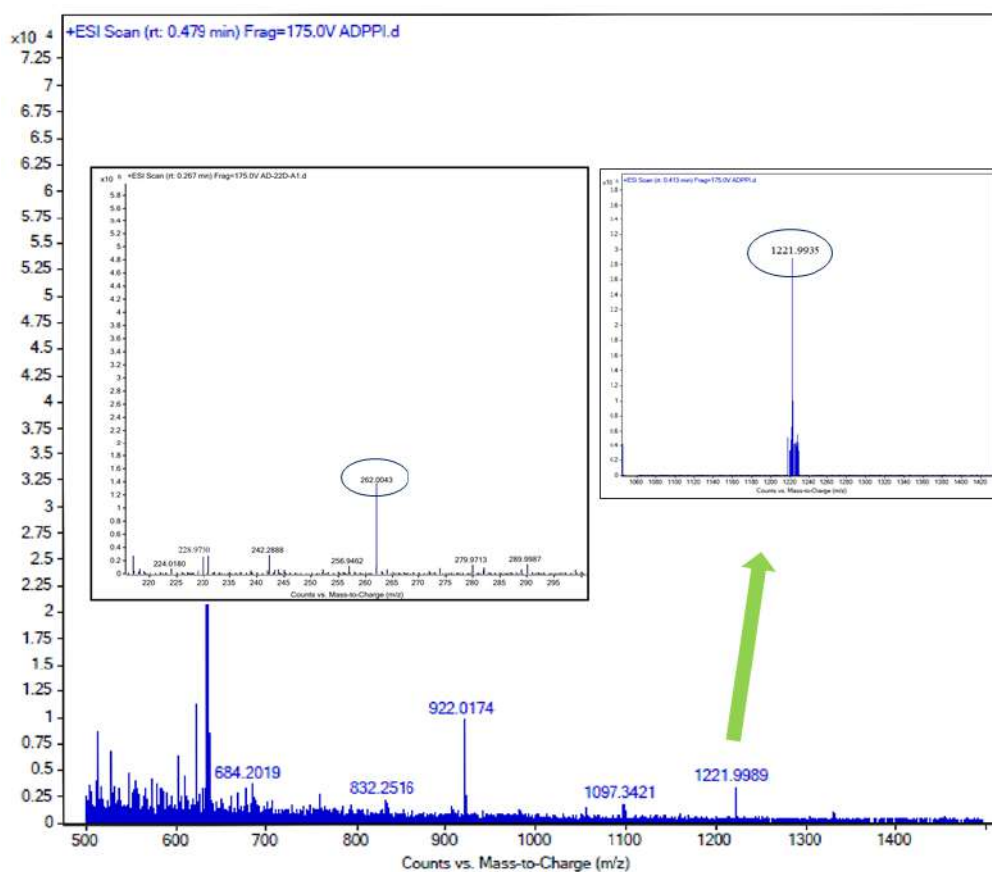


Figure A6A.12 Calculated mass for $[2L_9, 2Al + P_2O_7 + 3Cl + MeOH + 3H] = 1221.5232$, found 1221.9989. Inset: calculated mass for $[Al_2P_2O_7(OH)_2]^+$ = 261.8805, found 262.0043. (Positive mode).

TABLE A6A.1 Comparison of some recently reported Al³⁺ probes with the present work.

SI No.	References	Emission wavelength (s)	LOD	Solvent system
1	Present work	538 nm	1.97 μ M	0.1 mM HEPES buffer in CH ₃ OH aqueous system (9: 1; v/v; pH = 7.3)
2	A. K. Mahapatra, S. S. Ali, K. Maiti, S. K. Manna, R. Maji, S. Mondal, Md. R. Uddin, S. Mandal, P. Sahoo, <i>RSC Adv.</i> , 2015, 5 , 81203	416 nm	2.13 μ M	DMSO-H ₂ O (2 : 1; v/v; pH= 7.4)
3	S. Samanta, S. Goswami, Md. N. Hoque, A. Ramesh and G. Das <i>Chem. Commun.</i> , 2014, 50 , 11833-11836	537 nm	2.8 μ M	5 mM HEPES buffer in CH ₃ OH–aqueous system (9 : 1; v/v; pH = 7.3)
5	K. Ghosh, A. Majumdar and T. Sarkar, <i>RSC Adv.</i> , 2014, 4 , 23428	588 nm	13.8 μ M	10 mM Tris–HCl buffer in CH ₃ CN–H ₂ O (4 : 1; v/v; pH =7)
6	S. Suresh, N. Bhuvanesh, J. Prabhu, A. Thamilselvan, S. Rex Jeya Rajkumar, K. Kannan, V. Rajesh Kannan and R. Nandhakumar, <i>J. Photochem. Photobiol. A: Chem.</i> , 2018, 359 , 172-182	411 nm	4.13 μ M	50 mM HEPES in EtOH-H ₂ O solution (1:1; v/v; pH = 7.4)
7	A. Roy, U. Shee, A. Mukherjee, S. K. Mandal, and P. Roy, <i>ACS Omega</i> , 2019, 4 , 6864–6875	550 nm	10.98 nM	10 mM HEPES buffer in the CH ₃ OH/H ₂ O mixture (9:1; v/v; pH = 7.4)
8	A. Hazra, A. Roy, A. Mukherjee, Guru P. Maiti and P. Roy, <i>Dalton Trans.</i> , 2018, 47 , 13972-13989	376 nm	3.79 μ M	HEPES buffer in water : methanol (1 : 9; v/v; pH= 7.4)
9	A. K. Mahapatra, S. S. Ali, K. Maiti, S. K. Manna, R. Maji, S. Mondal, M. R. Uddin, S. Mandal and P. Sahoo, <i>RSC Adv.</i> , 2015, 5 , 81203	377 nm	2.16 μ M	DMSO–H ₂ O (2 : 1; v/v; pH= 7.4)

Chapter 6B

Chromone-based Symmetric Dipodal Probe as Multi-Analytic Sensor: Prospective Chemosensing Applications under Physiological Conditions



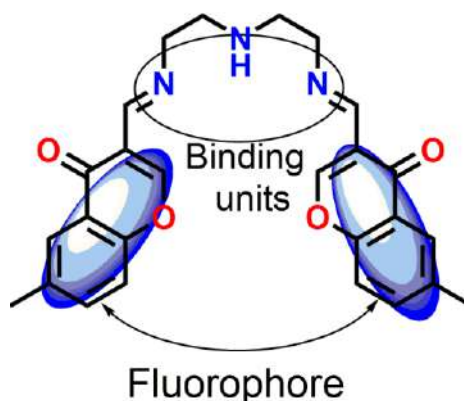
6B.1 Background and Focus of the Chapter

Immense efforts have been put to design multi-responsive chemical probes for the recognition of various biologically important ions/molecules due to their important roles in various physiological, biological, and environmental systems.^{6B.1-6B.4} Among the metal ions, aluminium (most abundant) and zinc (second most abundant) have been of great significance in the area of various biological, medicinal as well as enzymatic processes (living organism), food chemistry, pharmaceuticals, device manufacturing, cooking utensils, water plant treatment, industrial supplements in many more. Modern civilization without aluminium and human exposure to aluminium is unavoidable.^{6B.5-6B.8} Despite having numerous uses, elevated levels (or deficiencies) of these metals have some serious impact on the human body resulting in serious issues.^{6B.9-6B.18} On the other hand, pyrophosphate (PP_i) is a biologically crucial analyte due to its participation in several biological, pathological, and metabolic processes.^{6B.19-6B.23} Hence, recognition of PP_i has become the main target for research groups. Among spherical halides, the detection of fluoride has been the main focus due to its significant impact on the human body like osteoporosis, collagen breakdown, bone disorder, and thyroid activity.^{6B.24-6B.25} The presence of fluoride at a toxic level (such as in drinking water) results in skeletal and dental fluorosis.^{6B.26} Moreover, the Department of Health and Human Services has suggested an ideal fluoride level of 0.7–1.2 ppm for community water systems.^{6B.27} By using a dual responsive probe, we can simply regulate the presence of two elements by changing the solvent medium along with the change of excitation wavelengths and/or detecting the emission process. As a result, the development of efficient, simple-to-use fluorescent probes for detecting Al³⁺ and Zn²⁺ ions is vital for environmental and human health protection. A lot of single response probes are reported so far. Compared to single-analyte responsive probes, medium-dependent multi-responsive chemical probes, that can concurrently sense multiple analytes, display various advantages such as analytical as well as instrumental time reduction, suitability, and cost-efficiency. In comparison to other metal ions, few examples of dual responsive fluorescent probes for Al³⁺ and Zn²⁺ have been described, to date.^{6B.28-6B.31} In general, probes that rely on fluorescence emission at different wavelengths perform much better than those that rely only on fluorescence emission at a single wavelength, which may be achieved by modifying the media. On the other hand, to detect various analytes or ions, several strategies (such as metal ion complexes, excimer formation, conjugated polyelectrolytes, etc.) have been utilized. But probe-metal ensemble-based sensors for fluorometric detection of analyte rely on the interactions between the analyte and receptor-stabilized ions/ionic species.^{6B.32-6B.33} In recent years, many coumarin-derived fluorescence probes have been reported.^{6B.34-6B.35} To the best of our knowledge, most of the

reported chemical probes are utilized only in selective detection of a particular analyte and few of them were operated in organic or mixed organic medium. Thus, planning to design a multifunctional receptor for the detection of more than one analyte still creates a challenging task in the research area.^{6B.36-6B.40} So our focus was to plan a simple, water-soluble, interference-free fluorescent probe for the detection of various important ionic species in a physiological medium. As a continuation of our research probes for the detection of different analytes,^{6B.41-6B.42} Herein, we have designed and synthesized a simple chromone derivative-based multi-selective chemical probe **L₁₀** which was utilized for selective “turn-on” detection of Al³⁺ in an aqueous medium at physiological pH. The probe-Al³⁺ ensemble could be employed as a fluorescence “turn off” sensor for PP_i among all other common anions under the same experimental condition. On the other hand, **L₁₀** also exhibited small chelation enhanced quenching effect only with fluoride ions in acetonitrile medium *via* deprotonation mechanism. The adduct [**L₁₀**-F⁻] could also be used for the recognition of Zn²⁺ under an identical experimental milieu.

6B.2 Structural aspects of the chemosensor **L₁₀**

The chemosensor is decorated with a signaling unit (chromophore/fluorophore) and guest (metal/anion) coordination site (binding part) connected through a conventional imine bond. The chromone derivative moiety has increased the conjugation of the entire system (Scheme 6B.1).



Scheme 6B.1 Structural features of chemosensor **L₁₀**.

6B.3 Optical studies in the presence of analytes

6B.3.1 Absorption Studies

The detection ability of the probe **L₁₀** was investigated in the presence of various anions. It exhibited excellent optical sensing properties towards F⁻ through colorimetric responses in an acetonitrile medium (Fig. 6B.1a). It was assumed that potential hydrogen bonding of F⁻ with -NH unit and subsequent deprotonation of -NH proton produced a recognizable colour change in the solution. The free probe exhibits three absorption bands (presumably due to the chromone

units), a small band at 260 nm, broadband at 345 nm with a shoulder peak at 432 nm. However, after the addition of the fluoride ion, the shoulder band at 432 nm was shifted to 530 nm. There was also a prominent blue shift of ~ 27 nm (from 345 nm to 318 nm) observed for the 345 nm peak, but the other peak remained unaltered. The observation indicated the formation of an $[\mathbf{L}_{10}\text{-F}^-]$ complex in the medium. The addition of 20 equivalents of F^- to \mathbf{L}_{10} caused a prompt colour change from orange-red to almost colourless within seconds, detectable even with the naked eyes (Fig. 6B.1c). By spectral studies, the addition of CN^- (only at high concentration, 50 equiv.) also showed only weak changes in solution colour of \mathbf{L}_{10} , whereas the other anions (50 equiv.) did not exhibit visible colour change (Fig. 6B.1c). In this context, the formation of prominent isosbestic points (325 nm) and blue-shift in the absorption spectra implied some chemical interactions between \mathbf{L}_{10} and F^- ion.

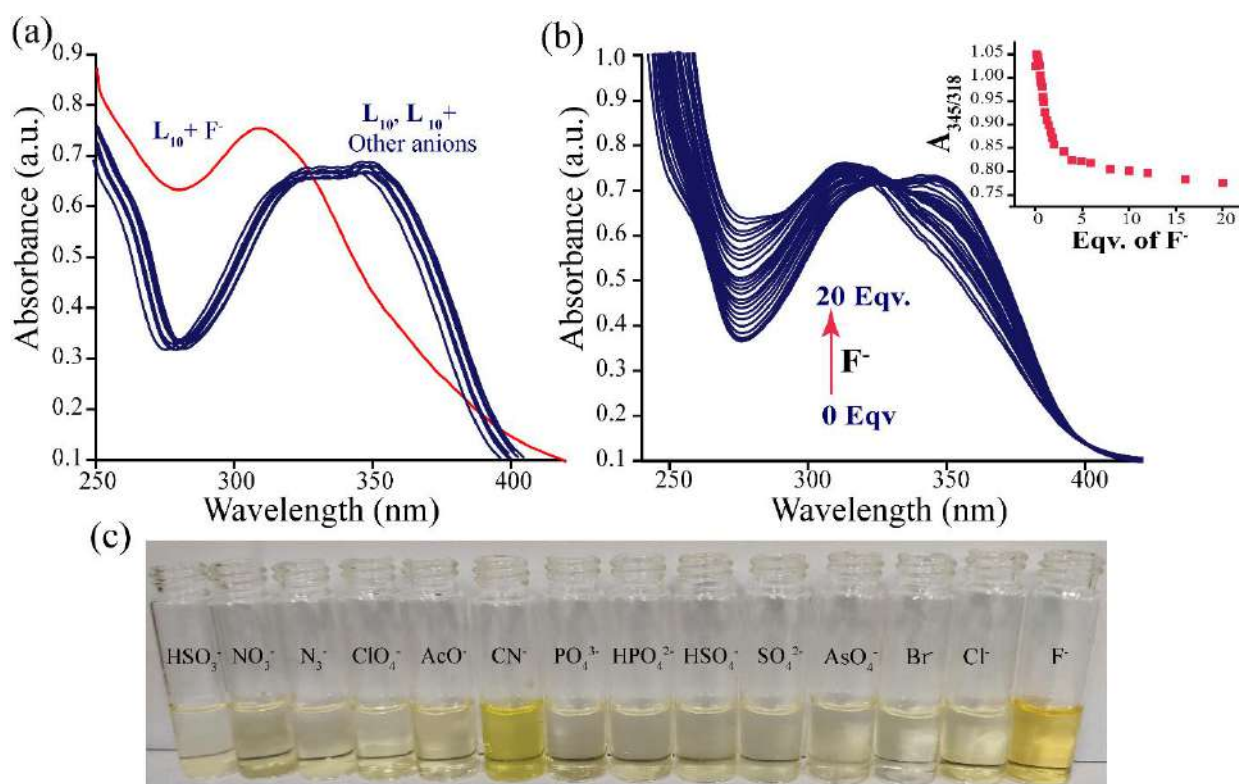


Figure 6B.1 UV-Vis spectra of (a) \mathbf{L}_{10} (50 μM) in presence of various anions (10 Eqv.) (b) changes in the absorption spectra of \mathbf{L}_{10} with incremental addition of F^- . Inset: Change in absorption ratio (345/318) vs. Eqv. of F^- ion in acetonitrile at 25 $^\circ\text{C}$; and (c) Visual color change of the probe in presence of anions such as F^- , Br^- , Cl^- , HSO_4^- , N_3^- , HPO_4^{2-} , ClO_4^- , AcO^- , CN^- , PO_4^{3-} , SO_4^{2-} , HSO_3^- , AsO_4^- , OCl^- under ambient light;

\mathbf{L}_{10} revealed the colorimetric selectivity towards F^- with a comfortable limit of detection (LOD) value of 4.81 μM (Fig. A6B.1). Further, to obtain a better as well as quantitative idea about the binding interaction between the probe \mathbf{L}_{10} and F^- , systematic titration was done with the incremental administration of F^- in the aforementioned medium. The titration profile (Fig. 6B.1b) showed that the gradual addition of F^- to \mathbf{L}_{10} , triggered a systematic and significant blue

shift in absorbance at 318 nm whereas, the shoulder band at 432 nm gradually shifted to 530 nm, upon addition of 20 equivalents (1000 μM) of F^- . On the systematic evaluation of the B–H (Benesi–Hildebrand) plot, the binding constant related to the formation of $[\text{L}_{10}\text{--F}^-]$, the association constant was estimated as $9.8 \times 10^5 \text{ M}^{-1}$, showing good interaction between the probe L_{10} and F^- ion (Fig. A6B.2).

6B.3.2 Fluorescence “off-on” response for Al^{3+}

Initially, probe L_{10} showed moderate emission at around 450 nm ($\lambda_{\text{ex}} = 370 \text{ nm}$) in the aqueous solvent of 1 mM HEPES buffer (pH 7.4) at 25 °C. The nature of this emission was primarily attributed to the rapid C=N isomerization along with the photo-induced electron transfer (PET) process. To study the fluorescence response behavior of L_{10} towards metal ions, the emission was investigated upon treatment with various nitrates or chloride salts of metal ions (50 μM) in the aforementioned medium. As depicted in Fig. 6B.2a, only Al^{3+} exhibited a substantial “turn-on” red-shifted fluorescence response at 462 nm with ~ 7 times enhancement in intensity. But importantly, the other tested trivalent/divalent cations displayed no noticeable changes in emission spectra under identical conditions. Despite similarities with Al^{3+} , Fe^{3+} or Cr^{3+} displayed no appreciable changes in the emission spectral profile of the probe. The low quantum yield value ($\Phi_{\text{L}} = 0.0029$) of the free probe corresponded to the fluorescence quenching *via* the PET process. The addition of Al^{3+} to the above solution led to an increase in the emission maximum with a quantum yield value of $\Phi_{\text{Al}^{3+}} = 0.0055$. To get better insight into the sensing ability of the probe, systematic titration experiments were conducted. Incremental administration of Al^{3+} into L_{10} triggered a systematic increase in the emission spectra of L_{10} with a regular bathochromic shift (Fig. 6B.2b) up to the addition of 25 equiv. of Al^{3+} ions. A sharp increase in emission spectra was detected up to 110 μM concentration of Al^{3+} ion (Fig. A6B.3), and afterward, the spectral enhancement touched a saturation. Additionally, a linear correlation (up to 20 equiv. of Al^{3+}) between the emission intensity at 462 nm ($I_{462\text{nm}}$) and Al^{3+} equivalents (Fig. 6B.3b, inset) hinted that the probe L_{10} could be used to detect the Al^{3+} ion equivalents with good accuracy. The LOD calculated from the systematic titration experiment (Fig. A6B.3) was $5.5 \times 10^{-7} \text{ M}$, which is far below compared to the USEPA acceptable quantity of Al^{3+} ions in drinking water (0.05 mg L^{-1} (1.85 μM)).^{6B.43} From competitive experiments, it was found that most of the tested metal ions did not interfere in the process of sensing Al^{3+} ions (Fig. 6B.3c). However, Cu^{2+} had little interference in the fluorescence spectra obtained with Al^{3+} alone. It is worth mentioning that probe L_{10} turned out to be a good sensor for Al^{3+} over competing metal ions in aqueous media.

The participation of two Schiff base N atoms (C=N units) and lone pair of NH units was used to coordinate with Al^{3+} and thus the rigidify the molecular framework was enhanced by confining the free rotation of the C=N group, which resulted in substantial enhancement *via* the process of chelation-enhanced fluorescence (CHEF) process. The appropriate size and more charge density of Al^{3+} and the inner-cavity of the probe permit good interaction between the host molecule and the corresponding metal ion.

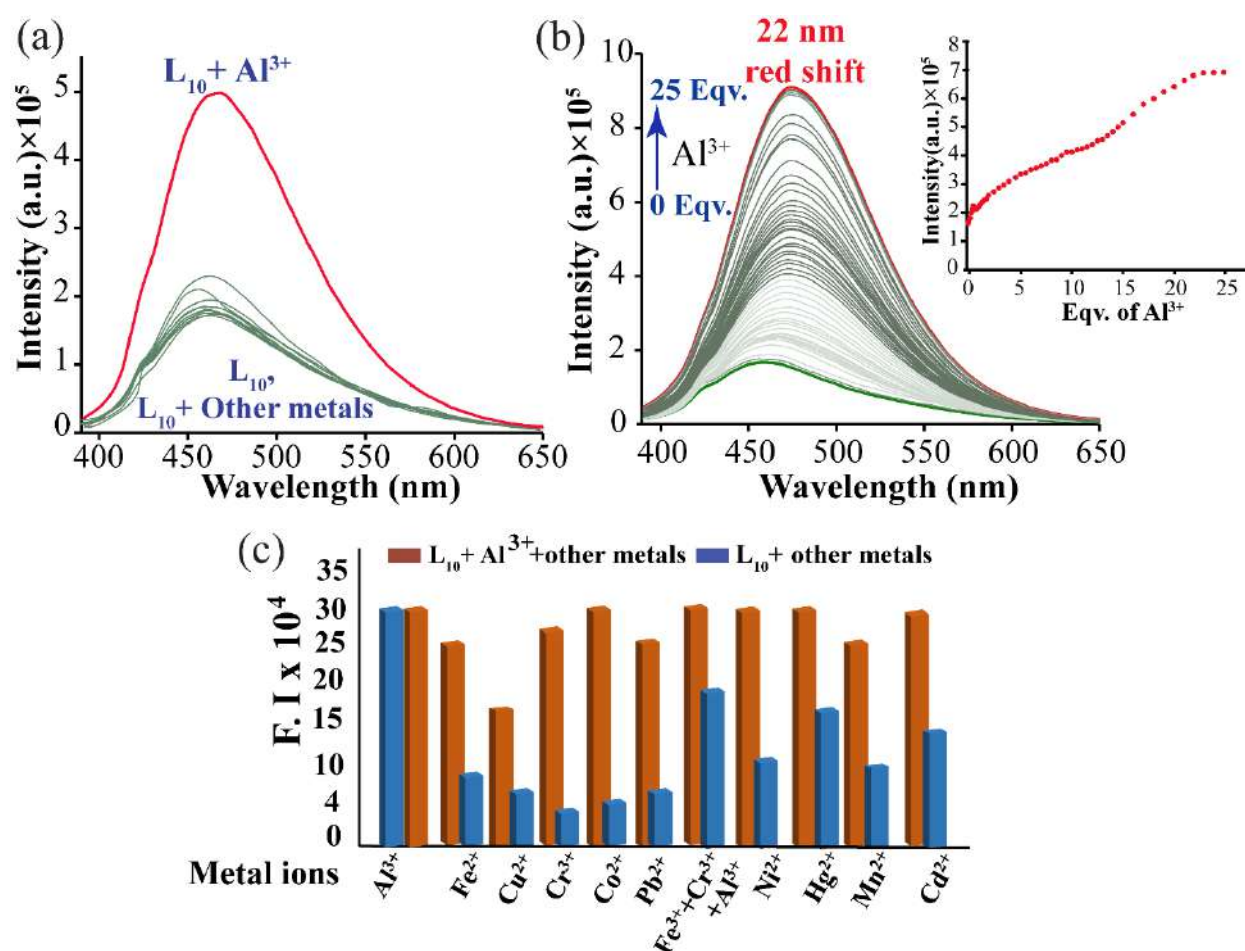


Figure 6B.2 (a) Changes in the fluorescence intensity of L_{10} (50 μM) in presence of 100 μM each various metal ions. Inset: Visual colour change of the probe in the presence of Al^{3+} under 366 nm UV light; (b) The fluorescence spectra of L_{10} upon addition increasing equivalent Al^{3+} in the aqueous solvent of 10 mM HEPES buffer (pH 7.4) at 25 $^\circ\text{C}$. Inset: changes in the fluorescence intensity ($I_{462\text{ nm}}$) of L_{10} (50 μM) with incremental addition of equivalent of Al^{3+} (0-25 Eqv.); (c) Portray the interference study of the probe L_{10} (50 μM) in the presence of various competitive metal ions (0.5 mM) such as Fe^{2+} , Cu^{2+} , Cr^{3+} , Co^{2+} , Pb^{2+} , $\text{Fe}^{3+} + \text{Cr}^{3+} + \text{Al}^{3+}$, Hg^{2+} , Ni^{2+} , Cd^{2+} , Mn^{2+} , alongside Al^{3+} .

6B.3.3 Fluorescence “on-off” response for F^-

The molecular framework of the dipodal probe L_{10} contained hydrogen donor site of NH, which can bind the anions, and chromone derivative was a fluorophore. Therefore, the amalgamation of

the NH fragment and chromone derivative within a single molecular architecture could be very important towards the anion binding nature. The dipodal probe displayed a sharp emission maximum at 520 nm in acetonitrile medium upon excitation at 440 nm ($\Phi_L = 0.00006$). In good agreement with the outcome of absorption studies, only the probe L_{10} interacted with F^- ion (among all the tetrabutylammonium or sodium salts of anions) in the excited state leading to a significant decrease of their intensities in the emission maxima ($\Phi_L = 0.00018$) (Fig. 6B.3a).

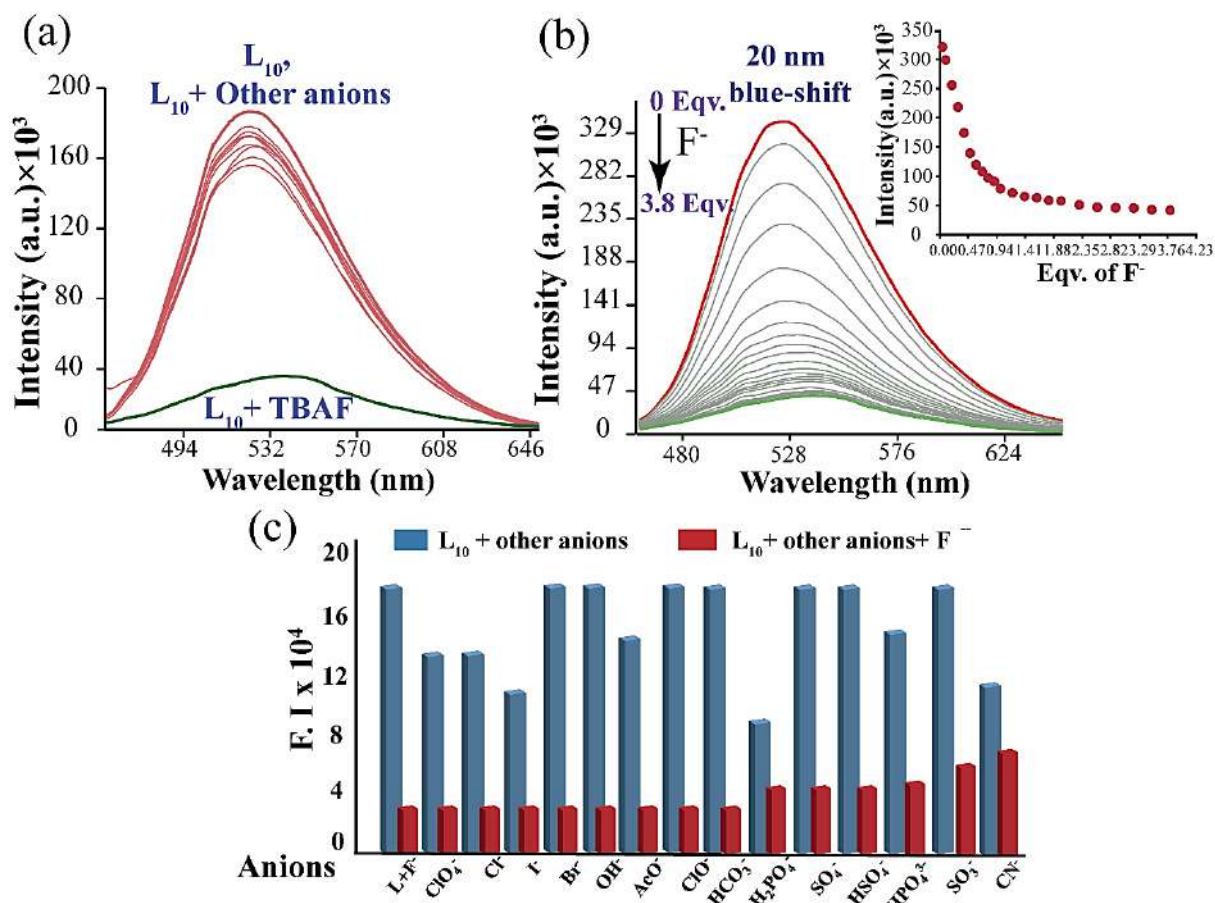


Figure 6B.3 (a) Change of emission spectra with various anionic analytes (5×10^{-2} M) in acetonitrile medium and the inset shows the corresponding colour changes in the presence of F^- under UV lamp, L_{10} (5×10^{-5} M); (b) Fluorescence emission titration in acetonitrile upon incremental addition of F^- to L_{10} (5×10^{-5} M each); Inset: Shows the emission intensity ($I_{536\text{ nm}}$ for L_{10}) as a function of the equivalent of F^- .

The protic solvents (like H_2O) were employed in the solution of L_{10} to verify the reversible nature of the probe. Interestingly, upon the addition of a small amount of water, the mother liquor of the probe L_{10} became colorless, which implied that protic solvents destroyed the hydrogen bonding between the probe and fluoride anions. The above findings hinted that the interactions between the probe and fluoride anions were mainly based on hydrogen bonding interaction while upon addition of an excess amount of ions de-protonation took place at the –NH unit attached with the framework. To attain a quantitative assessment of the binding

interaction, systematic fluorescence titration experiments were performed in the above-mentioned medium (Fig. 6B.3b). The emission intensity at 520 nm gradually decreased with the concentration of fluoride in the solution until it touched a plateau after the addition of 6 equivalents of fluoride ion. The limit of detection (LOD) was calculated to be 6.4×10^{-8} M (Fig. A6B.7), which is far lower than the enforceable drinking water standard for F^- (210 mM) set by the United States Environmental Protection Agency (EPA)^{6B.44} Further, the changes in the emission intensity were recorded upon the addition of various competitive anions along with F^- ion, which reveals that there is insignificant interference with the recognition ability of **L**₁₀ for F^- ions (Fig. 6B.3c). When the fluoride anion is bonded to the probe **L**₁₀, the “turn-off” emission phenomena could be interpreted by the PET process. In addition, the N–H part of the molecular framework tends to bind the fluoride anion through the $F^- \cdots H-N$ interaction due to the strong electronegative nature of the fluoride anion and then improve the acidity of the N-H proton. As a result, the increased acidity of the system may induce the deprotonation *via* H-bonding in the ground state to compensate for the charge separation as well as charge distribution, therefore leading to the fluorescence quenching by the PET mechanism.

6B.4 Plausible binding mechanism of **L**₁₀ with Al^{3+}

A fluorescence-based titration experiment and a careful investigation of the Job's plot recommend the 1:1 binding interaction between **L**₁₀ and Al^{3+} (Fig. A6B.4). The binding tendency of the probe **L**₁₀ for Al^{3+} was also ascribed to the apparent binding constant (K), which was calculated as $3.9 \times 10^5 M^{-1}$ (Fig. A6B.5). The mass analysis was also performed with the [**L**₁₀- Al^{3+}] ensemble in a 1:1 ratio (Fig. A6B.6) with a molecular ion peak at $m/z = 629.335$. Based on spectroscopic analysis plausible binding mechanism was plotted in Scheme 6B.2.

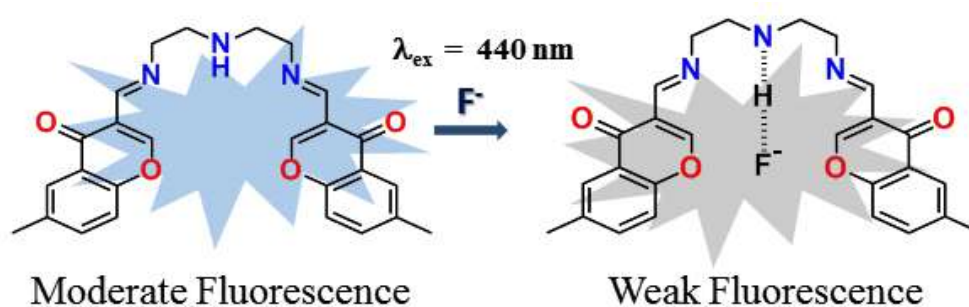


Scheme 6B.2 Plausible binding mechanism of **L**₁₀ towards Al^{3+} in aqueous medium.

6B.5 Plausible sensing mechanism of **L**₁₀ with F^-

The UV-vis absorption titration spectra (Fig. 6 B.1) and the fluorescence spectra (Fig. 6 B.2) of **L**₁₀ indeed showed minor bathochromic shift upon addition of fluoride. Such optical response

can possibly be ascribed to an H-aggregation between the two fluorophores induced by fluoride binding. Systematic job's plot experiment was performed to investigate the binding nature of **L**₁₀ and F⁻. The declining tendency of fluorescence intensity for the as-formed [**L**₁₀-F⁻] adduct revealed that the complex ratio of **L**₁₀ and F⁻ is 1:1 (Fig. A6B.8). The binding affinity of the probe towards F⁻ was also ascribed to the apparent binding constant (K), which is calculated to be $7.8 \times 10^6 \text{ M}^{-1}$ (Fig. A6B.9). Based on spectroscopic analysis plausible binding mechanism was plotted in Scheme 6B.3. Under extremely acidic or basic conditions, **L**₁₀ could not be used for the detection of F⁻. To simplify the sensing process, a TBAOH solution was added to **L**₁₀. The emission response of **L**₁₀ upon addition of TBAOH was dissimilar to that of the addition of F⁻ (Fig. A6B.10), which further indicates a hydrogen bonding between the probe and F⁻.



Scheme 6B.3 Plausible binding mechanism of **L**₁₀ towards F⁻ in organic medium.

6B.6 Application of the [**L**₁₀-Al³⁺] Ensemble on Anion Studies

Considering the high binding tendency of phosphate-based anions for Al³⁺, which is considered to be an oxophilic candidate, the **L**₁₀-Al³⁺ complex, was anticipated to act as a secondary sensor for phosphate-based anionic species.^{6B.45-6B.46} So, the *in situ* formed **L**₁₀-Al³⁺ ensemble was chosen for the anion recognition purpose. The positively charged metal ion could provide a suitable chance for the binding interaction with the anions of interest. Interestingly, the ensemble was able to detect the inorganic phosphate (P_i) family and lead to quenching the emission maxima. It was found that upon the addition of 50 Equiv. of each anion to the probe solution, only PP_i caused a substantial decrease in the original intensity of the ensemble *via* restoring the original colour of the probe solution (Fig. 6B.4a), while other anions showed either a minor or no change in the fluorescence emission spectra. The relative binding tendency of the [**L**₁₀-Al³⁺] ensemble for PP_i was verified by a systematic titration experiment with the gradual addition of PP_i and monitoring the continuous decline in the fluorescence intensity at 474 nm, signifying good selectivity of [**L**₁₀-Al³⁺] ensemble toward PP_i (Fig. 6B.4b). The limit of detection (LOD) of the [**L**₁₀-Al³⁺] ensemble for PP_i was found to be $1.02 \times 10^{-7} \text{ M}$ (Fig. A6B.11). The apparent association constant was estimated based on the titration experiment as $9.1 \times 10^5 \text{ M}^{-1}$ (Fig. A6B.12), while the sequestration of Al³⁺ ions by PP_i from the system and the generation of

$[\text{Al}^{3+}\text{-PPi}]$ adduct caused the liberation of L_{10} in the mother solution, interpreting a high-intensity emission.

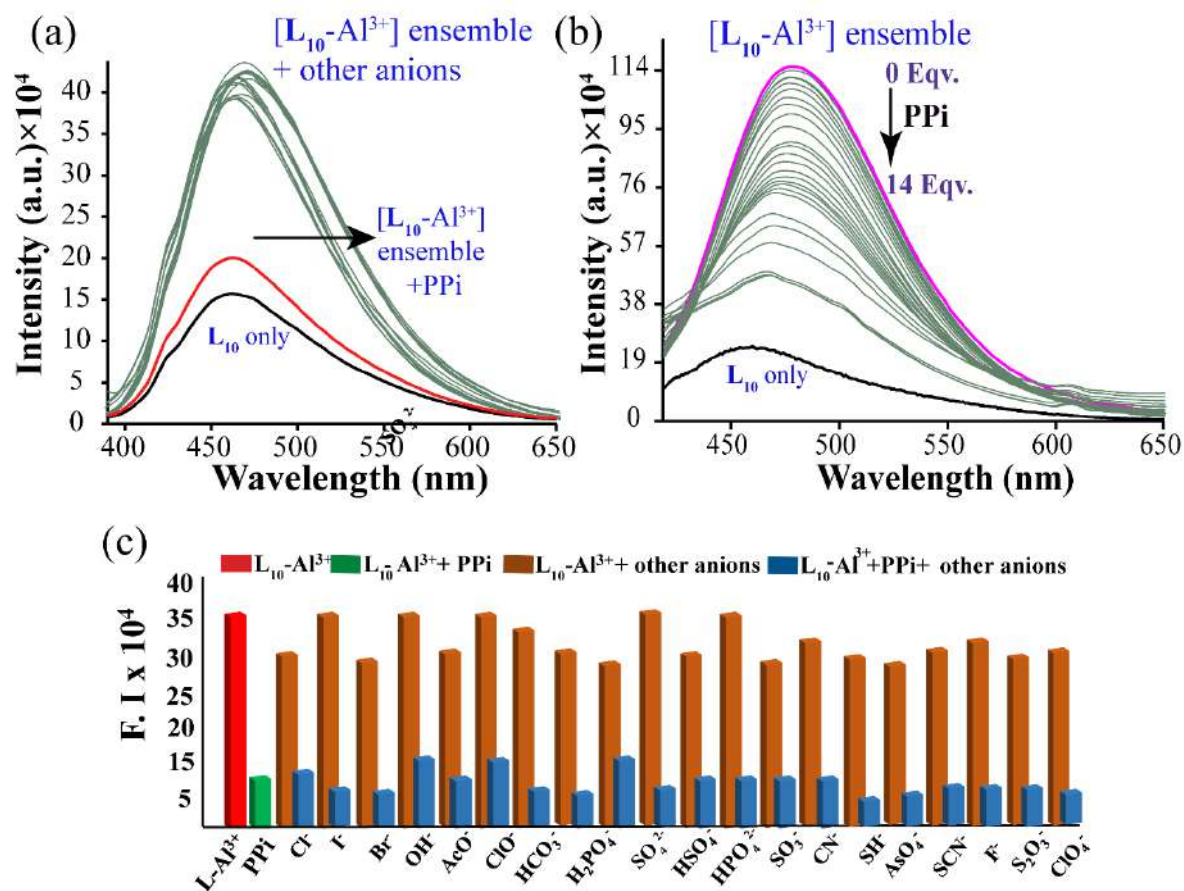


Figure 6B.4 (a) Change in emission spectra of $[\text{L}_{10}\text{-Al}^{3+}]$ ensemble in presence of various equivalents of anions (20 Equiv.); (b) Change in fluorescence emission ($\lambda_{\text{ex}} = 370$ nm) of the $[\text{L}_{10}\text{-Al}^{3+}]$ ensemble with the incremental addition of PPi (0–14 Equiv.); (c) Depict the interference study of the $[\text{L}_{10}\text{-Al}^{3+}]$ ensemble (50 μM) in the presence of various competitive anions (0.5 mM) such as F^- , Cl^- , Br^- , I^- , HSO_4^- , OH^- , H_2PO_4^- , HPO_4^{2-} , AcO^- , ClO_4^- , CN^- , AsO_4^- , HCO_3^- , $\text{S}_2\text{O}_3^{2-}$, SH^- , SO_4^{2-} , SO_3^- , SCN^- , OCl^- , ClO_4^- , alongside PPi anion.

The process of binding of PPi to the $[\text{L}_{10}\text{-Al}^{3+}]$ ensemble through the formation of a $[\text{Al}^{3+}\text{-PPi}]$ complex could be inferred from a clear decrease in emission intensity. This phenomenon is indicating an outstanding selectivity of the $[\text{L}_{10}\text{-Al}^{3+}]$ ensemble toward PPi in the aqueous buffer medium among other competitive anions (Fig. 6B.4c). So the ensemble-based fluorometric recognition of anions is believed to take place *via* subsequent interaction of phosphate groups with the metal ion.

6B.7 Application of the $[\text{L}_{10}\text{-F}^-]$ Ensemble on Metal Studies

Anion to cation-based recognition was planned with sequence specificity *via* $[\text{L}_{10}\text{-F}^-]$ ensemble $\rightarrow \text{Zn}^{2+}$ “on-off-on” phenomena in acetonitrile medium. Since the reported receptor provides chelating sites for metal ions and fluoride ions, we assumed it a proper platform to

verify the influence of anion on the coordination ability of L_{10} for the metal ions. We have selected Zn^{2+} (colourless salt) and F^- for the dual-response ability due to the negligible interference from the color of the salts and therefore it becomes easy to identify the spectral change associated with the complexation/decomplexation process. As depicted in Fig. 6B.5, the *in-situ* formed $[L_{10}-F^-]$ ensemble was directly employed for titration studies of the probe L_{10} with Zn^{2+} metal without further isolation. Upon addition of 1.8 equivalents of Zn^{2+} , a noticeable increase in the emission intensity was obtained at 520 nm proposing sequestration of Zn^{2+} with F^- to form ion-pair adduct.^{6B.47}

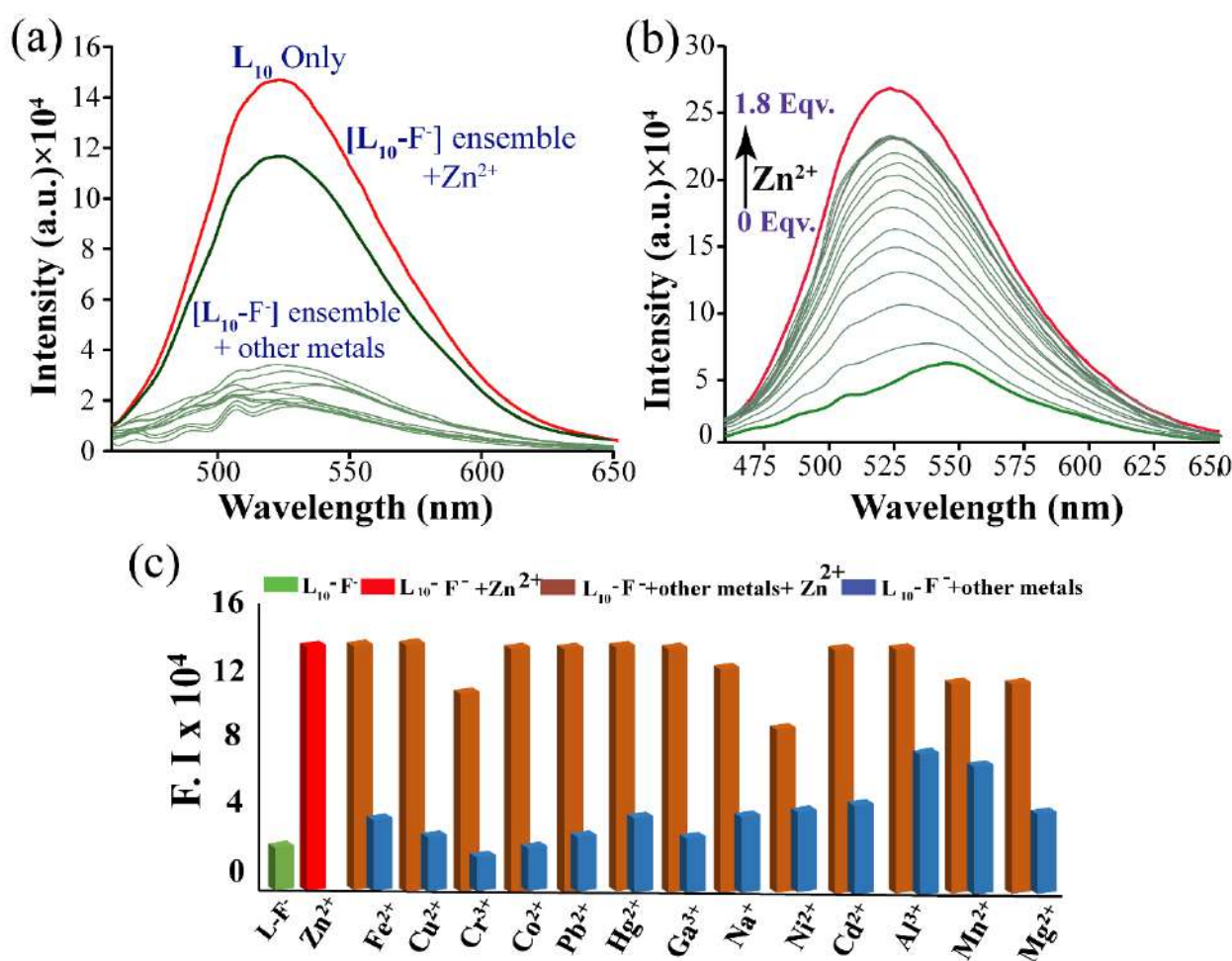


Figure 6B.5 (a) Change in emission spectra of $[L_{10}-F^-]$ ensemble in presence of various equivalents of metal ions (20 equiv.); (b) Change in fluorescence emission ($\lambda_{ex} = 440$ nm) of the $[L_{10}-F^-]$ ensemble with the incremental addition of Zn^{2+} (0–1.8 equiv.); (c) Depict the interference study of the $[L_{10}-F^-]$ ensemble (50 μ M) in the presence of various competitive metal ions (0.5 mM) such as Fe^{2+} , Cu^{2+} , Cr^{3+} , Co^{2+} , Pb^{2+} , Hg^{2+} , Ga^{3+} , Na^+ , Ni^{2+} , Cd^{2+} , Al^{3+} , Mn^{2+} , Mg^{2+} alongside Zn^{2+} .

The corresponding detection limit was calculated to be 2.96 μ M (Fig. A6B.13). The binding constant of $[L_{10}-F^-]$ ensemble in the presence of 1.8 Equiv. was calculated as 4.5×10^5 M^{-1} (Fig. A6B.14). In this case, the concentration of F^- ion always dominates over Zn^{2+} , while complete

sequestration of F⁻ ion by metal could not take place in the solution. As a result, ion-pair formation always got more priority over normal complexation phenomena. Moreover, to verify the experiment, we checked the response of various metal ions toward the [L₁₀-F⁻] ensemble but they remained almost silent towards F⁻.

6B.8 Conclusion

In summary, a chromone-based fluorescent probe L₁₀ is tested for the recognition of Al³⁺ (LOD of 5.5×10⁻⁷ M) with excellent fluorescent selectivity over other common interfering ions in aqueous media. The probe revealed a strong binding affinity ($K = 3.9 \times 10^5 \text{ M}^{-1}$) for Al³⁺ (*via* 1:1 coordination) even in the presence of the other competition metal ions *via* disrupting the C=N isomerization and leading to a chelation-enhanced fluorescence effect. Moreover, the [L₁₀-Al³⁺] system could be used as a sensor for PP_i subsequently owing to the strong attraction between Al³⁺ and PP_i *via* the “off-on-off” process. In addition, the probe L₁₀ displayed a selective fluorescent quenching effect with F⁻ ion deprotonation of -NH proton even in the presence of other halide ions in an organic solvent by both fluorescence and absorption spectra, while the in situ formed [L₁₀-F⁻] adduct, was also utilized for selective detection of Zn²⁺ ion induced by “on-off-on” mechanism under same experimental condition.

References

- 6B.1 M. Wang, X. M. Liu, H. Z. Lu, H. M. Wang and Z. H. Qin, *ACS Appl. Mater. Interfaces*, 2015, **7**, 1284 -1289.
- 6B.2 D.T. Quang and J.S. Kim, *Chem. Rev.*, 2010, **110**, 6280.
- 6B.3 T. Gunnlaugsson, H. D. P. Ali, M. Glynn, P. E. Kruger, G. M. Hussey and F. M. Pfeffer, *J. Fluoresc.*, 2005, **15**, 287-299.
- 6B.4 D. Wu, A. C. Sedgwick, T. Gunnlaugsson, E. U. Akkaya, J. Yoon and T. D. James, *Chem. Soc. Rev.*, 2017, **46**, 7105- 7123
- 6B.5 P. T. Srinivasan, T. Viraraghavan and K. S. Subramanian, *Water SA*, 1999, **25**, 47.
- 6B.6 J. Burgess, *Chem. Soc. Rev.*, 1996, **25**, 85.
- 6B.7 D. Krewski, R. A. Yokel, E. Nieboer, D. Borchelt, J. Cohen, J. Harry, S. Kacew, J. Lindsay, A. M. Mahfouz and V. Rondeau, *J. Toxicol. Environ. Health, Part B*, 2007, **10**, 1 -269.
- 6B.8 M. J. Cullen, M. J. Allwood, and D. M. Ambach, *Environ. Sci. Technol.*, 2012, **46**, 13048 -13055.
- 6B.9 C. A. Shaw and L. Tomljenovic, *Immunol. Res.*, 2013, **56**, 304 -316.
- 6B.10 B. Wang, W. Xing, Y. Zhao, and X. Deng, *Environ. Toxicol. Pharmacol.*, 2010, **29**, 308-313.
- 6B.11 A. M. Pierides, W. G. Edwards Jr, U. X. Cullum Jr, J. T. McCall, and H. A. Ellis, *Kidney Int.*, 1980, **18**, 115 -124.
- 6B.12 G. Berthon, *Coord. Chem. Rev.*, 2002, **228**, 319 -341.
- 6B.13 D. Noy, I. Solomonov, O. Sinkevich, T. Arad, K. Kjaer, and I. Sagi, *J. Am. Chem. Soc.*, 2008, **130**, 1376-1383.
- 6B.14 D. P. Perl and A. R. Brody, *Science*, 1980, **208**, 297-9.
- 6B.15 D. P. Perl, D. C. Gajdusek, R. M. Garruto, R. T. Yanagihara and C. J. Gibbs, *Science*, 1982, **217**, 1053-5.
- 6B.16 A. I. Bush, W. H. Pettingell, G. Multhaup, M. Paradis, J.-P Vonsattel, J. F. Gusella, K. Beyreuther, C. L. Masters and R. E. Tanzi, *Science*, 1994, **265**, 1464-1467.
- 6B.17 A. I. Bush, *Trends Neurosci.*, 2003, **26**, 207-14.
- 6B.18 M. D. Pluth, E. Tomat, and S. J. Lippard, *Annu. Rev. Biochem.*, 2011, **80**, 333-35.

- 6B.19 C. P. Mathews and K. E. van Hold, *Biochemistry, The Benjamin/ Cummings Publishing Company, Inc., Redwood City, CA*, 1990.
- 6B.20 J. K. Heinonen, *Biological Role of Inorganic Pyrophosphate, Kluwer Academic Publishers, Norwell*, 2001.
- 6B.21 R. E. Wuthier, *Calc. Tiss. Res.*, 1972, **10**, 198-206.
- 6B.22 S. A. Smith, S. H. Choi, R. Davis-Harrison, J. Huyck, J. Boettcher, C. M. Rienstra and J. H. Morrissey, *Blood*, 2010, **116**, 4353-4359.
- 6B.23 W. N. Limpcombe, N. Sträter, *Chem. Rev.*, 1996, **96**, 2375-2434.
- 6B.24 K. L. Kirk, *Biochemistry of the Elemental Halogens and Inorganic Halides, Plenum Press, New York*, 1991, 221-238.
- 6B.25 M. Laisalmi, H. Kokki, A. Soikkeli, H. Markkanen, A. Yli-Hankala, P. Rosenberg and L. Lindgren, *Acta Anaesthesiol. Scand.*, 2006, **50**, 982-987.
- 6B.26 S. Ayoob and A. K. Gupta, *Crit. Rev. Environ. Sci. Technol.*, 2006, **36**, 433-87.
- 6B.27 K. Sebelius, *Fed. Regist.*, 2011, **76**, 2383-2388.
- 6B.28 R. Purkait, S. Dey and C. Sinha, *New J. Chem.*, 2018, **42**, 16653-65.
- 6B.29 A. K. Bhanja, C. Patra, S. Mondal, S. Mishra, K. Das Saha, and C. Sinha, *Sens. Actuators, B*, 2017, **252**, 257-267.
- 6B.30 H. Liu, T. Liu, J. Li, Y. Zhang, J. Li, J. Song, J. Qu, and W.-Y. Wong, *J. Mater. Chem. B*, 2018, **6**, 5435-5442.
- 6B.31 W. Gao, Y. Zhang, H. Li and S. Pu, *Tetrahedron*, 2018, **74**, 6299-6309.
- 6B.32 D. H. Lee, J. H. Im, S. U. Son, Y. K. Chung and J.-I. Hong, *J. Am. Chem. Soc.*, 2003, **125**, 7752-7753.
- 6B.33 S. Mizukami, T. Nagano, Y. Urano, A. Odani and K. Kikuchi, *J. Am. Chem. Soc.*, 2002, **124**, 3920-3925.
- 6B.34 S. Warriar and P. S. Kharkar, *Spectrochim. Acta, Part A*, 2018, **188**, 659-665.
- 6B.35 S. Chen, P. Hou, J. Wang, L. Liu, and Q. Zhang, *Spectrochim. Acta, Part A*, 2017, **173**, 170-174.
- 6B.36 Z. Guo, I. Shin and J. Yoon, *Chem. Commun.*, 2012, **48**, 5956.
- 6B.37 T. Konry and D. R. Walt, *J. Am. Chem. Soc.*, 2009, **131**, 13232.
- 6B.38 M. Schmittel and H. W. Lin, *Angew. Chem., Int. Ed.*, 2007, **46**, 893.
- 6B.39 H. Komatsu, T. Miki, D. Citterio, T. Kubota, Y. Shindo, Y. Kitamura, K. Oka and K. Suzuki, *J. Am. Chem. Soc.*, 2005, **127**, 10798.
- 6B.40 H. Komatsu, D. Citterio, Y. Fujiwara, K. Minamihashi, Y. Araki, M. Hagiwara and K. Suzuki, *Org. Lett.*, 2005, **7**, 2857.
- 6B.41 A. Das and G. Das, *J. Photochem. Photobiol. A*, 2022, **425**, 113669.
- 6B.42 A. Das, S. De, and G. Das, *J. Photochem. Photobiol. A*, 2021, **418**, 113442.
- 6B.43 National Secondary Drinking Water Regulations of the US EPA: Maximum Contaminant Levels, <http://water.epa.gov/drink/contaminants/secondarystandards.cfm>, accessed 15 January 2021.
- 6B.44 X. Zheng, W. Zhu, D. Liu, H. Ai, Y. Huang, and Z. Lu, *ACS Appl. Mater. Interfaces* 2014, **6**, 7996-8000.
- 6B.45 C. Liang, W. Bu, C. Li, G. Men, M. Deng, Y. Jiangyao, H. Sun and S. Jiang, *Dalton Trans.*, 2015, **44**, 11352.
- 6B.46 S. M. Hwang, M. S. Kim, M. Lee, M. H. Lim and C. Kim, *New J. Chem.*, 2017, **41**, 15590.
- 6B.47 G. Tumcharern, T. Tuntulani, S. J. Coles, M. B. Hursthouse, and J. D. Kilburn, *Org. Lett.*, 2003, **5**, 4971.
- 6B.48. T. Ghosh, B. G. Maiya, and A. Samanta, *Dalton Trans.*, 2006, 795-801.

Annexure 6B

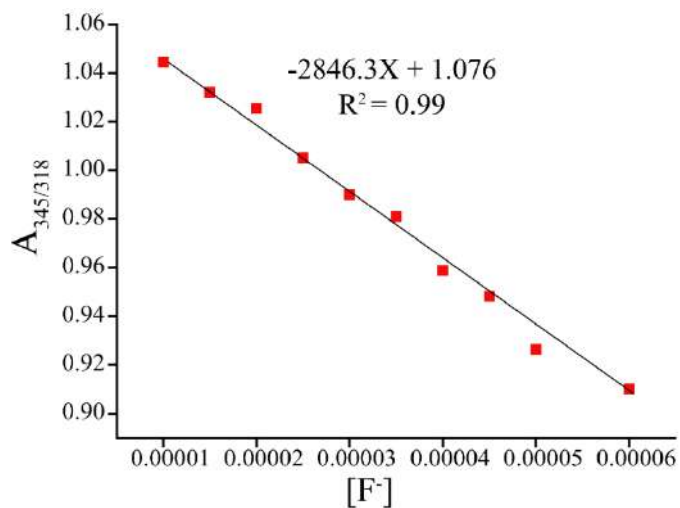


Figure A6B.1 Plot of absorbance ratio vs F^- [M] for the detection limit calculation (absorbance at $A_{345/318}$).

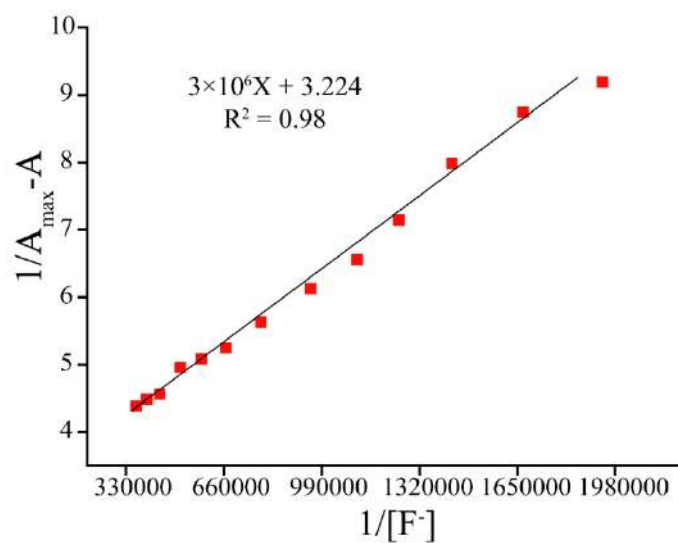


Figure A6B.2 Benesi-Hildebrand plot for calculation of association constant of F^- in acetonitrile medium from UV-visible experiment (absorbance at 318 nm).

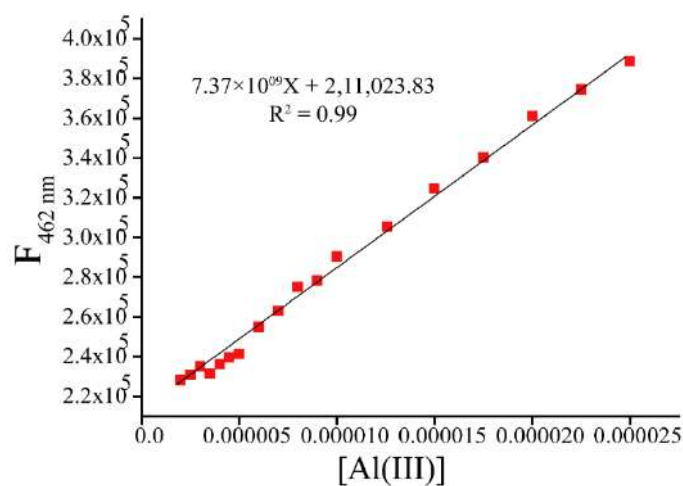


Figure A6B.3 Plot of emission intensity vs $[\text{Al}^{3+}]$ for the detection limit calculation (emission intensity at 462 nm).

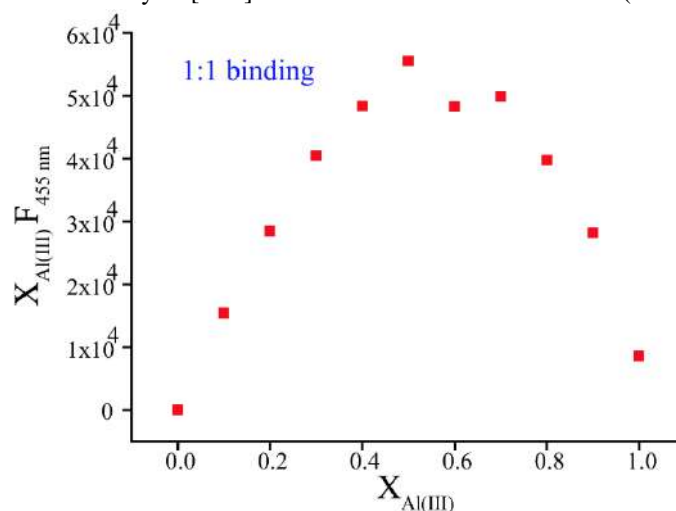


Figure A6B.4 Job's Plot for L_{10} with Al^{3+} from fluorescence emission spectrum at 455 nm. $X_{\text{Al(III)}}$ = mole fraction of Al^{3+} in the presence of the guest.

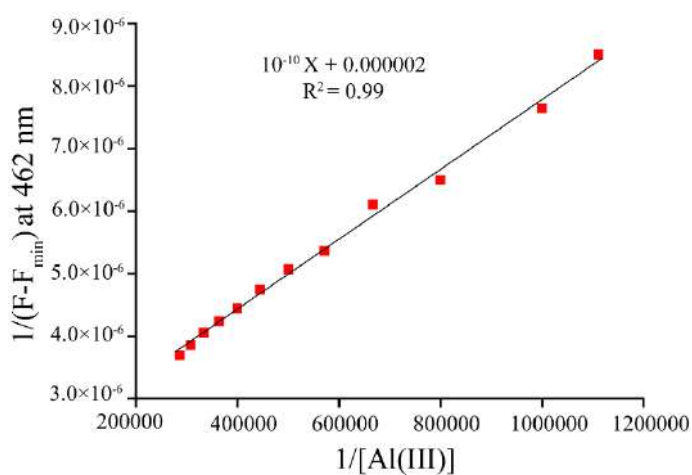


Figure A6B.5 Benesi-Hildebrand plot for calculation of association constant of Al^{3+} in aqueous medium from fluorescence experiment (emission intensity at 462 nm).

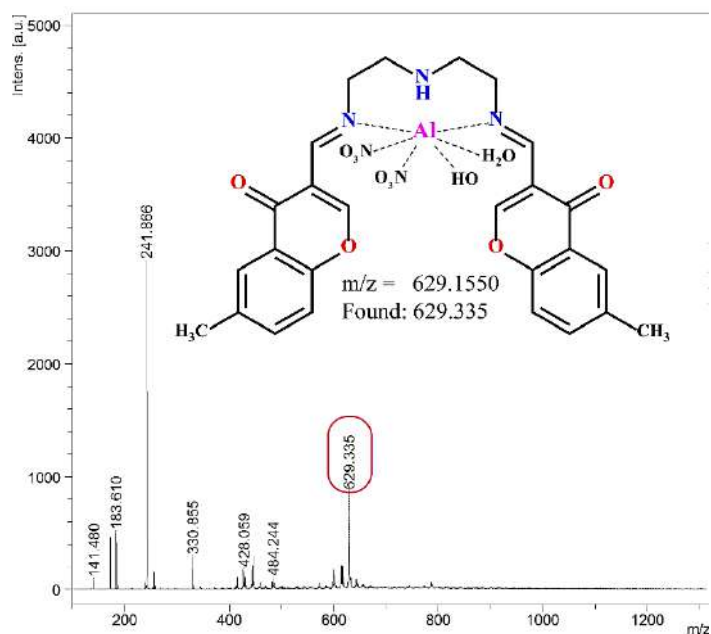


Figure A6B.6 Mass analysis of the solution of L_{10} with $\text{Al}(\text{NO}_3)_3 \cdot 9\text{H}_2\text{O}$. (positive mode).

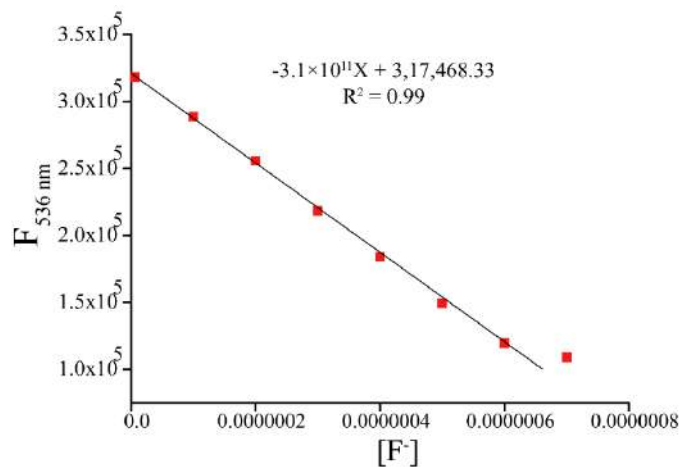


Figure A6B.7 Plot of emission intensity vs F^- [M] for the detection limit calculation. (emission intensity at 536 nm).

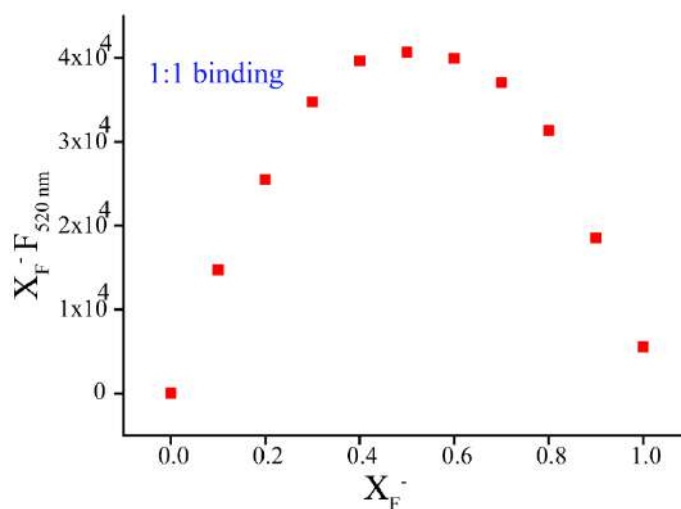


Figure A6B.8 Job's Plot for L_{10} with F^- from fluorescence emission spectrum at 520 nm. X_{F^-} = mole fraction of F^- in the presence of the guest.

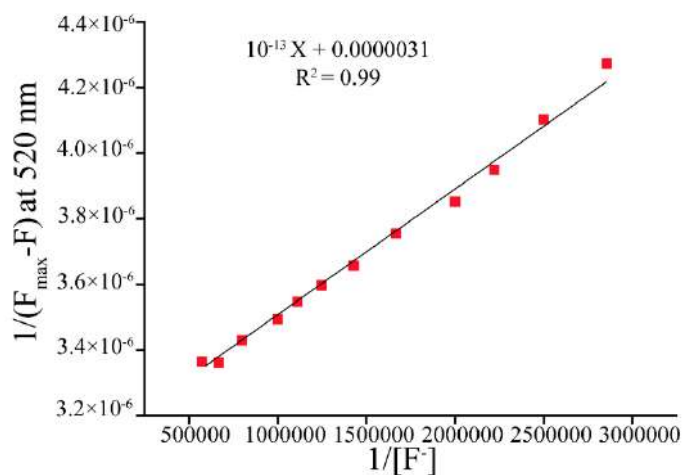


Figure A6B.9 Benesi–Hildebrand plot for calculation of association constant of F⁻ in acetonitrile medium from fluorescence experiment (emission intensity at 520 nm).

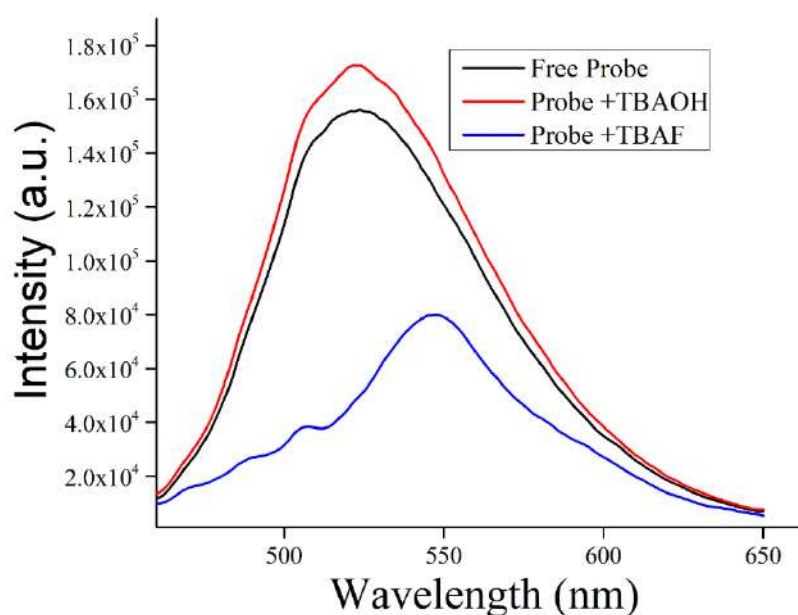


Figure A6B.10 Emission spectra of L_{10} with TBAOH and TBAF solution in acetonitrile medium

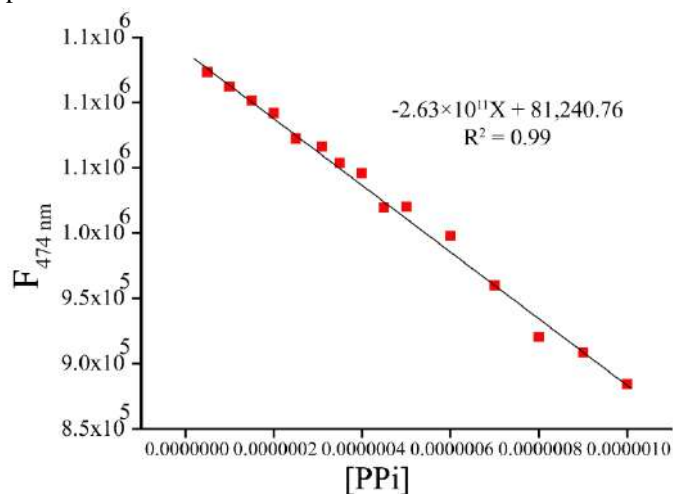


Figure A6B.11 Graph for the calculation of detection limit of PPi towards $[L_{10}-Al^{3+}]$ ensemble (emission intensity at 474 nm).

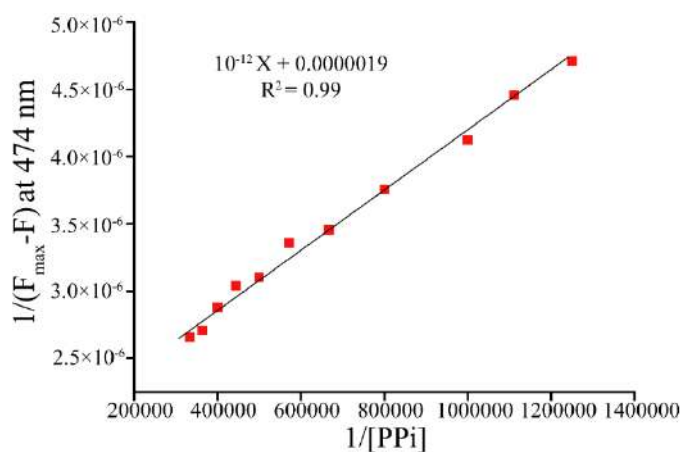


Figure A6B.12 Benesi-Hildebrand plot for calculation of association constant of PPI towards $[L_{10}\text{-Al}^{3+}]$ in aqueous medium from fluorescence experiment (emission intensity at 474 nm).

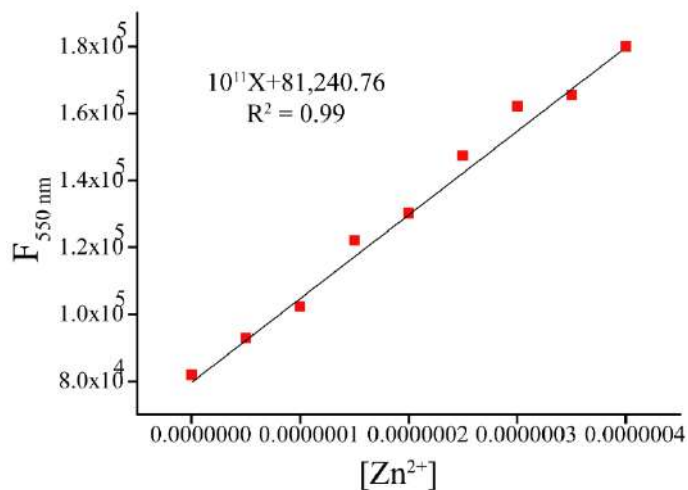


Figure A6B.13 Graph for the calculation of detection limit of Zn^{2+} towards $[L_{10}\text{-F}^-]$ ensemble (emission intensity at 550 nm).

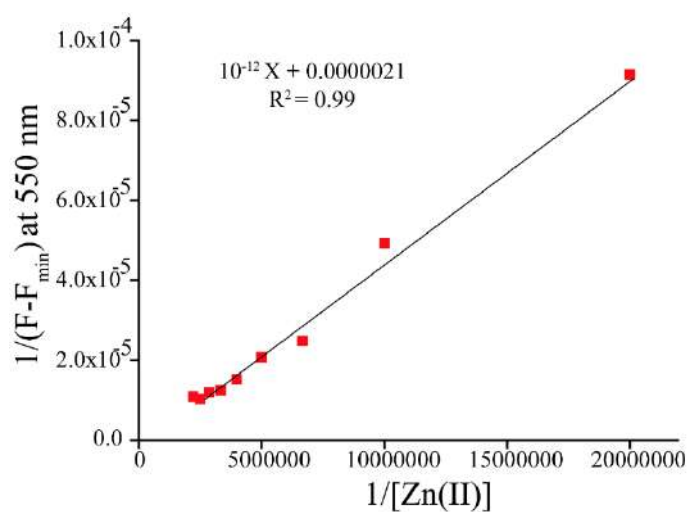


Figure A6B.14 Benesi-Hildebrand plot for calculation of association constant of Zn^{2+} towards $[L_{10}\text{-F}^-]$ in acetonitrile medium from fluorescence experiment (emission intensity at 550 nm).

Conclusion and Future Prospective

In summary, this thesis provides some substantial outcomes in the field of ‘supramolecular anion recognition chemistry’ where the anions or the hydrated anions or anionic associations are formed by some simply synthesized monopodial or dipodal acyclic receptors (**L**₁-**L**₆) decorated by the positional or electronic effect of terminal aryl substituents or anionic dimension or molecular host architectures in solid-state. Interestingly the dipodal receptors **L**₁-**L**₄ formed various halides/hydrated halide complexes whereas, among simple monopodial receptors **L**₅ and **L**₆, only **L**₅ could be able to form a dimeric association of $[\text{HCO}_3 \cdots \text{HCO}_3]^{2-}$ as well as of $[\text{HSO}_4 \cdots \text{HSO}_4]^{2-}$ which were supported by various non-covalent supramolecular interactions. Like dipodal receptors (**L**₁-**L**₄), monopodial receptors **L**₅ and **L**₆ also displayed the tendency to form various halide/hydrated halide complexes at room temperature. On the other hand, we are also interested in solution-state recognition of various ionic analytes in physiological medium. To aim that, at first, we have designed two simple pyrene/anthracene-based chemodosimeters namely, **L**₇ and **L**₈ connected through a C=C bond-forming D- π -A-type structure to facilitate interactions with ionic species where we have verified and studied the reactivity of C=C double bonds towards colorimetric (LOD = 0.09 ppm for **L**₇ and 0.76 ppm for **L**₈) and fluorometric (LOD = 0.55 ppm at 376 nm and 0.053 ppb at 455 nm for **L**₇ whereas 0.85 ppm for **L**₈) sensing of HSO_3^- based on Michael-type addition reaction in a mixed aqueous medium. To prove the feasibility of the probe in practical applications, we used **L**₇ for the quantitative detection of HSO_3^- in food, water samples, and dip-stick analysis.

Furthermore, probe **L**₉ was synthesized and the same displayed a selective “turn-on” emission response towards Al^{3+} (LOD = 1.97 μM) *via* chelation-enhanced fluorescence (CHEF) process. It could also deliver a naked-eye colorimetric response toward Cu^{2+} in a mixed aqueous medium. The *in situ* prepared [**L**₉- Al^{3+}] complex could selectively sense phosphate ions, particularly pyrophosphate (PP_i). The suggested detection pathway is the complexation-decomplexation pathway. As for biological applications, we have also investigated the DNA tracking ability of the ensemble mentioned above, and the present study established the utility of probe-coated dip-stick analysis with **L**₉ to detect Al^{3+} ions in the experimental medium. Finally, we have designed and synthesized a simple chromone derivative-based multi-selective chemical probe **L**₁₀ for selective “turn-on” detection of Al^{3+} (LOD = 5.5×10^{-7} M) in an aqueous medium followed by [**L**₁₀- Al^{3+}] ensemble-based subsequent detection of PP_i (LOD = 1.02×10^{-7} M) among all other common anions under the same experimental condition at physiological pH. On the other hand, **L**₁₀ could also be able to detect F^- (LOD = 6.4×10^{-8} M) in an acetonitrile medium

by deprotonation mechanism. The adduct (**L**₁₀-F) could also be used for recognition of Zn²⁺ (LOD = 2.96 μM) under an identical experimental milieu.

In the first portion of the thesis, we have simply focused on the design and synthesis of some simple dipodal or monopodial acyclic systems (host molecules) for recognition of anions, hydrated-anions, or anionic association in both solid- and solution-state that eventually has gained a significant response from the supramolecular research fraternity in recent times. But presently, more efforts have been invested into the design and synthesis of multi-arm or cyclic molecular receptors for various ionic species. So that we can explore more applications in catalyst, membrane transport, etc. which are known to be the most challenging field in supramolecular chemistry. However, to reach this area, basic work in tuning the coordination of anions/hydrated-anions inside the molecular association is highly appreciated. Research in these fields with importance on biomedical, technological, and environmental applications, based upon the extraordinary anion/hydrated-anion binding molecular system seems to be useful.

In the recent past, the chemistry of chromo-fluorogenic chemosensor/ chemodosimeter- based ionic analyte detection method has achieved exceptional importance. Successful recognition phenomena between a chemosensor/chemodosimeter and ionic guest (metals/anions) could be employed in physical chemistry, biochemistry, analytical chemistry, supramolecular chemistry, medical science, toxicology department, forensic sciences department. Major advantages of these kinds of sensor molecules are reflected from their ease of solubility in aqueous media and detection of an analyte in biological media with the brilliant spectral response at relatively long wavelengths (650-900 nm). All the results comprised in this thesis are very useful from any fundamental aspects and an application point of view in supramolecular chemistry. Again, the planning and preparation of new chemosensor ensembles for various analytes except anions is also recommendable. Research in these fields with an aim on technological as well as biomedical applications, based upon recognition of various ionic analytes looks to be helpful in the future.

Asesh Das

Department of Chemistry,

IIT Guwahati, Assam 781039, India

Ph. No.: +91-7001958685, +91-7578850891

Email: aseshdas12@gmail.com; aseshdas12@iitg.ac.in



Educational Qualification:

Qualifying Degree	Institution	Board/Council	Qualifying Year	CGPA or %
Ph.D.	Indian Institute of Technology Guwahati	IIT Guwahati	2022	
M.Sc.	Indian Institute of Technology Madras	IIT Madras	2016	8.00 (1 st Class)
B.Sc. (Hons.)	Ramakrishna Mission Vidyamandira, Belur Math	University of Calcutta	2014	71.5% (1 st Class)
Higher secondary (10+2)	Mahishadal Raj High School	WBCHSE	2011	75% (1 st Div.)
Secondary (10)	Vivekananda Mission Asram Sikshayatan	WBBSE	2009	85.25 (1 st Div.)

Past Project Experiences:

1. Worked as M. Sc. project (August 2015 - April 2016) under the supervision of Prof. K. Vidyasagar at IIT Madras.
2. Worked as Summer Project (June 2014 - July 2014) under the supervision of Prof. Sabyasachi Sarkar at IEST Shibpur

Present Research Area:

1. Supramolecular chemistry of biologically and environmentally relevant anions: Solid and solution-state studies of biologically and environmentally relevant anions in the highly electron-rich system and π -acidic systems.
2. Rational design and development of isomeric neutral hosts and their ability of binding with the anionic guests depending upon the electronic and positional isomeric effect of the terminal as well as core aromatic substituents.
3. Selective recognition of biologically crucial metal ions/anions with fluorescent and colorimetric sensors and dosimeters.

Languages known:

English, Bengali, Hindi

Analytical Skills:

Software operation: Microsoft Office (PowerPoint, Excel, and Word), Chem-Draw, Origin, Adobe Illustrator, Bruker D8 Venture, ORTEP, Mercury, SHELXL, WINGX, Crystal Explorer, MestreNova, Win-EQNMR, Bind-fit model, etc.

Instruments operation: X-ray Diffractometer SC-XRD (Trained operator), Spectro-fluorimeter, UV-Vis Spectrophotometer, FT-IR, NMR, Mass Spectra Analysis, pH meter.

Achievements and Qualification:

1. GATE exam (2016 and 2018) for admission in Master's and Doctoral courses in India-qualified.
2. NET (December 2015 and June 2016) examination-qualified (LS).
3. Diploma in Computer Application (August 2016).

Journal Publications:

1. Effect of substitution on halide/hydrated halide binding: a case study of neutral bis-urea receptors. **Ashesh Das**, Biswajit Nayak and Gopal Das, *Cryst. Eng. Comm.*, 2020, 22, 2197-2207.
2. Naphthyl-functionalized Ninhydrin-derived Receptor for 'CHEF'-based Sequential Sensing of Al(III) and PPI: Prospective Chemosensing Applications under Physiological Conditions. **Ashesh Das**, Sagnik De and Gopal Das, *Journal of Photochemistry and Photobiology A: Chemistry*, 2021, 418, 113442.
3. Selective chemodosimetric 'Turn-On' fluorescence sensor for HSO_3^- : Comparing the reactivity of the exocyclic vs. non-exocyclic C=C double bond. **Ashesh Das** and Gopal Das, *Journal of Photochemistry and Photobiology A: Chemistry*, 2022, 425, 113669.
4. Trapped Cyclic Dimeric Oxyanion Assembly by Urea-Functionalized Receptor: Potent Application in Linear Discriminant Analysis and as Antibacterial Agents. **Ashesh Das**, Biswajit Roy, Barlina Konwar, Aiyagari Ramesh and Gopal Das, *Cryst. Growth Des.*, 2022, 22, 3, 1778–1791.
5. Coumarin-based Symmetric Dipodal Probe as Multi-Analytic Sensor: Prospective Chemosensing Applications under Physiological Conditions. **Ashesh Das** and Gopal Das, Manuscript under review.
6. Self-Assemblies of Positional Isomeric Linear Bis-Urea Ligands with Oxyanions/Hydrated Oxyanions: Evidence of F^- and OH^- Induced Atmospheric CO_2 Fixation. Utsab Manna, **Ashesh Das**, and Gopal Das, *Cryst. Growth Des.*, 2018, 18, 11, 6801–6815.
7. Exploring Cyclohexane/Piperazine-urea Motifs for Spherical Halides ($\text{X} = \text{Cl}^- / \text{Br}^-$) Recognition: Effect on Anion Coordination, Photoluminescence, and Morphological Tunability, Megha Basak, **Ashesh Das**, and Gopal Das, *Cryst. Eng. Comm.*, 2021, 23, 7771-7780.

Teaching Experience

1. CH-415: Inorganic Chemistry Laboratory, MSc. Semester 2019
2. CH 101, Chemistry tutorial, B-Tech. Semester 2019
3. CH 110, Lab courses, B-Tech. Semester, 2021

Seminars and Conferences:

1. Active participation at **CiHS-2014** (on 13th August 2014 at IIT Madras)
2. Active participation at **CiHS-2015** (on 12th August 2015 at IIT Madras).
3. Poster presentation at “**MTIC XVIII**” (on 11-14 December 2019 at IIT Guwahati)
4. Oral presentation at “Research Industrial Conclave” (on 21-22 January 2022 at IIT Guwahati)

Workshop attended

Workshop on “**Single Crystal X-Ray Diffraction Techniques and its Applications**” organized by NECBH IIT Guwahati on 22nd - 23rd January 2021.